Modeling the Micellization Behavior of Fluorosurfactants using Molecular-Thermodynamic Theory

by

Jaisree Iyer

B. Tech., Chemical Engineering
Indian Institute of Technology, Bombay, India (2007)
M.S., Chemical Engineering Practice
Massachusetts Institute of Technology, Cambridge, USA (2012)

Submitted to the Department of Chemical Engineering in partial fulfillment of the requirements for the degree of

Doctor of Philosophy

at the

MASSACHUSETTS INSTITUTE of TECHNOLOGY

June 2013

Signature of Author……..
Department of Chemical Engineering
May 17, 2013

Certified by ……..
Daniel Blankschtein
Herman P. Meissner '29 Professor of Chemical Engineering
Thesis Supervisor

Accepted by……..
Patrick Doyle
Singapore Research Professor of Chemical Engineering
Chairman, Committee for Graduate Students

Modeling the Micellization Behavior of Fluorosurfactants using Molecular-Thermodynamic Theory

by

Jaisree Iyer

Submitted to the Department of Chemical Engineering on May 17, 2013
in Partial Fulfillment of the Requirements for the Degree of
Doctor of Philosophy

Abstract

Fluorinated surfactants are an important class of surfactants because they possess properties that are far superior than those of their hydrocarbon analogs. As a result, they are used in a wide variety of applications including in paints, polishes, fire-fighting foams, and emulsion polymerization processes. However, concerns regarding the non-biodegradability and toxicity of fluorinated surfactants have prompted the search for new, benign alternative surfactant formulations that possess micellization properties comparable to those of traditional fluorinated surfactants.

With this need in mind, this thesis focuses on gaining a molecular-level understanding of the micellization behavior of traditional fluorinated surfactants, and then using the acquired knowledge to design novel surfactant formulations that can reduce the use of fluorinated surfactants. Molecular-thermodynamic (MT) models were developed to calculate the various contributions to the free energy of micellization for discoidal and biaxial ellipsoidal micelles; two important micelle shapes in the context of fluorocarbon-based surfactants. These models explicitly incorporate the effect of the position-dependent curvature associated with discs and biaxial ellipsoids. Comparison between the models developed here with those that do not explicitly account for the varying curvature shows that accounting for the position-dependent curvature is extremely important in modeling these two micelle shapes. The new MT model for the free energy of micellization is also used to demonstrate the feasibility of realizing biaxial ellipsoidal micelles, a result refuted in the past in many theoretical studies on the basis of average geometrical properties of the micelle.

A new computer-simulation-molecular-thermodynamic (CSMT) framework was developed to predict the micellization behavior of mixtures of fluorocarbon-based surfactants. To facilitate the practical implementation of the mixture CSMT framework, which involves the computationally intensive task of simulating several mixed micelles, an approximation to the mixture CSMT model was developed. In this approximation, relevant properties for a mixed micelle are estimated using a micelle-composition based weighted average of the analogous properties obtained from simulations of the single-component surfactant micelles for each of the surfactants comprising the mixture. Therefore, in this approximation, the need for simulating mixed micelles is eliminated. The approximation was found to compare well

with the mixture CSMT model for various binary surfactant mixtures considered, except for those containing alkyl ethoxylate surfactants. A rationalization of this finding is presented. CMC predictions made using the mixture CSMT model were found to compare very well with the experimental CMCs for several binary mixtures of linear surfactants, thereby laying the foundation for using the CSMT model to predict micellization properties of mixtures of surfactants that have a more complex chemical architecture.

Finally, an MT framework was also developed to predict the micellization properties of mixtures of fluorocarbon-based and hydrocarbon-based surfactants. This mixing reduces the use of fluorinated surfactants in the surfactant formulation, thereby addressing the non-biodegradability and toxicity concerns associated with fluorinated surfactants. An enthalpy of mixing contribution resulting from the interactions between the fluorocarbon tails and the hydrocarbon tails, estimated using the Regular Solution Theory, was included in the MT framework. The ability of the MT framework to predict the coexistence of two types of mixed micelles in solution was demonstrated. The MT framework predictions of micelle population distributions, CMCs, and optimal micelle compositions were compared with the experimental values for various mixtures of fluorocarbon-based and hydrocarbon-based surfactants.

The models developed in this thesis provide a molecular level understanding of the micellization behavior of fluorocarbon-based surfactants and their mixtures. The models are able to predict several important micellization properties of surfactants and their mixtures that can guide surfactant formulators in the synthesis, characterization, design, and optimization of surfactant formulations that exhibit desirable properties.

Thesis Supervisor: Daniel Blankschtein

Title: Herman P. Meissner '29 Professor of Chemical Engineering

Acknowledgments

I would first like to thank my advisor, Professor Daniel Blankschtein. He gave me the freedom to pursue my own research ideas. His insistence on providing a physical meaning to mathematical solutions has helped me immensely in clearly communicating my ideas and explanations. My thesis would not have taken this shape without his tireless efforts. Research aside, his dedication towards teaching courses has always been inspirational. And the keen interest he shows in everyone's lives beyond research has always made for interesting conversations during group and research meetings. All in all, Professor Blankschtein has had a huge role to play in the cherished experience I had at MIT.

There are several others who contributed significantly towards this thesis. I would first like to thank my thesis committee members, Prof. Green and Dr. Nagarajan, who have always provided excellent feedback during my committee meetings. I benefited immensely from Dr. Nagarajan's expertise in the field as he provided a different perspective on my work and how it could be presented to the scientific community. In addition to the technical advice, I thank Prof. Green for his constant encouragement to invest time in seriously thinking about my career after MIT. I thank my industrial collaborators, Dr. Bruce Murch and Dr. David Eike from P&G, and Dr. John Green and Dr. Charlie Taylor from DuPont, for the much needed industrial perspective on how we can make our modeling work useful to them. I am grateful to the Dupont MIT Alliance and the Jerry & Geraldine S Mcafee Fellowship that funded my studies at MIT. And

special thanks to Iris, Mary, Katie, Suzanne, and Joel from the student office for their prompt support and timely reminders throughout my stay at MIT.

Among the DB group members, special thanks to Jonathan for his feedback on pretty much all the work I have done in the last six years. Thanks to Shangchao and Chih-Jen for their feedback on the simulations aspect of my thesis, and Vishnu for his assistance on a number of things over the last 2-3 years. Both Jonathan and Vishnu have always come up with solutions to my problems even if it meant they had to spend a few hours reading and thinking about it. I would also like to thank Diviya, Carl, Matheus and all other members of the DB group for creating the welcoming atmosphere we have in the lab.

Outside of research, participating in the Practice School program was a particularly rewarding experience. I was fortunate to be a part of a great group which included Prof. Claude Lupis, Prof. Bob Fisher, Jyoti, Kay, Justin, Bradley, Yuan, and Jinyoung. Working, traveling, and playing cards with them was truly an enjoyable experience. A special note of thanks to Jyoti who was my apartment mate for the two years she was at MIT. Her outgoing nature made me try many new things that I would not have tried on my own. Thanks to Jingqing, Justin, Kay, Shree, and Siddharth for providing great company in the last six years. And special thanks to Himanshu for being a great friend and introducing me to a lot of people around MIT.

Finally, a special thanks to my family for all their love. Everything that I am today is because of my parents. Thank you both. To Jani and Ramnath, thank you for all your love, support, and company during vacations. To Choma, my partner in a lot of things from a very young age, thank you for being a great brother. To my in-laws, thank you for being a wonderful

addition to my family. And to Daniel, the best thing that came out of MIT for me, thank you for your love, your encouragement, and everything else.

Contents

List of Figures

List of Tables

Chapter 1

Introduction

1.1 Fluorocarbon-Based Surfactants and their Applications

Surfactants are a unique class of chemicals that consist of a hydrophobic, traditionally alkyl, tail attached to a hydrophilic head.[1, 2] When added to water, surfactants partition between an available interface and the bulk water phase. At the interface, the surfactant's hydrophilic heads remain in contact with water, while the surfactant's hydrophobic tails stay away from water. Adsorption of surfactant molecules at the interface reduces the surface tension of water.[2] In the bulk water phase, at low surfactant concentrations, the surfactant molecules remain singly dispersed as surfactant monomers. Beyond a threshold surfactant concentration, known as the Critical Micelle Concentration (CMC), where there are sufficient singly-dispersed surfactant monomers, the surfactant molecules in the bulk water phase spontaneously self-assemble into aggregates called micelles.[2] In a micellar aggregate, the hydrophobic tails form the internal core and the hydrophilic heads shield it from the unfavorable contact with water.

Fluorinated surfactants are an important class of surfactant molecules in which the hydrogen atoms in the traditional alkyl tail are partially, or completely, replaced by fluorine atoms. Owing to its position in the periodic table, the fluorine atom exhibits many extreme

properties. It is the most electronegative element, making fluorinated molecules difficult to polarize.[3] This low polarizability leads to weak intermolecular interactions between perfluorocarbons (fully-fluorinated carbon backbones),[3] and makes fluorinated surfactants very efficient surface active agents. For example, the addition of 5 mM of perfluorooctanoic acid ($CF_3(CF_2)_6COOH$), a common fluorocarbon-based surfactant, to water reduces the surface tension of water from 73 mN/m to 15.3 mN/m at 25^0C.[3] In contrast, at the same temperature, the addition of 30 mM of sodium octanoate ($CH_3(CH_2)_6COOH$), a common hydrocarbon-based surfactant, to water reduces the surface tension of water from 73 mN/m to only 40 mN/m.[4]

The low polarizability of perfluorocarbons also implies that they do not exhibit strong attractions towards many other compounds, including hydrocarbons, making them both hydrophobic and lipophobic.[5] Another salient characteristic of fluorinated surfactants is the high strength of the C-F bond. A large amount of energy is required to break a C-F bond, making fluorocarbons thermally inert.[5] In addition, the fluorine atom is just big enough to effectively cover the carbon skeleton in perfluorocarbons. This results in very high activation energies for any reaction involving the formation of any new bonds with the carbon backbone.[6] As a result, perfluorocarbons are thermally stable and chemically inert, and therefore, widely used in applications where the environment is not conducive to utilizing hydrocarbon-based surfactants, for example, in environments with high temperatures and corrosive conditions.[5]

The ability of fluorinated surfactants to significantly reduce the surface tension of water makes them powerful wetting agents. This facilitates even spreading of different materials on surfaces, and results in uniform coatings. Therefore, fluorinated surfactants are used extensively in paints, polishes, and floor waxes to obtain a smoother finish. The special wetting properties of fluorinated surfactants find use in adhesives, where they improve contact between two surfaces.[5]

The lipophobicity of fluorinated surfactants is used in the paper industry to manufacture paper cartons used in fast food carry outs. Fluorinated surfactants make the cartons oil repellent, thereby preventing oil and grease from wetting the carton.[5] The chemical stability of fluorinated surfactants makes them useful in electroplating baths, where hydrocarbon surfactants would not work because of the acidic environment. The surfactant prevents mist formation by reducing the surface tension of the solution which decreases the size of the gas bubbles.[5] Use of fluorinated surfactants in fire fighting foams is an excellent example of an application where most of the special properties mentioned above are put to use. Indeed, owing to the low surface tension, the foam, with fluorinated surfactants as a constituent, is able to quickly spread over the hydrocarbon fuel surface, while its oil repelling property enhances the foam's fire extinguishing capability because the surfactant coat does not allow oil fumes to escape and spread.[5]

In all the above mentioned applications, fluorinated surfactants have been used to enhance the surface properties of materials. In addition, fluorinated surfactants find ample use in applications where there is a need to modify bulk solution properties. They are used as emulsifiers to synthesize fluoropolymers via emulsion polymerization. The advantage of utilizing emulsion polymerization is that it prevents coagulation of polymer particles and provides better control of particle size compared to polymerization in the bulk.[5] The cosmetic industry uses fluorinated surfactants as emulsifiers, lubricants, or lipophobic agents in hair products to modify their consistency, lubricity, and oil repelling character.[5] Fluorinated surfactants can also be utilized in environmental remediation processes in which surfactant micelles are used to solubilize hydrophobic contaminants which are later destroyed chemically (oxidation/reduction) or thermally. Here, the advantage of using fluorinated surfactants over their hydrocarbon counterparts is that due to their chemical and thermal inertness, they do not degrade

when the solubilized contaminants are destroyed, and can therefore be reused.[7]. Undoubtedly, the most publicized application of fluorinated surfactants is their potential use in blood substitutes. They are an attractive option for synthetic oxygen carriers because they are chemically inert and solubilize gases like oxygen and carbon dioxide. Currently, there are a few blood substitutes based on perfluorocarbon emulsions, for example, Oxycyte, which are undergoing clinical trials.[7,8]

1.2 Motivation

In most applications involving surfactant solutions, both the surface and the bulk properties of the solution are affected by the surfactant micellization behavior. For example, it is well-known that the surface tension of water decreases upon addition of a single surfactant type, varying linearly with the logarithm of the surfactant concentration until the CMC is reached, and becoming approximately constant beyond the CMC.[8] Accordingly, the maximum reduction of surface tension is achieved by adding sufficient surfactant such that the resulting solution concentration is approximately equal to the CMC. Adding more surfactant to the solution does not result in any further significant reduction of the surface tension and is therefore unwarranted. To predict the CMC, one needs to model surfactant micellization, because the CMC is the surfactant concentration that marks the onset of micelle formation in the bulk solution. Note that in the case of mixed surfactant systems, the surface tension of the solution continues to vary even after the onset of micellization. Beyond the CMC, surfactant molecules present in micelles, as monomers, and at the interface are in thermodynamic equilibrium with each other. This three-way equilibrium needs to be modeled in order to predict the surfactant adsorption behavior and associated surface tension reduction as a function of bulk surfactant concentration.

As another example, in the case of emulsion polymerization reactions in water, the role of the surfactant micelles is to solubilize monomers, which undergo polymerization and act as polymer nucleation sites.[9] As a result, an increase in the number of micelles leads to an increase in the number of polymer nucleation sites, resulting in higher polymerization rates. In addition, the larger the number of polymer nucleation sites, the smaller the size of the polymer particles formed, because the same amount of monomer is distributed among a larger number of particles. Furthermore, it is expected that the shape and size of the micelles should play a key role in determining the shape and size of the resulting polymer particles. Clearly, a fundamental understanding of the micellization behavior of fluorinated surfactants in aqueous solution will allow prediction of important solution properties, including CMCs, micelle shapes, micelle aggregation numbers, micelle compositions in the case of mixed micelles, and degrees of counterion binding in the case of ionic surfactant micelles, which are all key properties for the practical use of fluorinated surfactants.

The downside of using fluorinated surfactants is that they are not biodegradable due to their chemical and thermal inertness.[5] Most organic fluorinated compounds of industrial relevance degrade to either perfluoro carboxylic acids ($CF_3(CF_2)_{n-2}COOH$) or perfluoro sulfonates ($CF_3(CF_2)_{n-1}SO^{3-}$).[10] Therefore, the majority of toxicology studies involving organic fluorinated compounds have focused on the toxicity of these two compounds. Perfluoro carboxylic acids and perfluoro sulfonates have been detected in the environment and in living beings including humans. The concentrations of these compounds are high among those who are occupationally exposed to these chemicals. These chemicals are retained in their blood even years after they stopped working. Both perfluoro carboxylic acids and perfluoro sulfonates have long retention rates in the human body.[10,11] In tests with rodents, perfluorooctanoic acid

($CF_3(CF_2)_6COOH$, PFOA) was found to be mildly carcinogenic,[10] and can also lead to malfunctioning of the liver.[11] Perfluorooctyl sulfonate ($CF_3(CF_2)_7SO^{3-}$, PFOS) has also been shown to be toxic to aquatic animals. However, these compounds are toxic only if their concentration exceeds a threshold value. Hekster et al.[10] derived an indicative maximum permissible concentration for PFOA and PFOS based on the available toxicity data. They calculated a value of 300µg/l for PFOA and 5µg/l for PFOS. Except in cases of accidental fire-fighting foam spills, the contamination is within this safety threshold, and therefore, should not affect the well being of animals. However, in the absence of biochemical degradation, these chemicals can accumulate over time, resulting in sufficiently high concentrations capable of inducing toxicity.[10]

The potential toxic effects of PFOA, due to its non biodegradable nature, have prompted the need to find new alternative surfactant formulations that possess properties similar to those of traditional fluorinated surfactant formulations. However, before exploring potential alternatives, it is beneficial to gain a molecular-level understanding of the micellization behavior of traditional fluorinated surfactants. Indeed, the knowledge acquired by understanding the micellization behavior of traditional fluorinated surfactants will better equip us to design novel surfactants that have the potential to replace or reduce the use of fluorinated ones. Potential replacements for fluorocarbon-based surfactants include: (i) surfactants with one head and two tails – one fluorocarbon and one hydrocarbon, and (ii) surfactants with a partially-fluorinated tail.[12] The use of fluorinated surfactants can also be reduced by mixing fluorocarbon-based surfactants with other benign surfactants like hydrocarbon-based surfactants.

1.3 Research Objectives

With the background and motivation presented in Sections 1.1 and 1.2 in mind, the central goal of this thesis is to develop a theoretical framework to predict the micellization behavior of fluorinated surfactants at the molecular level. The fundamental and practical insights gained from the modeling presented here can be used to evaluate potential substitutes for fluorinated surfactant formulations that possess the desired properties, but use a minimal amount of fluorocarbon material. These insights can also be used to model and evaluate the micellization behavior of mixtures of surfactants having minimal amount of fluorinated material obtained by mixing fluorocarbon-based surfactants with other benign surfactants. This ability to predict micellization properties will greatly reduce the number of carefully-executed experiments required to synthesize substitute formulations for fluorinated surfactants, including characterizing their properties. In addition, this will also contribute to the overall fundamental understanding of the micellization behavior of fluorinated surfactants in aqueous solution.

In order to accomplish the broad goal of my thesis, the following three research objectives will be pursued:

1. Modeling the micellization behavior of single fluorocarbon-based surfactants.

2. Modeling the micellization behavior of binary mixtures of two fluorocarbon-based surfactants.

3. Modeling the micellization behavior of binary mixtures of a hydrocarbon-based and a fluorocarbon-based surfactant.

1.4 Thesis Overview

Before discussing the model developments associated with aims 1, 2, and 3 above, a brief overview of the Molecular-Thermodynamic (MT) framework, which constitutes the foundation of this thesis, is presented in Chapter 2. This chapter also includes a brief description of the recently developed Computer-Simulation-Molecular-Thermodynamic (CSMT) framework, which blends microstructural information, derived from all-atomistic molecular dynamics simulations of surfactant monomers and micelles, with the well-established MT framework, to model complex surfactants that are not amenable to traditional MT modeling. Subsequently, Chapters 3, 4, and 5 address specific issues associated with research aims 1, 2, and 3 above. Specifically, Chapter 3 discusses the development of the MT framework for discoidal micelles (an important micelle shape for fluorocarbon-based surfactants) and biaxial ellipsoidal micelles (an importance transition shape between spherical and cylindrical or discoidal micelles). The MT framework for these micelle shapes is significantly more complex that the previous MT models developed for spherical, cylindrical, and bilayer-like micelles due to the varying curvature associated with discs and ellipsoids. The importance of the new curvature-corrected model developed for discoidal micelles is highlighted by comparing it with an approximate model for discoidal micelles, where the effect of curvature is not accounted for rigorously. In the final section of Chapter 3, the model developed for biaxial ellipsoidal micelles is used to predict the micelle shape distribution for several single nonionic fluorocarbon-based surfactants to shed light on the feasibility of forming biaxial ellipsoidal micelles, a topic of great controversy in the literature on micelle shapes.

In Chapter 4, a CSMT framework for mixtures of surfactants is developed. Recognizing the computational costs associated with the implementation of the mixture CSMT framework, an

approximate method based on a composition-weighted average is also developed. The applicability of the approximate model is evaluated by comparing its results with the mixture CSMT results for a variety of binary mixtures of surfactants. Due to the scarcity of experimental micellization data for binary mixtures of fluorocarbon-based surfactants, the mixture CSMT framework is used to predict CMCs of binary mixtures of hydrocarbon-based surfactants, including comparing the CMC predictions with the experimental CMC values. The model is also used to predict the CMC of a binary mixture of fluorocarbon-based surfactants for which experimental CMC data is available.

In Chapter 5, an MT model for binary mixtures of fluorocarbon-based surfactants and hydrocarbon-based surfactants is developed. These mixtures are different from mixtures of fluorocarbon-based surfactants because of the antagonistic enthalpic interactions between the hydrocarbon tails and the fluorocarbon tails, which can lead to the formation of two types of micelles in solution: one rich in the fluorocarbon-based surfactant and the other rich in the hydrocarbon-based surfactant. The new model is used to predict micellization properties, including CMCs and micelle population distributions, for binary mixtures of fluorocarbon-based and hydrocarbon-based surfactants for which the relevant experimental data is available.

In Chapter 6, a summary of the key findings in the thesis are presented. Ideas for further research based on the findings presented in Chapters 3, 4, and 5 are also presented. Finally, the Appendix at the end of the thesis in Chapter 7 contains valuable information that supplements the material presented throughout this thesis.

Chapter 2

Molecular-Thermodynamic Theory of Micellization

2.1 Introduction

Surfactant micellization has been modeled using various theories, including cell and lattice theories,[13] self-consistent field theories,[14] quantitative structure-property relationships,[15,16] and more recently, simulation-based techniques.[15] Most of these theories require experimental data, or values of parameters quantifying interactions between the surfactant heads and tails. This limitation is mitigated in the molecular-thermodynamic (MT) theories of micellization.[16, 17] Indeed, in the MT approach, the bulk thermodynamics of the micellization phenomenon is combined with a molecular-level description of the surfactant to predict micellization properties. Consequently, no experimental micellization data is required to make predictions of micellization properties of single surfactants and their mixtures using the MT framework. In addition, due to the inclusion of a molecular-level description, the MT framework sheds light on the roles of the surfactant chemical structure, including its hydrophilic head and hydrophobic tail, as well as of the surfactant solution conditions, including temperature,[18] salt concentration,[19]

pH,[20] surfactant concentration[18] and composition,[21] in the micellization process. A brief background on the current state of the MT framework, which constitutes the foundation of this thesis, is presented in this chapter. Specifically, Section 2.2 and Section 2.3 discuss the thermodynamics of micellization and the molecular model for the free energy of micellization, respectively. Subsequently, Section 2.4 provides a brief overview of the recently developed Computer-Simulation-Molecular-Thermodynamic (CSMT) framework, which blends information from molecular dynamics simulations of surfactant monomers and micelles with the MT framework discussed in Sections 2.2 and 2.3. Finally, Section 2.5 discusses the methods used to calculate micellization properties, including critical micelle concentrations, micelle shapes, sizes, compositions and degrees of counterion binding.

2.2 Thermodynamics of Micellization

The molecular-thermodynamic (MT) framework blends a thermodynamic description of a micellar solution with a molecular-level description of the free energy of micellization. The free energy of micellization is a quantitative measure of the tendency of a surfactant molecule to micellize, that is, to transfer from the monomeric state to the micellar state. Given the chemical structure of a surfactant and the solution conditions, the MT framework can predict several micellization properties, including the critical micelle concentration, and the micelle shape and size in solution, without using any experimental micellization data.[17]

Using concepts from thermodynamics, the free energy, G, of an aqueous surfactant solution at temperature, T, and pressure, P, containing $N_{S,i}$ molecules of surfactant i, dispersed in N_W water molecules, can be written as the sum of: (i) the free energy of the constituents of the surfactant solution, (ii) the free energy associated with forming micelles from surfactant

monomers, and (iii) the free energy associated with the mixing of the different constituents of the surfactant solution. This is illustrated pictorially in Figure 2-1 for the case of an aqueous solution of a single nonionic surfactant. For the more general case of mixtures of surfactants with a single associated counterion, the free energy of the micellar solution, G, can be written as follows:[22]

$$G = N_W \mu_{W,0} + \sum_i N_{S,i} \mu_{S,i,0} + N_c \mu_{c,0} + \sum_{n>1} N_n n g_{mic} + kT \left(N_W \ln X_W + \sum_i N_{1,i} \ln X_{1,i} + N_{1,c} \ln X_{1,c} + \sum_{n>1} N_n \ln X_n \right) \quad (2\text{-}1)$$

where $\mu_{W,0}$, $\mu_{S,i,0}$, and $\mu_{c,0}$ are the chemical potentials of pure water, of monomers of surfactant i at infinite dilution, and of the surfactant counterions at infinite dilution, N_c is the number of surfactant counterions added to the surfactant solution, N_n is the number of surfactant micelles with an aggregation number n, g_{mic} is the free energy of micellization per surfactant molecule (a

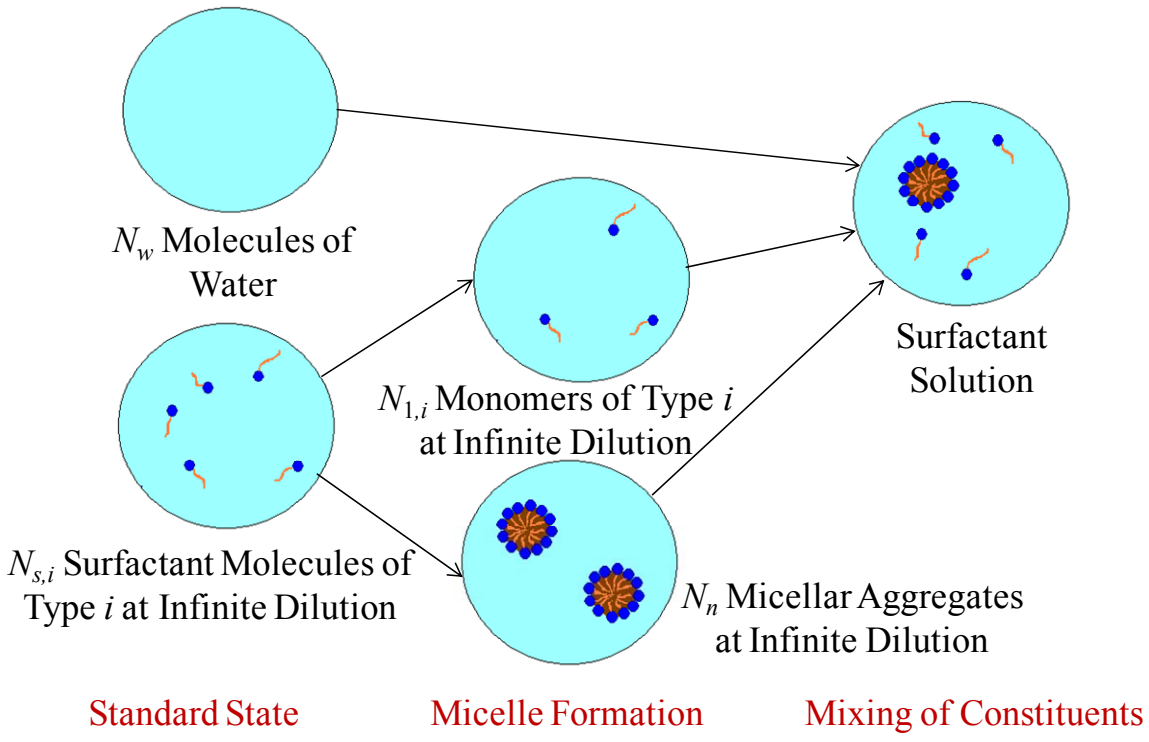

Figure 2-1: Conceived hypothetical process for the formation of a surfactant solution consisting of nonionic surfactants.

function of the characteristics of the micelle, including its shape, size, composition, and degree of counterion binding), k is the Boltzmann constant, T is the absolute temperature, $N_{1,i}$ and $N_{1,c}$ are the number of free monomers of surfactant i and free surfactant counterions, respectively, and X_W, $X_{1,i}$, X_{1c}, and X_n denote the mole fractions of water, monomer of surfactant i, free surfactant counterion, and micelle of aggregation number n, respectively. Note that the mole fraction X_j is defined as $X_j = N_j / \left(N_W + N_S \right)$.[23] The first three terms in Eq. (2-1) represent the free energy of the constituents of the surfactant solution in their corresponding standard states, the fourth term represents the free energy of forming the micelles from the surfactant monomers, and the last term represents the free energy of mixing the different constituents of the surfactant solution. Note that the free energy model in Eq. (2-1) is valid only for dilute surfactant solutions, where intermicellar interactions may be neglected and the free energy of mixing may be by modeled as being ideal. In addition, Eq. (2-1) assumes that there is only one counterion type associated with the ionic surfactants comprising the mixture. Note, however, that Eq. (2-1) can be readily extended to systems having multiple counterions.

Surfactant micellization is modeled by accounting for the equilibrium that exists between the singly-dispersed surfactant monomers and the micellar aggregates present in the micellar solution above the CMC.[16, 24] Thermodynamically, this equilibrium is attained when the Gibbs free energy of the micellar solution attains its minimum value. Note that in Eq. (2-1), $G = G(T, P, N_w, N_{s,i}, N_c, N_{1,i}, N_{1,c}, N_n)$, and is subject to the following mass balance constraints[24] on each of the constituent species:

$$N_w = \text{constant} \tag{2-2}$$

$$N_{1,i} + \sum_{n>1} n\alpha_{n,i} N_n = N_{S,i} = \text{constant} \qquad \forall i \tag{2-3}$$

$$N_{1,c} + \sum_{n>1} n\beta_n N_n = N_c = \text{constant} \tag{2-4}$$

where $\alpha_{n,i}$ is the micelle composition of surfactant i, and β_n is the degree of counterion binding and is defined as the number of counterions, per surfactant molecule, bound to the micelle. Equations (2-2) - (2-4) show that, at constant T and P, G is only a function of N_n. Minimizing G in Eq. (2-1) with respect to N_n, at constant T and P, subject to the constraints on N_w, $N_{s,i}$, N_c, $N_{1,i}$, and $N_{1,c}$ in Eqs. (2-2) - (2-4), yields:

$$\begin{aligned}
&\left(\frac{\partial G}{\partial N_n}\right)_{T,P,N_w,N_{s,i},N_c,N_k\neq N_n} = 0 \\
&\Rightarrow n g_{mic} + kT\left(\sum_i \left(-n\alpha_{n,i}\right)\left(\ln X_{1,i}+1\right) + \left(-\beta_n n\right)\left(\ln X_{1,c}+1\right) + \left(\ln X_n + 1\right)\right) = 0 \\
&\Rightarrow \ln X_n = \sum_i n\alpha_{n,i} \ln X_{1,i} + n\beta_n \ln X_{1,c} - \frac{n g_{mic}}{kT} + n + n\beta_n - 1 + \left(n \ln X_1 - n \ln X_1\right) \\
&\Rightarrow X_n = \frac{1}{e}\exp\left(n\left(-\frac{g_{mic}}{kT} + 1 + \beta_n + \sum_i \alpha_{n,i} \ln \frac{X_{1,i}}{X_1} + \beta_n \ln X_{1,c}\right) + n \ln X_1\right) \\
&\Rightarrow X_n = \frac{1}{e}\left(\frac{X_1}{\exp\left(\frac{g_{mic}}{kT} - 1 - \beta_n - \sum_i \alpha_{n,i} \ln \alpha_{1,i} - \beta_n \ln X_{1,c}\right)}\right)^n
\end{aligned} \tag{2-5}$$

where $\alpha_{1,i} = {X_{1,i}}\Big/{\sum_i X_{1,i}} = {X_{1,i}}\Big/{X_1}$ is the monomer composition. Equation (2-5) indeed yields the minimum value of G because $\frac{d^2 G}{dN_n^2} = kT\left(\sum_i \frac{\left(-n\alpha_{n,i}\right)^2}{N_{1,i}} + \frac{\left(-\beta_n n\right)^2}{N_{1,c}} + \frac{1}{N_n}\right) > 0$. Note that the concentration of micelles of aggregation number n, X_n, given in Eq. (2-5), depends on the micelle shape, size, composition, degree of counterion binding, surfactant monomer concentration, and free counterion concentration, and not just on the aggregation number, n, as the subscript suggests. The concentration of every micelle type can be calculated by substituting the free

energy of micellization associated with that micelle type in Eq. (2-5). The molecular model to calculate the free energy of micellization is presented in the following section.

2.3 Free Energy of Micellization

The free energy of micellization is the free-energy change experienced by a surfactant molecule as it transfers from the monomeric state to the micellar state. Since free energy is a state function, we can construct a convenient hypothetical path to calculate the free energy of micellization, g_{mic}. This hypothetical path for a cationic surfactant with an associated negative counterion is illustrated in Figure 2-2. For the general case of a mixture of surfactants, g_{mic} can be decomposed as shown below, where each free-energy contribution listed is on a per surfactant molecule basis:[17, 25]

$$g_{mic} = g_{tr} + g_{int} + g_{pack} + g_{st} + g_{elec} + g_{mix} \tag{2-6}$$

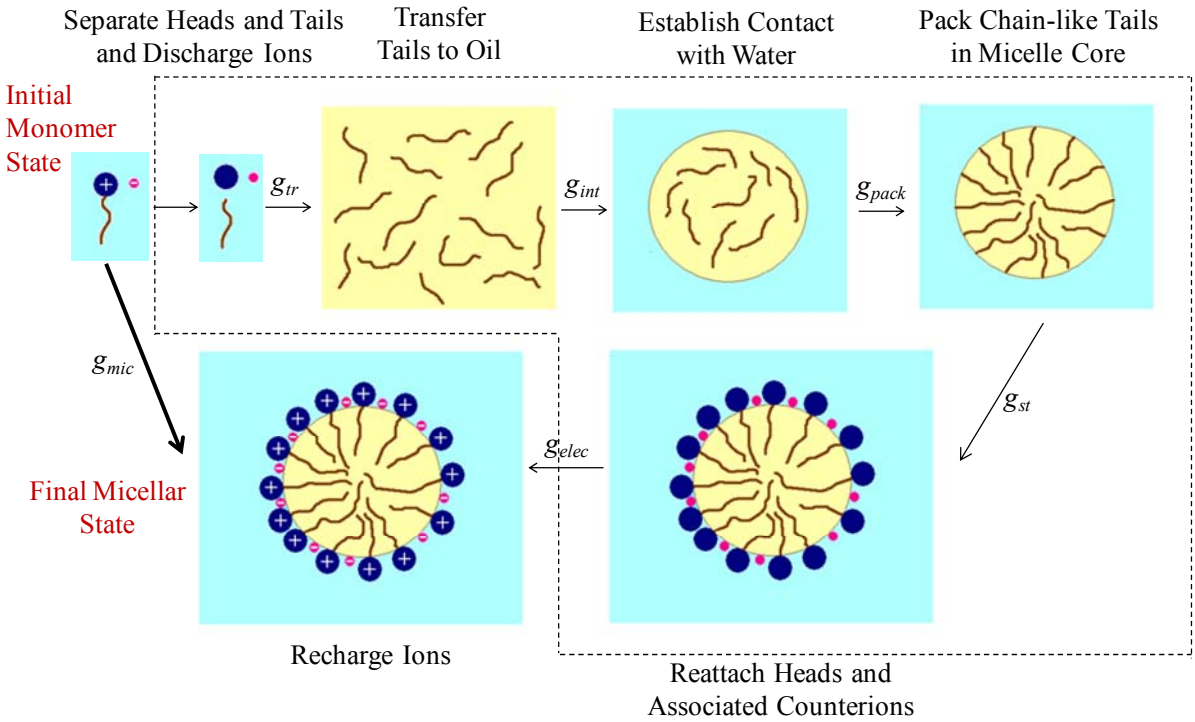

Figure 2-2: Hypothetical process for the formation of a micelle from surfactant monomers.

In Eq. (2-6), g_{tr} is the transfer free energy, g_{int} is the interfacial free energy, g_{pack} is the packing free energy, g_{st} is the steric free energy, g_{elec} is the electrostatic free energy, and g_{mix} is the mixing contribution to the micellization free energy. As indicated in Section 2.2, Eq. (2-6) can be obtained by conceiving a hypothetical path in which one first breaks the bonds between the surfactant heads and tails to separate the heads from the tails, and also discharges all the ionic species. Subsequently, one transfers the tails from an aqueous environment to a bulk tail-like (oil) phase. The free-energy change associated with this step is referred to as the transfer free energy, g_{tr}, and can be expressed in terms of the aqueous solubility of the tail of surfactant i, S_i, as follows:[17, 25]

$$g_{tr} = \sum_i \alpha_{n,i} kT \ln S_i \tag{2-7}$$

The transfer free energy of a hydrocarbon surfactant tail, $g_{tr,H}$, having n_{tail} carbon atoms is calculated based on the aqueous solubility of the hydrocarbon tail and is given by:[17, 25]

$$\frac{g_{tr,H}}{kT} = \frac{905}{T} - \frac{313}{T} n_{tail} - 5.06 - 0.44 n_{tail} \tag{2-8}$$

where T is the absolute temperature. Note that Eq. (2-8) was obtained by fitting the temperature variation of the experimental solubility of alkanes having different number of carbon atoms to obtain the transfer free energy contributions of a CH_2 and a CH_3 group. Equation (2-8) shows that, at 25 ^{0}C, the contributions of a CH_3 and a CH_2 group to the transfer free energy are -3.51 kT and -1.49 kT, respectively. Therefore, at 25 ^{0}C $g_{tr,H}$ is given by:

$$\frac{g_{tr,H}}{kT} = -3.51 - 1.49\left(n_{tail} - 1\right) \tag{2-9}$$

Similarly, at 25 ^{0}C, the contributions of a CF_3 and a CF_2 group to the transfer free energy of a fluorocarbon surfactant tail, calculated based on the solubility data reported by Kabalnov et al.,[25,

[26] are -4.85 kT and -2.30 kT, respectively. Therefore, at 25 ^{0}C, the transfer free energy of a linear fluorocarbon surfactant tail, $g_{tr,F}$, having n_{tail} carbon atoms is given by:

$$\frac{g_{tr,F}}{kT} = -4.85 - 2.30\left(n_{tail} - 1\right) \tag{2-10}$$

Following the transfer process, one re-establishes the contact between the tail phase and water by forming a drop from the tail phase. The free-energy change associated with this step is known as the interfacial free energy, g_{int}, and is modeled as follows:[17]

$$g_{int} = \sigma_{mix}\left(a - \sum_i \alpha_{n,i} a_{0,i}\right) = \sum_i \alpha_{n,i}\sigma_i\left(a - \sum_i \alpha_{n,i} a_{0,i}\right) \tag{2-11}$$

where σ_{mix} is the curvature-corrected interfacial tension between water and the oil drop, σ_i is the curvature-corrected interfacial tension between water and the oil drop formed by surfactant i,[27] a is the surface area per molecule, and $a_{0,i}$ is the surface area per molecule of the oil drop that is shielded from contact with water due to the physical connection between the head and tail of surfactant i. Note that a_0 is equal to 21.0 Å^2 and 29.8 Å^2 for linear hydrocarbon-based surfactants and linear fluorocarbon-based surfactants, respectively.[17, 28] We believe that it is necessary to incorporate the effect of curvature on the interfacial tension because micelles are small in size, thus resulting in high curvatures, for which the interfacial tension is known to deviate from its value for flat interfaces.[27, 29] Consequently, in Eq. (2-11), we use Tolman's correction to estimate the interfacial tension of a curved interface, σ, using the mean curvature of the interface, c, the Tolman distance, δ, and the interfacial tension across a flat interface, σ_0.[27] Specifically,

$$\sigma \approx \sigma_0\left(1 - 2c\delta\right) \tag{2-12}$$

The mean curvature of the interface, c, depends on the shape of the micelle. For example, for the three regular shapes, spheres, infinite cylinders, and infinite bilayers, c = 1/r, 1/2r and 0,

respectively, where r is the radius of the sphere or infinite cylinder. To obtain agreement with experimental results, the value of the Tolman distance for a 11-carbon hydrocarbon tail was set at 2.0 Å. The same value was also used for an 11-carbon fluorocarbon tail. The values of δ for all the other linear tails having n_{tail} carbons in the tail were calculated using the equation below:[30, 31]

$$\delta\left(n_{tail}\right)=\delta\left(11\right)\left(\frac{l_{\max}\left(n_{tail}\right)}{l_{\max}\left(11\right)}\right) \tag{2-13}$$

where l_{max} is the maximum length of the surfactant tail. Note that l_{max} is calculated based on the bond lengths, bond angles, and van der Waals radii characterizing the tail. For hydrocarbon tails, the maximum tail length is given by:[1]

$$l_{\max,H}=1.54+1.265n_{tail}\quad\left(\text{in Å}\right) \tag{2-14}$$

For fluorocarbon tails, the maximum tail length is given by:[28]

$$l_{\max,F}=2.04+1.30n_{tail}\quad\left(\text{in Å}\right) \tag{2-15}$$

The interfacial tension, in dyne/cm, between the micelle core and water for a hydrocarbon-based surfactant having n_{tail} carbon atoms in the tail, obtained by fitting the experimental interfacial tension data reported by Aveyard et al., is given by:[31, 32]

$$\sigma_{0,H}=\frac{1.381\left(57.868n_{tail}+117.99-T\left(0.059n_{tail}+0.1768\right)\right)}{n_{tail}+2.4} \tag{2-16}$$

where T is the absolute temperature. Based on the interfacial tensions between perfluorocarbons and water reported by Kabalnov et al.,[25] a value of 55.0 dyne/cm (independent of the surfactant tail length) was chosen for the interfacial tension between the micelle core and water for all the fluorocarbon-based surfactants considered.[28]

Finally, the surface area per molecule, a, is calculated using knowledge of the total surface area of the micelle core, A, which depends on the micelle shape and size, and the volumes of the surfactant tails, v_{tail}, residing in the micelle core. Specifically,

$$a = \frac{A}{n} = \frac{A}{\left(V / v_{tail}\right)} \tag{2-17}$$

where V is the volume of the micelle core. The tail volumes of a hydrocarbon tail, $v_{tail,H}$, and a fluorocarbon tail, $v_{tail,F}$, were estimated based on the densities of alkanes[1] and perfluorocarbons,[25, 28, 33] respectively. Specifically,

$$v_{tail,H} = 54.3 + 26.9\left(n_{tail} - 1\right) \quad \left(\text{in Å}^3\right) \tag{2-18}$$

$$v_{tail,F} = 84.0 + 41.6\left(n_{tail} - 1\right) \quad \left(\text{in Å}^3\right) \tag{2-19}$$

Following the formation of the oil drop, one needs to recognize that it does not mimic the micelle core precisely because the surfactant tails are subject to stricter conformational constraints in the micelle core than in the oil drop. The free-energy change associated with constraining the surfactant tails to mimic the micelle core is referred to as the packing free energy, g_{pack}. It is calculated based on a mean-field, statistical-mechanical method pioneered by Ben-Shaul et al.[34] In this approach, the free energy of the packed state, $g_{mic\ core}$, and the free energy of the free oil drop, $g_{oil\ drop}$, are calculated using the following equation:[28]

$$g = \sum_{\alpha} P(\alpha)\varepsilon(\alpha) + kT\sum_{\alpha} P(\alpha)\ln P(\alpha) \tag{2-20}$$

where α denotes the surfactant tail conformation, $\varepsilon(\alpha)$ is the energy associated with conformation α, $P(\alpha)$ is the probability of finding the surfactant tail in conformation α, k is the Boltzmann constant, and T is the absolute temperature. For linear hydrocarbon or fluorocarbon chains, $\varepsilon(\alpha)$

is calculated using the Rotational Isomeric State (RIS) model developed for alkanes[35, 36] and fluoroalkanes,[37] respectively.

The free energy of packing, g_{pack}, is the difference between the gs computed using Eq. (2-20) for the packed state and for the free oil drop state. To use Eq. (2-20), one needs an expression for $P(\alpha)$. Typically, $P(\alpha)$ would only be a function of the energy of the surfactant tail conformation α. However, due to the constraints imposed on the micelle core, $P(\alpha)$ is governed not only by the energy of the conformation, but also by these constraints. The three constraints imposed on the micelle core are: (i) no part of the surfactant tail can be on the water side of the micelle core-water interface, (ii) the end of the tail which is connected to the head is tethered at the interface, and (iii) the entire micelle core volume is occupied by the surfactant tails. The first two constraints limit the type of conformation that the surfactant tail can adopt, that is, any conformation which violates the first two constraints has zero probability of being realized. The third constraint can be stated mathematically as follows:

$$\sum_{\alpha} P(\alpha)\phi(x,\alpha) = V(x) \tag{2-21}$$

where x is the direction perpendicular to the micelle core surface, $\phi(x,\alpha)$ is the volume occupied by a surfactant tail in conformation α between surfaces positioned at x and at $x+dx$, and $V(x)$ is the volume available per surfactant molecule between the surfaces at x and at $x+dx$. An expression for $P(\alpha)$ can be obtained by minimizing g subject to the constraint given in Eq. (2-21). The resulting expression for $P(\alpha)$ is given by:[34, 38]

$$P(\alpha) = \frac{\exp\left[-\varepsilon(\alpha)/kT - 1/kT \sum_{x} \pi(x)\phi(\alpha,x)dx\right]}{\sum_{\alpha} \exp\left[-\varepsilon(\alpha)/kT - 1/kT \sum_{x} \pi(x)\phi(\alpha,x)dx\right]} \tag{2-22}$$

where $\pi(x)$ is the Lagrange multiplier associated with the constraint given in Eq. (2-21). Note that $\pi(x)$ may be interpreted as the pressure that has to be exerted to force the surfactant tails to occupy the entire micelle core volume. Equations (2-21) and (2-22) can be solved self consistently for $\pi(x)$, and subsequently, Eq. (2-20) can be used to compute the free energy of the packed state.

To solve Eqs. (2-21) and (2-22), the surfactant head-tail connection is pinned at a location on the micelle core-water interface [constraint (ii)], and all the internal conformations of the surfactant tail are enumerated using the appropriate RIS model. For each internal conformation, 500 external conformations are sampled, which involves changing the orientation of the surfactant tail with respect to the micelle core-water interface, as well as the position of the surfactant head-tail connection with respect to the micelle core-water interface. For each combination of internal and external conformations, constraint (i) is used to determine if the conformation is a valid one. For all valid conformations, $\varepsilon(\alpha)$ and $\phi(x,\alpha)$ are computed and then used to solve Eqs. (2-21) and (2-22) self consistently.[28]

As mentioned before, the packing free energy, g_{pack}, is the difference between the free energy in the packed state and the free energy of the initial oil-drop state calculated using Eq. (2-20). Note that in the initial oil-drop state, the surfactant tails can move freely anywhere inside the micelle. Intuitively, for an oil drop, one expects that there is no need to exert an artificial pressure to ensure that the entire micelle volume in the core is occupied by surfactant tails, that is, in Eq. (2-22), $\pi(x)$ is equal to 0. Accordingly, the probability $P(\alpha)$ is simply a function of the energy of the conformations and is given by:

$$P(\alpha) = \frac{\exp\left[-\varepsilon(\alpha)/kT\right]}{\sum_{\alpha}\exp\left[-\varepsilon(\alpha)/kT\right]} \tag{2-23}$$

In this manner, one can compute the free energies corresponding to the initial free oil-drop state, $g_{oil\ drop}$ and the final packed state, $g_{mic\ core}$, from which g_{pack} can be calculated.[28]

The packing step completes the formation of the micelle core. Next, one rejoins the surfactant heads and tails, and places the discharged counterions in the micelle head region. Since this process involves the localization of several finite-sized surfactant heads and counterions in a finite region, there is a free-energy penalty associated with it, which is referred to as the steric free energy, g_{st}. This is calculated by estimating the free-energy change associated with the excluded-volume interactions between the surfactant heads and the counterions. Specifically,[17, 39]

$$g_{st} = -(1+\beta_n)kT\ln\left(1-\frac{\sum_i \alpha_{n,i}a_{h,i} + \beta_n a_{h,c}}{a}\right) \tag{2-24}$$

where $a_{h,i}$ is the cross-sectional area of the head of surfactant i, and $a_{h,c}$ is the cross-sectional area of the counterion. These areas are calculated based on the structure of the surfactant head and the counterion, and bond lengths, bong angles, and van der Waals radii information.

Finally, one restores the charge of all the charged species, which contributes to the electrostatic free energy, g_{elec}. The electrostatic free energy is the sum of the free energies associated with discharging the charged species at the beginning of the thought process, and with charging the micelle at the end of the thought process. The discharge free energy, g_{disch}, is

calculated using the Debye-Hückel expression for the self energy of ionic species,[40] and is given by:

$$g_{disch} = -\frac{z^2 e_0^2}{8\pi\varepsilon_r r_h \left(1+\kappa r_h\right)} \tag{2-25}$$

where z is the valence of the ionic species, e_0 is the electronic charge, ε_r is the electrical permittivity of the dielectric medium (water for aqueous systems), r_h is the hydrated radius of the ionic species, and κ is the inverse of the Debye Hückel screening length. Note that κ will be defined later in Eq. (3-90) in Section 3.6.

The extensive charging free energy, G_{ch}, is equal to the electric work required to charge the micelle from an initial charge of $Q = 0$ to its final charge of $Q = Q_f$ in the presence of an ionic solution. This electric work is calculated using the equation shown below:[41]

$$G_{ch} = \int_{Q=0}^{Q=Q_f} \psi_{ch} dQ \tag{2-26}$$

where ψ_{ch} is the electrostatic potential of the charged micelle surface. For the purpose of model calculations, it is assumed that the charge on the micelle is smeared uniformly on the micelle surface. In addition, because of the finite size of the ions, a Stern surface is defined such that no free ions are present in the region bounded by the charged surface and the Stern surface.[21] Therefore, to calculate the potential of the charged surface, we define two regions. In the first region, located between the charged surface and the Stern surface, the electrostatic potential is governed by the Laplace equation due to the absence of any charged species. Beyond the Stern surface, the governing equation is the Poisson-Boltzmann (PB) equation.[21] Figure 2-3 shows a schematic of a section of a model charged micelle. The charged surface is characterized by

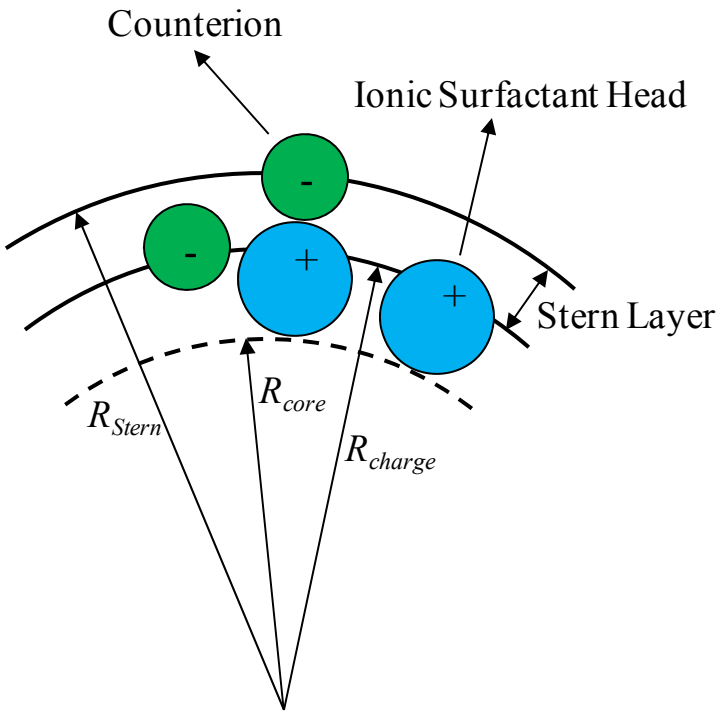

Figure 2-3: Schematic of a section of the head region of a charged micelle.

R_{charge} and the Stern surface is characterized by R_{Stern}. For a spherical and cylindrical micelle, R_{charge} corresponds to the radius of the charged surface, while for a bilayer, it corresponds to the distance of the charged surface from the center of the bilayer.

As stated above, the charge density in the region between the charged surface and the Stern surface is 0. Therefore, the governing equation for the electrostatic potential is given by the Laplace equation as shown below:

$$\nabla^2\psi = 0 \tag{2-27}$$

The region beyond the Stern surface contains all the free ions. As a result, the electric potential in this region satisfies the PB equation. Specifically,

$$\nabla^2\psi = -\frac{1}{\varepsilon_r}\sum_i I_{i,0} z_i e_0 \exp\left(-\frac{z_i e_0 \psi}{k_B T}\right) \tag{2-28}$$

where $I_{i,0}$ is the number density of species i in the bulk solution, and z_i is the valence of species i. Since Eqs. (2-27) and (2-28) are second-order differential equations, two boundary conditions are required for each of the differential equations to complete the problem definition. These are given below:

1. The micellar charged surface is assumed to be a constant potential surface with an unknown electrostatic potential. However, the total charge on the charged surface is known to be equal to Q_f. To relate Q_f to ψ, we apply Gauss' law to the micellar charged surface,[41] and integrate it over the surface area of the micellar charged surface to obtain the following equation:

$$\int_{A_{charge}} \left(-\frac{\partial \psi}{\partial \hat{n}}\bigg|_{R_{charge}} \right) dA_{charge} = \int_{A_{charge}} \frac{\sigma}{\varepsilon_{Stern}} dA_{charge} = \frac{Q_f}{\varepsilon_{Stern}} \tag{2-29}$$

where $\hat{n}$ is the unit vector normal to the micellar charged surface, (for example, for a sphere, $\hat{n}$ would be a unit vector in the radial direction), ε_{Stern} is the electrical permittivity of the region between the Stern surface and the micellar charged surface, and A_{charge} is the surface area of the charged surface. Note that due to the high degree of structuring of water in the Stern layer, the electrical permittivity in the Stern layer, ε_{Stern}, is assumed to be half of that of bulk water, ε_{bulk}.[28]

2. The electrostatic potential at the Stern surface is continuous. In other words, approaching the Stern surface from the Stern layer side or from the bulk solution side results in the same electrostatic potential.

3. The gradient of the electrostatic potential in a direction normal to the Stern surface is discontinuous due to the abrupt change in the electric permittivity. Since the Stern surface has no surface charge associated with it, the normal derivatives of ψ on both sides of the Stern surface are related as follows:[41]

$$-\varepsilon_{bulk}\left.\frac{\partial\psi}{\partial\hat{n}}\right|_{R_{Stern},\text{bulk soln side}} = -\varepsilon_{Stern}\left.\frac{\partial\psi}{\partial\hat{n}}\right|_{R_{Stern},\text{Stern layer side}} \tag{2-30}$$

4. Far away from the micellar charged surface, the electrostatic potential ψ attains a finite constant value (assumed to be 0 here).

While analytical solutions to Eq. (2-27) are available for spheres, cylinders, and bilayers, analytical solutions to the PB equation are more difficult to come by due to the nonlinearity of the equation. Therefore, it is convenient to rewrite Eq. (2-26) as follows:

$$G_{ch} = \int_{Q=0}^{Q=Q_f}\left(\psi_{Stern} + \left(\psi_{ch} - \psi_{Stern}\right)\right)dQ = \int_{Q=0}^{Q=Q_f}\psi_{Stern}dQ + \int_{Q=0}^{Q=Q_f}\left(\psi_{ch} - \psi_{Stern}\right)dQ \tag{2-31}$$

where the second integral can be computed by solving the Laplace equation in Eq. (2-27) which, as stated before, has an analytical solution. Specifically,[21]

$$\int_{Q=0}^{Q=Q_f}\left(\psi_{ch} - \psi_{Stern}\right)dQ = \begin{cases} \dfrac{q_f^2}{2\varepsilon_{Stern}a_{charge}}\left(R_{Stern} - R_{charge}\right), & \text{for a bilayer} \\ \dfrac{q_f^2}{2\varepsilon_{Stern}a_{charge}}\ln\left(R_{Stern}/R_{charge}\right), & \text{for a cylinder} \\ \dfrac{q_f^2}{2\varepsilon_{Stern}a_{charge}}\left(R_{Stern} - R_{charge}\right)\left(\dfrac{R_{Stern}}{R_{charge}}\right), & \text{for a sphere} \end{cases} \tag{2-32}$$

where q_f is the final charge on the micelle on a per surfactant molecule basis, and a_{charge} is the surface area of the charged surface on a per surfactant molecule basis.

The first integral in Eq. (2-31) has an analytical solution only for planar surfaces. Therefore, for spheres and cylinders, we use the Ohshima, Healy, and White (OHW) approximation to evaluate ψ_{Stern}. Specifically,[21, 42]

$$s = 2\sinh\left(\frac{y_0}{2}\right) + \frac{2(S-1)}{x_0}\tanh\left(\frac{y_0}{4}\right) \tag{2-33}$$

where s is a dimensionless charge defined as $s = qe_0/(kT\kappa a_{Stern}\varepsilon_{bulk})$ [a_{Stern} is the surface area of the Stern surface on a per surfactant molecule basis], y_0 is the dimensionless electric potential defined as $y_0 = e_0\psi_{Stern}/kT$, S is the shape factor which takes values of 1, 2, and 3 for bilayers, cylinders, and spheres, respectively, and x_0 is a dimensionless length defined as $x_0 = \kappa R_{Stern}$. Since Eq. (2-33) is an implicit equation in ψ_{Stern}, the first integral in Eq. (2-31) is rewritten in dimensionless form and modified as follows:[43]

$$\begin{aligned}\int_0^{q_f}\psi_{Stern}dq &= \psi_{Stern}(q_f)q_f - \int_0^{q_f} q d\psi_{Stern} \\ &= \frac{kT}{e_0}q_f\left(y_f - \frac{1}{s_f}\int_0^{y_f} s(y)dy\right) \\ &= \frac{kT}{e_0}q_f\left(y_f - \frac{1}{s_f}\left(4\cosh\left(\frac{y_f}{2}\right) - 4 + \frac{8(S-1)}{x_0}\ln\left(\cosh\left(\frac{y_f}{4}\right)\right)\right)\right)\end{aligned} \tag{2-34}$$

where y_f and s_f denote y_0 and s evaluated for $q = q_f$, respectively. Note that evaluation of Eq. (2-34) requires knowledge of y_f, which can be calculated by solving the implicit Eq. (2-33).

The contributions associated with mixing the different surfactant tails forming the mixed micelle, as well as with mixing the surfactant heads with the counterions, are not included in any of the free-energy contributions. Therefore, an additional mixing contribution, g_{mix}, is added. Specifically,[28]

$$g_{mix} = kT\left(\sum_i \ln\left(\frac{\alpha_{n,i}}{\sum_i \alpha_{n,i} + \beta_n}\right) + \beta_n \ln\left(\frac{\beta_n}{\sum_i \alpha_{n,i} + \beta_n}\right)\right)$$

$$= kT\left(\sum_i \ln\left(\frac{\alpha_{n,i}}{1+\beta_n}\right) + \beta_n \ln\left(\frac{\beta_n}{1+\beta_n}\right)\right) \tag{2-35}$$

Note that Eq. (2-35) used to calculate the mixing free energy neglects the enthalpic contribution, and accounts solely for the entropic contribution. This is reasonable for mixtures of hydrocarbon-based surfactants because they are expected to behave ideally, that is, their enthalpy of mixing is expected to be 0. In addition, the non idealities associated with mixing charged counterions with oppositely-charged, or uncharged, surfactant heads are accounted for in the electrostatic free energy, g_{elec}. In Chapter 5, g_{mix} will be redefined for mixtures of fluorocarbon-based and hydrocarbon-based surfactants, where the surfactant tails have a non-zero enthalpy of mixing. Adding all the free-energy contributions, namely, g_{tr}, g_{int}, g_{pack}, g_{st}, g_{elec}, and g_{ent}, yields g_{mic} as shown in Eq. (2-6).

2.4 Computer-Simulation-Molecular-Thermodynamic (CSMT) Framework to Model Surfactant Micellization

The MT framework is based on several simplifying assumptions about the hydration states of a surfactant molecule in the monomeric and the micellar states. For example, in the MT framework, the surfactant head is considered to be fully hydrated in both the monomeric and the micellar states. The surfactant tail is assumed to be partially hydrated, and the degree of hydration depends only on the shape and size of the micelle core. To relax these assumptions, recently, Stephenson et al. developed a Computer-Simulation-Molecular-Thermodynamic (CSMT) framework to model single-surfactant systems. In the CSMT approach structural details obtained using all-atomistic MD simulations of micelles and monomers are incorporated into the well-established MT framework for surfactant micellization to obtain a better quantification of the hydrophobic effect.[44-46]

In the MT framework, the hydrophobic effect is quantified by the sum of g_{tr} and g_{int}. To improve upon this, in the CSMT framework, Stephenson et al. proposed the following replacement for $(g_{tr} + g_{int})$:[45]

$$g_{tr} + g_{\text{int}} \rightarrow g_{dehydr} + g_{hydr} \tag{2-36}$$

where g_{dehydr} is the dehydration free energy and g_{hydr} is the hydration free energy. These two new free-energy contributions are calculated using information obtained from MD simulations of the surfactant in two different states: (1) the monomeric state in water, and (2) the micellar state in water. The dehydration free energy per molecule is a measure of the free-energy change associated with the dehydration of the surfactant molecule when it is incorporated in the micelle core and is given by:[45]

$$g_{dehydr} = \sum_{i} \left(1 - f_i\right) g_{tr,i} \tag{2-37}$$

where i denotes the constituent groups (typically a heavy atom and any associated hydrogen atoms) of a surfactant, $g_{tr,i}$ denotes the contribution of group i to the transfer free energy, and f_i denotes the degree of hydration of group i which is defined as follows:

$$f_i = \frac{\text{number of hydrating contacts of group } i \text{ in the micelle simulation}}{\text{number of hydrating contacts of group } i \text{ in the monomer simulation}} \tag{2-38}$$

Equation (2-38) shows that: (i) f_i is 1 when the hydration state of group i remains unchanged as it moves from the monomer state to the micelle state, and (ii) f_i is 0 when group i undergoes complete dehydration when it is incorporated in the micelle. In Eq. (2-38), a hydrating contact is defined as 'contact' with any atomic group that is capable of participating in hydrogen bonding (for example, water; oxygen and hydrogen in carboxylic acid; oxygen in ether and ketone; and oxygen and hydrogen in alcohol), or in coordinate bonding.[44, 46] Quantitatively, 'contact' with

group *i* means the presence of an atomic group within a threshold distance of group *i*. Here, the threshold distance for 'contact' is set at 0.50 *nm*. This cutoff distance is based on the distance of the first hydration shell about each group of interest, and typically varies between 0.45 – 0.55 *nm*.[47]

The second free-energy contribution is the hydration free energy per molecule, g_{hydr}, which is the change in free energy due to the change in the hydrogen-bonding network of water around a surfactant molecule in the micelle state relative to that in the monomer state. It is known that the water structure around a hydrophobic entity depends on the size of the cavity created by the hydrophobic entity.[48] In the micellization process, a surfactant molecule transfers from a small cavity state (monomer) to a large cavity state (micelle), and this transfer is responsible for the hydration free energy per molecule. This free energy can be quantified as follows:[45, 46]

$$g_{hydr} = \sum_m f_m \cdot SASA_m \left(\frac{\sigma \left(A_{core} - A_0 \right)}{\left(SASA_{core} - A_0 \right)} - \frac{-g_{tr,m}}{SASA_m} \right) \tag{2-39}$$

where *m* denotes surfactant groups that form the micelle core, $SASA_m$ is the solvent accessible surface area of group *m*, σ is the curvature-corrected interfacial tension between the micelle core and water, A_{core} is the surface area of the micelle core if it was assumed that the surfactant tails form a spherical micelle core, A_0 is the surface area of the micelle core that is shielded from contact with water due to the physical bond between the surfactant head and tail, and $SASA_{core}$ is the solvent accessible surface area of the micelle core. Conceptually, the solvent accessible surface area is the area of the surface formed by the center of a probe as it is rolled over the molecules of interest. Here, we have used a probe radius of 0.14 *nm*, which is equal to the van der Waals radius of water.[49] In Eq. (2-39), the first term is a measure of the free energy

associated with the interactions between the surfactant molecules and water in the micellar state, while the second term is a measure of the free energy associated with the interactions between the surfactant molecule and water in the monomeric state.

Equations (2-37) and (2-39) clearly show that the dehydration and the hydration free energies per molecule depend on the size of the simulated micelle. The size dependence of these two new free-energy contributions makes it difficult to blend them with the MT framework. This follows because one does not know a priori the shape and size of the micelle that will exist in the surfactant solution, and therefore, one does not know the shape and size of the micelle that should be simulated. To address this challenge, Stephenson et al. rearranged Eq. (2-36) as follows:[45]

$$g_{tr,CSMT} = g_{dehydr} + g_{hydr} - \hat{g}_{int} \tag{2-40}$$

where $\hat{g}_{int}$ is the interfacial free energy per molecule calculated for the simulated micelle using Eq. (2-11). The rearrangement in Eq. (2-36) was motivated by the observation that, in the MT framework, the transfer free energy, g_{tr}, is independent of the micelle characteristics, as can be seen from Eq. (2-7). Through calculations of $g_{tr,CSMT}$ for simulated micelles of different sizes, we have confirmed that $g_{tr,CSMT}$ is quite insensitive to the size of the simulated micelle.[45, 47] This $g_{tr,CSMT}$ is used to replace g_{tr} in Eq. (2-6) in order to incorporate the information obtained from the molecular dynamics simulations into the MT framework, giving rise to the CSMT framework.

It is noteworthy that the CSMT framework improves on the traditional MT framework because it: (1) provides a better quantification of the hydration state of the surfactant molecules in the monomeric and the micellar states,[45] (2) can be used to systematically identify the polar

head and the non polar tail groups in a surfactant molecule, which are both important inputs to the MT framework,[47] and (3) can be used to model surfactants possessing a complex chemical architecture that are not amenable to traditional MT modeling.[45, 47] Due to (2) and (3) above, the range of applicability of the CSMT framework is significantly broader than that of the MT framework.

2.5 Predicting Micellization Properties

Having discussed the model for the free energy of micellization, the next step is to use it to predict micellar solution properties of practical significance, including critical micelle concentrations (CMCs), micelle shapes, and micelle aggregation numbers. Recall that the CMC is the surfactant concentration that marks the onset of micellization. Therefore, below the CMC, one expects that the concentration of micellar aggregates is negligible, while above the CMC, one expects it to be of the order of the added surfactant concentration. In other words, X_n~0 for $X_s<<X_{cmc}$, while X_n~X_s for $X_s>X_{cmc}$, where X_s denotes the surfactant concentration in mole fraction units, and X_{cmc} denotes the CMC in mole fraction units. To define the CMC, it is insightful to analyze Eq. (2-5) which relates X_n and X_1. Typically, the aggregation number, n, is a large number, and therefore, Eq. (2-5) shows that: (i) X_n is negligible when X_1 is significantly smaller than the denominator of Eq. (2-5), (ii) X_n~X_s when X_1 is of the order of the denominator in Eq. (2-5), and (iii) X_1 cannot exceed the denominator of Eq. (2-5), because this would result in unphysical values of X_n. These three considerations prompted the definition of the CMC as the denominator of Eq. (2-5). Specifically,[17]

$$X_{cmc} = \exp\left(\frac{g_{mic}}{kT} - 1 - \beta_n - \sum_i \alpha_{n,i} \ln \alpha_{1,i} - n\beta_n \ln X_{1,c} \right) \tag{2-41}$$

To define a unique CMC, one needs a unique set of micelle attributes, which include the shape, S, of the micelle, the core-minor radius of the micelle, l_c, (which is equal to the radius for spheres and cylinders, and to half the thickness for bilayers), the degree of counterion binding, β_n, in the case of charged surfactants, and the micelle composition, $\alpha_{n,i}$, in the case of a mixture of surfactants, at which Eq. (2-41) is evaluated. These micelle attributes are chosen such that they correspond to the smallest value of X_{cmc}. This follows because each set of micelle attributes is associated with a specific free energy of micellization and a corresponding value of X_n. The set of micelle attributes that yields the smallest value of X_{cmc} corresponds to the micelle that has the lowest free energy of micellization and the highest value of X_n. This way, the characteristics of the micelle that forms in the surfactant solution, namely, the optimal micelle shape, size, composition, and degree of counterion binding, are obtained by finding the set of micelle characteristics that yields the minimum value for X_{cmc}, as defined in Eq. (2-41).[28]

The MT and the CSMT frameworks discussed in this chapter constitute the foundation of this thesis. The following three chapters discuss the work carried out as part of this thesis towards research aims 1, 2, and 3 presented in Section 1.3. Specifically, in Chapter 3, the MT framework, discussed in Sections 2.2 and 2.3, is generalized to model discoidal and ellipsoidal micelle shapes, which are important micelle shapes in the context of fluorocarbon-based surfactants. The CSMT framework, discussed in Section 2.4, is generalized for mixtures of surfactants in Chapter 4. Finally, in Chapter 5, the MT framework discussed in this chapter is generalized to predict the micellization properties of mixtures of fluorocarbon-based and hydrocarbon-based surfactants.

Chapter 3

Modeling the Micellization Behavior of Single Fluorocarbon-Based Surfactants

3.1 Introduction

At a fundamental level, molecularly modeling the micellization behavior of fluorinated surfactants presents several new challenges. Structurally, the main difference between a fluorocarbon chain and a hydrocarbon chain is that a fluorine atom occupies more space than a hydrogen atom.[26] As a result, fluorocarbon chains favor forming micellar aggregates having shapes with lower curvature.[26] To better understand this tendency, let us consider a micellar aggregate of a predetermined shape and size made of a hydrocarbon-based surfactant. Then, if we replace the hydrocarbon tails with fluorocarbon ones, we will be able to accommodate fewer surfactant tails in the aggregate core because fluorocarbons occupy more volume. However, the surface area of the micellar aggregate remains the same. This implies that the surface area per surfactant molecule increases, which in turn, increases the interfacial free-energy penalty, g_{int}, introduced in Section 2.3. As a result, the fluorocarbon tails of fluorinated surfactants prefer to aggregate in a micelle shape that has a lower surface area for the same volume, which is a

characteristic of low-curvature shapes.[26] A similar reasoning also explains why phospholipids (double-tailed zwitterionic surfactants) form bilayers. In the case of phospholipids, the increase in volume is due to the presence of two tails in these surfactants.

The second important difference between fluorocarbon-based and hydrocarbon-based surfactants is that the energies associated with the different conformations of a fluorocarbon chain are higher than those of a hydrocarbon chain. This makes a fluorocarbon chain stiffer, and is another reason why fluorocarbon-based surfactants prefer to form aggregates with low-curvature shapes.[26] To understand how rigidity affects the packing of surfactant tails, let us compare packing a collection of sticks to packing pieces of rope in both a sphere and a bilayer. The rope can bend and occupy any available volume, thereby easily packing in a sphere. On the other hand, because of the inability of sticks to bend, they cannot pack in the sphere without leaving empty spaces near the periphery of the sphere. Instead, the stick packing would be similar to the arrangement of spokes on a bicycle wheel, with denser packing at the center which becomes increasingly sparse towards the periphery of the wheel. Such an arrangement violates the constraint that the micelle core should be completely occupied by the surfactant tails (see Eq. (2-21) in Section 2.3). On the other hand, in the case of packing in a bilayer, the sticks pack very efficiently because they can stack next to each other between the two flat surfaces to fill the entire volume. However, in the case of the rope, although all the pieces can stretch out and fill the entire volume like in the stick case, the probability of that occurring is low. Indeed, unlike the sticks, the rope has an equal probability of taking any conformation, and therefore, the probability that all the rope pieces assume the same fully-stretched out conformation is very low. Accordingly, based on this analogy, one can conclude that fluorocarbon chains, similar to sticks, owing to their rigidity, prefer to pack in low-curvature shapes, like disks, over high-curvature

shapes, like spheres. Although unlike sticks the fluorocarbon tails can bend, this analogy sheds light on how the rigidity of the surfactant tail affects the preferred micelle shape.

The results discussed above are also supported by experimental studies which have shown that some fluorinated surfactants, for example, cesium perfluorooctanoate, form discoidal micelles.[50, 51] Therefore, it appears beneficial to develop a model for discoidal aggregates in order to model the micellization behavior of fluorocarbon-based surfactants.

The main challenge in modeling discoidal micelles is that, unlike the three basic micelle shapes that are commonly modeled, namely, spheres, infinite cylinders, and infinite bilayers, discs have a varying curvature. In an earlier attempt to model discoidal micelles, Srinivasan and Blankschtein modeled the micelle as bilayers with a semi-toroidal rims wrapped around the bilayers.[26] The semi-toroidal rim was modeled as a semi-cylinder with an increased surface area to account for bending. Of the various free-energy contributions presented in Section 2.3, those that depend on the surface area per molecule, namely, the interfacial free energy, g_{int}, the steric free energy, g_{st}, and the electrostatic free energy, g_{elec}, were modified by replacing the surface area per molecule with an increased surface area per molecule to account for the bending of the semi-cylinder. Since the packing free energy, g_{pack} is not directly related to the surface area per molecule, g_{pack} for the semi-toroidal rim was approximated using the g_{pack} of a cylinder. This way, an explicit dependence of the free energy of micellization, g_{mic}, on the position-dependent curvature of the semi-toroidal rim was avoided.[26] Although the model by Srinivasan and Blankschtein was able to qualitatively predict various experimentally observed trends, the predictions did not always agree quantitatively.[28] A possible reason for the discrepancy may be that the curvature dependence of the different free-energy contributions was not accounted for with sufficient accuracy. With this in mind, in this chapter, I have developed a model that

explicitly incorporates the effect of curvature on the various free-energy contributions to g_{mic}. In addition to discoidal micelles, in this chapter, I have extended the model to describe a biaxial ellipsoidal micelle, which is a commonly reported micelle shape.[52-54] For fluorosurfactants, the biaxial ellipsoidal micelle shape may be particularly important when the fluorosurfactant has a large head group. This follows because while the bulky head group prefers to micellize in high-curvature micelle shapes due to their higher surface area-to-volume ratios, the bulky fluorocarbon tail prefers to micellize in low-curvature micelle shapes as discussed earlier in this section. Since the ellipsoidal shape, on average, has a curvature which is smaller than that of a sphere, but higher than that of a disc, it can be the optimal micelle shape. Moreover, biaxial ellipsoids can also represent a realistic transition shape between a sphere and a cylinder or a disc. Consequently, the biaxial ellipsoidal shape will also be modeled in this Chapter.

Before developing the micellization models for discoidal and biaxial ellipsoidal micelles, Section 3.2 introduces concepts of differential geometry which are essential to model the effect of curvature on the different free-energy contributions to g_{mic}. Sections 3.3, 3.4, 3.5, and 3.6 present the development of the model equations for the interfacial free energy, the packing free energy, the steric free energy, and the electrostatic free energy for discoidal and ellipsoidal micelles, respectively. Following the model development, Section 3.7 compares the curvature-corrected model with the previous model for discs developed by Srinivasan and Blankschtein.[28] Finally, Section 3.8 utilizes the new model to shed some light on the feasibility of biaxial ellipsoids as micelle shapes.

3.2 Geometrical Properties

To incorporate the effect of curvature in the various free-energy contributions, it is necessary to derive expressions for geometrical properties, including the mean curvature, the differential area, and the differential volume, for the different shapes to be modeled. These can be derived using concepts of differential geometry. Note that the methods described in this section are adopted from the book on differential geometry by Milliman and Parker.[55]

In differential geometry, properties related to a surface are derived in terms of the first and second fundamental forms of the surface. A surface, $\overline{S}$, in three dimensions, can be parameterized using two independent variables. Let $\overline{x}$ denote the parameterization of $\overline{S}$ in terms of the variables u_1 and u_2, that is, $\overline{S}$ is given by $\overline{x} = \left(f_1(u_1,u_2), f_2(u_1,u_2), f_3(u_1,u_2)\right)$. In addition, let x_1 and x_2 denote the partial derivatives of $\overline{x}$ with respect to u_1 and u_2, that is:

$$x_i = \frac{\partial \overline{x}}{\partial u_i} \quad i = 1,2 \tag{3-1}$$

It can be shown that at any point on the surface, the vectors x_1 and x_2 form a basis (not necessarily orthonormal) for the tangent space (the plane created by the all tangents to the surface at a point). Therefore, any two tangents, X and Y, at a point on the surface can be written as a linear combination of x_1 and x_2. In other words,

$$X = \sum_{i=1,2} X^i x_i \tag{3-2}$$

and

$$Y = \sum_{i=1,2} Y^i x_i \tag{3-3}$$

where X^i and Y^i denote coefficients. The first fundamental form, $I(X,Y)$, of a surface is the rule that gives the inner product between any two vectors, X and Y, belonging to the tangent space of the surface at a point:

$$I(X,Y) = \langle X,Y \rangle = \sum_{i=1,2,j=1,2} X^i Y^j \langle x_i, x_j \rangle = \sum_{i=1,2,j=1,2} X^i Y^j g_{ij} \tag{3-4}$$

where g_{ij} is the inner product of x_i with x_j. The first fundamental form is mostly used to derive properties that are intrinsic to the surface, that is, properties that depend only on the surface and not on the space in which it is embedded. The surface area is one such property and is given by:

$$A = \iint \sqrt{|g|}\, du_1 du_2 \tag{3-5}$$

Here, $|g|$ denotes the determinant of the matrix g which is formed by the elements g_{ij}.

The mean curvature of a surface, on the other hand, depends on the embedment of the surface in 3-dimensional space. As a result, expressions for the mean curvature cannot be written in terms of just the first fundamental form of the surface, and requires the second fundamental form as well. The second fundamental form, $II(X,Y)$, for two vectors, X and Y, which belong to the tangent space of the surface at a point is given by:

$$II(X,Y) = \sum_{i=1,2,j=1,2} L_{ij} X^i Y^j \tag{3-6}$$

The following equations are used to define L_{ij}:

$$\hat{n} = \frac{x_1 \times x_2}{|x_1 \times x_2|} \tag{3-7}$$

$$x_{ij} = \frac{\partial^2 x}{\partial u_j \partial u_i} \tag{3-8}$$

$$L_{ij} = \left\langle x_{ij}, n \right\rangle \tag{3-9}$$

Using the parameters L_{ij} and g_{ij} from the second and the first fundamental forms, respectively, another set of parameters, L_k^l, is obtained which is used to calculate the mean curvature:

$$L_k^l = \sum_{i=1,2} L_{ik} g^{il} \tag{3-10}$$

where g^{il} is the element in the i^{th} row and l^{th} column in the g^1 matrix. The mean curvature, c, is then given by half the trace of the matrix which has L_k^l as a matrix element in the l^{th} row and k^{th} column:

$$c = \frac{1}{2}\left(L_1^1 + L_2^2\right) \tag{3-11}$$

To calculate the differential volume, let us first consider a body parameterized in the Cartesian coordinates. The differential volume in this case is given by *dxdydz*. In many cases it is more convenient to parameterize the body in terms of different coordinates. The differential volumes in two different coordinate systems are related to each other via the Jacobian, *J*. For example, let a body be parameterized in two different sets of coordinates: (*x,y,z*) and (*p,q,r*). The differential volume element in the (*x,y,z*) coordinate system, $(dV)_{(x,y,z)}$, is related to that in the (*p,q,r*) coordinate system, $(dV)_{(p,q,r)}$, as follows:

$$\left(dV\right)_{(x,y,z)} = dxdydz = \left|J\right| \cdot \left(dV\right)_{(p,q,r)} = \left|J\right| dpdqdr \tag{3-12}$$

where $|J|$ is the determinant of the Jacobian matrix, *J*, which is defined as follows:

$$J = \begin{bmatrix} \frac{\partial x}{\partial p} & \frac{\partial x}{\partial q} & \frac{\partial x}{\partial r} \\ \frac{\partial y}{\partial p} & \frac{\partial y}{\partial q} & \frac{\partial y}{\partial r} \\ \frac{\partial z}{\partial p} & \frac{\partial z}{\partial q} & \frac{\partial z}{\partial r} \end{bmatrix} \tag{3-13}$$

Using expressions for the surface area, the mean curvature, and the differential volume in Eqs. (3-5), (3-11), and (3-12), appropriate equations for discs and ellipsoids are derived in the next two sections.

3.2.1 Geometrical Properties of a Discoidal Micelle

Figure 3-1 shows a schematic of a discoidal micelle which is modeled as a central bilayer with a semi-toroidal rim wrapped around the bilayer. Model equations for the central bilayer were derived and presented in Section 2.3. To calculate the geometrical properties of the semi-toroidal rim, it is first parameterized as follows:

$$\begin{aligned} &x = \left(b + r\cos v\right)\cos u \\ &y = \left(b + r\cos v\right)\sin u\,, \quad 0 \le r \le b'\,, \quad 0 \le u < 2\pi\,, \quad \text{and} \quad -\pi/2 \le v < \pi/2 \\ &z = r\sin v \end{aligned} \tag{3-14}$$

where the various geometric variables are shown in Figure 3-1.

The differential volume of the semi-toroidal rim can be calculated by computing the Jacobian matrix for the parameterization in (3-14), and then substituting it in Eq. (3-12) (for details of the calculation see Section 7.1.1 of the Appendix). This yields:

$$dV = dxdydz = r\left(b + r\cos v\right)drdudv \tag{3-15}$$

For a discoidal micelle, the surface at $r = b'$ would represent the micelle core-water

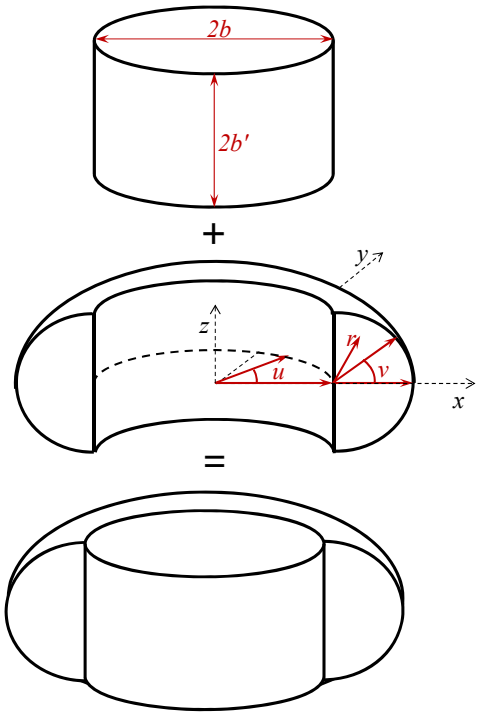

Figure 3-1: Schematic of a model discoidal micelle.

interface. Therefore, the parameterization of the surface for which the differential area and mean curvature needs to be determined is obtained by setting r equal to 1 in Eq. (3-14). This yields:

$$\bar{x}(x,y,z) = \left((b+b'\cos v)\cos u, (b+b'\cos v)\sin u, b'\sin v\right), 0 \le u < 2\pi \text{ and } -\pi/2 \le v < \pi/2 \quad (3\text{-}16)$$

Using the first fundamental form, the differential area associated with the surface parameterization in Eq. (3-16) is given by:

$$dA = b'(b+b'\cos v)\,du dv \quad (3\text{-}17)$$

Similarly, using the second fundamental form, the mean curvature is given by:

$$c = -\frac{1}{2b'}\left(\frac{b+2b'\cos v}{b+b'\cos v}\right) \quad (3\text{-}18)$$

Note that the negative sign in c is due to the sign of the normal, n. At each point on a surface, there are two normals that differ from each other by a negative sign. As a result, the sign of the

mean curvature depends on the choice of the normal. The value of the mean curvature of the surface is required only in the evaluation of the interfacial tension to determine the interfacial free energy introduced in Section 2.3. For the case of a spherical micelle, the mean curvature is taken to be positive. Since the orientation of the semi-toroidal surface is similar to that of a sphere (the torus is curved in a similar manner), the sign of the mean curvature for the torus is taken to be equal to that for a sphere, that is, positive. Therefore, c, is defined as follows:

$$c = \frac{\left(b + 2b'\cos v\right)}{2b'\left(b + b'\cos v\right)} \tag{3-19}$$

Note that evaluations of the first and second fundamental forms that yield Eqs. (3-15), (3-17), and (3-19) are presented in Section 7.1.2 of the Appendix.

3.2.2 Geometrical Properties of a Biaxial Ellipsoidal Micelle

A schematic illustrating the various geometric variables characterizing a biaxial ellipsoidal micelle is shown in Figure 3-2. A convenient parameterization for a biaxial ellipsoid is given by:

$$\begin{aligned} x &= pr\cos u\sin v \\ y &= pr\sin u\sin v, \quad 0 \le r \le 1, \quad 0 \le u < 2\pi, \quad and \quad 0 \le v \le \pi \\ z &= qr\cos v \end{aligned} \tag{3-20}$$

The angle u is equivalent to the azimuthal angle in spherical coordinates, while the angle v is similar, but not identical, to the polar angle used in spherical coordinates. Note that the parameterization of the biaxial ellipsoid reduces to that of a sphere when $p = q$.

The differential volume of the biaxial ellipsoid parameterized in Eq. (3-20) can be calculated by computing the Jacobian matrix, and then substituting it in Eq. (3-12). Specifically,

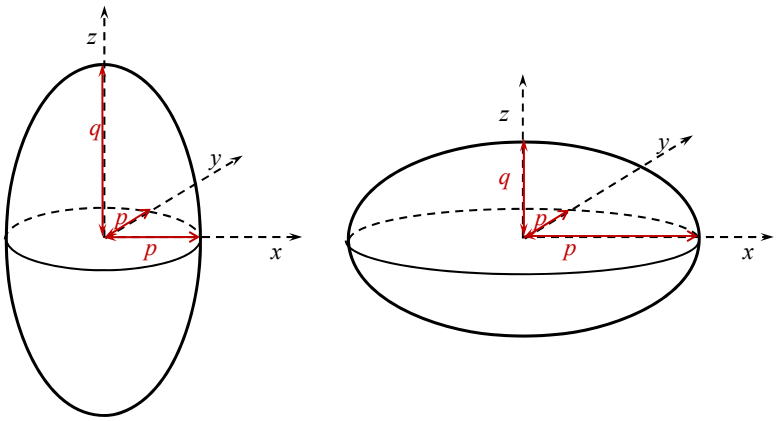

Prolate Ellipsoid ($p < q$) Oblate Ellipsoid ($p > q$)

Figure 3-2: Schematic of model prolate ellipsoidal and oblate ellipsoidal micelles.

$$dV = dxdydz = p^2 qr^2 \sin v dr du dv \tag{3-21}$$

To calculate the mean curvature and the differential area, the parameterization of the micelle core-water interface is derived by setting r equal to 1 in Eq. (3-20). This yields:

$$\bar{x}(x,y,z) = (p\cos u \sin v, p \sin u \sin v, q \cos v), \quad 0 \le u < 2\pi \quad and \quad 0 \le v \le \pi \tag{3-22}$$

Using the first fundamental form, the differential area associated with the surface parameterization in Eq. (3-22)is given by:

$$dA = \sqrt{|g|}dudv = p \sin v \sqrt{p^2 \cos^2 v + q^2 \sin^2 v} dudv \tag{3-23}$$

Similarly, using the second fundamental form, the mean curvature is given by:

$$c = \frac{q}{2p} \frac{\left(p^2 + p^2 \cos^2 v + q^2 \sin^2 v\right)}{\left(p^2 \cos^2 v + q^2 \sin^2 v\right)^{3/2}} \tag{3-24}$$

Note that, similar to Section 3.2.1, the details of the derivation of Eqs. (3-21), (3-23), and (3-24) are presented in Sections7.1.3 and 7.1.4 of the Appendix.

3.3 Interfacial Free Energy

As discussed in Section 2.3, the interfacial free energy per surfactant molecule, g_{int}, is the product of the interfacial tension between water and the micelle core, σ, and the surface area per surfactant molecule of the micelle core that is exposed to water. A change in curvature changes the surface area of the micelle core, and therefore, affects g_{int}, an effect that is accounted for in the previous discoidal model developed by Srinivasan and Blankschtein.[26] In addition, the curvature of the micelle also affects the interfacial tension between water and the micelle core, an effect which is not accounted for in the model by Srinivasan and Blankschtein.[26]

To incorporate the effect of the position-dependent curvature on the interfacial tension, let us consider the micelle core-water interface. The interface between two phases is, in fact, a thin, highly inhomogeneous transition region which separates the two homogeneous phases. This non-homogeneity complicates the analysis of the transition region, and therefore, to simplify the treatment of such a system, Gibbs proposed a model system in which the two phases are assumed to meet at an imaginary dividing surface, known as the Gibbs dividing surface, which precisely separates two distinct homogeneous phases.[56] The properties of the entire transition layer can then be modeled in terms of the properties of the dividing surface. The Gibbs dividing surface exhibits various excess properties to make all extensive properties of the model system equal to those of the real system. The surface on which the surface tension acts is referred to as the surface of tension. The surface of tension has a superficial mass density to account for the difference between the total mass in the real system and the sum of the masses in the two homogeneous phases in the model system that are separated by this imaginary surface of tension.[29] Based on the Gibbs adsorption equation and the Young-Laplace equation, Tolman

derived an equation relating the surface tension, σ, to the mean curvature of the surface of tension, c:[29]

$$d\sigma = -\frac{\Gamma}{\rho' - \rho''} d(2\sigma c) \tag{3-25}$$

where Γ is the superficial mass density at the surface of tension which is a measure of the number of particles adsorbed on the surface of tension per unit area, ρ' and ρ'' are the mass densities of the two homogeneous phases separated by the surface of tension, and c is the position dependent mean curvature characterizing the surface of tension. Let x be a measure of the distance from any point on the surface of tension, in a direction perpendicular to the surface. Therefore, if $x = 0$ denotes the surface of tension (shown as the solid curve in Figure 3-3), then $x = x'$ (shown as the dashed curve in Figure 3-3) is a surface concentric to the surface of tension such that a line drawn perpendicular to the surface of tension will intersect the dashed surface at a distance of x'. If r (=1/c) is the mean radius of curvature of the surface of tension, then, the local surface area at the surface of tension, $A(x = 0)$, is equal to $r^2 dw$ where dw is the solid angle subtended by the surface of tension. The surface area, $A(x)$, of a surface concentric to the surface of tension, at a perpendicular distance x from it, is $A(0)(r + x)^2/r^2 = A(0)(1 + cx)^2$ Therefore, the volume between the surfaces x and $x+dx$ is $A(0)(1 + cx)^2 dx$. Using these expressions, a mass balance for the entire two-phase system yields:

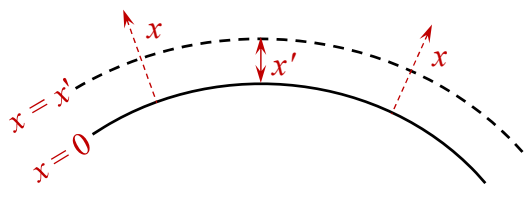

Figure 3-3: Diagram showing the surface of tension and other relevant parameters.

$$\Gamma\left(x=0\right)A\left(0\right)=\int_{-\infty}^{0}\left(\rho-\rho'\right)A\left(0\right)\left(1+cx\right)^{2}dx+\int_{0}^{\infty}\left(\rho-\rho''\right)A\left(0\right)\left(1+cx\right)^{2}dx \tag{3-26}$$

where ρ is the local mass density which is a function of x, and $\pm\infty$ represents a large x beyond which the phase is homogeneous, that is, $\rho = \rho'$ and $\rho = \rho''$ and the integrands are equal to 0. If $x = \delta$ denotes the position of a dividing surface that has a zero superficial mass density associated with it, that is, $\Gamma(x = \delta) = 0$, then:

$$\Gamma\left(x=\delta\right)A\left(\delta\right)=\int_{-\infty}^{\delta}\left(\rho-\rho'\right)A\left(0\right)\left(1+cx\right)^{2}dx+\int_{\delta}^{\infty}\left(\rho-\rho''\right)A\left(0\right)\left(1+cx\right)^{2}dx=0 \tag{3-27}$$

Combining Eqs. (3-26) and (3-27) yields:

$$\Gamma\left(x=0\right)=\int_{0}^{\delta}\left(\rho'-\rho''\right)\left(1+cx\right)^{2}dx=\left(\rho'-\rho''\right)\left(\delta+c\delta^{2}+\tfrac{1}{3}c^{2}\delta^{3}\right) \tag{3-28}$$

which can be used in Eq. (3-25) to eliminate Γ to obtain an expression for σ in terms of the local curvature and the distance between the surface of tension and the surface with zero superficial mass density, δ, known at the Tolman distance.[29] Specifically,

$$d\sigma=-2\left(1+c\delta+\frac{1}{3}\left(c\delta\right)^{2}\right)d\left(\sigma c\delta\right) \tag{3-29}$$

In the limit when $c\delta << 1$, Eq. (3-29) reduces to:

$$\begin{aligned} &d\sigma=-2\left(\sigma d\left(c\delta\right)+c\delta d\sigma\right)\Rightarrow\left(1+2c\delta\right)d\sigma=-2\sigma d\left(c\delta\right)\\ &\Rightarrow\frac{d\sigma}{\sigma}=-2d\left(c\delta\right) \end{aligned} \tag{3-30}$$

which can be integrated from ($\sigma = \sigma_0$, $c\delta = 0\delta$) [flat interface] to (σ, $c\delta$) and simplified in the limit when $\sigma - \sigma_0 << \sigma_0$ to yield a relation between the interfacial tension and the mean curvature of the interface:

$$\ln\frac{\sigma}{\sigma_0}=\ln\left(1+\left(\frac{\sigma-\sigma_0}{\sigma_0}\right)\right)\approx\left(\frac{\sigma-\sigma_0}{\sigma_0}\right)=-2c\delta$$
$$\Rightarrow\sigma=\sigma_0\left(1-2c\delta\right) \tag{3-31}$$

Equation (3-31) incorporates the effect of curvature on σ. Additionally, the effect of curvature on the surface area has to be incorporated to obtain a curvature-corrected interfacial free energy per molecule, g_{int}. This is done by deriving an expression for the local interfacial free energy penalty as a function of position, followed by integrating this expression over the entire micelle core-water interface. To this end, an expression for the local differential extensive interfacial free energy, $dG_{int,local}$, is given by:

$$dG_{int,local}=\sigma\left(dA-a_0dn\right) \tag{3-32}$$

where dn denotes the differential number of molecules and $a_0\,dn$ denotes the differential shielding area. Using the constraint that the micelle core has a uniform density, dn can be written as follows:

$$dn=\left(n/V\right)dV \tag{3-33}$$

where dV and V are the differential volume and the total volume, respectively. Using Eq. (3-32), one can calculate the interfacial free energy per molecule, g_{int}, as follows:

$$g_{int}=\frac{\int dG_{int,local}}{\int dn}=\frac{\int\sigma\left(dA-a_0dn\right)}{n} \tag{3-34}$$

3.3.1 g_{int} of the Semi-Toroidal Rim of a Discoidal Micelle

To calculate g_{int} for the semi-toroidal rim associated with a discoidal micelle, first, the differential volume, dV, is calculated using Eq. (3-15). Specifically,

$$dV = \int_{r=0}^{r=b'} \left(r\left(b + r\cos v\right) du dv \right) dr = \left(\frac{bb'^2}{2} + \frac{b'^3}{3}\cos v \right) du dv \tag{3-35}$$

It should be noted that the purpose of defining the differential volume as shown in Eq. (3-35) is to obtain an expression for the differential shielding area which is meaningful only at the surface and not in the interior of the torus. Using Eqs. (3-17), (3-19), (3-31), (3-33), (3-34), and (3-35), $dG_{int,local}$ for a semi-toroidal rim can be written as follows:

$$\begin{aligned} dG_{int,local} &= \sigma\left(dA - a_0 \cdot dn\right) = \sigma\left(dA - a_0 \frac{n}{V} dV \right) \\ &= \sigma_0 \left(1 - 2c\delta\right)\left(b'\left(b + b'\cos v\right) du dv - a_0 \frac{n}{V}\left(\frac{bb'^2}{2} + \frac{b'^3}{3}\cos v \right) du dv \right) \\ &= \sigma_0 \left(1 - \left(\frac{\delta}{b'} \right)\left(\frac{b + 2b'\cos v}{b + b'\cos v} \right) \right)\left(b'\left(b + b'\cos v\right) - a_0 \frac{n}{V}\left(\frac{bb'^2}{2} + \frac{b'^3}{3}\cos v \right) \right) du dv \end{aligned} \tag{3-36}$$

and

$$\begin{aligned} g_{int,local} &= \frac{dG_{int,local}}{dn} \\ &= \frac{\sigma_0 \left(1 - \left(\frac{\delta}{b'} \right)\left(\frac{b + 2b'\cos v}{b + b'\cos v} \right) \right)\left(b'\left(b + b'\cos v\right) - a_0 \frac{n}{V}\left(\frac{bb'^2}{2} + \frac{b'^3}{3}\cos v \right) \right)}{\frac{n}{V}\left(\frac{bb'^2}{2} + \frac{b'^3}{3}\cos v \right)} \end{aligned} \tag{3-37}$$

For the example case of a discoidal micelle formed by a 6-carbon fluorocarbon tail at 298.15 K, Figure 3-4 shows the variation of the local interfacial free energy per molecule of the semi-toroidal rim, $g_{int,local}$, as a function of the angle v when $b = 3b'$ and b' is equal to the maximum surfactant tail length given by Eq. (2-15). Figure 3-4 shows that $g_{int,local}$ attains its maximum value at $v = 0$, corresponding to the central plane of the semi-toroidal rim. This follows because the semi-toroidal rim has the highest curvature at $v = 0$ which also corresponds to the largest surface area per molecule. Since the interfacial free energy per molecule is

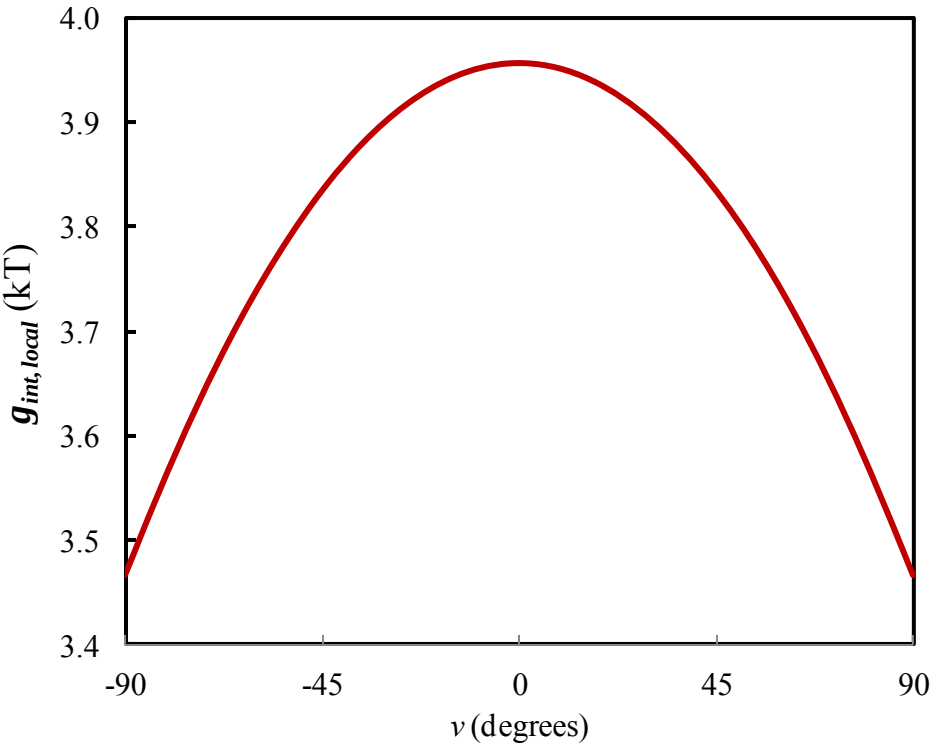

Figure 3-4: Variation of the local interfacial free energy per molecule, $g_{int,local}$, as a function of the angle v.

proportional to the surface area per molecule, $g_{int,local}$ attains its maximum value at the highest curvature region.

After obtaining $g_{int,local}$, one can calculate the average interfacial free energy per molecule for the semi-toroidal rim, g_{int}, by integrating Eq. (3-36), which requires expressions for the total surface area, A, and the total volume, V, of the semi-toroidal rim. These are given by:

$$A = \int_{v=-\pi/2}^{v=\pi/2} \int_{u=0}^{u=2\pi} b'\left(b + b'cosv\right) dudv = 2\pi b'\left(\pi b + 2b'\right) \tag{3-38}$$

and

$$V = \int_{v=-\pi/2}^{v=\pi/2} \int_{u=0}^{u=2\pi} \left(\frac{bb'^2}{2} + \frac{b'^3}{3}\cos v \right) dudv = 2\pi \int_{v=-\pi/2}^{v=\pi/2} \left(\frac{bb'^2}{2} + \frac{b'^3}{3} cosv \right) dv = \frac{\pi}{3}\left(3bb'^2\,\pi + 4b'^3\right) \tag{3-39}$$

The following equations show the various steps involved in integrating Eq. (3-36) to obtain g_{int}:

$$
\begin{aligned}
g_{int} &= \int_{v=-\pi/2}^{v=\pi/2}\int_{u=0}^{u=2\pi}\frac{\sigma_0}{n}\left(1-\left(\frac{\delta}{b'}\right)\left(\frac{b+2b'\cos v}{b+b'\cos v}\right)\right)\left(b'\left(b+b'\cos v\right)dudv - a_0\frac{n}{V}\left(\frac{bb'^2}{2}+\frac{b'^3}{3}\cos v\right)dudv\right) \\
&= \frac{2\pi\sigma_0}{n}\left(\begin{array}{l} b'b\pi + 2b'^2 - \delta\left(b\pi+4b'\right) - a_0\frac{n}{V}\left(\frac{bb'^2\pi}{2}+\frac{2b'^3}{3}\right) + \\ a_0\frac{n}{V}\left(\frac{\delta}{b'}\right)\int_{v=-\pi/2}^{v=\pi/2}\left(\frac{b+2b'\cos v}{b+b'\cos v}\right)\left(\frac{bb'^2}{2}+\frac{b'^3}{3}\cos v\right)dv \end{array}\right) \\
&= \frac{\sigma_0}{n}\left(A - 2\pi\delta\left(b\pi+4b'\right) - a_0 n + 2\pi a_0\frac{n}{V}\left(\frac{\delta}{b'}\right)\int_{v=-\pi/2}^{v=\pi/2}\left(\frac{b+2b'\cos v}{b+b'\cos v}\right)\left(\frac{bb'^2}{2}+\frac{b'^3}{3}\cos v\right)dv\right) \\
&= \frac{\sigma_0}{n}\left(A - 2\pi\delta\left(b\pi+4b'\right) - a_0 n + 2\pi a_0\frac{n}{V}\left(\frac{\delta}{b'}\right)\left(\frac{V}{\pi}-\frac{bb'^2\pi}{3}-\int_{v=-\pi/2}^{v=\pi/2}\left(\frac{b^2b'^2}{6\left(b+b'\cos v\right)}\right)dv\right)\right) \\
&= \frac{\sigma_0}{n}\left(A - 2\pi\delta\left(b\pi+4b'\right) - a_0 n + 2\pi a_0\frac{n}{V}\left(\frac{\delta}{b'}\right)\left(\begin{array}{l}\frac{V}{\pi}-\frac{bb'^2\pi}{3} \\ -\int_{v=-\pi/2}^{v=\pi/2}\frac{b^2b'^2\sec^2 v/2}{6\left(b+b'\right)\left(\frac{\left(b-b'\right)}{\left(b+b'\right)}\tan^2 v/2+1\right)}dv\end{array}\right)\right)
\end{aligned}
\tag{3-40}
$$

The integral in Eq. (3-40) attains different forms depending on whether $b > b'$, $b = b'$, or $b < b'$. A more complete derivation of Eq. (3-40) is given in Section 7.1.5 of the Appendix. The final expressions for the average interfacial free energy per molecule, g_{int}, are given by:

$$
g_{int}\left(b>b'\right) = \sigma_0\left(\begin{array}{l} a - a_0 - a\frac{2\pi\delta\left(b\pi+4b'\right)}{A} + a_0\left(\frac{2\delta}{b'}\right) \\ -a_0\frac{2\pi bb'\delta}{3V}\left(\pi + \frac{2b}{\left(b+b'\right)\sqrt{\frac{\left(b-b'\right)}{\left(b+b'\right)}}}\tan^{-1}\sqrt{\frac{\left(b-b'\right)}{\left(b+b'\right)}}\right)\end{array}\right)
\tag{3-41}
$$

$$g_{int}\left(b<b'\right)=\sigma_0\left(\begin{array}{l} a-a_0-a\dfrac{2\pi\delta\left(b\pi+4b'\right)}{A}+a_0\left(\dfrac{2\delta}{b'}\right) \\ -a_0\dfrac{2\pi bb'\delta}{3V}\left(\pi+\dfrac{b}{\left(b+b'\right)\sqrt{\dfrac{\left(b-b'\right)}{\left(b+b'\right)}}}\ln\left(\dfrac{1+\sqrt{\dfrac{\left(b'-b\right)}{\left(b'+b\right)}}}{1-\sqrt{\dfrac{\left(b'-b\right)}{\left(b'+b\right)}}}\right)\right)\end{array}\right) \tag{3-42}$$

$$g_{int}\left(b=b'\right)=\sigma_0\left(a-a_0-a\frac{2\pi\delta\left(b\pi+4b'\right)}{A}+a_0\left(\frac{2\delta}{b'}\right)-a_0\frac{2\pi bb'\delta}{3V}\left(\pi+\frac{2b}{\left(b+b'\right)}\right)\right) \tag{3-43}$$

Note that in the limiting case when $b = 0$ and $A = 4\pi b'^2$, the above expression for g_{int} in Eq. (3-42) becomes equal to that for a sphere. Similarly, for the limiting case when $b \rightarrow \infty$, $A = (1/2)2\pi b'(2\pi b)$ and $V = (1/2)\pi b'^2(2\pi b)$, the above expression for g_{int} in Eq. (3-41) becomes equal to that for a cylinder. The proofs are presented in Section 7.1.6 of the Appendix.

The variation of the average interfacial free energy per molecule, g_{int}, as a function of the torus parameters, b and b', for a 6-carbon fluorocarbon tail having b' equal to the maximum surfactant tail length, is shown in Figure 3-5. For comparison, the interfacial free energy for the same surfactant tail for a spherical and a cylindrical micelle core having their radii equal to b' are plotted in red and blue, respectively. Additionally, the interfacial free energy calculated using the model developed by Srinivasan and Blankschtein is plotted in purple.[28] Figure 3-5 shows that g_{int} for the semi-toroidal rim, in green, has a value equal to that for a sphere at $b/b' = 0$ and then approaches the value for a cylinder as $b/b' \rightarrow 0$. Note that g_{int} decreases with increasing b/b' because as b/b' increases, it results in a reduction in curvature which brings about a reduction in the surface area per molecule, thereby decreasing g_{int}. Finally, g_{int} calculated using the curvature-corrected model (green curve) is always lower than g_{int} calculated using the model developed by

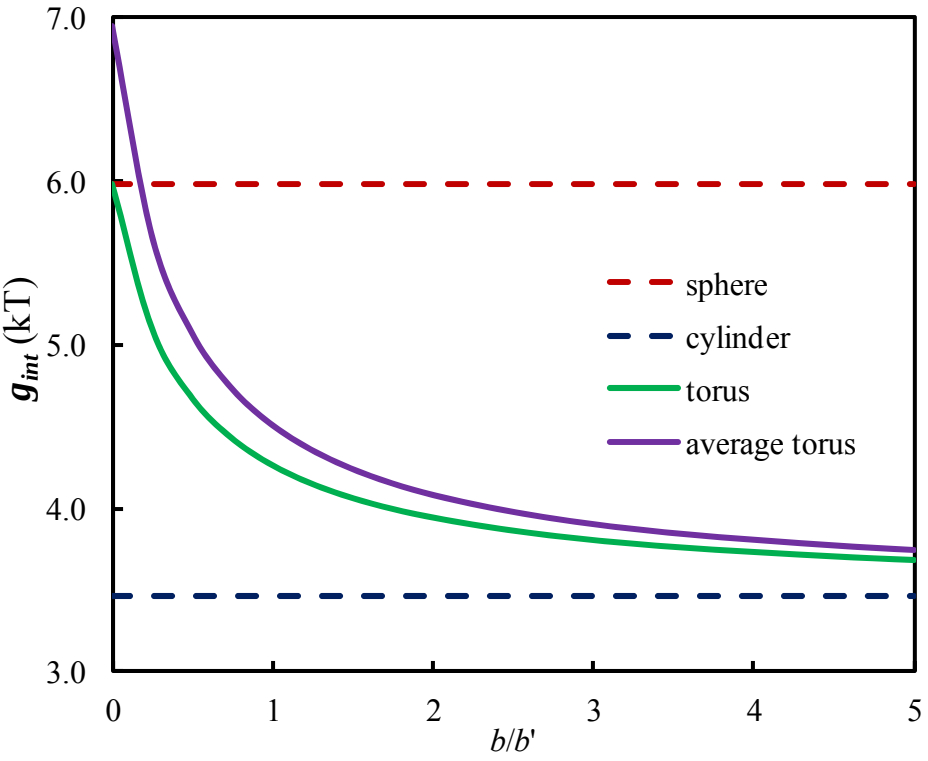

Figure 3-5: Variation of the interfacial free energy per molecule, g_{int}, of a semi-toroidal rim as a function of b/b'. Also shown for comparison are g_{int} for a sphere and a cylinder of radius b', and an average torus (see text).

Srinivasan and Blankschtein (purple curve) where the effect of curvature was only accounted for in the calculation of the area per molecule.[28] This follows because for the purpose of calculating the interfacial tension, the model of Srinivasan and Blankschtein assumes that the curvature of the rim is equal to that of a cylinder, which is lower than the curvature of the semi-toroidal rim. This results in an overestimation of the interfacial tension leading to a higher value of g_{int}.

3.3.2 g_{int} of a Biaxial Ellipsoidal Micelle

Similar to Section 3.3.1, here, expressions for g_{int} of a biaxial ellipsoid are derived. First, the differential volume is calculated using Eq. (3-21) to obtain an expression for the differential shielding area at the surface of the biaxial ellipsoid. Specifically,

$$dV = \int_{r=0}^{r=1} \left(p^2 q r^2 \sin v du dv \right) dr = \frac{p^2 q}{3} \sin v du dv \tag{3-44}$$

Then, using Eqs. (3-23) (3-33) and (3-44), $dG_{int,local}$ can be derived as follows:

$$\begin{aligned} dG_{int,local} &= \sigma_0 (1 - 2c\delta) \left(dA - a_0 \frac{n}{V} dV \right) \\ &= \sigma_0 p \sin v \left(1 - \frac{q}{p} \frac{\left(p^2 + p^2 \cos^2 v + q^2 \sin^2 v \right)}{\left(p^2 \cos^2 v + q^2 \sin^2 v \right)^{3/2}} \delta \right) \left(\sqrt{p^2 \cos^2 v + q^2 \sin^2 v} - a_0 \frac{n}{V} \frac{pq}{3} \right) du dv \end{aligned} \tag{3-45}$$

and

$$\begin{aligned} g_{int,local} &= \frac{dG_{int,local}}{dn} \\ &= \frac{\sigma_0 p \sin v \left(1 - \frac{q}{p} \frac{\left(p^2 + p^2 \cos^2 v + q^2 \sin^2 v \right)}{\left(p^2 \cos^2 v + q^2 \sin^2 v \right)^{3/2}} \delta \right) \left(\sqrt{p^2 \cos^2 v + q^2 \sin^2 v} - a_0 \frac{n}{V} \frac{pq}{3} \right) du dv}{\frac{n}{V} \left(\frac{p^2 q}{3} \sin v du dv \right)} \\ &= \frac{\sigma_0 \left(1 - \frac{q}{p} \frac{\left(p^2 + p^2 \cos^2 v + q^2 \sin^2 v \right)}{\left(p^2 \cos^2 v + q^2 \sin^2 v \right)^{3/2}} \delta \right) \left(\sqrt{p^2 \cos^2 v + q^2 \sin^2 v} - a_0 \frac{n}{V} \frac{pq}{3} \right)}{\frac{n}{V} \frac{pq}{3}} \end{aligned} \tag{3-46}$$

To understand the variation of the local interfacial free energy per molecule, $g_{int,local}$, along the surface of a prolate ellipsoidal micelle core, a plot of $g_{int,local}$ for a 6-carbon fluorocarbon tail at 298.15 K forming a prolate ellipsoidal core having p equal to the maximum surfactant tail length, calculated using Eq. (2-15), is shown in Figure 3-6. Figure 3-6 shows that $g_{int,local}$ is highest at $v = \pi/2$ (90 degrees), and decreases close to the poles of the prolate ellipsoid located at $v = 0$ and π (180 degrees). This is somewhat counter intuitive, because one would have expected that the local interfacial free energy per molecule would attain its maximum value when the curvature is highest, which corresponds to $v = 0$ or π (180 degrees) in this case. However, upon further reflection, this result can be explained based on the shielding term [a_0 in ($a - a_0$)]. Specifically,

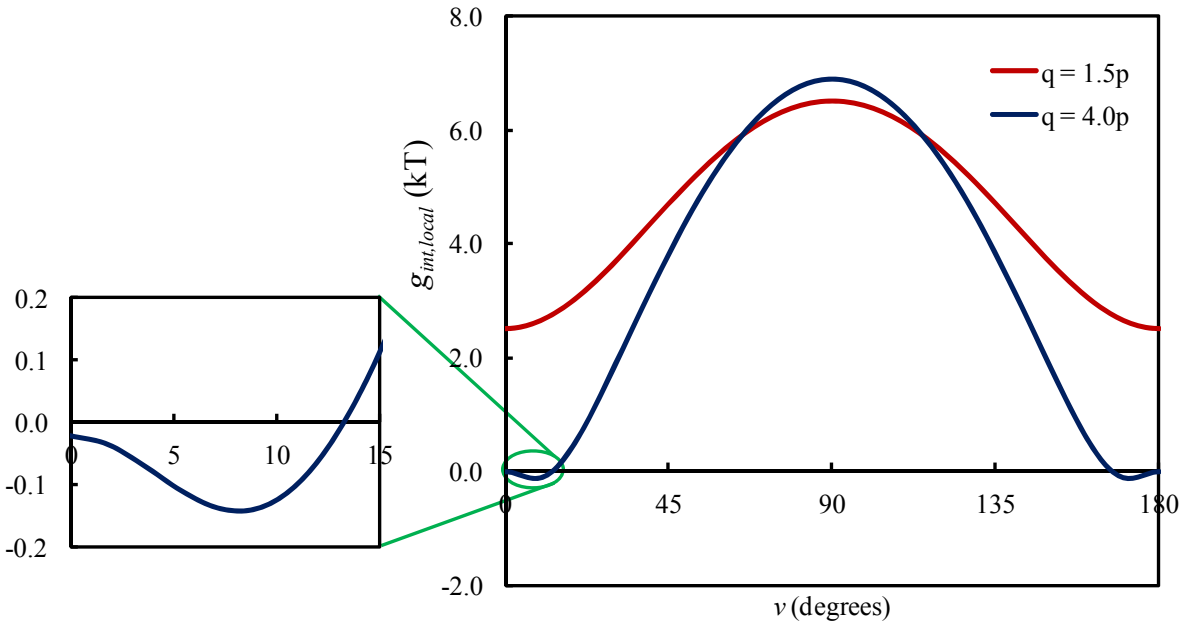

Figure 3-6: Variation of the local interfacial free energy per molecule, $g_{int,local}$, as a function of the angle v of a prolate ellipsoidal micelle.

with an increase in curvature, as the surface area per molecule increases, the local volume also increases, resulting in accommodation of a larger number of surfactant molecules. This, in turn, increases the shielding of the micelle core, and results in the observed decrease of $g_{int,local}$ close to the poles.

Another interesting feature of the plot in Figure 3-6 is that at the higher aspect ratio considered (q/p = 4.0), $g_{int,local}$ becomes negative near the poles (see the zoomed in view of the blue curve corresponding to q/p = 4.0 in Figure 3-6). This follows because at high aspect ratios, the amount of shielding in the polar region exceeds the available surface area. Because this is not physically realizable, it indicates that a prolate ellipsoid with such a high aspect ratio is not a feasible micelle shape. This feasibility criterion can be derived using Eq. (3-45) as follows:

$$dG_{int,local} > 0$$

$$
\begin{aligned}
&\Rightarrow \sqrt{p^2\cos^2 v + q^2 \sin^2 v} - a_0 \frac{n}{V}\frac{pq}{3} > 0, \quad 0 \le v \le \pi \\
&\Rightarrow \begin{cases} p - a_0 \dfrac{n}{nv_{tail}}\dfrac{pq}{3} > 0, & 0 \le v \le \pi, \quad p < q \\ q - a_0 \dfrac{n}{nv_{tail}}\dfrac{pq}{3} > 0, & 0 \le v \le \pi, \quad p > q \end{cases} \\
&\Rightarrow \begin{cases} q < \dfrac{3v_{tail}}{a_0}, & p < q \\ p < \dfrac{3v_{tail}}{a_0}, & p > q \end{cases}
\end{aligned}
\tag{3-47}
$$

where v_{tail} is the volume of the surfactant tail. Note that $dG_{int,local}$ can also be negative if $1>2c\delta$ (which corresponds to negative values of the curvature corrected interfacial tension). However, for typical sizes of surfactant micelles, such a scenario is not encountered.

Based on Eq. (3-47), it follows that knowledge of the structure of the surfactant tail is sufficient to establish a theoretical limit on the size of feasible ellipsoidal micelles using the curvature-corrected model presented here. Note that this result is consistent with the qualitative claims made in a few theoretical studies on ellipsoidal micelles that highly-elongated ellipsoidal micelles are not feasible micelle shapes.[57, 58]

A plot similar to that in Figure 3-6 for an oblate ellipsoidal micelle core formed a by 6-carbon fluorocarbon tail at 298.15 K having q equal to the maximum surfactant tail length is shown in Figure 3-7. Figure 3-7 shows that $g_{int,local}$ is highest at v = 0 and π (180 degrees) and decreases close to the equatorial region located at $v = \pi/2$ (90 degrees). At higher aspect ratios, results similar to those obtained for prolate ellipsoids are obtained for oblate ellipsoids as well. All these observations can be explained based on the same reasons given above for the prolate ellipsoidal case.

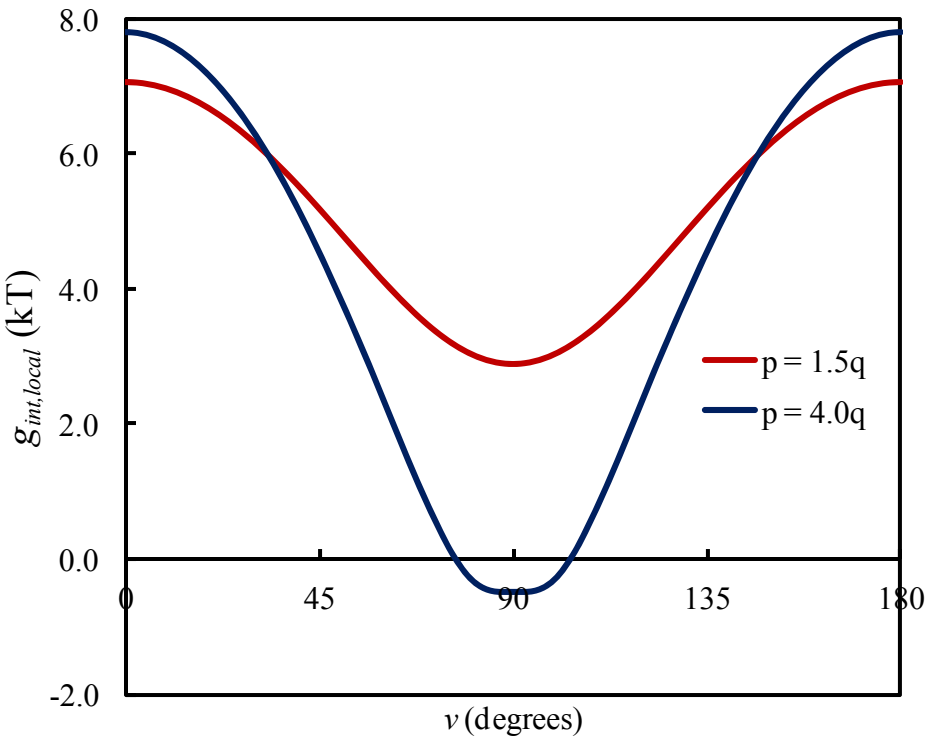

Figure 3-7: Variation of the local interfacial free energy per molecule, $g_{int,local}$, as a function of the angle v of an oblate ellipsoidal micelle.

To obtain the average interfacial free energy per molecule, g_{int}, expressions for the total surface area, A, and the total volume, V, of the biaxial ellipsoid are derived as follows:

$$A = \int_{v=0}^{v=\pi}\int_{u=0}^{u=2\pi} p\sin v\sqrt{p^2\cos^2 v + q^2\sin^2 v}\,du\,dv = 2\pi p\int_{v=0}^{v=\pi}\sin v\sqrt{p^2\cos^2 v + q^2\sin^2 v}\,dv$$

$$= 2\pi p\int_{v=0}^{v=\pi}\sin v\sqrt{\left(p^2 - q^2\right)\cos^2 v + q^2}\,dv$$

$$A = \begin{cases} 2\pi pq\left(\dfrac{p}{q} + \dfrac{\ln\left|\dfrac{p}{q} + \sqrt{\left(\dfrac{p}{q}\right)^2 - 1}\right|}{\sqrt{\left(\dfrac{p}{q}\right)^2 - 1}}\right), & p > q \\ 2\pi pq\left(\left(\dfrac{p}{q}\right) + \dfrac{\sin^{-1}\sqrt{1 - \left(\dfrac{p}{q}\right)^2}}{\sqrt{1 - \left(\dfrac{p}{q}\right)^2}}\right), & p < q \end{cases} \tag{3-48}$$

and

$$V = \int_{v=0}^{v=\pi}\int_{u=0}^{u=2\pi} \frac{p^2 q}{3}\sin v\,du\,dv = \int_{v=0}^{v=\pi} 2\pi\frac{p^2 q}{3}\sin v\,dv = \frac{4}{3}\pi p^2 q \tag{3-49}$$

Note that details of the integration process involved in Eq. (3-48) are presented in Section 7.1.7 of the Appendix.

Using Eqs. (3-34), (3-45), (3-48), and (3-49), the following equations show the various steps involved in obtaining an expression for g_{int}. To be able to write the equations in a manageable form, let $p^2\cos^2 v + q^2\sin^2 v$ be written as w. It then follows that:

$$\begin{aligned} g_{int} &= \int_{v=0}^{v=\pi}\int_{u=0}^{u=2\pi} \frac{\sigma_0 p\sin v}{n}\left(1 - \frac{q}{p}\frac{p^2 + w}{w^{3/2}}\delta\right)\left(w^{1/2} - a_0\frac{n}{V}\frac{pq}{3}\right)du\,dv \\ &= \frac{2\pi\sigma_0 p}{n}\left(\begin{array}{l} \displaystyle\int_{v=0}^{v=\pi} w^{1/2}\sin v\,dv - \int_{v=0}^{v=\pi} a_0\frac{n}{V}\frac{pq}{3}\sin v\,dv - \int_{v=0}^{v=\pi}\frac{qp\delta}{w}\sin v\,dv - \int_{v=0}^{v=\pi}\frac{q\delta}{p}\sin v\,dv \\ \displaystyle + \int_{v=0}^{v=\pi} a_0\frac{n}{V}\frac{q^2 p^2\delta}{3w^{3/2}}\sin v\,dv + \int_{v=0}^{v=\pi} a_0\frac{n}{V}\frac{q^2\delta}{3w^{1/2}}\sin v\,dv \end{array}\right) \end{aligned}$$

$$
= \begin{cases} \dfrac{\sigma_0}{n}\left(\begin{array}{l} A - a_0 \dfrac{n}{V} \cdot V - \dfrac{4\pi p^2 \delta}{\sqrt{p^2 - q^2}} \tan^{-1}\left(\dfrac{\sqrt{p^2 - q^2}}{q} \right) - 4\pi q \delta \\ + a_0 \dfrac{4\pi n p^2 \delta}{3V} + a_0 \dfrac{4\pi n q^2 p \delta}{3V\sqrt{p^2 - q^2}} \ln \left| \dfrac{p}{q} + \sqrt{\left(\dfrac{p}{q} \right)^2 - 1} \right| \end{array} \right), & p > q \\ \dfrac{\sigma_0}{n}\left(\begin{array}{l} A - a_0 \dfrac{n}{V} \cdot V - \dfrac{4\pi p^2 \delta}{\sqrt{\left(q^2 - p^2 \right)}} \ln \left| \dfrac{q}{p} + \sqrt{\left(\dfrac{q}{p} \right)^2 - 1} \right| - 4\pi q \delta \\ + a_0 \dfrac{4\pi n p^2 \delta}{3V} + a_0 \dfrac{4\pi n q^2 p \delta}{3V\sqrt{\left(q^2 - p^2 \right)}} \sin^{-1} \sqrt{1 - \left(\dfrac{p}{q} \right)^2} \end{array} \right), & p < q \end{cases}
$$

$$
g_{int} = \begin{cases} \sigma_0 \left(a - a_0 - \dfrac{4\pi q \delta}{n} \left(\dfrac{\left(\dfrac{p}{q} \right)^2}{\sqrt{\left(\dfrac{p}{q} \right)^2 - 1}} \tan^{-1} \sqrt{\left(\dfrac{p}{q} \right)^2 - 1} + 1 \right) + \dfrac{2\delta A}{3V} a_0 \right), & p > q \\ \sigma_0 \left(a - a_0 - \dfrac{4\pi q \delta}{n} \left(\dfrac{\left(\dfrac{p}{q} \right)^2}{\sqrt{1 - \left(\dfrac{p}{q} \right)^2}} \ln \left| \dfrac{q}{p} + \sqrt{\left(\dfrac{q}{p} \right)^2 - 1} \right| + 1 \right) + \dfrac{2\delta A}{3V} a_0 \right), & p < q \end{cases} \tag{3-50}
$$

A more complete derivation of Eq. (3-50) is presented in Section 7.1.8 of the Appendix. Note that in the limiting case when $p = q$, the expression for g_{int} in Eq. (3-50) becomes equal to that for a sphere. The proof is presented in Section 7.1.9 of the Appendix.

Finally, Figure 3-8 shows the variation of g_{int} for prolate and oblate ellipsoidal micelles, and compares these with the g_{int} for spherical and cylindrical micelle. All the curves in Figure 3-8 correspond to micelles formed by a 6-carbon fluorocarbon tail having the semi-minor axis length (for ellipsoidal micelles) and radii (for spherical and cylindrical micelles) equal to the maximum surfactant tail length. g_{int} for a spherical and a cylindrical micelle core are plotted in red and blue, respectively. Note that g_{int} for a bilayer micelle core formed by the same surfactant and having a bilayer thickness equal to the minor axis length of the biaxial ellipsoid micelle is negative. In other words, such a bilayer micelle core is not feasible. Consequently, a curve for

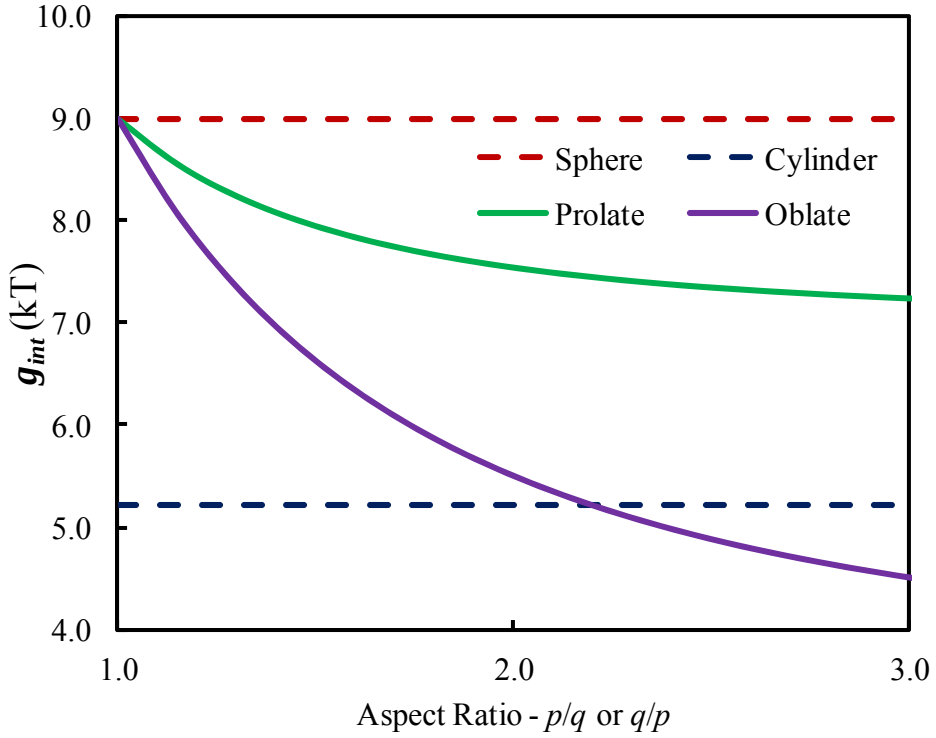

Figure 3-8: Variation of the interfacial free energy per molecule, g_{int}, for biaxial ellipsoidal micelles as a function of the aspect ratio. Also shown for comparison are g_{int} for a sphere and a cylinder of radius equal to the semi-minor axis length.

the bilayer shape is not shown in Figure 3-8. In addition, Figure 3-8 shows that for both ellipsoidal shapes, g_{int} decreases as the aspect ratio increases. This follows because the average surface area per molecule decreases as the aspect ratio increases. Additionally, Figure 3-8 shows that g_{int} corresponding to an oblate ellipsoid (purple curve), having the same semi-minor axis length and aspect ratio as a prolate ellipsoid (green curve), is significantly lower than g_{int} corresponding to a prolate ellipsoidal micelle. This difference follows because, for the same semi-minor axis length and aspect ratio, an oblate ellipsoid has a lower average surface area per molecule than a prolate ellipsoid.

3.4 Packing Free Energy

To generalize the method to calculate the packing free energy introduced in Section 2.3 to micelles of varying curvature, the free energy of the packed state, g, in Eq. (2-20) is modified as follows:

$$g = \sum_{\alpha, v_{surface}} P\left(\alpha, v_{surface}\right)\varepsilon\left(\alpha\right) + kT \sum_{\alpha, v_{surface}} P\left(\alpha, v_{surface}\right)\ln P\left(\alpha, v_{surface}\right) \tag{3-51}$$

where $v_{surface}$ denotes the location on the micelle surface where the surfactant tail is tethered and $P(\alpha,v_{surface})$ is the probability of finding the surfactant tail in conformation α tethered at the location $v_{surface}$ on the micelle surface. Note that $v_{surface}$ in Eq. (3-51) does not appear in Eq. (2-20) because the later equation applies to micelles of constant curvature. Indeed, this follows because for regular shapes, including spheres, infinite cylinders and infinite bilayers, all locations on the micelle surface are identical. Consequently, the probability of finding a surfactant tail in a particular conformation is the same everywhere on the micelle surface. However, since the curvatures of a disc and a biaxial ellipsoid vary with position, this simplification is no longer valid. Therefore, the next two sections discuss the calculations of $P(\alpha,v_{surface})$ and of the packing free energy, first for a discoidal micelle (Section 3.4.1) and then for a biaxial ellipsoidal micelle (Section 3.4.2).

3.4.1 g_{pack} of a Discoidal Micelle

From a geometric viewpoint, the semi-toroidal rim of a disc is a surface of revolution generated by revolving a semi-circle of radius b' about the z-axis at a distance, b, from it, where the angle u is a measure of the angle of revolution. This is shown in Figure 3-1. It then follows that the curvature of the rim is a function of v, but independent of u [see Eq. (3-19)]. Therefore, the equations related to the packing of a surfactant tail have to be modified to incorporate the

functional dependence on the angle v. For example, Eq. (3-33) is modified as follows to incorporate the v dependence:

$$\sum_{\alpha, v_{surface}} P\left(\alpha, v_{surface}\right)\phi\left(r, v, v_{surface}, \alpha\right) = V\left(r, v\right) = \frac{2\pi}{v_{tail}}\left(\frac{b}{2}\left(\left(r+dr\right)^2 - r^2\right)dv + \frac{1}{3}\left(\left(r+dr\right)^3 - r^3\right)\left(\sin\left(v+dv\right) - \sin\left(v\right)\right)\right) \tag{3-52}$$

where, as before, r is the direction perpendicular to the surface as defined in Eq. (3-14) and shown in Figure 3-1, v is the angle defined in Eq. (3-14) and shown in Figure 3-1, $\phi\left(r, v, v_{surface}, \alpha\right)$ is the volume occupied by a surfactant tail in conformation, α, tethered at $v = v_{surface}$, between the surfaces at r and $r+dr$ and at v and $v+dv$, and $V(r,v)$ is the volume available per surfactant molecule between the same four surfaces. Note that the equation for $V(r, v)$ in Eq. (3-52) in terms of b, r, and v is calculated by integrating Eq. (3-15), and is valid only for the semi-toroidal portion of the disc. Using Eq. (3-52) and Eq.(2-22), the modified equation for $P(\alpha, v_{surface})$ is given by:

$$P\left(\alpha, v_{surface}\right) = \frac{\exp\left[-\varepsilon\left(\alpha\right)/kT - 1/kT\sum_r\sum_v \pi\left(r,v\right)\phi\left(r,v,\alpha,v_{surface}\right)\right]}{\sum_{v_{surface}}\sum_{\alpha}\exp\left[-\varepsilon\left(\alpha\right)/kT - 1/kT\sum_r\sum_v \pi\left(r,v\right)\phi\left(r,v,\alpha,v_{surface}\right)\right]} \tag{3-53}$$

To carry out the summations in Eqs. (3-51) - (3-53), the discoidal micelle surface is divided into a grid to sample all the surfactant tail conformations at all the grid points. Furthermore, the interior of the discoidal micelle is divided into cells to correctly capture the v dependence of the πs in Eq. (3-53). The disc shape has an axis of symmetry and a plane of symmetry that is perpendicular to the axis of symmetry, as shown using the blue dashed line and the red plane in Figure 3-9. As a result, the curve marked in green in Figure 3-9 is representative of the entire disc surface, and all the surfactant tail conformations have to be sampled only for surfactant tails

tethered along the green curve instead of along the entire surface of the disc. Note that not all locations on this curve are equally probable. Indeed, consider the top view of the disc, as shown in Figure 3-10. The inner solid circle in black corresponds to the bilayer portion of the disc, while the outer solid circle in black corresponds to the top view of the rim of the disc. The green solid line is the projection of the green curve shown in Figure 3-9. Consider the location on the green line marked a_n. All locations on the circle associated with this marker are identical to the location of the marker itself. This circle associated with a_n has a higher circumference compared

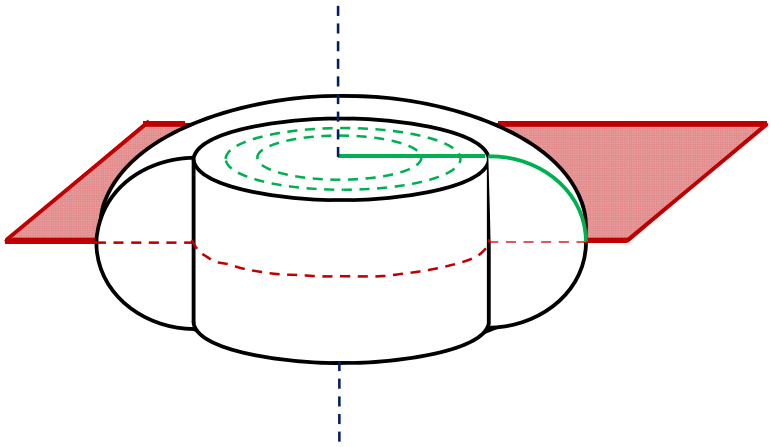

Figure 3-9: Schematic showing the plane of symmetry and the axis of symmetry for a disc.

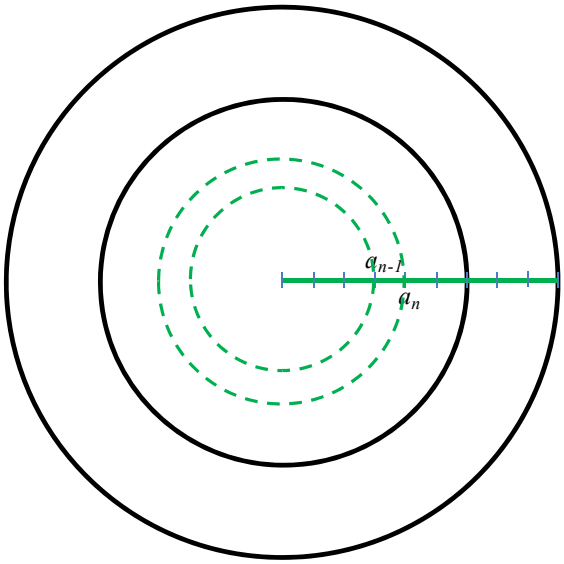

Figure 3-10: Schematic illustrating the need for different weights at different locations on the disc surface.

to the circle associated with a_{n-1}. As a result, it is more likely to find a surfactant tail tethered at the circle associated with a_n than at the circle associated with a_{n-1}. Therefore, each location on the solid green line, where all the surfactant tail conformations are sampled, is given a weight corresponding to the relative probability of finding a surfactant tail tethered at that location, which is proportional to the circumference of the circle associated with that location.

To determine the exact locations where the surfactant tail conformations will be sampled, we divide the solid green line in Figure 3-9 such that the distance between two consecutive points is equal to the length scale used to determine the thickness of a layer in a spherical micelle, which is equal to the length of a C-C bond. In other words, the distance between a_{n-1} and a_n in Figure 3-10 is approximately equal to the length of a C-C bond. Note that the length of the solid green line is equal to:

$$b + \pi b'/2 \tag{3-54}$$

The number of cells into which the interior of the disc is divided is also reduced by taking advantage of the symmetry of the disc. Two dimensional cells are created, as shown in Figure 3-11, and these two dimensional cells are rotated about the axis of symmetry of the disc (blue axis in Figure 3-11) to obtain three dimensional cells. It is further noted that the cells below the plane of symmetry (shown in red in Figure 3-11) are merely reflections of the cells above the plane of symmetry, and are not different from them. All the cells shown in the green shaded region are part of the cells in the unshaded region. For example, the cell colored red above and below the plane of symmetry, as well as on the right and left of the axis of symmetry, are parts of the same cell rather than four different cells.

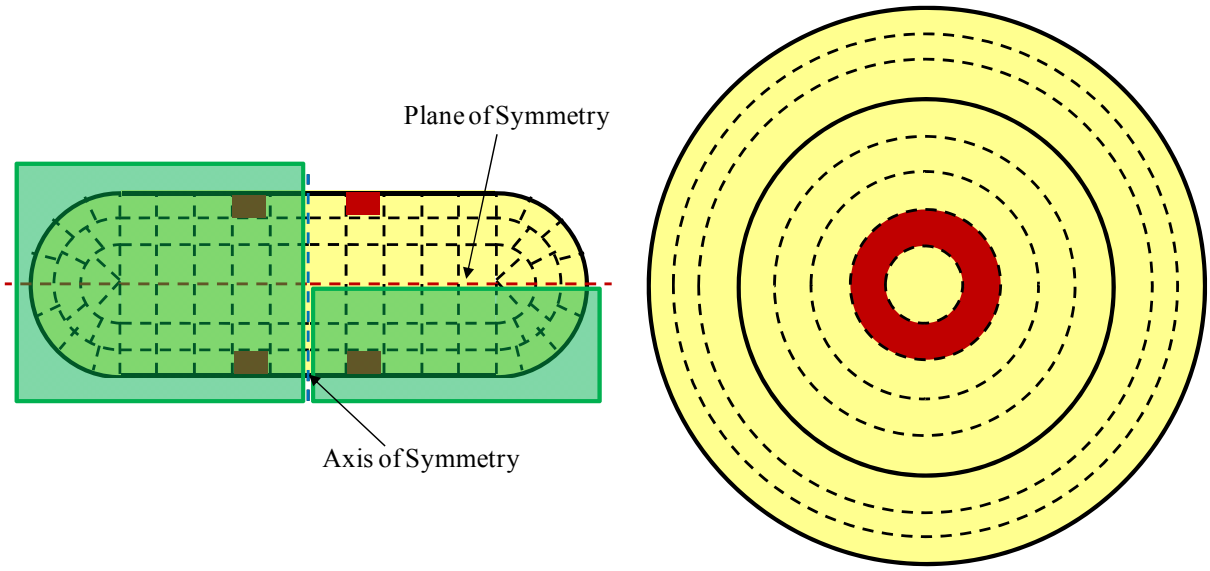

Figure 3-11: Schematic showing the cells created in a discoidal micelle to calculate the packing free energy.

The validity of the method presented above, including its implementation, was verified by using it to calculate the packing free energy of a 6-carbon fluorocarbon tail packed in a sphere. This was done by setting b equal to 0. The g_{pack} obtained using the new method compared very well with the g_{pack} calculated for spheres. Subsequently, to understand the variation of g_{pack} as a function of the discoidal size parameters, b and b', Figure 3-12 plots g_{pack} for a 6-carbon fluorocarbon tail as a function of b/b' for two different values of b'. Note that it is difficult to pack a tail in a bilayer having b' equal to the maximum surfactant tail length which is equal to 9.84 Å using Eq. (2-15). Consequently, the chosen values of b' are less than 9.84 Å.

Figure 3-12 was generated by calculating g_{pack} for five replicates. The symbols represent the average value, while the error bars represent the standard deviation. Figure 3-12 shows that for a smaller value of b' g_{pack} decreases as b increases (red symbols). This follows because, when both b and b' are small, the rim of the disc has a very high curvature. Consequently, the

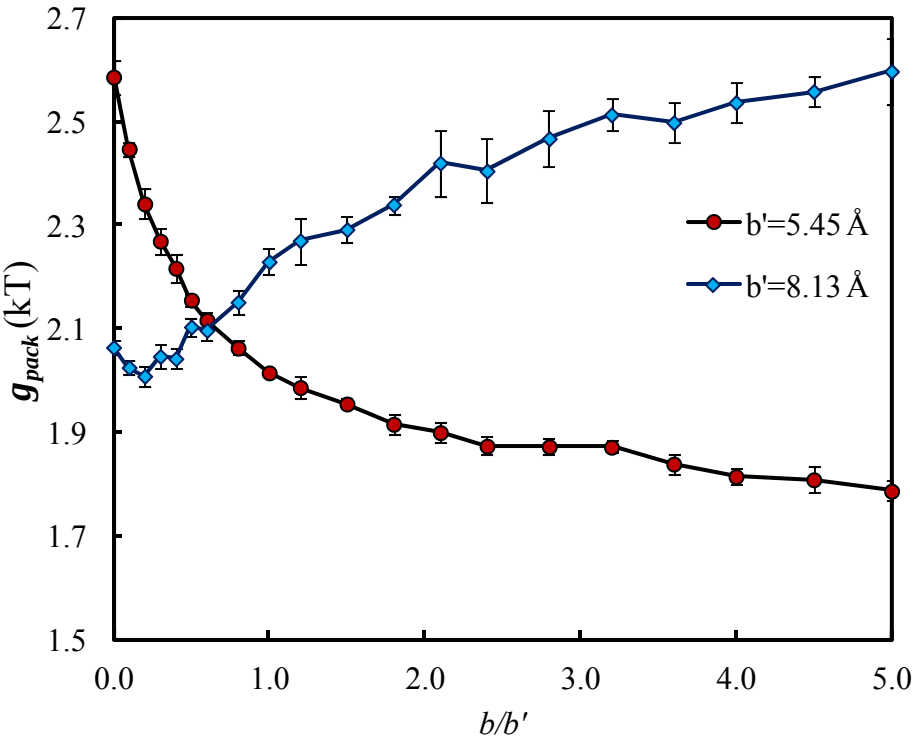

Figure 3-12: Plot of the variation of g_{pack} as a function of b/b'.

surfactant tail has to twist quite a bit to remain completely in the interior of the disc. However, as b increases, the curvature of the rim of the disc decreases, and it becomes easier to keep the surfactant tails within the disc, thereby resulting in a lower g_{pack}. This trend gets reversed for the case of a high value of b' (blue symbols). This follows because, as b' increases, the two surfaces of the bilayer in the bilayer portion of the disc move apart, making it difficult for the surfactant tails to completely fill up the volume in the center of the bilayer (to maintain dry core). In other words, to completely fill up the volume in the centre of the bilayer, almost all the surfactant tails have to stretch until the center which decreases the conformational degrees of freedom, thereby increasing the value of g_{pack}. When b is small, the contribution of the bilayer part of the disc to g_{pack} is small, and therefore, the net value of g_{pack} is small. However, as b increases, the contribution of the bilayer portion starts to dominate, and therefore, g_{pack} increases.

The g_{pack} values calculated using the above approach are fitted to polynomial equations in terms of b' and b/b' for each surfactant tail to facilitate the calculation of g_{mic}. The packing polynomials corresponding to the surfactants considered in this thesis are presented in Section 7.2 of the Appendix.

3.4.2 g_{pack} of a Biaxial Ellipsoidal Micelle

The method used to calculate g_{pack} for a biaxial ellipsoid is identical to the one described in Section 3.4.1, because like the discoidal shape, the biaxial ellipsoidal shape is also a surface of revolution. Consequently, its curvature is only a function of the angle v, and does not depend on the angle u defined in Eq. (3-20). One of the differences between the equations for a disc and a biaxial ellipsoid is the expression for $V(r, v)$ in Eq. (3-52). Similar to the discoidal micelle case, first, the ellipsoidal interior is divided into layers by dividing the semi-minor axis length such that the distance between two consecutive points is equal to the length of a C-C bond. This is illustrated in Figure 3-13 for the case of a prolate ellipsoid, where p_{n-1} and p_n denote two divisions along the semi-minor axis length. The layer bound by these two divisions is shown in yellow. Unlike the discoidal case, to maintain the thickness of the layer almost constant, the two biaxial ellipsoids associated with p_{n-1} and p_n have to be separately parameterized as follows:

$$\begin{aligned} x &= p_n r \cos u \sin v \\ y &= p_n r \sin u \sin v, \quad 0 \le r \le 1, \quad 0 \le u < 2\pi, \quad and \quad 0 \le v \le \pi \\ z &= q_n r \cos v \end{aligned} \tag{3-55}$$

$$\begin{aligned} x &= p_{n-1} r' \cos u \sin v' \\ y &= p_{n-1} r' \sin u \sin v', \quad 0 \le r' \le 1, \quad 0 \le u < 2\pi, \quad and \quad 0 \le v' \le \pi \\ z &= q_{n-1} r' \cos v' \end{aligned} \tag{3-56}$$

where $p_{n\text{-}1} = p_n - \delta_{C\text{-}C}$, $q_{n\text{-}1} = q_n - \delta_{C\text{-}C}$, and $\delta_{C\text{-}C}$ is the C-C bond length.

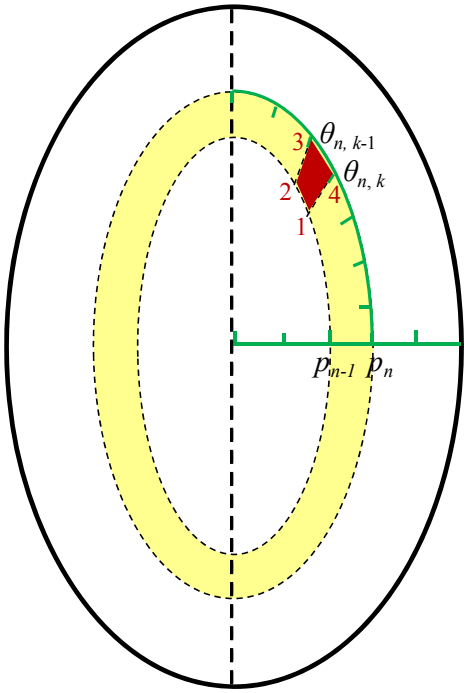

Figure 3-13: Schematic illustrating the choice of layers and cells to calculate g_{pack} for a biaxial ellipsoidal micelle.

To determine the number of cells in each layer, the circumference of the outer ellipse enclosing the layer, that is, the ellipsoid associated with p_n shown in Figure 3-13 and parameterized in Eq. (3-55), is divided such that the arc length between two consecutive points is equal to the C-C bond length. This is also illustrated in Figure 3-13, where $\theta_{n,\,k\text{-}1}$ and $\theta_{n,\,k}$ denote two such divisions. It should be noted that there is no simple equation describing the circumference of an ellipse. Instead, the first few terms of the Gauss-Kummer series gives a reasonable approximation for the circumference of the ellipse.[59] Specifically,

$$\pi\left(p+q\right)\left(1+\frac{1}{4}\left(\frac{q-p}{q+p}\right)^{4}+\frac{1}{64}\left(\frac{q-p}{q+p}\right)^{8}\right) \tag{3-57}$$

Finally, to calculate the volume of a cell, $V(r, v)$, consider the cell shown in red in Figure 3-13. Since points 3 and 4 lie on the ellipsoid associated with p_n, their coordinates are obtained from

Eq. (3-55) with $r = 1$ and $v = \theta_{n,k\text{-}1}$ for point 3, and with $r = 1$ and $v = \theta_{n,k}$ for point 4. Specifically,

$$(x_3, y_3, z_3) = (p_n \sin\theta_{n,k-1} \cos u, p_n \sin\theta_{n,k-1} \sin u, q_n \cos\theta_{n,k-1}) \tag{3-58}$$

and

$$(x_4, y_4, z_4) = (p_n \sin\theta_{n,k} \cos u, p_n \sin\theta_{n,k} \sin u, q_n \cos\theta_{n,k}) \tag{3-59}$$

Points 1 and 2 are chosen such that when they are represented using the parameterization in Eq. (3-55), the angle v is given by $\theta_{n,k}$ and $\theta_{n,k\text{-}1}$, respectively. Therefore, the coordinates of points 1 and 2 in the two parameterizations given in Eqs. (3-55) and (3-56) are given by:

$$\begin{aligned}(x_1, y_1, z_1) &= (p_n r_1 \sin\theta_{n,k} \cos u, p_n r_1 \sin\theta_{n,k} \sin u, q_n r_1 \cos\theta_{n,k}) \\ &= (p_{n-1} \sin v_1' \cos u, p_{n-1} \sin v_1' \sin u, q_n \cos v_1')\end{aligned} \tag{3-60}$$

$$\begin{aligned}(x_2, y_2, z_2) &= (p_n r_2 \sin\theta_{n,k-1} \cos u, p_n r_2 \sin\theta_{n,k-1} \sin u, q_n r_2 \cos\theta_{n,k-1}) \\ &= (p_{n-1} \sin v_2' \cos u, p_{n-1} \sin v_2' \sin u, q_{n-1} \cos v_2')\end{aligned} \tag{3-61}$$

Using Eqs. (3-60) and (3-61), $\theta_{n,k}$ and $\theta_{n,k\text{-}1}$ can be related to v_1' and v_2' as follows:

$$\begin{aligned}&\frac{x_1}{z_1} = \frac{p_n r_1 \sin\theta_{n,k} \cos u}{q_n r_1 \cos\theta_{n,k}} = \frac{p_{n-1} \sin v_1' \cos u}{q_{n-1} \cos v_1'} \\ &\Rightarrow \frac{p_n}{q_n} \tan\theta_{n,k} = \frac{p_{n-1}}{q_{n-1}} \tan v'\end{aligned} \tag{3-62}$$

$$\frac{p_n}{q_n} \tan\theta_{n,k-1} = \frac{p_{n-1}}{q_{n-1}} \tan v_2' \tag{3-63}$$

Similarly, using Eqs. (3-60) and (3-61), r_1 and r_2 can be related to $\theta_{n,k}$ and $\theta_{n,k\text{-}1}$ as follows:

$$r_i^2 = \frac{x_i^2 + y_i^2}{p_n^2} + \frac{z_i^2}{q_n^2} = \left(\frac{p_{n-1}}{p_n}\right)^2 \sin^2 v_i' + \left(\frac{q_{n-1}}{q_n}\right)^2 \cos^2 v_i' = \left(\frac{p_{n-1}}{p_n}\right)^2 + \left(\left(\frac{q_{n-1}}{q_n}\right)^2 - \left(\frac{p_{n-1}}{p_n}\right)^2\right) \cos^2 v_i' \tag{3-64}$$

Substituting Eqs. (3-62) and (3-63) in Eq. (3-64) yields:

$$r_1^2 = \left(\frac{p_{n-1}}{p_n}\right)^2 + \left(\left(\frac{q_{n-1}}{q_n}\right)^2 - \left(\frac{p_{n-1}}{p_n}\right)^2\right)\left(\tan^2 v_1' + 1\right)^{-1} = \left(\frac{p_{n-1}}{p_n}\right)^2 + \frac{\left(\frac{q_{n-1}}{q_n}\right)^2 - \left(\frac{p_{n-1}}{p_n}\right)^2}{\left(\frac{p_n q_{n-1}}{q_n p_{n-1}}\right)^2 \tan^2 \theta_{n,k} + 1} \quad (3\text{-}65)$$

and

$$r_2^2 = \left(\frac{p_{n-1}}{p_n}\right)^2 + \left(\left(\frac{q_{n-1}}{q_n}\right)^2 - \left(\frac{p_{n-1}}{p_n}\right)^2\right)\left(\tan^2 v_2' + 1\right)^{-1} = \left(\frac{p_{n-1}}{p_n}\right)^2 + \frac{\left(\frac{q_{n-1}}{q_n}\right)^2 - \left(\frac{p_{n-1}}{p_n}\right)^2}{\left(\frac{p_n q_{n-1}}{q_n p_{n-1}}\right)^2 \tan^2 \theta_{n,k-1} + 1} \quad (3\text{-}66)$$

Finally, using Eqs. (3-65), (3-66), and (3-21), the volume of the cell shown in red in Figure 3-13 can be calculated as follows:

$$V = \int_{\theta_{n,k-1}}^{\theta_{n,k}} \int_0^{2\pi} \int_{r(v)}^1 p_n^2 q_n r^2 \sin v \, dr du dv = 2\pi p_n^2 q_n \int_{\theta_{n,k-1}}^{\theta_{n,k}} \frac{1}{3}\left(1 - \left(\left(\frac{p_{n-1}}{p_n}\right)^2 + \frac{\left(\frac{q_{n-1}}{q_n}\right)^2 - \left(\frac{p_{n-1}}{p_n}\right)^2}{\left(\frac{p_n q_{n-1}}{q_n p_{n-1}}\right)^2 \tan^2 v + 1}\right)^{\frac{3}{2}}\right) \sin v \, dv \quad (3\text{-}67)$$

$$= \frac{2\pi}{3}\left(p_n^2 q_n \left(\cos\theta_{n,k-1} - \cos\theta_{n,k}\right) + p_{n-1}^2 q_{n-1}\left(\left(1 + \left(\frac{p_n q_{n-1}}{q_n p_{n-1}}\right)^2 \tan^2 \theta_{n,k}\right)^{-\frac{1}{2}} - \left(1 + \left(\frac{p_n q_{n-1}}{q_n p_{n-1}}\right)^2 \tan^2 \theta_{n,k-1}\right)^{-\frac{1}{2}}\right)\right)$$

Note that Eq. (3-67) is valid for $0 < \theta_{n,k}, \theta_{n,k\text{-}1} < \pi/2$, which corresponds to the range that we are interested in. Details of the integration process are provided in Section 7.1.10 of the Appendix. Using Eq. (3-67), the ellipsoid equivalent of the volume filling packing constraint in Eq. (3-52) can be evaluated.

Similar to the disc case, the validity of the approach presented above was verified by using it to calculate the packing free energy of a 6-carbon fluorocarbon tail packed in a sphere.

This was done by setting the aspect ratio to 1. The g_{pack} calculated using the new approach compared very well with the g_{pack} calculated for spheres. Subsequently, to understand the variation of g_{pack} as a function of the biaxial ellipsoid size parameters, p and q, Figure 3-14 plots g_{pack} for a 6-carbon fluorocarbon tail as a function of the aspect ratio which is equal to p/q for an oblate ellipsoid, and to q/p for a prolate ellipsoid. Note that it is difficult to pack a tail in an elongated oblate ellipsoid with q equal to the maximum tail length which is equal to 9.84 Å in this case. Consequently, the chosen values of p and q for the prolate and oblate ellipsoids, respectively, are less than 9.84 Å.

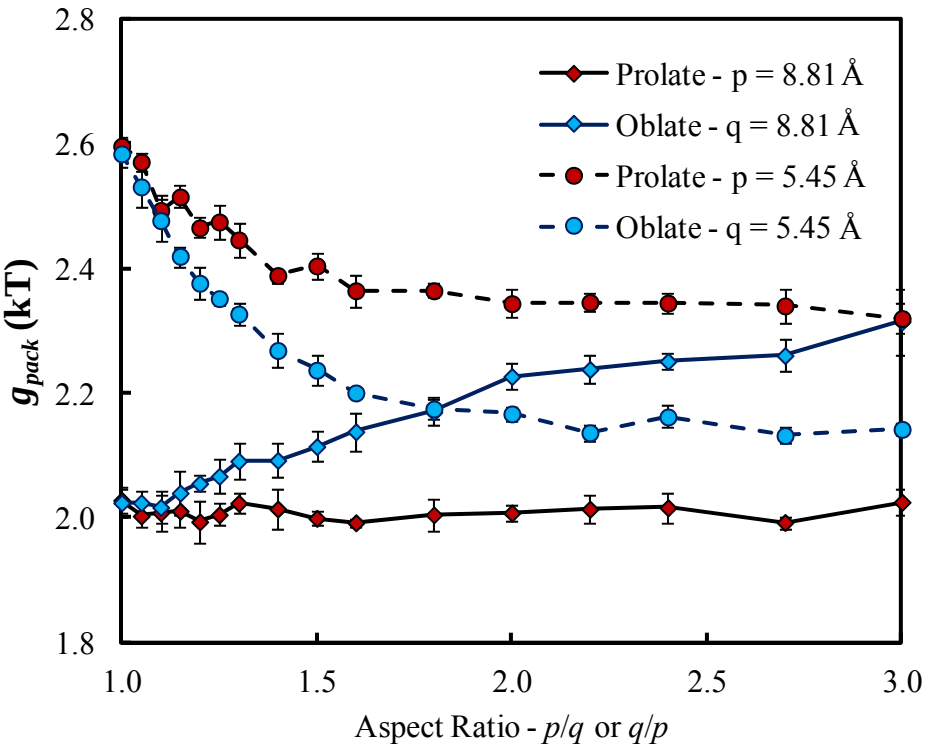

Figure 3-14: Variations of g_{pack} as a function of p/q and q/p for an oblate and a prolate ellipsoid, respectively.

The red and blue curves in Figure 3-14 correspond to g_{pack} for prolate and oblate ellipsoidal micelle cores, respectively, while the dashed and solid curves correspond to semi-minor axis lengths equal to 5.45 Å and 8.81 Å, respectively. An examination of the dashed

curves shows that, for small semi-minor axis lengths, g_{pack} decreases as the aspect ratio increases and plateaus off at higher aspect ratios similar to our findings for discoidal micelles (see Figure 3-12). This follows because when both semi-axis lengths are small, the ellipsoidal surface has a very high curvature. Consequently, the surfactant tails have to twist considerably to remain completely in the interior of the ellipsoid, leading to many gauche defects, and therefore, to higher g_{pack} values. However, as the aspect ratio increases, more volume is available to the surfactant tails in the ellipsoid. This allows them to adopt several other chain conformations which were not allowed at smaller aspect ratios, thereby resulting in a lower value of g_{pack}. This trend is observed for both prolate and oblate ellipsoidal micelles, as reflected in the dashed curves in Figure 3-14. At higher aspect ratios, the decrease in g_{pack} due to the increase in the volume of the ellipsoidal core and the increase in g_{pack} due to the increase in curvature at the equatorial region (for oblate ellipsoids), or at the polar region (for prolate ellipsoids), seem to offset each other, resulting in the flattening of the dashed curves.

At low aspect ratios, an increase in the semi-minor axis length (the solid curves) leads to a decrease in g_{pack} for both prolate and oblate ellipsoidal micelles. This follows because an increase in the semi-minor axis length leads to a decrease in the curvature, which in turn leads to less stringent restrictions on the types of conformations that a surfactant tail can adopt, and therefore, to a lower g_{pack}. However, at large semi-minor axis lengths, the trend for g_{pack} as a function of the aspect ratio for a prolate ellipsoidal micelle (the solid red curve) differs from that for an oblate ellipsoidal micelle (the solid blue curve). Specifically, for a prolate ellipsoid, g_{pack} does not change significantly with an increase in the aspect ratio in spite of the increase in curvature at the poles of the prolate ellipsoid. This follows because not many molecules occupy the poles of the prolate ellipsoid, and therefore, the polar region does not contribute greatly to the

value of g_{pack}. In contrast, for an oblate ellipsoid, g_{pack} increases with the aspect ratio. As the aspect ratio of an oblate ellipsoid increases, the curvature at the equatorial region also increases. Therefore, molecules occupying the equatorial region are not only subjected to stringent conformational constraints due to the high curvature, but also need to stretch out (adopt almost an all-trans conformation) to fill out the volume in the center of the ellipsoid. Since many molecules occupy the equatorial region, their loss of conformational degrees of freedom due to these two requirements leads to an increase in g_{pack}.

Similar to the disc case, the g_{pack} values calculated using the approach discussed above for biaxial ellipsoids are fitted to polynomial functions in terms of the semi-minor axis length (p or q) and the aspect ratio (q/p or p/q) to facilitate the calculation of g_{mic}. The packing polynomials for the surfactants considered in this thesis are presented in Section 7.2 of the Appendix

3.5 Steric Free Energy

The method used to calculate the steric free energy for a discoidal or a biaxial ellipsoidal micelle is very similar to the method used to compute the interfacial free energy. In short, first, using concepts from differential geometry, expressions for the local geometric features are derived. Using these expressions, and Eq. (2-24) in Section 2.3, an equation for the differential steric free energy, $dG_{st,local}$, is subsequently derived which is then integrated over the micelle surface and divided by the aggregation number of the micelle to yield the average steric free energy per molecule, g_{st}. Specifically,

$$dG_{st,local} = -dn \cdot kT \ln\left(1 - \frac{a_h \cdot dn}{dA}\right) = -\left(\frac{n}{V} dV\right) \cdot kT \ln\left(1 - \frac{a_h \cdot \left(\frac{n}{V}\right) dV}{dA}\right) \tag{3-68}$$

$$g_{st} = \frac{\int dG_{st,local}}{\int dn} = \frac{\int -\left(\frac{nkT}{V}\right) \ln\left(1 - \frac{na_h dV}{VdA}\right) dV}{n} = -\frac{kT}{V} \int \ln\left(1 - \frac{na_h dV}{VdA}\right) dV \tag{3-69}$$

The key equations and results for discoidal and biaxial ellipsoidal micelles are presented next in Section 3.5.1 and Section 3.5.2, respectively.

3.5.1 g_{st} of the Semi-Toroidal Rim of a Discoidal Micelle

$dG_{st,local}$ is calculated by substituting the differential geometric properties derived in Eqs. (3-17) and (3-35) in Eq. (3-68). Specifically,

$$dG_{st,local} = -dn \cdot k_B T \ln\left(1 - \frac{a_h \left(n \Big/ \left(\frac{\pi b'^2}{3}(3b\pi + 4b')\right)\right)\left(bb'^2/2 + \left(b'^3/3\right)\cos v\right) du dv}{b'\left(b + b'\cos v\right) du dv} \cdot \frac{A}{A}\right) \tag{3-70}$$

$$= -dn \cdot k_B T \ln\left(1 - \left(\frac{a_h}{a}\right)\left(\frac{\pi b + 2b'}{3b\pi + 4b'}\right)\left(\frac{3b + 2b'\cos v}{b + b'\cos v}\right)\right)$$

$$g_{st,local} = \frac{dG_{st,local}}{dn} = -k_B T \ln\left(1 - \left(\frac{a_h}{a}\right)\left(\frac{\pi b + 2b'}{3b\pi + 4b'}\right)\left(\frac{3b + 2b'\cos v}{b + b'\cos v}\right)\right) \tag{3-71}$$

Figure 3-15 shows the variation of the local steric free energy per molecule of the semi-toroidal rim, $g_{st,local}$, as a function of the angle v for a discoidal micelle formed by a surfactant having a 6-carbon fluorocarbon tail and a head area, a_h, of 50.0 Å^2 at 298.15 K. The discs have b = 3b' and b' is equal to the maximum surfactant tail length calculated using Eq. (2-15). Figure 3-15 shows that $g_{st,local}$ attains its maximum value at $v = \pm\pi/2$ and its minimum value at $v = 0$. This follows because the semi-toroidal rim has the highest curvature at $v = 0$, which corresponds

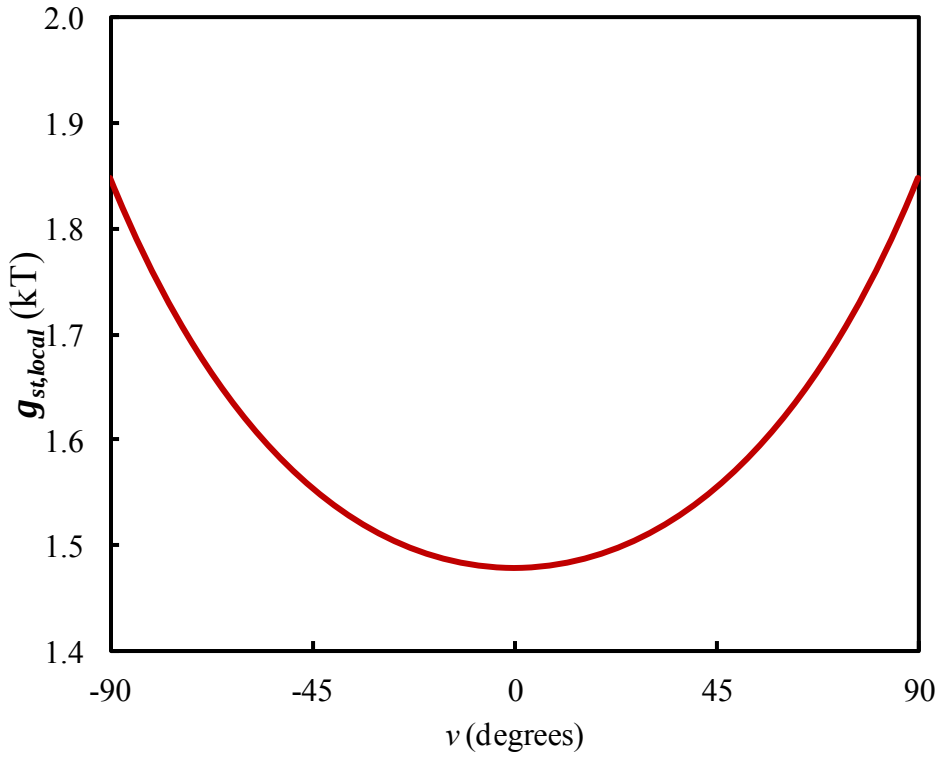

Figure 3-15: Variation of the local steric free energy, $g_{st,local}$, as a function of the angle v.

to the highest surface area per molecule, and the lowest curvature at $\pm\pi/2$ which corresponds to the lowest surface are per molecule. Since the steric free energy per molecule has an inverse dependence on the surface area per molecule, $g_{st,local}$ attains its maximum value at the lowest curvature region.

Using Eq. (3-70), the average steric free energy per molecule, g_{st}, can be calculated by substituting it in Eq. (3-69) as follows:

$$g_{st} = \int_{v=-\pi/2}^{v=\pi/2} -\frac{kT}{\frac{\pi b'^2}{3}(3b\pi+4b')} \ln\left(1-\left(\frac{a_h}{a}\right)\left(\frac{\pi b+2b'}{3b\pi+4b'}\right)\left(\frac{3b+2b'\cos v}{b+b'\cos v}\right)\right)\frac{\pi b'^2}{3}(3b+2b'\cos v)\,dv \tag{3-72}$$

$$= -\frac{kT}{(3b\pi+4b')}\int_{v=-\pi/2}^{v=\pi/2} \ln\left(1-\left(\frac{a_h}{a}\right)\left(\frac{\pi b+2b'}{3b\pi+4b'}\right)\left(\frac{3b+2b'\cos v}{b+b'\cos v}\right)\right)(3b+2b'\cos v)\,dv$$

Because the integral in Eq. (3-72) cannot be evaluated analytically, the Gaussian quadrature numerical integration technique was used to calculate g_{st} of the semi-toroidal rim of a discoidal micelle.

Figure 3-16 shows the variation of g_{st} as a function of b/b' of the semi-toroidal rims of discoidal micelles formed by the same surfactant considered in Figure 3-15. All the discoidal micelles considered in Figure 3-16 have b' equal to the maximum surfactant tail length. For comparison, the steric free energies for the same surfactant forming spherical and cylindrical micelles having their radii equal to the semi-minor axis length are plotted in red and blue, respectively. Additionally, the steric free energy calculated using the model developed by Srinivasan and Blankschtein is plotted in purple.[28] Figure 3-16 shows that g_{st} for the semi-

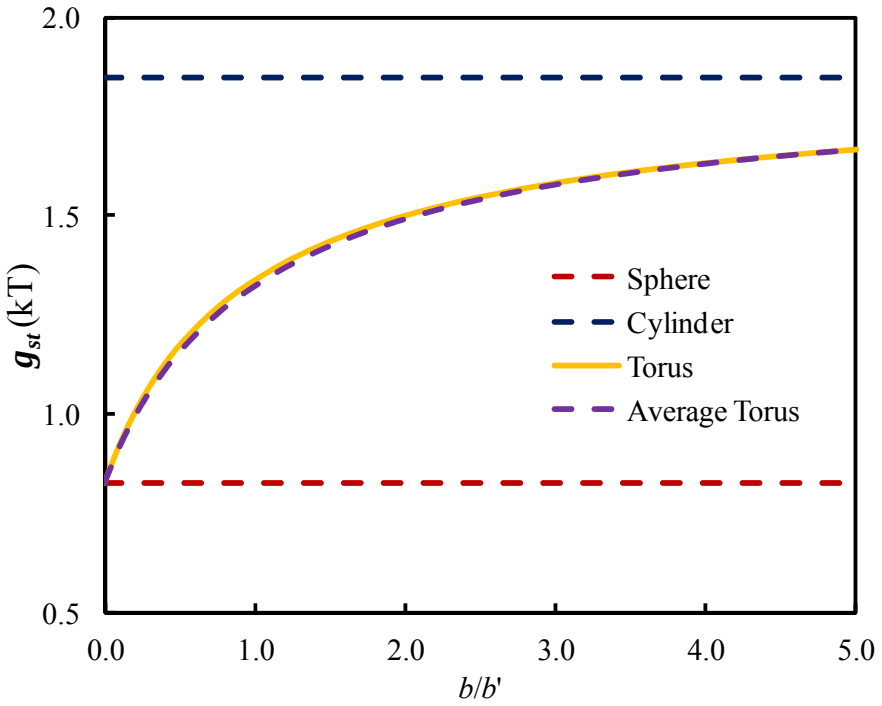

Figure 3-16: Variation of the steric free energy per molecule, g_{st}, of the semi-toroidal rim of a discoidal micelle as a function b/b'. Also shown for comparison are g_{st} for a sphere and a cylinder of radius b', and an average torus (see text).

toroidal rim, in yellow, starts at the value equal to that for a sphere at $b/b' = 0$ and then approaches the value for a cylinder as $b/b' \to \infty$. g_{st} increases with increasing b/b' because an increase in b/b' results in a reduction in the average curvature, which in turn reduces the average surface area per molecule, thereby increasing g_{st}. It is also interesting to note that the g_{st} calculated using the curvature-corrected model (yellow curve) is very close to the g_{st} calculated using the model developed by Srinivasan and Blankschtein (purple dashed curve) in which the effect of curvature was accounted for approximately by calculating an average area per molecule.[28] This finding may be because, for semi-toroidal rims of discoidal micelles, the curvature does not show extreme deviations from the average mean curvature. Therefore, the model developed by Srinivasan and Blankschtein, which is simpler and does not require numerical integration, may be utilized to calculate g_{st} for discs without introducing significant error.

3.5.2 g_{st} of a Biaxial Ellipsoidal Micelle

$dG_{st,local}$ for a biaxial ellipsoid is calculated by substituting the differential geometric properties derived in Eqs. (3-23) and (3-44) in Eq. (3-68). Specifically,

$$dG_{st,local} = -dn \cdot k_B T \ln\left(1 - \frac{a_h\left(n \Big/ \left(\frac{4}{3}\pi p^2 q\right)\right)\frac{p^2 q}{3}\sin v\, du\, dv}{p \sin v \sqrt{p^2 \cos^2 v + q^2 \sin^2 v}\, du\, dv}\right)$$

$$= -dn \cdot k_B T \ln\left(1 - \frac{n a_h}{4\pi p \sqrt{p^2 \cos^2 v + q^2 \sin^2 v}}\right) \tag{3-73}$$

$$g_{st,local} = \frac{dG_{st,local}}{dn} = -k_B T \ln\left(1 - \frac{n a_h}{4\pi p \sqrt{p^2 \cos^2 v + q^2 \sin^2 v}}\right) \tag{3-74}$$

Similar to Figure 3-15, Figure 3-17 shows a plot of the variation of the local steric free energy per molecule, $g_{int,local}$, at 298.15 K of a surfactant having a 6-carbon fluorocarbon tail and a head area of 50.0 Å^2 forming a prolate ellipsoidal micelle. The prolate ellipsoidal micelle has p equal to the maximum surfactant tail length. Figure 3-17 shows that $g_{int,local}$ is smallest at $v = \pi/2$ (90 degrees), and increases close to the poles of the prolate ellipsoid located at $v = 0$ and π (180 degrees). This result can be explained based on the same reasoning provided in Section 3.3.2 to explain Figure 3-6.

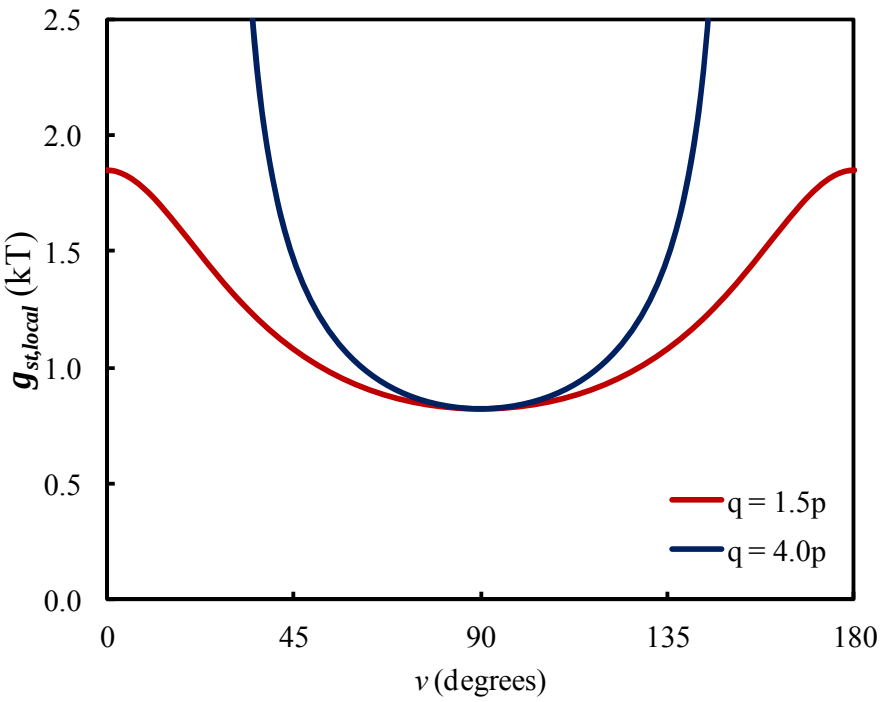

Figure 3-17: Variation of the local steric free energy per molecule, $g_{st,local}$, as a function of the angle v for a prolate ellipsoidal micelle.

Note that at higher aspect ratios, $g_{st,local}$ for a prolate ellipsoidal micelle diverges near $v = \pi/2$ (90 degrees). This follows because the available surface area is not sufficient to accommodate the surfactant heads. This is similar to the observation made in Figure 3-6regarding $g_{int,local}$. Consequently, an equation similar to Eq. (3-47) regarding the threshold size

of ellipsoidal micelles can be derived using the local steric free energy. From the expression for $dG_{st,local}$ in Eq. (3-68), it follows that the steric free energy will diverge if:

$$
\begin{aligned}
&1-\frac{a_h dn}{dA}<0 \Rightarrow \sqrt{p^2\cos^2 v+q^2\sin^2 v}-\frac{a_h}{v_{tail}}\frac{pq}{3}>0, \quad 0\le v\le \pi \\
&\Rightarrow \begin{cases} p-\dfrac{a_h}{v_{tail}}\dfrac{pq}{3}>0, & 0\le v\le \pi, \quad p<q \\ q-\dfrac{a_h}{v_{tail}}\dfrac{pq}{3}>0, & 0\le v\le \pi, \quad p>q \end{cases} \\
&\Rightarrow \begin{cases} q<\dfrac{3v_{tail}}{a_h}, & p<q \\ p<\dfrac{3v_{tail}}{a_h}, & p>q \end{cases}
\end{aligned}
\tag{3-75}
$$

Based on Eqs. (3-47) and (3-75), it follows that there are two theoretical limits on the size of feasible ellipsoidal micelles using the curvature-corrected model presented here. As a result, the limit on the size of the ellipsoidal micelle is determined by the stricter of the two conditions.

A plot similar to the one in Figure 3-17 for an oblate ellipsoidal micelle core formed by the same surfactant and having the same semi-minor axis length is shown in Figure 3-18. Figure 3-18 shows that $g_{st,local}$ is highest at $v = \pi/2$ (90 degrees), and decreases close to $v = 0$ and π (180 degrees). At higher aspect ratios, similar to the result obtained for prolate ellipsoids, $g_{st,local}$ tends to infinity for oblate ellipsoids. All these observations can be explained based on the reasons presented earlier in the case of prolate ellipsoidal micelles.

Using Eq. (3-73) in Eq. (3-69), the average steric free energy per molecule, g_{st}, for ellipsoidal micelles can be calculated as follows:

$$
g_{st}=-\frac{kT}{2}\int_{v=0}^{v=\pi}\ln\left(1-\frac{na_h}{4\pi p\sqrt{p^2\cos^2 v+q^2\sin^2 v}}\right)\sin v\,dv \tag{3-76}
$$

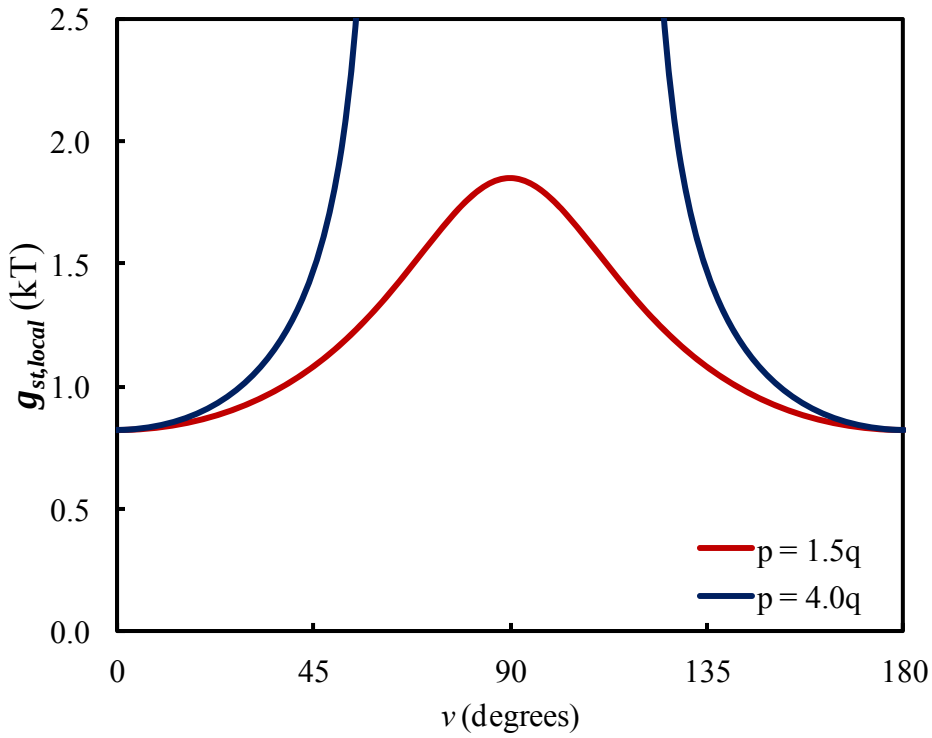

Figure 3-18: Variation of the local steric free energy, $g_{st,local}$, as a function of the angle v for an oblate ellipsoidal micelle.

Similar to Eq. (3-72), the integral in Eq. (3-76) is evaluated using the Gaussian quadrature numerical integration technique. Figure 3-19 shows the variation of g_{st} as a function of the aspect ratio of a biaxial ellipsoidal micelle formed by the same surfactant considered in Figures 2-20 and 2-21. All the ellipsoidal micelles considered in Figure 3-19 have a semi-minor axis length equal to the maximum surfactant tail length. For comparison, the steric free energies for the same surfactant forming spherical and cylindrical micelles having their radii equal to the semi-minor axis length are plotted in red and blue, respectively. Additionally, the steric free energy per molecule calculated by substituting the average surface area per molecule in place of a in Eq. (2-24) for prolate and oblate ellipsoidal micelles are plotted as dashed curves in green and purple, respectively. Figure 3-19 shows that g_{st} for biaxial ellipsoidal micelles, in green and purple, start at the value equal to that for a sphere at an aspect ratio of 1, and then increases as

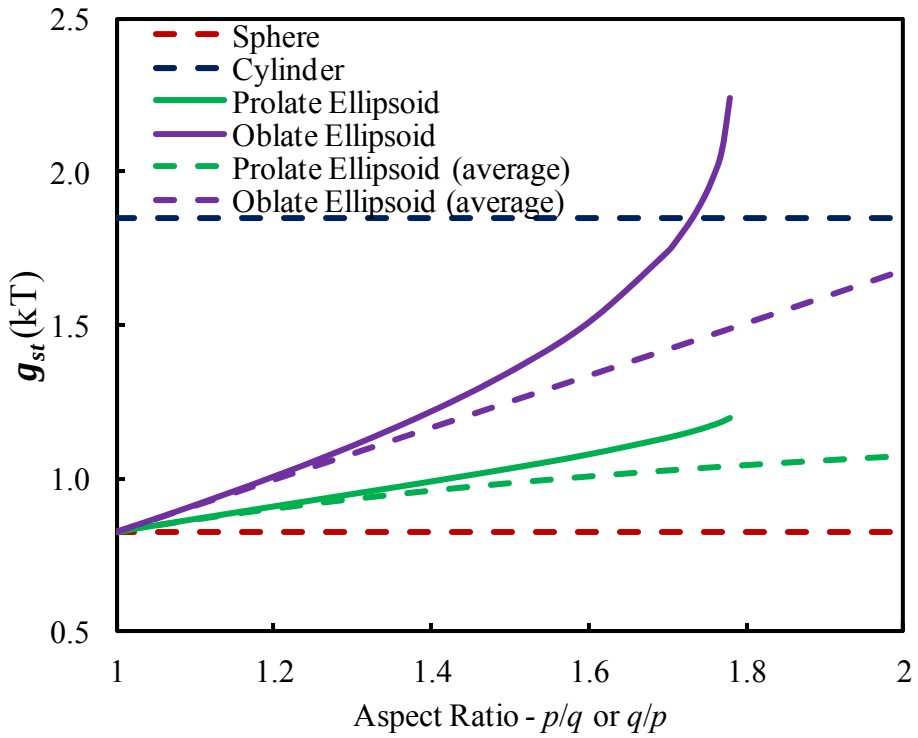

Figure 3-19: Variation of the steric free energy per molecule, g_{st}, for biaxial ellipsoidal micelles as a function of the aspect ratio. Also shown for comparison are g_{st} for a sphere and a cylinder of radius equal to the semi-minor axis length.

the aspect ratio increases. This follows because an increase in the aspect ratio, while keeping the semi-minor axis length constant, results in a smaller average surface area per molecule, which in turn leads to a higher steric free energy per molecule. Additionally, g_{st} for a prolate ellipsoid is lower than g_{st} for an oblate ellipsoid having the same semi-minor axis length and aspect ratio. This follows because, for the same semi-minor axis length and aspect ratio, the prolate ellipsoidal shape has a higher average surface area per molecule than the oblate ellipsoidal shape.

Finally, Figure 3-19 indicates that g_{st} calculated using the average surface area per molecule (green and purple dashed curves) shows significant deviation from g_{st} calculated using the curvature-corrected model (green and purple solid curves). This follows because the extremes in the local curvature are unaccounted for if one simply uses the average area per

molecule in Eq. (2-24), instead of explicitly accounting for the curvature. This clearly shows that it is necessary to use the curvature-corrected model to accurately quantify the steric free energy per molecule in the case of biaxial ellipsoidal micelles.

3.6 Electrostatic Free Energy

The electrostatic free energy consists of two free-energy contributions, namely, the discharging free energy, g_{disch}, and the charging free energy, g_{ch}, as was discussed in Section 2.3. The discharging free energy is not a function of the micelle shape, and therefore, is calculated using Eq. (2-25) for discs and ellipsoids as well. However, the charging free energy depends strongly on the shape of the micelle.

The development of a model to calculate g_{ch} for discs and biaxial ellipsoids is quite challenging. This follows because while in the case of spheres, infinite cylinders, and infinite bilayers the governing equations in (2-27) - (2-30) are one dimensional, thus yielding ordinary differential equations, in the case of discs and biaxial ellipsoids, the governing equations are two dimensional, thus yielding partial differential equations. This reflects the varying curvature of these micelle shapes. Moreover, no analytical or approximate solutions are available to solve the resulting set of partial differential equations. As a result, the set of equations in (2-27) - (2-30) needs to be solved numerically in the case of discs and biaxial ellipsoids.

Incorporating a model that numerically solves a set of nonlinear partial differential equations (recall that the Poisson-Boltzmann equation is nonlinear) into our molecular-thermodynamic framework to predict micellization properties, including the critical micelle concentration and other micelle characteristics, is computationally very challenging. This follows because in order to determine these micellization characteristics, it is necessary to determine the

optimal free energy of micellization, as discussed in Section 2.5. This optimization process requires the evaluation of the free energy of micellization, g_{mic}, at several solution conditions and micelle properties (such as the dimensions of the micelle and the degree of counterion binding). From a computational viewpoint, numerically solving a nonlinear partial differential equation every time that g_{mic} needs to be evaluated is very inefficient. Therefore, to overcome this problem, the required solution to the set of partial differential equations to calculate g_{ch}, which is the surface electric potential ψ_{ch} in this case, was calculated for a large data set that spans all the variables that affect ψ_{ch}. These variables include micelle sizes (designated by two size variables, b and b' for discs, and p and q for biaxial ellipsoids), Stern-layer thicknesses, ionic strengths, and surface charges, based on the typical surfactant tail lengths, tail volumes, head lengths, and counterion radii that are expected. These values of the inputs and the corresponding outputs were stored in a database. The surface electric potential at any point that is not in the database was calculated using an interpolation-based method.

To facilitate the implementation of the interpolation scheme, the data set was sorted and then stored using pointers. For any given point for which the value of the surface electric potential is sought, the interpolation scheme first finds the 32 ($=2^5$) nearest neighbors. Note that 2^5 nearest neighbors are found because the surface electric potential depends on five variables (two micelle size variables, the Stern-layer thickness, the ionic strength, and the micelle charge), and along each variable the given point is bound by two neighbors, one above and one below it. These points form a polyhedron enclosing the given point. This is illustrated in Figure 3-20 for the three- dimensional equivalent of the actual five-dimensional problem. The red point in Figure 3-20 represents the point for which the nearest neighbors are sought. Subsequently, the surface electric potential at the given point is calculated by using a weighted-average of the surface

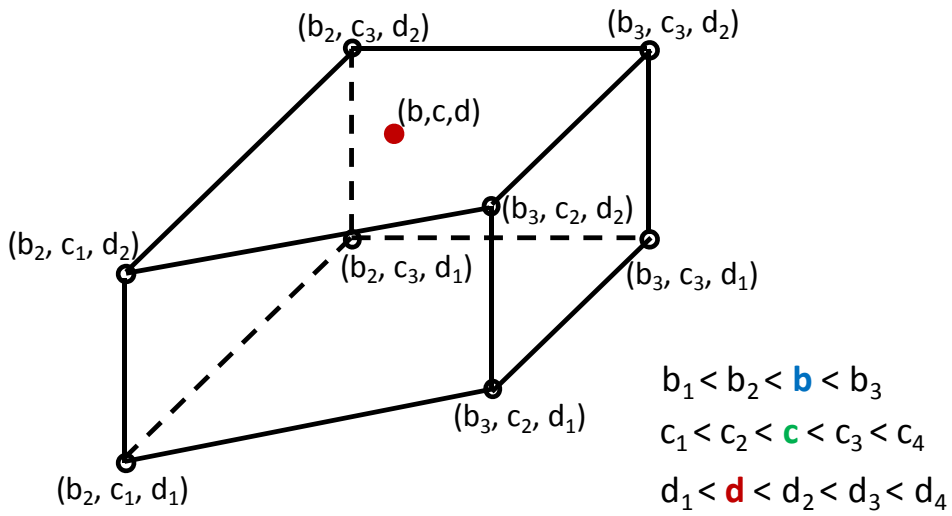

Figure 3-20: Schematic showing the polyhedron formed by the eight nearest neighbors of the red point.

electric potential of the 32 nearest neighbors. The weights for the different neighbor points are proportional to the inverse of the product of the projected distance along each variable axis between the given point and the nearest neighbor. Note that the commonly used Euclidean-distance based weighting scheme performs poorly in this case because the ranges of values spanned by the five independent variables are very different. For example, the surface charge is on the order of 10^{-19} - 10^{-18} C, while the ionic strength is on the order of 10^{24} – 10^{26} molecules/m^3. This results in the Euclidean distance being a measure of the distance along the axis with the largest order of magnitude. The weighting scheme described above does not exhibit this problem. In fact, for a regular grid, it can be shown that this scheme is equivalent to the multilinear interpolation scheme (see Section 7.1.11 in the Appendix), which is a reasonable interpolation scheme for a function that is monotonic.

Using the interpolation database, g_{ch} is finally calculated by numerically integrating the surface electric potential as a function of the surface charge using the Gauss quadrature technique. This method of interpolation and numerical integration was applied to a simplified model of the Poisson-Boltzmann equation for a spherical particle for which an approximate

analytical solution is available,[43] and it was found that the root-mean square error between the analytical value and the numerical value of the charging free energy is 0.3 kT, which is less than 10% of the typical values of g_{ch}.

The method outlined above to calculate the charging free energy was applied to both discs and biaxial ellipsoids. The difference in the geometry of the two shapes is captured by the differences in the form of the governing equations, (2-27) - (2-30), when represented in the appropriate coordinate system. For any general 3-D coordinate system characterized by the variables x_1, x_2, and x_3, the Laplace operator used in Eqs. (2-27) and (2-28) is given by:

$$\nabla^2 = \frac{1}{h_1 h_2 h_3}\left(\frac{\partial}{\partial x_1}\left(\frac{h_2 h_3}{h_1}\frac{\partial}{\partial x_1}\right)+\frac{\partial}{\partial x_2}\left(\frac{h_3 h_1}{h_2}\frac{\partial}{\partial x_2}\right)+\frac{\partial}{\partial x_3}\left(\frac{h_1 h_2}{h_3}\frac{\partial}{\partial x_3}\right)\right) \tag{3-77}$$

where h_i is defined as follows:

$$h_i = \left|\frac{\partial \bar{r}}{\partial x_i}\right| \tag{3-78}$$

Similarly, the gradient operator acting on ψ is defined as follows:

$$\nabla \psi = \sum_i \left(\frac{1}{h_i}\frac{\partial \psi}{\partial x_i}\right)\hat{x}_i \tag{3-79}$$

where $\hat{x}_i$ is the unit vector along the x_i direction. The governing equations and boundary conditions specific for discs and biaxial ellipsoids are presented next in Section 3.6.1 and Section 3.6.2, respectively.

3.6.1 g_{ch} of the Semi-Toroidal Rim of a Discoidal Micelle

g_{ch} of a disc is approximated as the sum of g_{ch} of the central bilayer and g_{ch} of the semi-toroidal rim. Calculation of g_{ch} of a bilayer was discussed in Section 2.3. The parameterization introduced in Eq. (3-14) is sufficient to calculate g_{ch} for the semi-toroidal rim. The only difference is that, for the purpose of calculating g_{ch}, r takes values corresponding to the bulk solution instead of between 0 and b', which corresponds to the micelle core. For the parameterization in Eq. (3-14), the Laplace operator calculated using Eqs. (3-77) and (3-78) is given by:

$$\nabla^2\psi = \frac{1}{r\left(b+r\cos v\right)}\left(\frac{\partial}{\partial r}\left(r\left(b+r\cos v\right)\frac{\partial\psi}{\partial r}\right)+\frac{\partial}{\partial v}\left(\frac{b+r\cos v}{r}\frac{\partial\psi}{\partial v}\right)+\frac{\partial}{\partial u}\left(\frac{r}{b+r\cos v}\frac{\partial\psi}{\partial u}\right)\right) \quad (3\text{-}80)$$

The details of deriving the Laplace operator are provided in Section 7.1.12 of the Appendix. Note that because the z axis is an axis of symmetry, we do not expect ψ to depend on the angle u. Consequently, the third term on the right-hand side of Eq. (3-80) is equal to 0. Using Eqs. (2-27), (2-28), and (3-80), the governing equations inside the Stern layer and beyond the Stern surface are given by:

$$\nabla^2\psi = \frac{1}{r\left(b+r\cos v\right)}\left(\frac{\partial}{\partial r}\left(r\left(b+r\cos v\right)\frac{\partial\psi}{\partial r}\right)+\frac{\partial}{\partial v}\left(\frac{b+r\cos v}{r}\frac{\partial\psi}{\partial v}\right)\right)=0, \quad b'_{charge}\le r < b'_{Stern} \text{ and } -\pi/2\le v\le\pi/2 \quad (3\text{-}81)$$

$$\nabla^2\psi = \frac{1}{r\left(b+r\cos v\right)}\left(\frac{\partial}{\partial r}\left(r\left(b+r\cos v\right)\frac{\partial\psi}{\partial r}\right)+\frac{\partial}{\partial v}\left(\frac{b+r\cos v}{r}\frac{\partial\psi}{\partial v}\right)\right)=-\frac{1}{\varepsilon_{bulk}}\sum_i I_{i,0}z_i e_0\exp\left(-\frac{z_i e_0\psi}{kT}\right), \quad b'_{Stern}\le r<\infty \text{ and } -\pi/2\le v\le\pi/2 \quad (3\text{-}82)$$

where b'_{Stern} and b'_{charge} represent the Stern surface and the charged surface, respectively. To generalize the four boundary conditions provided in Section 2.3 on pages 44 and 45 in the semi-torus coordinate system, the gradient operator is given by:

$$\nabla \psi = \frac{\partial \psi}{\partial r}\hat{r} + \frac{1}{r}\frac{\partial \psi}{\partial v}\hat{v} + \frac{\dfrac{\partial \psi}{\partial u}}{b + r\cos v}\hat{u} \tag{3-83}$$

where similar to Eq. (3-80), the last term is equal to 0 because ψ does not dependent on u. Using Eq. (3-83), the four boundary conditions introduced in Section 2.3 can be written in the semi-torus coordinate system as follows:

1. The micellar charged surface is at a constant unknown electric potential with a total charge of Q_f. Specifically,

$$\int_A \left(-\frac{\partial \psi}{\partial r}\hat{r} - \frac{1}{r}\frac{\partial \psi}{\partial v}\hat{v} \right) . \hat{r}\, dA \Bigg|_{r=b'_{charge}} = \frac{Q_f}{\varepsilon_{Stern}} \Rightarrow -2\pi b'_{charge} \int_{v=-\pi/2}^{v=\pi/2} \left(b + b'_{charge}\cos v \right) \left(\frac{\partial \psi}{\partial r} \right) \Bigg|_{r=b'_{charge}} dv = \frac{Q_f}{\varepsilon_{Stern}} \tag{3-84}$$

2. The potential at the Stern surface is continuous. Specifically,

$$\psi \big|_{r \to \left(b'_{Stern}\right)^+} = \psi \big|_{r \to \left(b'_{Stern}\right)^-} \tag{3-85}$$

3. Since the Stern surface has no surface charge associated with it, the normal derivatives of ψ on both sides of the Stern surface are related as follows:[41]

$$\varepsilon_{bulk} \frac{\partial \psi}{\partial r} \Bigg|_{r \to \left(b'_{charge}\right)^+} = \varepsilon_{stern} \frac{\partial \psi}{\partial r} \Bigg|_{r \to \left(b'_{charge}\right)^-} \tag{3-86}$$

4. The potential is 0 at ∞, that is,

$$\psi \left(r \to \infty \right) = 0 \tag{3-87}$$

It should be noted that the differential equations shown in (3-81) and (3-82) are second order in both r and v, and therefore, require two boundary conditions for v as well. Since the semi-toroidal rim is symmetric about the z axis, and the electric potential due to the central bilayer has no angular dependence, the gradient of the electric potential with respect to v be 0

near the axis, for the potential to be smooth near the axis. This gives rise to the following two boundary conditions:

$$\left.\frac{\partial \psi}{\partial v}\right|_{v=\pm\pi/2} = 0 \tag{3-88}$$

To develop a robust method to numerically solve a differential equation, it is often essential to scale the problem correctly. The exponential nonlinear term on the right-hand side of Eq. (3-82) shows that there is a natural scale for the electric potential in the form of kT/e_0. The other scale for ψ can be obtained from Eq. (3-84) as $Q_f \Big/ \left(2\pi b'_{charge}\varepsilon_{Stern}\right)$. Here, we have chosen kT/e_0 as the scale for ψ because Eq. (3-82) is applicable over a larger portion of the r domain compared to Eq. (3-84), and the exponential is more likely to behave erratically if Eq. (3-82) is improperly scaled. Therefore, the electric potential is non-dimensionalised as $\overline{\psi} = \left(\psi e_0\right)/kT$.

We note that the coordinate r does not have a finite domain ($b'_{charge} \le r < \infty$). An infinite domain is not easy to implement in a numerical scheme because it is difficult to define ∞ numerically. To overcome this problem, we define a new coordinate, ξ, which is like a non-dimensional distance and is proportional to $1/r$. This would force ξ to tend to 0 when r tends to ∞, thereby making the domain of the independent variable finite. ξ is defined as follows:

$$\begin{aligned} \xi &= b'_{charge}/r \\ d\xi &= -b'_{charge}\left(1/r^2\right)dr = -\left(\xi^2/b'_{charge}\right)dr \end{aligned} \tag{3-89}$$

Next, we non-dimensionalise the system of equations, (3-81) - (3-88), by introducing $\overline{\psi}$, ξ, and κ, where κ is the inverse of the Debye Hückel screening length, and is defined as follows:

$$\kappa = \sqrt{\frac{\sum_i I_{i,0} z_i^2 e_0^2}{\varepsilon_{bulk} kT}} \tag{3-90}$$

This yields:

$$\xi^4 \frac{\partial^2 \overline{\psi}}{\partial \xi^2} + \left(\frac{\xi^4 b}{\left(\xi b + b^{/}_{charge} \cos v \right)} \right) \frac{\partial \overline{\psi}}{\partial \xi} + \xi^2 \frac{\partial^2 \overline{\psi}}{\partial v^2} - \left(\frac{\xi^2 b^{/}_{charge} \sin v}{\left(\xi b + b^{/}_{charge} \cos v \right)} \right) \frac{\partial \overline{\psi}}{\partial v} = 0, \quad 1 > \xi > b^{/}_{charge} \big/ b^{/}_{Stern} \tag{3-91}$$

$$\left(\xi^4 \frac{\partial^2 \overline{\psi}}{\partial \xi^2} + \left(\frac{\xi^4 b}{\left(\xi b + b^{/}_{charge} \cos v \right)} \right) \frac{\partial \overline{\psi}}{\partial \xi} + \xi^2 \frac{\partial^2 \overline{\psi}}{\partial v^2} - \left(\frac{\xi^2 b^{/}_{charge} \sin v}{\left(\xi b + b^{/}_{charge} \cos v \right)} \right) \frac{\partial \overline{\psi}}{\partial v} \right) = - \frac{\left(\kappa b^{/}_{charge} \right)^2 \sum_i I_{i,0} z_i \exp\left(-z_i \overline{\psi} \right)}{\sum_i I_{i,0} z_i^2}, \quad 0 < \xi < b^{/}_{charge} \big/ b^{/}_{Stern} \tag{3-92}$$

$$\overline{\psi}\left(\xi = 1 \right) = \overline{\psi}_{charge,unknown} \tag{3-93}$$

$$\int_{v=-\pi/2}^{v=\pi/2} \left(\frac{\partial \overline{\psi}}{\partial \xi} \right)\Bigg|_{\xi=1} \left(b + b^{/}_{charge} \cos v \right) dv = \frac{Q_f e_0}{2\pi kT \varepsilon_{Stern}} \tag{3-94}$$

$$\overline{\psi}\Big|_{\xi \to \left(b^{/}_{charge} / b^{/}_{Stern} \right)^-} = \overline{\psi}\Big|_{\xi \to \left(b^{/}_{charge} / b^{/}_{Stern} \right)^+} \tag{3-95}$$

$$\varepsilon_{bulk} \frac{\partial \overline{\psi}}{\partial \xi}\Bigg|_{\xi \to \left(b^{/}_{charge} / b^{/}_{Stern} \right)^-} = \varepsilon_{Stern} \frac{\partial \overline{\psi}}{\partial \xi}\Bigg|_{\xi \to \left(b^{/}_{charge} / b^{/}_{Stern} \right)^+} \tag{3-96}$$

$$\overline{\psi}\left(\xi \to 0 \right) = 0 \tag{3-97}$$

$$\frac{\partial \overline{\psi}}{\partial v}\Bigg|_{v=\pm\pi/2} = 0 \tag{3-98}$$

Equations (3-91) - (3-98) are solved numerically using the finite difference technique. Let the number of grid points along the v axis be denoted by N_v, and the number of grid points along the ξ axis in the Stern layer and the bulk solution be denoted by N_{Stern} and N_{bulk}, respectively. Let the indices j and k denote grid points along the ξ and v axes, respectively. As a result, $j = 1$, $j =$

N_{bulk} and $j = N_\xi = N_{bulk} + N_{Stern} - 1$ correspond to $\xi = 0$, $\xi = b'_{charge} \big/ b'_{Stern}$, and $\xi = 1$, respectively, while $k = 1$ and $k = N_v$ correspond to $v = -\pi/2$ and $v = \pi/2$, respectively.

Using a second-order central difference approach, the derivatives that appear in Eqs. (3-91) and (3-92) can be approximated as follows:

$$\left.\frac{\partial^2 \overline{\psi}}{\partial \xi^2}\right|_{j,k} = \frac{\overline{\psi}_{j+1,k} + \overline{\psi}_{j-1,k} - 2\overline{\psi}_{j,k}}{(\Delta\xi)^2}; \quad \left.\frac{\partial \overline{\psi}}{\partial \xi}\right|_{j,k} = \frac{\overline{\psi}_{j+1,k} - \overline{\psi}_{j-1,k}}{2\Delta\xi} \tag{3-99}$$

$$\left.\frac{\partial^2 \overline{\psi}}{\partial v^2}\right|_{j,k} = \frac{\overline{\psi}_{j,k+1} + \overline{\psi}_{j,k-1} - 2\overline{\psi}_{j,k}}{(\Delta v)^2}; \quad \left.\frac{\partial \overline{\psi}}{\partial v}\right|_{j,k} = \frac{\overline{\psi}_{j,k+1} - \overline{\psi}_{j,k-1}}{2\Delta v} \tag{3-100}$$

The boundary condition in Eq. (3-93) can be written as follows:

$$\overline{\psi}_{N_\xi,k} = \overline{\psi}_{N_\xi,k-1}, \quad k \in [2, N_v] \tag{3-101}$$

Using the trapezoidal rule, the integral boundary condition in Eq. (3-94) can be approximated as follows:

$$\begin{aligned} &\left(b + b'_{charge}\cos v_1\right)\left(\Delta v/2\right)\left.\left(\frac{\partial \overline{\psi}}{\partial \xi}\right)\right|_{N_\xi,1} + \sum_{k=2}^{N_v-1}\left(b + b'_{charge}\cos v_k\right)\Delta v\left.\left(\frac{\partial \overline{\psi}}{\partial \xi}\right)\right|_{N_\xi,k} \\ &+\left(b + b'_{charge}\cos v_{N_v}\right)\left(\Delta v/2\right)\left.\left(\frac{\partial \overline{\psi}}{\partial \xi}\right)\right|_{N_\xi,N_v} = \frac{Q_f e_0}{2\pi\varepsilon_{Stern} kT} \end{aligned} \tag{3-102}$$

This can be further simplified by approximating the derivatives using the backward-difference approach. This yields:

$$\begin{aligned} &\left(\frac{3\overline{\psi}_{N_\xi,1} - 4\overline{\psi}_{N_\xi-1,1} + \overline{\psi}_{N_\xi-2,1}}{2\Delta\xi}\right)\left(b/b'_{charge} + \cos v_1\right)\left(\Delta v/2\right) + \sum_{k=2}^{N_v-1}\left(\frac{3\overline{\psi}_{N_\xi,k} - 4\overline{\psi}_{N_\xi-1,k} + \overline{\psi}_{N_\xi-2,k}}{2\Delta\xi}\right)\left(b/b'_{charge} + \cos v_k\right)\Delta v \\ &+\left(\frac{3\overline{\psi}_{N_\xi,N_v} - 4\overline{\psi}_{N_\xi-1,N_v} + \overline{\psi}_{N_\xi-2,N_v}}{2\Delta\xi}\right)\left(b/b'_{charge} + \cos v_{N_v}\right)\left(\Delta v/2\right) = \frac{Q_f e_0}{2\pi kT\varepsilon_{Stern} b'_{charge}} \end{aligned} \tag{3-103}$$

The boundary condition in Eq. (3-95) is automatically satisfied since the Stern surface is characterized by a single value of j (N_{bulk}), and consequently, the electric potential satisfies the continuity condition. The boundary condition in Eq. (3-96) involves derivatives at the boundary. Since the central-difference approach is not applicable at the boundary, the backward-difference and the forward-difference approach are used to approximate the derivatives in Eq. (3-96). Specifically,

$$\varepsilon_{bulk}\left(\frac{3\overline{\psi}_{N_{bulk},k}-4\overline{\psi}_{N_{bulk}-1,k}+\overline{\psi}_{N_{bulk}-2,k}}{2\Delta\xi}\right)=\varepsilon_{Stern}\left(\frac{-3\overline{\psi}_{N_{bulk},k}+4\overline{\psi}_{N_{bulk}+1,k}-\overline{\psi}_{N_{bulk}+2,k}}{2\Delta\xi}\right),\quad k\in\left[2,N_v-1\right] \tag{3-104}$$

The boundary condition given in Eq. (3-97) can be written as follows:

$$\overline{\psi}_{1,k}=0,\quad k\in\left[1,N_v\right] \tag{3-105}$$

Finally, the two boundary conditions in v given in Eq. (3-98) are approximated as follows:

$$\left(\frac{-3\overline{\psi}_{j,1}+4\overline{\psi}_{j,2}-\overline{\psi}_{j,3}}{2\Delta v}\right)=0\quad j\in\left[2,N_\xi-1\right] \tag{3-106}$$

$$\left(\frac{3\overline{\psi}_{j,N_v}-4\overline{\psi}_{j,N_v-1}+\overline{\psi}_{j,N_v-2}}{2\Delta v}\right)=0\quad j\in\left[2,N_\xi-1\right] \tag{3-107}$$

The corner points, corresponding to (1, 1), (1, N_v), (N_ξ, 1), and (N_ξ, N_v) are forced to satisfy Eq. (3-101) or Eq. (3-105), instead of Eq. (3-106) or Eq. (3-107) , whichever is applicable.

To solve for the electric potential, one needs to determine a set of $\overline{\psi}_{j,k}$ such that the system of non-linear equations presented above is satisfied. To solve a system of non-linear equations, an initial guess for the values of $\overline{\psi}_{j,k}$ needs to be provided, which in this case is done by solving the linearised version of the non-linear set of equations. The non-linearity in this

system of equations stems from the exponential on the right-hand side of Eq. (3-92). Upon linearising it, one obtains:

$$\left(\xi_j^4 \left.\frac{\partial^2 \overline{\psi}}{\partial \xi^2}\right|_{j,k} + \frac{\xi_j^4 b}{\left(\xi_j b + b'_{charge}\cos v_k\right)} \left.\frac{\partial \overline{\psi}}{\partial \xi}\right|_{j,k} + \xi_j^2 \left.\frac{\partial^2 \overline{\psi}}{\partial v^2}\right|_{j,k} - \frac{\xi_j^2 b'_{charge}\sin v}{\xi_j b + b'_{charge}\cos v_k} \left.\frac{\partial \overline{\psi}}{\partial v}\right|_{j,k} \right) = \left(b'_{charge}\kappa\right)^2 \overline{\psi}_{j,k} \tag{3-108}$$

The details of the linearization are presented in Section 7.1.13 of the Appendix. The linearised version of the equation is a lot simpler to solve. However, the initial guess is not the best if $\overline{\psi} > 1$, because the linearization becomes inaccurate. Using this initial guess, the system of nonlinear algebraic equations created by using the finite different technique is solved to obtain the surface electric potential, which is then stored in the interpolation database.

3.6.2 g_{ch} of a Biaxial Ellipsoidal Micelle

To calculate g_{ch} for a prolate ellipsoid, the following convenient parameterization was used:

$$\begin{aligned} \overline{x} = \left(f\sinh\xi\sin v\cos u, f\sinh\xi\sin v\sin u, f\cosh\xi\cos v\right) \\ \xi_{charge} \le \xi < \infty, 0 \le v \le \pi, \text{ and } 0 \le u < 2\pi \end{aligned} \tag{3-109}$$

where surfaces of constant ξ are confocal ellipsoids centered at the origin and having a focal length equal to f. Note that ξ and f can be expressed in terms of the variables introduced in the ellipsoidal parameterization described in Eq. (3-20), namely, p, q, and r. Specifically, ξ and f are equal to $\tanh^{-1}(p/q)$ and $r.(q^2 - p^2)^{1/2}$, respectively. The size and the shape of a prolate ellipsoid described by Eq. (3-109) are jointly determined by f and ξ. For a fixed value of f, a small value of ξ results in a smaller and elongated ellipsoid. On the other hand, for a given value of ξ, a smaller value of f results in a smaller ellipsoid. However, it should be noted that f is not a variable here.

Indeed once the ellipsoidal surface is defined as the micellar charged surface, f and ξ_{charge} are fixed, and only ξ (in addition to v and u) varies from ξ_{charge} to ∞ to span the entire space.

Note that unlike the parameterization in Eq. (3-20), the parameterization in Eq. (3-109) is valid only for prolate ellipsoids and not for oblate ellipsoids because the hyperbolic cosine of ξ is always greater than the hyperbolic sine of ξ. Instead, for an oblate ellipsoid, the parameterization is given by:

$$\bar{x} = \left(f'\cosh\xi'\sin v\cos u, f'\cosh\xi'\sin v\sin u, f'\sinh\xi'\cos v \right) \qquad 0 \le \xi' < \infty, 0 \le v \le \pi, \text{ and } 0 \le u < 2\pi \tag{3-110}$$

where ξ' is equal to $\tanh^{-1}(q/p)$ and f' is equal to $r.(p^2 - q^2)^{1/2}$. Because the two parameterizations for prolate ellipsoids and oblate ellipsoids shown in Eqs. (3-109) and (3-110) are similar in form, most of the derivations and analyses presented in this section are for prolate ellipsoids unless otherwise stated. Note that similar equations can be derived for oblate ellipsoids.

Using Eqs. (3-77) - (3-79) for the parameterization in Eq. (3-109), the Laplace and the gradient operators are given by:

$$\nabla^2\psi = \frac{\frac{\partial}{\partial\xi}\left(f\sinh\xi\sin v\frac{\partial\psi}{\partial\xi}\right) + \frac{\partial}{\partial v}\left(f\sinh\xi\sin v\frac{\partial\psi}{\partial v}\right) + \frac{\partial}{\partial u}\left(\frac{f\left(\sin^2 v + \sinh^2\xi\right)}{\sinh\xi\sin v}\frac{\partial\psi}{\partial u}\right)}{f^3\sinh\xi\sin v\left(\sin^2 v + \sinh^2\xi\right)} \tag{3-111}$$

$$\nabla\psi = \frac{\frac{\partial\psi}{\partial\xi}\hat{\xi} + \frac{\partial\psi}{\partial v}\hat{v}}{f\left(\sin^2 v + \sinh^2\xi\right)^{1/2}} + \frac{\frac{\partial\psi}{\partial u}}{f\sinh\xi\sin v}\hat{u} \tag{3-112}$$

Details of the derivations of Eq. (3-111) and Eq. (3-112) are provided in Section 7.1.14 of the Appendix. Note that because the z axis is an axis of symmetry, we do not expect ψ to depend on the angle u. Consequently, all the derivatives of ψ with respect to u are 0.

Before using the Laplace operator to derive the governing equations in the Stern layer and the bulk region for a prolate ellipsoid, it is necessary to define the Stern surface. Based on the properties of the Stern layer, the Stern surface is defined by the shortest distance between any mobile charged species and the charged micelle surface. This enforces the condition that the Stern layer, that is, the region between the Stern surface and the charged surface is devoid of any charged species. In the case of a regular shape, for example, in the case of a sphere, the Stern surface is defined as a sphere concentric to the charged surface with a separation equal to the sum of the radii of the ion (assuming that they are spherical with the charge located at the center of the sphere) and the distance of the charge on the surfactant head from the top of the surfactant.[43] However, in the case of an ellipsoidal charged surface, a Stern surface defined such that, at all points, the separation between the Stern surface and the charged surface is equal to the sum of the radii of the ion and the surfactant head leads to a surface which is no longer an ellipsoid. Defining such a surface would lead to a complicated analysis to determine the electrostatic free energy. Therefore, to simplify the analysis, the Stern surface is approximated to be an ellipsoidal surface which is confocal to the micellar charged surface so that it can be characterized by a single value of ξ, denoted as ξ_{Stern}. This approximation is shown pictorially in Figure 3-21, where the solid lines are confocal ellipsoids, the inner one representing the micellar charged surface and the outer one representing the approximated Stern surface. The dashed line is the exact Stern surface. Out of the infinitely many ellipsoids that are confocal to the micellar charged surface, the Stern surface is chosen to be the one which coincides with the exact Stern

surface at the low curvature points (the x and y axes in this case). Due to this approximation, a small region of the Stern layer is modeled as being part of the bulk solution (see Figure 3-21).

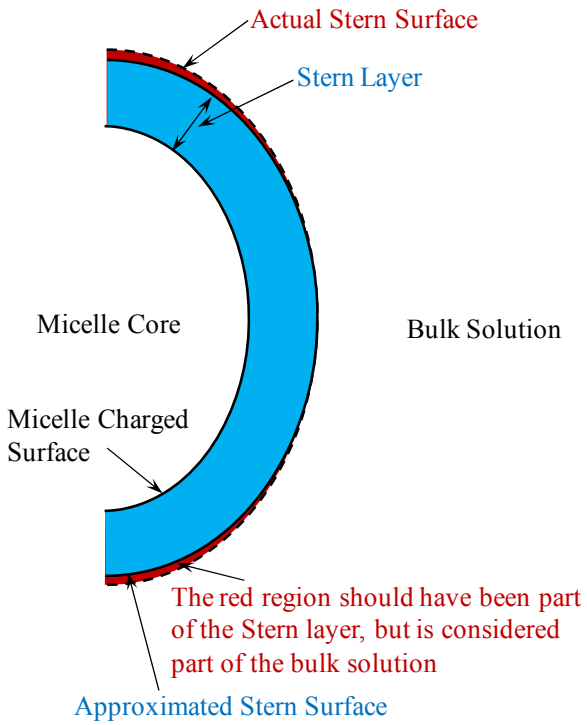

Figure 3-21: Schematic showing the difference between the approximated Stern surface and the actual Stern surface.

Using the above definition of the Stern surface and Eqs. (2-27), (2-28), and (3-111), the governing equations inside the Stern layer and in the bulk solution are given by:

$$\nabla^2\psi = \frac{\frac{\partial}{\partial\xi}\left(f\sinh\xi\sin v\frac{\partial\psi}{\partial\xi}\right)+\frac{\partial}{\partial v}\left(f\sinh\xi\sin v\frac{\partial\psi}{\partial v}\right)}{f^3\sinh\xi\sin v\left(\sin^2 v+\sinh^2\xi\right)} = 0, \qquad \xi_{charge}\le\xi<\xi_{Stern} \text{ and } 0\le v\le\pi \tag{3-113}$$

$$\nabla^2\psi = \frac{\frac{\partial}{\partial\xi}\left(f\sinh\xi\sin v\frac{\partial\psi}{\partial\xi}\right)+\frac{\partial}{\partial v}\left(f\sinh\xi\sin v\frac{\partial\psi}{\partial v}\right)}{f^3\sinh\xi\sin v\left(\sin^2 v+\sinh^2\xi\right)} = -\frac{1}{\varepsilon_{bulk}}\sum_i I_{i,0}z_i e_0\exp\left(-\frac{z_i e_0\psi}{kT}\right), \qquad \xi_{Stern}\le\xi<\infty \text{ and } 0\le v\le\pi \tag{3-114}$$

where ξ_{Stern} and ξ_{charge} denote the Stern surface and the charged surface, respectively.

The following equations generalize the boundary conditions for the partial differential equations in the case of the prolate ellipsoidal coordinate system:

1. The micellar charged surface is at a constant unknown potential with a total charge of Q_f. Specifically,

$$\psi\left(\xi=\xi_{charge}\right)=\psi_{charge,unknown} \tag{3-115}$$

$$\int_A -\frac{\left(\frac{\partial\psi}{\partial\xi}\right)\Big|_{charge} dA}{f\left(\sin^2 v+\sinh^2 \xi_{charge}\right)^{1/2}}=\frac{Q_f}{\varepsilon_{Stern}} \tag{3-116}$$

The differential area element, dA, in the above equation is calculated using the method described in Section 3.2 to yield:

$$dA=f^2\sinh\xi\sin v\left(\sin^2 v+\sinh^2\xi\right)^{1/2}dvdu \tag{3-117}$$

Substituting Eq. (3-117) in Eq. (3-116) yields:

$$\begin{aligned}&\int_{\phi=0}^{\phi=2\pi}\int_{\eta=0}^{\eta=\pi} -\frac{\left(\frac{\partial\psi}{\partial\xi}\right)f^2\sinh\xi\sin v\left(\sin^2 v+\sinh^2\xi\right)^{1/2}dvdu}{f\left(\sin^2 v+\sinh^2\xi\right)^{1/2}}\Bigg|_{\xi=\xi_{charge}}=\frac{Q_f}{\varepsilon_{Stern}}\\ &\Rightarrow -2\pi f\sinh\xi_{charge}\int_{v=0}^{v=\pi}\left(\frac{\partial\psi}{\partial\xi}\right)\Big|_{\xi=\xi_{charge}}\sin\eta d\eta=\frac{Q_f}{\varepsilon_{Stern}}\end{aligned} \tag{3-118}$$

2. The electric potential at the Stern surface is continuous, that is,

$$\psi\big|_{\xi\to(\xi_{Stern})^+}=\psi\big|_{\xi\to(\xi_{Stern})^-} \tag{3-119}$$

3. Since the Stern surface has no surface charge associated with it, the normal derivatives of ψ on both sides of the Stern surface are related as follows:[41]

$$\varepsilon_{bulk}\left.\frac{\partial\psi}{\partial\xi}\right|_{\xi\to(\xi_{Stern})^{+}} = \varepsilon_{Stern}\left.\frac{\partial\psi}{\partial\xi}\right|_{\xi\to(\xi_{Stern})^{-}} \tag{3-120}$$

4. The electric potential is 0 at ∞, that is,

$$\psi\left(\xi\to\infty\right)=0 \tag{3-121}$$

5. The gradient of the electric potential with respect to v is 0 near the axis of revolution that is,:

$$\left.\frac{\partial\psi}{\partial v}\right|_{v=0}=0 \tag{3-122}$$

$$\left.\frac{\partial\psi}{\partial v}\right|_{v=\pi}=0 \tag{3-123}$$

Similar to the equations for the semi-toroidal rim, ψ in the above governing equations is scaled to yield $\overline{\psi}=\left(\psi e_0\right)/kT$. Additionally, the size variable ξ is scaled as follows:

$$\begin{aligned}\overline{\xi} &= \frac{f\sinh\xi_{charge}}{f\sinh\xi}=\frac{\sinh\xi_{charge}}{\sinh\xi}\\ d\overline{\xi} &= -\left(\frac{\sinh\xi_{charge}}{\sinh^2\xi}\right)\cosh\xi d\xi=-\left(\frac{\overline{\xi}^2}{\sinh\xi_{charge}}\right)\sqrt{1+\left(\sinh\xi_{charge}/\overline{\xi}\right)^2}\,d\xi\end{aligned} \tag{3-124}$$

Non-dimensionalising the system of equations (3-113) - (3-115) and (3-118) - (3-123) by introducing $\overline{\psi}$, $\overline{\xi}$, and κ yields:

$$\frac{\overline{\xi}^2\left(\left(\overline{\xi}^4\operatorname{cosech}^2\xi_{charge}+\overline{\xi}^2\right)\frac{\partial^2\overline{\psi}}{\partial\overline{\xi}^2}+\overline{\xi}^3\operatorname{cosech}^2\xi_{charge}\frac{\partial\overline{\psi}}{\partial\overline{\xi}}+\frac{\partial^2\overline{\psi}}{\partial v^2}+\cot v\frac{\partial\overline{\psi}}{\partial v}\right)}{\left(\overline{\xi}^2\sin^2 v+\sinh^2\xi_{charge}\right)}=0, \qquad (3\text{-}125)$$

$$1>\overline{\xi}>\sinh\xi_{charge}/\sinh\xi_{Stern}$$

$$\frac{\overline{\xi}^2\left(\left(\overline{\xi}^4\operatorname{cosech}^2\xi_{charge}+\overline{\xi}^2\right)\frac{\partial^2\overline{\psi}}{\partial\overline{\xi}^2}+\overline{\xi}^3\operatorname{cosech}^2\xi_{charge}\frac{\partial\overline{\psi}}{\partial\overline{\xi}}+\frac{\partial^2\overline{\psi}}{\partial v^2}+\cot v\frac{\partial\overline{\psi}}{\partial v}\right)}{\left(\overline{\xi}^2\sin^2 v+\sinh^2\xi_{charge}\right)}=-\frac{(f\kappa)^2\sum_i I_{i,0}z_i\exp\left(-z_i\overline{\psi}\right)}{\sum_i I_{i,0}z_i^2}, \qquad (3\text{-}126)$$

$$\sinh\xi_{charge}/\sinh\xi_{Stern}>\overline{\xi}>0$$

$$\overline{\psi}\left(\overline{\xi}=1\right)=\overline{\psi}_{charge,unknown} \qquad (3\text{-}127)$$

$$\int_{v=0}^{v=\pi}\left(\frac{\partial\overline{\psi}}{\partial\overline{\xi}}\right)\Bigg|_{\overline{\xi}=1}\sin v dv=\frac{Q_f e_0}{2\pi f\varepsilon_{Stern}\cosh\xi_{charge}kT} \qquad (3\text{-}128)$$

$$\overline{\psi}\Big|_{\overline{\xi}\to\left(\sinh\xi_{charge}/\sinh\xi_{Stern}\right)^-}=\overline{\psi}\Big|_{\overline{\xi}\to\left(\sinh\xi_{charge}/\sinh\xi_{Stern}\right)^+} \qquad (3\text{-}129)$$

$$\varepsilon_{bulk}\frac{\partial\overline{\psi}}{\partial\overline{\xi}}\Bigg|_{\overline{\xi}\to\left(\sinh\xi_{charge}/\sinh\xi_{Stern}\right)^-}=\varepsilon_{Stern}\frac{\partial\overline{\psi}}{\partial\overline{\xi}}\Bigg|_{\overline{\xi}\to\left(\sinh\xi_{charge}/\sinh\xi_{Stern}\right)^+} \qquad (3\text{-}130)$$

$$\overline{\psi}\left(\overline{\xi}\to 0\right)=0 \qquad (3\text{-}131)$$

$$\frac{\partial\overline{\psi}}{\partial v}\Bigg|_{v=0}=0 \qquad (3\text{-}132)$$

$$\frac{\partial\overline{\psi}}{\partial v}\Bigg|_{v=\pi}=0 \qquad (3\text{-}133)$$

Equations (3-125) - (3-133) are solved numerically using the finite-difference technique introduced in Section 3.6.1 to calculate ψ_{ch}, which is then stored in an interpolation table for the calculation of g_{ch}.

All the governing equations [analogous to Eqs. (3-125) - (3-133)] for an oblate ellipsoid are listed below:

$$\frac{\overline{\xi}'^2\left(\left(\overline{\xi}'^2-\overline{\xi}'^4\operatorname{sech}^2\xi_{charge}\right)\frac{\partial^2\overline{\psi}}{\partial\overline{\xi}'^2}-\overline{\xi}'^3\operatorname{sech}^2\xi'_{charge}\frac{\partial\overline{\psi}}{\partial\overline{\xi}'}+\frac{\partial^2\overline{\psi}}{\partial v^2}+\cot v\frac{\partial\overline{\psi}}{\partial v}\right)}{\left(\cosh^2\xi'_{charge}-\overline{\xi}'^2\sin^2 v\right)}=0, \qquad 1>\overline{\xi}>\cosh\xi'_{charge}\Big/\cosh\xi'_{charge} \tag{3-134}$$

$$\frac{\overline{\xi}'^2\left(\left(\overline{\xi}'^2-\overline{\xi}'^4\operatorname{sech}^2\xi_{charge}\right)\frac{\partial^2\overline{\psi}}{\partial\overline{\xi}'^2}-\overline{\xi}'^3\operatorname{sech}^2\xi'_{charge}\frac{\partial\overline{\psi}}{\partial\overline{\xi}'}+\frac{\partial^2\overline{\psi}}{\partial v^2}+\cot v\frac{\partial\overline{\psi}}{\partial v}\right)}{\left(\cosh^2\xi'_{charge}-\overline{\xi}'^2\sin^2 v\right)}=-\frac{\left(f'\kappa\right)^2\sum_i I_{i,0}z_i\exp\left(-z_i\overline{\psi}\right)}{\sum_i I_{i,0}z_i^2}, \qquad \cosh\xi'_{charge}\Big/\cosh\xi'_{charge}>\overline{\xi}>0 \tag{3-135}$$

$$\overline{\psi}\left(\overline{\xi}'=1\right)=\overline{\psi}_{charge,unknown} \tag{3-136}$$

$$\int_{v=0}^{v=\pi}\left(\frac{\partial\overline{\psi}}{\partial\overline{\xi}'}\right)\Bigg|_{\overline{\xi}'=1}\sin v dv=\frac{Q_f e_0}{2\pi f'\varepsilon_{Stern}\sinh\xi'_{charge}kT} \tag{3-137}$$

$$\overline{\psi}\Big|_{\overline{\xi}'\to\left(\cosh\xi'_{charge}/\cosh\xi'_{Stern}\right)^-}=\overline{\psi}\Big|_{\overline{\xi}'\to\left(\cosh\xi'_{charge}/\cosh\xi'_{Stern}\right)^+} \tag{3-138}$$

$$\varepsilon_{bulk}\frac{\partial\overline{\psi}}{\partial\overline{\xi}'}\Bigg|_{\overline{\xi}'\to\left(\cosh\xi'_{charge}/\cosh\xi'_{Stern}\right)^-}=\varepsilon_{Stern}\frac{\partial\overline{\psi}}{\partial\overline{\xi}'}\Bigg|_{\overline{\xi}'\to\left(\cosh\xi'_{charge}/\cosh\xi'_{Stern}\right)^+} \tag{3-139}$$

$$\overline{\psi}\left(\overline{\xi}'\to 0\right)=0 \tag{3-140}$$

$$\frac{\partial\overline{\psi}}{\partial v}\Bigg|_{v=0}=0 \tag{3-141}$$

$$\frac{\partial\overline{\psi}}{\partial v}\Bigg|_{v=\pi}=0 \tag{3-142}$$

The method used to solve the system of equations generated using the finite-difference scheme described above is identical to those discussed in Section 3.6.1. The interpolation table created by the solution to the above set of equations can then be used to calculated g_{ch}.

The charging free energy is the final free-energy contribution that is affected by the varying curvature of the discoidal and ellipsoidal shapes. The curvature-corrected model for the

free energy of micellization can be obtained by adding the curvature-corrected expressions for the various free energies presented in Sections 3.3 - 3.6. Following the model development of the different free-energy contributions, the curvature-corrected model for discoidal micelles is compared with the model developed by Srinivasan and Blankschtein in Section 3.7. Finally, in the final section of Chapter 3, the curvature-corrected model for biaxial ellipsoidal micelles is used to evaluate their feasibility as micelle shapes, a topic of controversy in the literature of micelle shapes.

3.7 Curvature-Corrected Model for Discoidal Micelles

The free energy of micellization, g_{mic}, consists of various free-energy contributions discussed in Chapter 2 (see Eq. (2-6)). These include the transfer free energy, g_{tr}, the interfacial free energy, g_{int}, the packing free energy, g_{pack}, the steric free energy, g_{st}, the electrostatic free energy, g_{elec}, and the mixing free energy, g_{mix}. Of these free energies, g_{int}, g_{pack}, g_{st}, and g_{elec} depend on the curvature of the micelle shape. Curvature-corrected models for these free-energy contributions were presented in Sections 3.3 - 3.6 for the discoidal micelle shape. These models are significantly more complicated, and therefore, more difficult to implement than the molecular model developed by Srinivasan and Blankschtein.[28] Therefore, in this section, the free-energy contributions calculated using the two models are compared to ascertain in which cases it is essential to model discoidal micelles using the curvature-corrected model.

3.7.1 Interfacial Free Energy

Figure 3-22 compares g_{int} for discoidal micelles with aggregation numbers varying between 6 and 60 formed by cesium perfluorooctanoate, calculated based on the curvature-corrected (CC) model and the Srinivasan and Blankschtein (SB) model.[28] Note that an upper

limit of 60 was chosen on the aggregation number because the predicted concentration of aggregates having an aggregation number higher than 60 was found to be negligible. Moreover, the weight-average aggregation number reported by Iijima et al. is about 50 at a surfactant concentration of 65 mM.[50] Note that for the purpose of generating the plots presented in this section, the surfactant monomer concentration was fixed at 25 mM, which is close to the CMC of cesium perfluorooctanoate.[60] In addition, note that the monomer concentration affects solely the calculation of g_{elec}, and not of g_{int}, g_{pack}, and g_{st}.

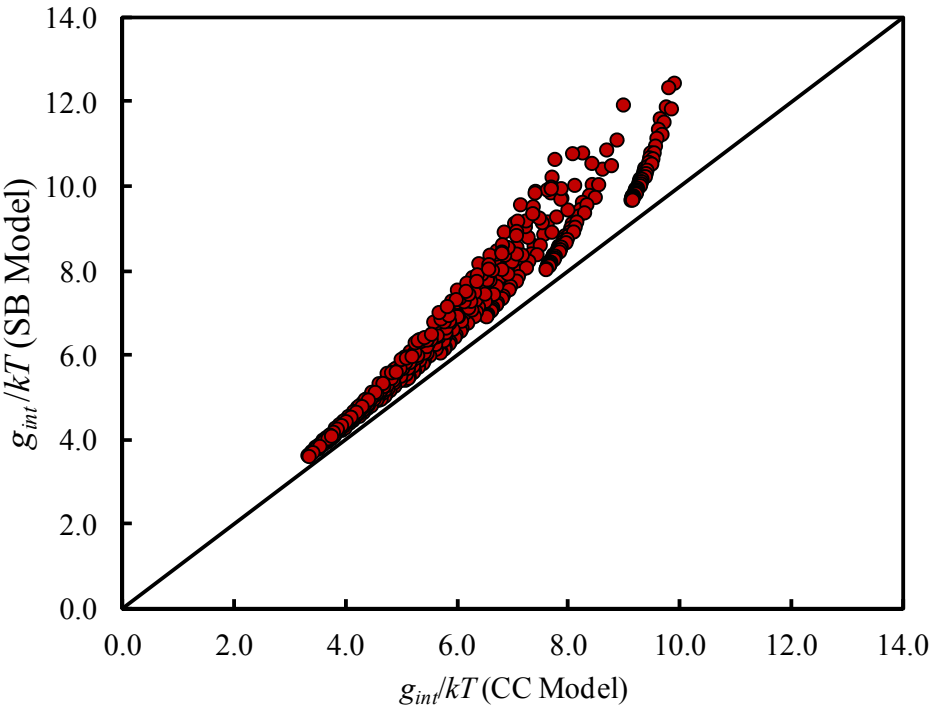

Figure 3-22: Comparison of g_{int} for cesium perfluorooctanoate calculated using the curvature-corrected (CC) model and the Srinivasan and Blankschtein (SB) model

All the points shown in Figure 3-22 lie above the 45° line, indicating that g_{int} calculated using the SB model is systematically higher than g_{int} calculated using the CC model. In both models, g_{int} is high when b or b' take small values. This follows because small values of b and b' result in high values of the curvature, which increases g_{int}. This point was also discussed in

Section 3.3.1. The higher values of g_{int} are also associated with higher discrepancies between the two models, with the average difference between the g_{int} values calculated using the two models being about 0.7 kT.

The key difference between the CC model and the SB model,[28] in the context of the interfacial free energy, g_{int}, is that the effect of the position-dependent curvature on the interfacial tension is incorporated in the former while not in the latter. Indeed, in the discoidal model developed by Srinivasan and Blankschtein,[28] the curvature for the semi-toroidal rim, for the purpose of calculating the curvature-corrected interfacial tension, is assumed to be equal to that of a cylinder having a radius equal to b' of the semi-toroidal rim. However, the actual curvature of the semi-toroidal rim is higher than that of the cylinder because a semi-toroidal rim is a bent cylinder, and the curvature of that shape increases due to the bending action. Accordingly, the curvature-corrected interfacial tension of a semi-toroidal rim is lower than that of the associated cylinder, as follows from Eq. (2-12). This results in the overprediction of g_{int} based on the SB model relative to that predicted by the CC model. The difference between the two models becomes smaller as the bilayer portion of the discoidal micelle becomes larger, that is, as b increases. This follows because the semi-toroidal rim behaves more like a hemi-cylinder as b increases.

3.7.2 Packing Free Energy

Figure 3-23 compares g_{pack} for discoidal micelles with aggregation numbers varying between 6 and 60 formed by cesium perfluorooctanoate, calculated based on the CC model and the SB model.[28] The points shown in Figure 3-23 lie predominantly below the 45^o line, indicating that g_{pack} calculated using the SB model is typically lower than g_{pack} calculated using the CC model.

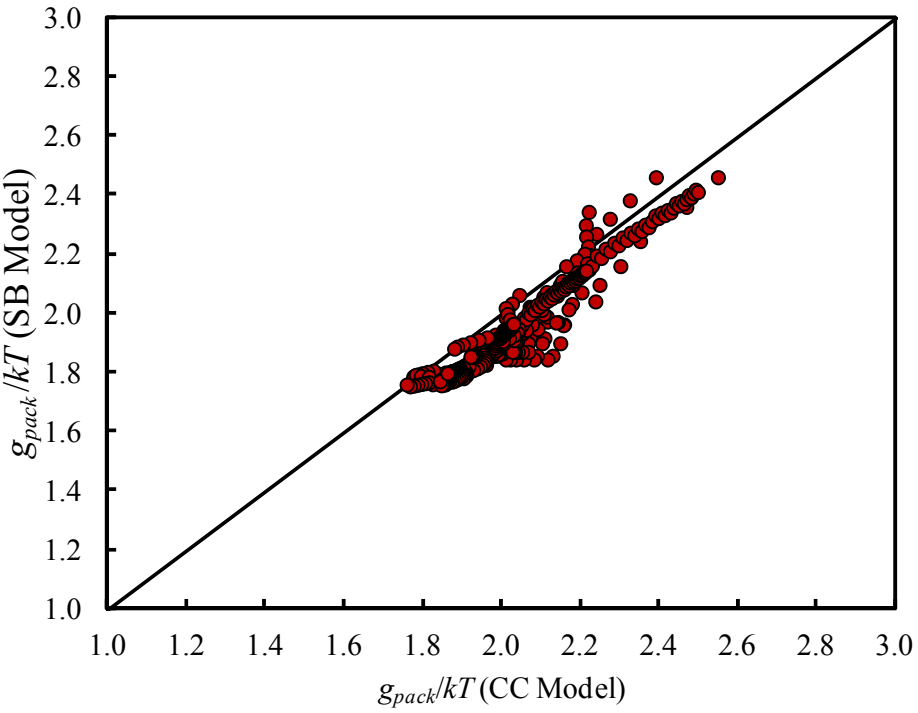

Figure 3-23: Comparison of g_{pack} for cesium perfluorooctanoate calculated using the CC model and the SB model

In both models, g_{pack} is high when b' takes on very small, or very large, values. When b' is very small, the high curvature of the disc results in high values of the packing free energy, while when b' is very high, the inability to pack the center of the bilayer portion of the disc results in high values of g_{pack}. This was discussed in more detail in Section 3.4.1. On average, the difference between the g_{pack} values calculated using the two models is 0.09 kT, which is about atenth of the average difference found in the case of g_{int}. Note that Srinivasan and Blankschtein approximated the packing of the semi-toroidal rim of a disc as that corresponding to the packing of a cylinder.[28] Since this approximation does not account for the increase in volume or for the change in curvature due to the bending of the cylinder, it cannot be compared with the disc model for g_{pack} developed in Section 3.4.1. As a result, it is not possible to precisely determine the cause of the lower g_{pack} values predicted by the SB model relative to the CC model.

3.7.3 Steric Free Energy

Figure 3-24 compares g_{st} for discoidal micelles with aggregation numbers varying between 6 and 60 formed by cesium perfluorooctanoate, calculated based on the CC model and the SB model.[28] All the points shown in Figure 3-24 lie systematically below the 45° line, which indicates that g_{st} calculated using the SB model is systematically lower than g_{st} calculated using the CC model. In both models, g_{st} is low when b' is small. This follows because small values of b' result in high values of the curvature, which reduces g_{st}. This point was also discussed in Section 3.5.1. The average difference between the g_{st} values calculated using the two models is about 0.02 kT, which is an order of magnitude lower than the average difference found in the calculation of g_{int}. The magnitude of the difference is smaller because g_{st} is typically lower than g_{int}, as can be seen by comparing Figure 3-22 and Figure 3-24.

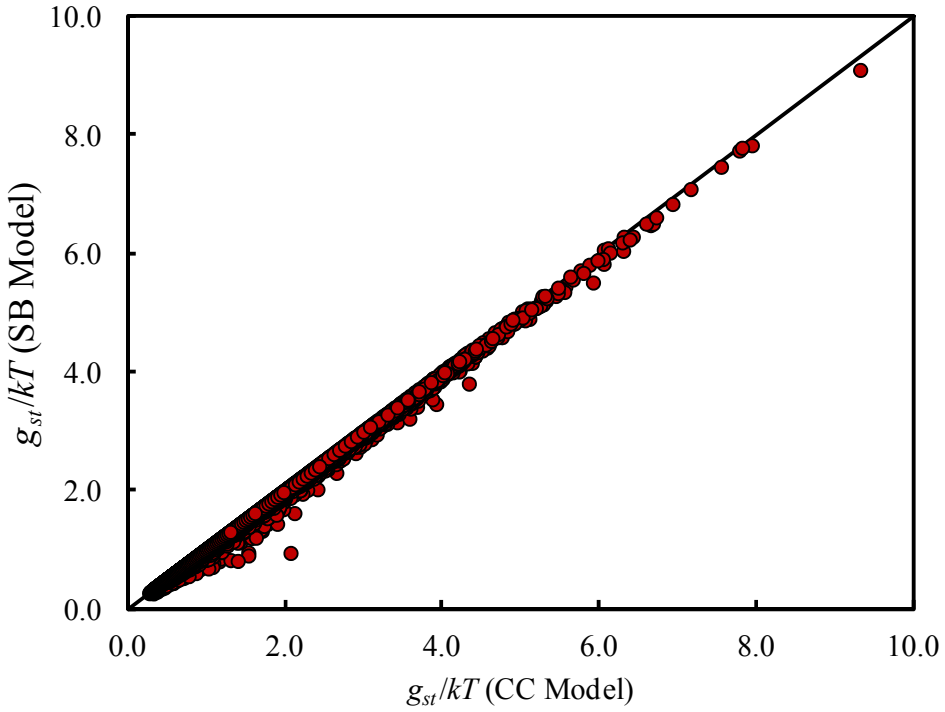

Figure 3-24: Comparison of g_{st} for cesium perfluorooctanoate calculated using the CC Model and the SB model

The systematic difference between the CC model and the SB model, in the context of g_{st}, may result because of the different averaging techniques used to calculate the average steric free energy per molecule in both models. Indeed, in the SB model, the area per molecule is averaged, and then it is used in Eq. (2-24) to yield the average steric free energy per molecule.[28] This corresponds to taking the negative logarithm of an average quantity. On the other hand, in the CC model, the local steric free energy per molecule is averaged to yield the average steric free energy per molecule. This corresponds to taking an average of negative logarithmic terms. One can show that the average of logarithmic terms is smaller than the logarithm of the average of the terms. Specifically (see Section 7.1.15 of the Appendix),

$$\left\langle \ln\left(x_i\right)\right\rangle \le \ln\left\langle x_i\right\rangle \Rightarrow -\left\langle \ln\left(x_i\right)\right\rangle \ge -\ln\left\langle x_i\right\rangle \tag{3-143}$$

Equation (3-143) explains the systematic discrepancy between the SB model and the CC model for discs.

3.7.4 Charging Free Energy

Figure 3-25 compares g_{ch} for discoidal micelles with aggregation numbers varying between 6 and 60 formed by cesium perfluorooctanoate, calculated based on the CC model and the SB model.[28] Note that g_{ch} depends on the shape of the micelle, as described in Section 2.3 and Section 3.6. Note also that the surfactant monomer concentration is about 25 mM, which is close to the CMC of cesium perfluorooctanoate. The points shown in Figure 3-25 lie predominantly above the 45^{o} line, which indicates that g_{ch} calculated using the SB model is typically higher than g_{ch} calculated using the CC model. In both models, g_{ch} is higher when the degree of counterion binding, β_n, is lower, because a small β_n implies a higher effective charge on the micelle, thereby leading to a high value of g_{ch}. On average, the difference between the g_{ch}

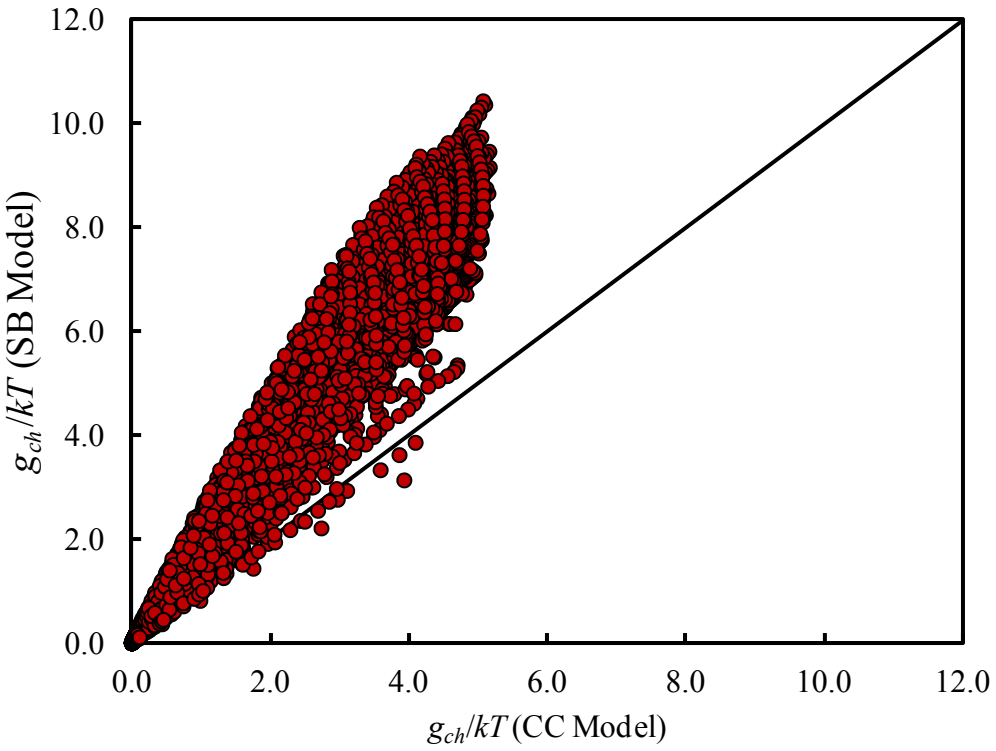

Figure 3-25: Comparison of g_{ch} for cesium perfluorooctanoate calculated using the CC model and the SB model

values calculated using the two models is about 1.4 kT, which is of the same order of magnitude as the difference found in the calculated g_{int}. Note that in the SB model, g_{ch} corresponding to the semi-toroidal rim of a disc is calculated by simply replacing the surface area per molecule at the micellar charged surface and at the Stern surface, a_{charge} and a_{Stern}, respectively, in Eqs. (2-32) and (2-34) for cylinders, by the average area per molecule for a semi-toroidal rim. As a result, itis not simple to understand the origin of the significant discrepancy between the two models.

3.7.5 Micellization Free Energy

Based on the results presented in Sections 3.7.1 and 3.7.4, it follows that the major differences in the free energy of micellization calculated using the SB model[28] and the CC model for discs results from the differences in g_{int} and g_{elec}. Recall that the differences in g_{pack} and g_{st} are

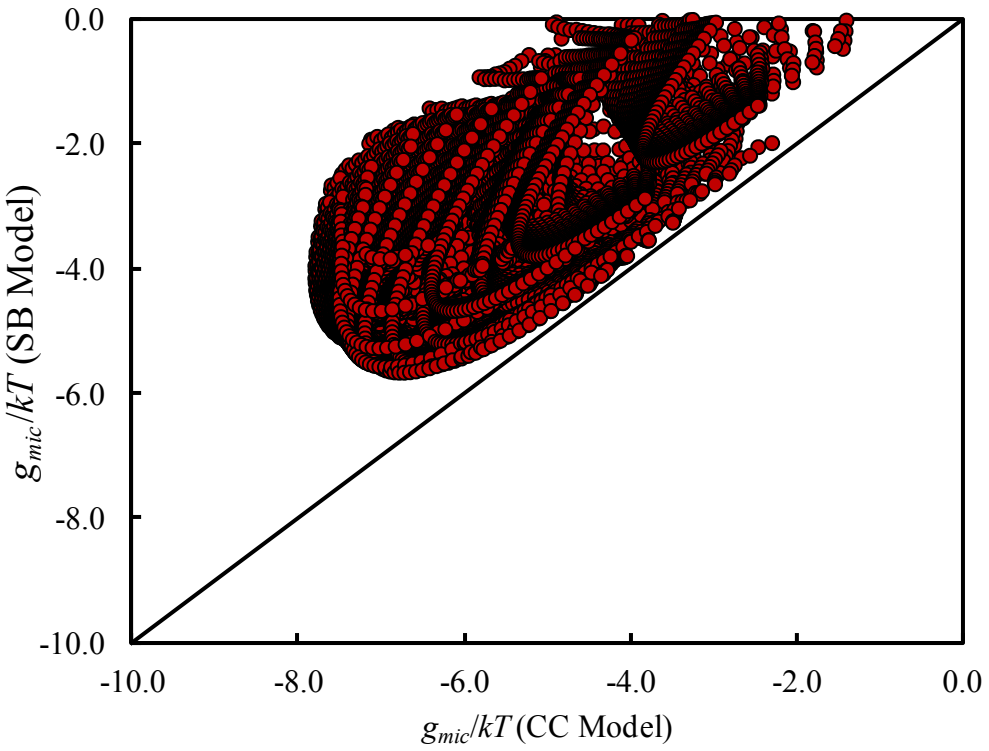

Figure 3-26: Comparison of g_{mic} for cesium perfluorooctanoate calculated using the CC model and the SB model

an order of magnitude lower than those in g_{int} and g_{elec}. Moreover, since the SB model yields a higher value than the CC model for both g_{int} and g_{elec}, it follows that g_{mic} calculated using the SB model is higher than g_{mic} calculated using the CC model. This finding is clearly shown in Figure 3-26, which compares g_{mic} for discoidal micelles with aggregation numbers varying between 6 and 60 formed by cesium perfluorooctanoate, calculated based on the CC model and the SB model. Figure 3-26 shows that all the points lie above the 45^{o} line, indicating that g_{mic} calculated using the SB model is higher than g_{mic} calculated using the CC model. On average, the difference between the g_{mic} values calculated using the two models is 2.1 kT, which represents a significant deviation. This clearly shows that the approximations underlying the SB model severely affect the calculation of g_{mic}. In addition, because g_{mic} predicted by the CC model is lower than g_{mic} predicted by the SB model, the CR model favors the formation of discs more than the SB model.

3.8 Feasibility of Biaxial Ellipsoidal Micelles

In the literature on micelle shapes, there has been some controversy about the shape of globular micelles. Many experimental studies claim that some surfactants under certain solution conditions form ellipsoidal micelles. For example, for an aqueous solution of the nonionic surfactant n-dodecyl octaethylene glycol monoether, Tanford et al. compared the experimental viscosities and the experimental Stokes radii obtained from sedimentation velocity measurements to their respective theoretical predictions, and concluded that the micelles are oblate ellipsoidal (disk like) in shape.[61] Kawaguchi et al. utilized X-ray scattering to show that nonionic short-chain fatty acid sucrose monoester surfactants (C_nSE; n = 10, 12, and 14) form oblate ellipsoidal micelles in aqueous solution.[52] Recently, experimental techniques like small-angle X-ray scattering and small-angle neutron scattering have been widely used to probe the structure of micelles.[62] For example, using small-angle X-ray scattering, Caetano et al. showed that the anionic surfactant sodium dodecyl sulfate in the presence of small amounts of chlorpromazine (a clinical antipsychotic drug) forms prolate ellipsoidal micelles in aqueous solution.[53] Sarkar et al. showed that nonionic alkyl-propoxy-ethoxylate surfactants in the presence of alcohol cosolvents form oblate ellipsoidal micelles in aqueous solution.[54] However, contrary to these experimental studies, several theoretical studies have refuted the premise that ellipsoids can be feasible micelle shapes. The most noteworthy of these studies is the seminal work of Israelachvili et al.[63] In response to the theoretical work of Tartar[64] and Tanford[65] where they studied the formation of ellipsoidal micelles once the surfactant molecules can no longer pack into spherical micelles, Israelachvili et al. invoked their packing criterion to claim that an ellipsoid cannot be an optimum micelle shape. They showed that, for an ellipsoidal micelle, the surface area per surfactant molecule varies throughout the micelle surface, and is therefore different from the

optimal surface area per surfactant molecule almost everywhere. As a result, from a free-energy viewpoint, an ellipsoidal shape can never be the optimal shape.[63] Subsequently, other authors also rejected the ellipsoid as a feasible micelle shape. In particular, Leibner and Jacobus claimed that ionic surfactants prefer to micellize in shapes with higher surface area per molecule in the head region. As a result, the spherocylinder shape is superior to the ellipsoid shape because spherocylinders have a higher surface area per molecule than those of prolate or oblate ellipsoids.[66] In another study, Taddei rejected the ellipsoidal shape based on the fact that ellipsoids have regions with high curvature (the polar region in a prolate ellipsoid and the equatorial region in an oblate ellipsoid), which will prevent the surfactant molecules from packing efficiently.[57, 58]

Among the few studies on the theoretical modeling of the formation of ellipsoidal micelles, the most comprehensive one was undertaken by Halle et al. These authors calculated the free-energy change associated with the shape fluctuations of a spherical micelle that leads to the formation of an ellipsoidal micelle. Specifically, they accounted for the effect of the position-dependent curvature of the ellipsoidal shape on the free energy of micelle formation.[67] While their theoretical development of the electrostatic free energy of deformation was very thorough, Halle et al. did not account for the free-energy contributions arising from: (i) the loss of conformational degrees of freedom of the surfactant tails in the micelle core, (ii) the steric interactions between the head groups of the surfactants, and (iii) the curvature dependence of the interfacial tension associated with the interfacial free energy of deformation.[67] Using their model, Halle et al. showed that under certain conditions, both prolate and oblate ellipsoidal micelles can exist in aqueous solution. However, in their analysis, the authors only considered prolate ellipsoids, oblate ellipsoids, and spheres, as possible shapes, leaving out cylinders and bilayers.

A few other studies on the structure of micelles include a molecular-thermodynamic model by Nagarajan and Ruckenstein[16], and a model based on shape fluctuations by Borkovec.[68] In both of these studies, the position-dependent curvature was not explicitly accounted for in the free-energy calculations. Instead, average geometrical properties of the ellipsoidal shape were used. As it has been shown in Sections 3.3.2 and 3.5.2, as well as for discs in Section 3.7, not explicitly accounting for the position-dependent curvature of micelle shapes can result in significant discrepancies in the calculation of the free energy of micellization. Based on the limitations of past modeling work on ellipsoidal micelles, it is clear that a rigorous theoretical study on ellipsoidal micelles that incorporates the effect of the position-dependent curvature on the free energy of micelle formation has not been undertaken to evaluate the feasibility of forming ellipsoidal micelles relative to other commonly-formed micelle shapes, including spheres, spherocylinders, and discs. Therefore, using the curvature-corrected model developed for biaxial ellipsoidal micelles (see Sections 3.3.2, 3.4.2, 3.5.2, and 3.6.2), we next evaluate the feasibility of biaxial ellipsoids as a micelle shape.

3.8.1 Shape Distribution of Micelles for Different Nonionic Surfactants

To evaluate the feasibility of forming biaxial ellipsoidal micelles, the shape distribution of micelles formed by a 6-carbon fluorocarbon-based nonionic surfactant having a head area of 60 $Å^2$, at its CMC, was predicted under two different scenarios. In the first scenario, it was assumed that micelles can exist in only three shapes, namely, spheres, spherocylinders (finite cylinders with hemi-spherical end caps having the same radius as the cylinder), and discs (finite bilayers with semi-toroidal rims modeled using the Srinivasan and Blankschtein model[26]). In the second scenario, it was assumed that micelles can exist in five shapes, namely, spheres, spherocylinders, discs, prolate ellipsoids, and oblate ellipsoids. The shape distribution

corresponding to each of the scenarios was predicted by calculating the total number of surfactant molecules forming micelles of a particular shape using Eq. (2-5). The number of surfactant molecules forming a particular micelle of aggregation number, n, is given by $nX_n(N_W+N_S)$. Note that the curvature-corrected model is only used for the biaxial ellipsoids and not for discs to clearly differentiate between models in which the effect of curvature has been explicitly incorporated (the CC model) and those in which it has not (the SB model).

The shape distributions corresponding to the two scenarios are shown in Figure 3-27 and Figure 3-28. In the first scenario shown in Figure 3-27, 69% of the surfactant molecules in the micellar state form spherocylindrical micelles, while the remaining 31% form spherical micelles. The weight-average aspect ratio $\langle AR \rangle_W$ of the cylindrical micelles is 4.3, while that of the entire micellar solution (including cylindrical and spherical micelles) is 3.2. Here, the aspect ratio of a

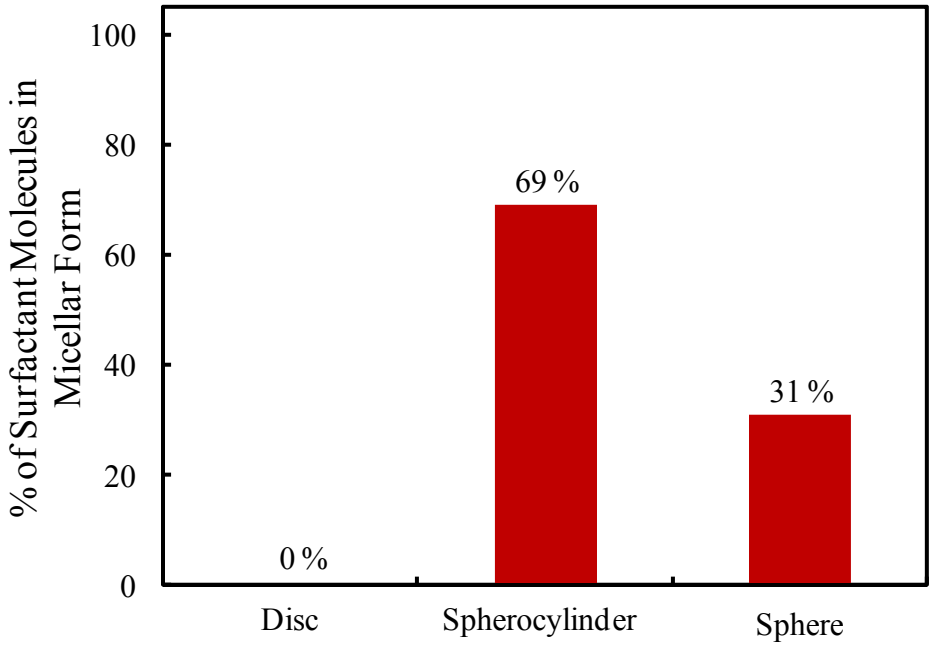

Figure 3-27: Shape distribution of micelles corresponding to the scenario where they can adopt spherical, spherocylindrical, and discoidal shapes.

cylinder is defined as $(h+2r)/2r$, where h is the height of the cylinder and r is the radius of the cylinder. The aspect ratio for a sphere is 1. The weight average of the aspect ratio is calculated using the following expression:

$$\langle AR \rangle_W = \frac{\sum_{n>1} AR \cdot nX_n}{\sum_{n>1} nX_n} \tag{3-144}$$

In the second scenario (Figure 3-28), in which the formation of ellipsoidal micelles was allowed, 84% of the surfactant molecules in the micellar state form oblate ellipsoidal micelles, 15% form prolate ellipsoidal micelles, and only 1% of the surfactant molecules in the micellar state form spherical, spherocylindrical, and discoidal micelles. Contrary to claims made in several theoretical studies,[57, 58, 63, 66] this result clearly suggests that, in the context of our theoretical framework, ellipsoidal micelles are indeed feasible micelle shapes when compared

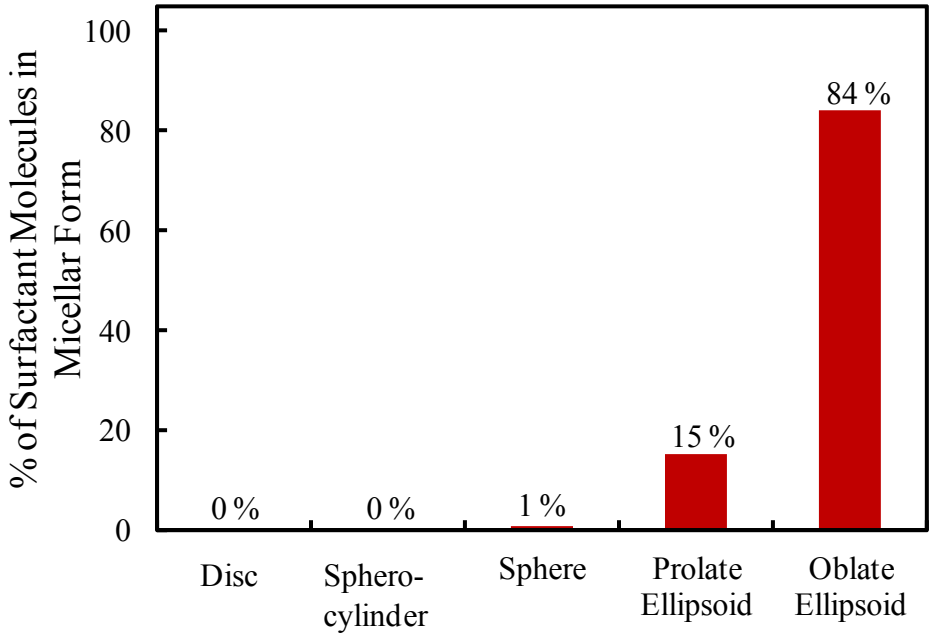

Figure 3-28: Shape distribution of micelles corresponding to the scenario where they can adopt spherical, spherocylindrical, discoidal, prolate ellipsoidal, and oblate ellipsoidal shapes.

with spheres, spherocylinders, and discs. The average aspect ratio of the micelles is 1.23, which suggests that the micelles are globular and not very elongated.

Of all the five shapes considered, we found that an infinite cylinder of radius 8.54 Å has the lowest free energy of micellization (-8.81 kT). The next lowest free energy of micellization of (-8.54 kT) corresponds to an oblate ellipsoidal micelle of aggregation number 21 having a semi minor axis-length equal to 9.14 Å. This observation, along with the results shown in Figure 3-28, indicates that in spite of having a higher micellization free energy, the oblate ellipsoidal shape is the preferred one. This can be attributed to two factors. First, in practice, only finite-size micelles can exist in solution, and in this case, the free energy associated with forming the spherical end caps of a spherocylindrical micelle is significantly higher than that associated with forming the cylindrical portion. As a result, shorter spherocylinders have a much higher micellization free energy than longer spherocylinders. Second, the entropic penalty associated with localizing n surfactant monomers to form a surfactant micelle of aggregation number n is not included in the definition of the free energy of micellization introduced in Eq. (2-6). Instead, it is included when calculating the concentration of micelles using Eq. (2-5). This entropic penalty is smallest for small micelles, and increases as the micelle aggregation number increases. As a result, at low concentrations, when fewer surfactant molecules are available to form micelles, smaller micelles are preferred. Due to these two reasons, in the case considered above, oblate ellipsoids are the preferred shape in spite of having a higher free energy of micellization relative to an infinite cylindrical micelle. However, it should be noted that it is not impossible for an ellipsoidal micelle to have a free energy of micellization which is lower than those corresponding to the three regular shapes. In fact, for certain surfactants, it has been observed that an oblate ellipsoidal shape has a lower free energy of micellization that that of a spherical,

infinite cylindrical, or infinite bilayer micelle. Therefore, although the free energy of micellization per molecule varies with position for ellipsoidal micelles, its average value can still be sufficiently low to make it the preferred micelle shape.

Next, the shape distribution of micelles was compared when the various molecular descriptors of the surfactant are changed by varying: (i) the tail length of the surfactant (by changing the number of carbon atoms in the surfactant tail), (ii) the surfactant head area, and (iii) the chemistry of the surfactant tail. Figure 3-29 shows the shape distribution of micelles at the CMC for a series of fluorocarbon-based surfactants having a head area of 60.0 $Å^2$, and 5, 6, and 7 carbon atoms in the tail. The figure shows no discernible difference between the shape distributions of micelles for the three different surfactants considered. The weight-average aspect ratio does not show a lot of variation either, with values between 1.23 and 1.27 for the three

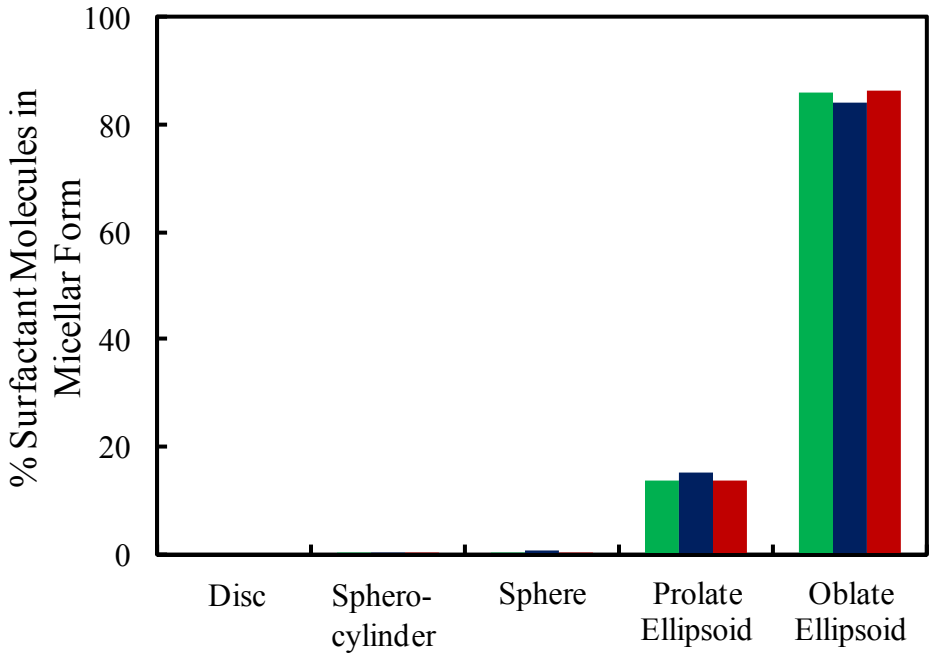

Figure 3-29: Shape distribution of micelles at the CMC for a series of fluorocarbon-based surfactants having different numbers of carbon atoms in the tail. Color Code: Green – 5-carbon fluorocarbon tail, Blue – 6-carbon fluorocarbon tail, and Red – 7-carbon fluorocarbon tail.

surfactants considered. This follows because with an increase in the number of carbon atoms in the tail of the fluorocarbon-based surfactant, not only does the volume of the surfactant tail increase, but also the length of the semi-minor axis of the ellipsoidal micelle increases. These two factors offset each other's effect, leading to shape distributions that are very similar for the three different surfactants considered.

Figure 3-30 shows the effect of the head area on the shape distribution of micelles at the surfactant CMC. Specifically, the figure shows the shape distribution of micelles at the CMC for three fluorocarbon-based surfactants with a 6-carbon fluorocarbon tail having head areas of 50.0 $Å^2$, 60.0 $Å^2$, and 70.0 $Å^2$. Figure 3-30 shows that as the head area increases, the fraction of surfactant molecules in the micellar state that form oblate ellipsoidal micelles decreases from 95% to 72%, while that for prolate ellipsoidal micelles increases from 4% to 27%. In addition, the calculated weight-average aspect ratio decreases from 1.42 to 1.15, i.e., the micelles become

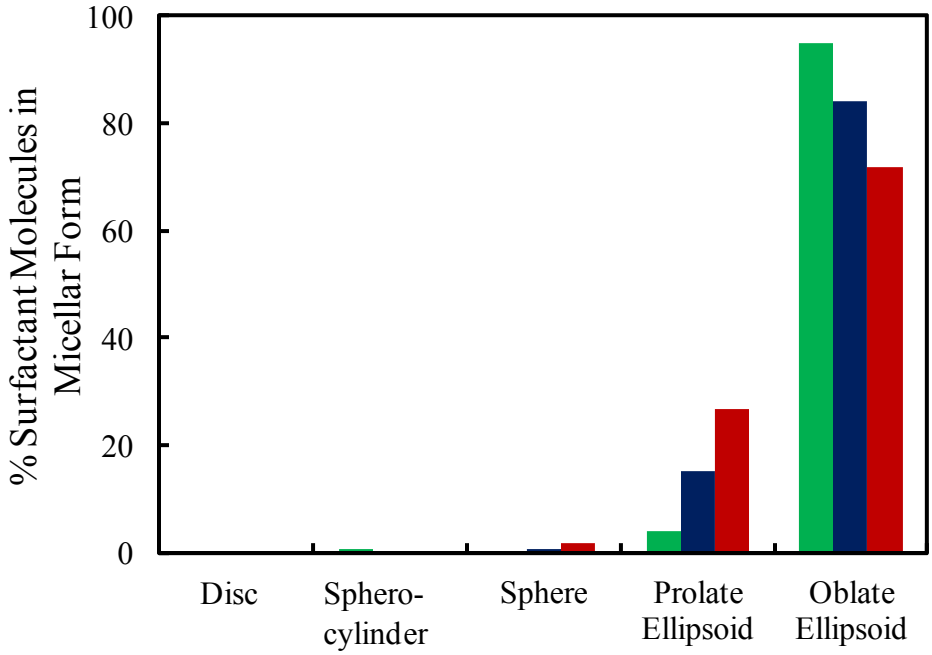

Figure 3-30: Shape distribution of micelles at the CMC for a series of 6-carbon fluorocarbon-based surfactants having different head areas. Color Code: Green – 50.0 $Å^2$, Blue – 60.0 $Å^2$, and Red – 70.0 $Å^2$.

increasingly globular. For this set of surfactants, the length of the surfactant tail remains the same. As a result, the semi-minor axis length of the micelle also remains the same (at about 90-100% of the surfactant tail length). However, the head area increases. Consequently, the steric repulsions between the heads increase, leading to a more globular-shaped micelle which has a higher surface area-to-volume ratio. Note that the increase in the contribution of the prolate ellipsoidal shape is also due to the same reason, since for the same semi-minor axis length and aspect ratio, a prolate ellipsoid has a higher surface area per molecule than an oblate ellipsoid.

Finally, Figure 3-31 compares the shape distribution of micelles formed by a 6-carbon fluorocarbon-based surfactant and a 6-carbon hydrocarbon-based surfactant having the same head area of 50 $Å^2$. For the fluorocarbon-based surfactant, 95% of the surfactant molecules in the micellar state form oblate ellipsoidal micelles. On the other hand, for the hydrocarbon-based surfactant, about 63%, 17%, and 20% of the surfactant molecules in the micellar state form

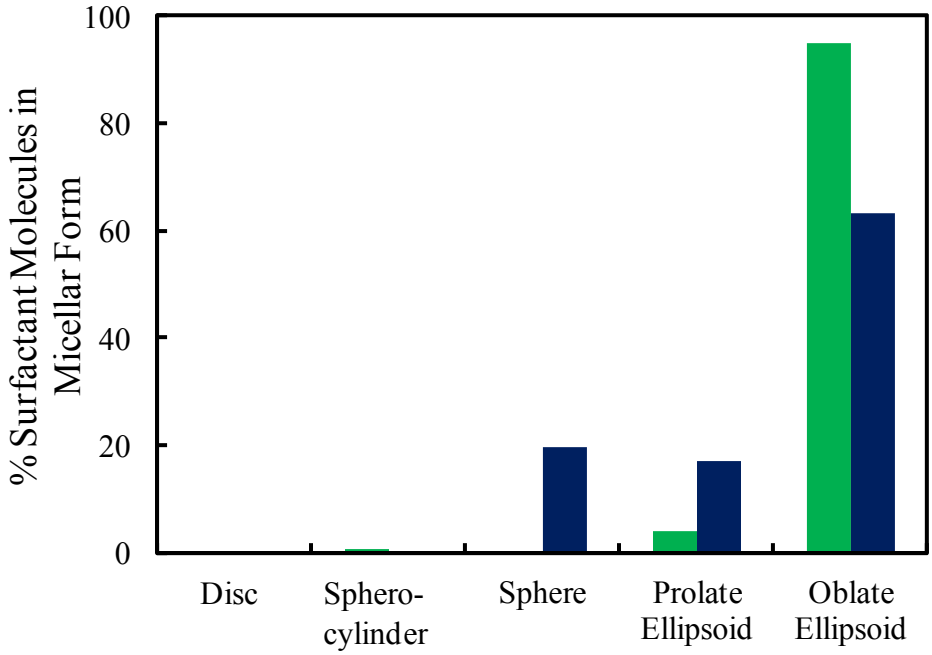

Figure 3-31: Shape distribution of micelles at the CMC for a 6-carbon fluorocarbon-based surfactant (Green), and a 6-carbon hydrocarbon-based surfactant (Blue), both having a head area of 50.0 $Å^2$.

oblate ellipsoidal, prolate ellipsoidal, and spherical micelles, respectively. The calculated weight-average aspect ratio for the fluorocarbon-based surfactant micelles is 1.42, while that for the hydrocarbon-based surfactant micelles is 1.12. These results can be explained on the basis of the volume of the two surfactant tails. Since the fluorocarbon tail is bulkier than the hydrocarbon tail (see Section (2-18) and (2-19)), the fluorocarbon-based surfactant prefers to micellize in a shape having a higher volume-to-surface area ratio. Since an oblate ellipsoidal shape has a higher volume-to-surface area ratio, the fluorocarbon-based surfactant prefers to micellize in this shape more than its hydrocarbon counterpart. In addition, for the same semi-minor axis length, an elongated ellipsoidal shape has a higher volume-to-surface area ratio. Therefore, the fluorocarbon-based surfactant prefers to form elongated micelles relative to the hydrocarbon-based surfactant.

Finally, based on the results presented in Figures 3-28 – 3-31, it follows that for the set of surfactants considered here, out of the two biaxial ellipsoidal shapes, oblate ellipsoids are preferred over prolate ellipsoids. This follows because at a semi-minor axis length of 95% of the surfactant tail length (which is the preferred value), the oblate ellipsoidal shape is the preferred shape from an interfacial free-energy viewpoint, while the prolate ellipsoidal shape is the preferred shape from the steric free-energy viewpoint (the packing free energies are not very different for the two shapes). However, the difference in the interfacial free energies of the two shapes is much higher than the difference in the steric free energies. As a result, the shape with the lower interfacial free energy, the oblate ellipsoidal shape in this case, becomes the preferred micelle shape. Note that with an increase in the head area, the difference in the steric free energies of the two ellipsoidal shapes becomes increasingly significant, and this can lead to a change in the preferred shape from an oblate ellipsoidal to a sphere/prolate ellipsoidal shape.

Furthermore, if the surfactants are ionic, there would be an additional electrostatic free-energy penalty, which may have a larger effect on the micelle shape distribution than that of the steric free energy.

3.9 Conclusions

In summary, in this chapter, an MT model was developed for discoidal and biaxial ellipsoidal micelles, which are both important micelle shapes in the context of fluorocarbon-based surfactants. The model incorporated the effect of the position-dependent curvature on the various free-energy contributions to the free energy of micellization. The model for discoidal micelles was compared with a previous model for discoidal micelles that did not incorporate the effect of the position-dependent curvature on the free energy of micellization.[28] The comparison showed that it is imperative to explicitly incorporate the effect of the varying curvature, especially in the case of the interfacial free energy and the electrostatic free energy, to yield accurate results. In the context of biaxial ellipsoidal micelles, the model was used to show that the biaxial ellipsoidal shape is indeed a feasible micelle shape, a conclusion that was previously challenged in several theoretical studies.[57, 58, 63, 66]

In the next chapter, I discuss modeling the micellization behavior of mixtures of surfactants, where a new Computer-Simulation-Molecular-Thermodynamic (CSMT) framework is presented to model such mixtures. The CSMT framework is particularly useful for mixtures of surfactants having a complex chemical structure, which are therefore, not amenable to traditional MT modeling.

Chapter 4

Modeling the Micellization Behavior of Binary Mixtures of Fluorocarbon-Based Surfactants

4.1 Introduction

In most industrial applications, a surfactant formulation consists of several surfactants mixed together. These mixtures can form as a result of the synthesis process in which various, difficult to separate, homologous surfactants are produced, and therefore, yield an impure end product.[5] However, multiple surfactants are often deliberately mixed to improve the performance characteristics of a surfactant formulation.[69, 70] For example, nonionic alkyl ethoxylate surfactants are often added in surfactant formulations because they have better tolerance towards hard water and have a low foaming tendency.[69]

The choice of a particular surfactant mixture formulation is made based on the desired solution properties, including the mixture critical micelle concentration (CMC), and the mixed-

micelle shape, size, and composition. As a result, the formulator is faced with the challenging task of choosing the most appropriate mixture of surfactants from a broad class of available surfactants that range from simple linear surfactants to complex branched or aromatic surfactants. Several models have been developed to gain a theoretical understanding of the behavior of the CMCs of mixtures of surfactants. Most of these models are based on the pseudophase approximation, and include Clint's ideal solution model,[71] Holland and Rubingh's regular solution model,[72] Hao et al.'s two-parameter Margules model,[73] and Georgiev's two-parameter Markov chain model.[74] Use of all these models require knowledge of the CMCs of the constituent surfactants, as well as of other experimental results to estimate the values of the various parameters used in the models. Recently, models based on Monte Carlo simulations have also been developed to describe mixed micellization.[75-79] However, these models also require knowledge of parameters that quantify the interactions between the different heads and tails of the surfactants comprising the mixture. This limitation is mitigated in the molecular-thermodynamic (MT) approaches developed to model the micellization of surfactant mixtures.[80-84]

Due to recent advances in computational capabilities, molecular dynamics (MD) simulations have become an attractive tool to study micellar properties.[15] Although MD simulations can certainly be utilized to obtain molecular-level details about the micellization process,[85-88] their use is currently limited by constraints on the system size (of the order of nanometers) and on the time scales (of the order of nanoseconds). Micellization properties like CMCs are not easy to calculate using all-atomistic simulations alone, and therefore, several indirect methods have been used to calculate such micellization properties.[15, 46, 89-94]

Notably, in spite of the extensive practical use of mixtures of surfactants, a very small fraction of the simulation studies available in the literature focus on mixed micellization. For example, Yakovlev et al. used MD simulations to determine the change in micelle shape as a function of the composition of a mixed micelle containing an anionic and a cationic surfactant.[95] More recently, Ferreira et al. published a study in which they probed the interactions between the tails of homologous surfactants forming a mixed micelle.[96] Stephenson et al. used an alchemical computer simulation method to calculate the free-energy change associated with varying the composition of a mixed micelle, which can in turn be correlated to the change in the mixture CMC.[97] The major limitation of the method developed by Stephenson et al.[97] is that it does not yield realistic predictions for binary surfactant mixtures in which the two surfactant components possess very different chemical structures.[98]

In this chapter, we develop a model that may be used to predict micellization properties of mixtures of surfactants by incorporating structural details obtained using all-atomistic MD simulations of micelles and monomers into the well-established molecular-thermodynamic framework introduced in Chapter 2 for mixed surfactant micellization.[21, 99] The model is based on the computer simulation–molecular-thermodynamic (CSMT) framework developed by Stephenson et al. for single surfactants which was discussed in Section 2.4.[44-46] The theoretical basis of the mixture CSMT framework is presented in Section 4.2. Additionally, the challenges associated with the practical implementation of the mixture CSMT framework are addressed by formulating a simpler mixture CSMT model based on a composition-weighted average approach involving single-component micelle simulations of the mixture constituents. The molecular dynamics simulation protocol followed in the study is discussed in Section 4.3 followed by a discussion of results in Sections 4.4 and 4.5. Specifically, a comparison between the mixture

CSMT model and the simpler mixture CSMT model is presented in Sections 4.4 and a comparison between the CMCs predicted using the mixture CSMT model and the experimental CMC values is presented in Section 4.5.

4.2 CSMT Framework for Surfactant Mixtures

In order to extend the CSMT framework to surfactant mixtures, expressions analogous to Eqs. (2-37) and (2-39) for a simulated mixed micelle containing N_j molecules of surfactant *j* need to be derived. To this end, we first derive expressions for the extensive free energies of dehydration and hydration, G_{dehydr} and G_{hydr}, respectively, to include the contributions from all the constituents of the simulated mixed micelle. This is done by adding up the free-energy contributions of the various surfactant molecules comprising the simulated mixed micelle. The resulting expressions for G_{dehydr} and G_{hydr} are subsequently divided by the total aggregation number of the mixed micelle to obtain g_{dehydr} and g_{hydr} for the simulated mixed micelle. Specifically,

$$G_{dehydr} = \sum_j N_j g_{dehydr,j} = \sum_j N_j \sum_{i_j} \left(1 - f_{i_j}\right) g_{tr,i_j} \tag{4-1}$$

$$g_{dehydr} = \frac{\sum_j N_j \sum_{i_j} \left(1 - f_{i_j}\right) g_{tr,i_j}}{\sum_j N_j} = \sum_j \alpha_j \sum_{i_j} \left(1 - f_{i_j}\right) g_{tr,i_j} \tag{4-2}$$

where α_j is the composition of surfactant *j* in the simulated mixed micelle, and the index, i_j, denotes group *i* in surfactant *j*. Note that $\alpha_{n,j}$ introduced in Eq. (2-5) is identical to α_j introduced in Eq. (4-2) where the subscript *n*, denoting the aggregation number, has been omitted for clarity.

Analogous expressions can be derived for G_{hydr} and g_{hydr}. Specifically,

$$G_{hydr} = \sum_j N_j \sum_{c_j} f_{c_j} \cdot SASA_{c_j} \left(\frac{\sigma_{mix} \left(A_{core} - \sum_j N_j a_{0,j} \right)}{\left(SASA_{core} - \sum_j N_j a_{0,j} \right)} - \frac{-g_{tr,c_j}}{SASA_{c_j}} \right) \tag{4-3}$$

$$g_{hydr} = \frac{G_{hydr}}{\sum_j N_j} = \sum_j \alpha_j \sum_{c_j} f_{c_j} \cdot SASA_{c_j} \left(\frac{\sigma_{mix} \left(A_{core} - \sum_j N_j a_{0,j} \right)}{\left(SASA_{core} - \sum_j N_j a_{0,j} \right)} - \frac{-g_{tr,c_j}}{SASA_{c_j}} \right) \tag{4-4}$$

where c_j denotes the groups in surfactant j that reside in the micelle core. Substituting Eqs. (4-2) and (4-4) in Eq. (2-40) yields $g_{tr,CSMT}$ for a mixed micelle.

Equations (4-2) and (4-4) clearly show that $g_{tr,CSMT}$ for a mixed micelle depends on the composition of the simulated mixed micelle. Because one has no a priori knowledge of the composition of the mixed micelle that exists in solution, one does not know the composition at which the mixed micelle should be simulated. As a result, the implementation of the above model for $g_{tr,CSMT}$ would require knowledge of $g_{tr,CSMT}$ as a function of the micelle composition. This, in turn, would require carrying out mixed-micelle simulations at compositions spanning the entire composition range, which is computationally very expensive. To facilitate implementation of the CSMT model for mixtures of surfactants, a simplified mixture CSMT model is proposed in which $g_{tr,CSMT}$ of a simulated mixed micelle is estimated using a composition-weighted average of the $g_{tr,CSMT}$ values of the individual surfactants comprising the mixture, which can be calculated from the single-component micelle simulations. The composition-weighted average model for $g_{tr,CSMT}$ is referred to hereafter as $g_{tr,CSMT}^{\alpha-avg}$, and for a binary mixture of surfactants, is given by:

$$g_{tr,CSMT}^{\alpha-avg} = \alpha_A g_{tr,CSMT,A} + \alpha_B g_{tr,CSMT,B} \tag{4-5}$$

where the mixed micelle consists of surfactants A and B, α_A and α_B are the compositions of A and B in the micelle, respectively, and $g_{tr,CSMT,A}$ and $g_{tr,CSMT,B}$ are the $g_{tr,CSMT}$ values calculated using single-component micelle simulations of surfactants A and B, respectively, using the method described in Section 2.4. Clearly, if this approximation is valid, it would greatly simplify the estimation of $g_{tr,CSMT}$ for mixed micelles. Indeed, such an approximate $g_{tr,CSMT}$ model would only require carrying out micelle simulations of the individual surfactant components. Therefore, if the approximate model is valid, once one generates such a library of single surfactant micelle and monomer simulations, one can then predict the micellization behavior of mixtures of any number of surfactants available in the library.

To test the range of applicability of the above composition-weighted average model for $g_{tr,CSMT}$, comparison between $g_{tr,CSMT}^{\alpha-avg}$ and $g_{tr,CSMT}$ calculated from the mixed-micelle simulation was carried out for various binary surfactant mixtures. The following binary surfactant mixtures were considered: (i) a set of surfactants having the same head but different tails, (ii) a set of surfactants having the same tail but different heads, and (iii) a set of ionic and nonionic surfactants. Note that the binary surfactant mixtures in (i), (ii), and (iii) above were selected to enable testing the validity of the above approximation by systematically varying the head and tail regions of the surfactants. This selection allows for the identification of those surfactant mixtures for which the approximation is valid, including drawing general conclusions about the applicability of the approximation. Note that the most important difference between the two models is that a mixed-micelle simulation is required to calculate $g_{tr,CSMT}$ for the mixed micelle. On the other hand, only single-component micelle simulations are required to calculate $g_{tr,CSMT}^{\alpha-avg}$ for the mixed micelle.

4.3 Molecular Dynamics Simulations Protocol

All the simulations reported in this thesis are all-atomistic, explicit solvent simulations carried out using GROMACS version 4.5.1.[100, 101] The OPLS-AA force field was used for all parameterizations.[102, 103] Custom parameters from the literature were used in cases for which the OPLS-AA parameters were missing. Usually, the OPLS-AA parameters were missing for the head groups of surfactants (for example sulfate head in alkyl sulfates), and for these cases, parameters available in the literature were used. For the alkyl sulfates and alkyl sulfonates considered here, the parameters developed by Lopes et al.[104] were used. For the alkyl ethoxylate heads, parameters developed by Anderson and Wilson were used.[105] Finally, parameters developed by Stephenson et al. were used for the alkyl glucosides.[46] Water was modeled using the SPC/E model for water.[106] The van der Waals interactions were modeled using a 12-6 Lennard-Jones potential with a short cut-off distance of 0.9 nm, and a long-range dispersion correction to the energy and the pressure.[45, 107] The Coulombic interactions were modeled using a three-dimensional particle-mesh Ewald summation.[47, 107-110] The temperature of the simulation was maintained at 298.15 K using a velocity-rescaling thermostat,[107, 111] and the pressure was maintained at 1 bar using a Berendsen coupling algorithm.[107, 112]

Note that two types of molecular dynamics (MD) simulations need to be carried out to calculate $g_{tr,CSMT}$ of a mixed micelle.[46] These include an MD simulation for monomers of each of the surfactants forming the mixed micelle, which are referred to as the *monomer simulations*, and an MD simulation of the mixed-micellar aggregate, referred to as the *micelle simulation*. The same simulation protocol described above is implemented for both the monomer simulation, in which a surfactant molecule is simulated in a box of water, and the micelle simulation, in which a preformed surfactant aggregate is allowed to equilibrate in a box of water. The size of the

simulation box is chosen such that there would be at least a 2 *nm* separation between the surfactant monomer, or micelle, and its periodic image.[46] This is done to avoid any interactions between the surfactant monomer, or micelle, and its periodic image. Note that to ensure this, results obtained from a micelle simulation of sodium dodecyl sulfate simulated in a cubic box having an edge length of 5.75 nm were compared with the results obtained from a micelle simulation in a cubic box having an edge length of 11.50 nm. It was found that the results show no significant difference.

Instead of allowing the surfactant molecules to self-aggregate, a preformed surfactant aggregate was used for the micelle simulation because the aggregation process in a fully-dispersed surfactant solution would require significant computational time to reach equilibrium. The various steps required to preform the surfactant aggregate include:[47] (1) carrying out separate MD simulations in vacuum of a single molecule of each of the surfactant species to build up a library of surfactant configurations,[86] (2) randomly placing surfactant molecules from the library created in step (1), in accordance with the aggregation number of the different surfactant species, at equidistant locations on a sphere with the surfactant tails pointing towards the center of the sphere, (3) increasing the size of the sphere in step (2) until there are no overlaps between the different surfactant molecules, and (4) reducing the size of the sphere by pushing the surfactant molecules towards the center of the sphere by means of a fictitious force. This is done until the resulting micellar structure has a sufficiently low void fraction that a solvent molecule (water in this case) fails an insertion test at some threshold level (typically 90% yields a dry micelle core). This preformed micelle is then introduced into a box which is subsequently completely filled with water molecules. The box of water with the preformed micelle is then simulated sufficiently long (~25 ns), such that rearrangement of the surfactant

molecules is allowed and equilibration is attained. The simulation is considered to have equilibrated when the solvent accessible surface area (SASA) has equilibrated, since SASA is proportional to the degree of hydration, which is the quantity that one is primarily interested in when utilizing the CSMT framework.[46] A representative plot of the variation of SASA during the course of the simulation of an equimolar mixed micelle of sodium dodecyl sulfate and sodium dodecyl sulfonate is shown in Figure 4-1 below. The mean value of SASA in the last 20 ns is 42.2 nm^2, with a block averaged error of 0.2 nm^2 which is about 0.5 % of the mean value.

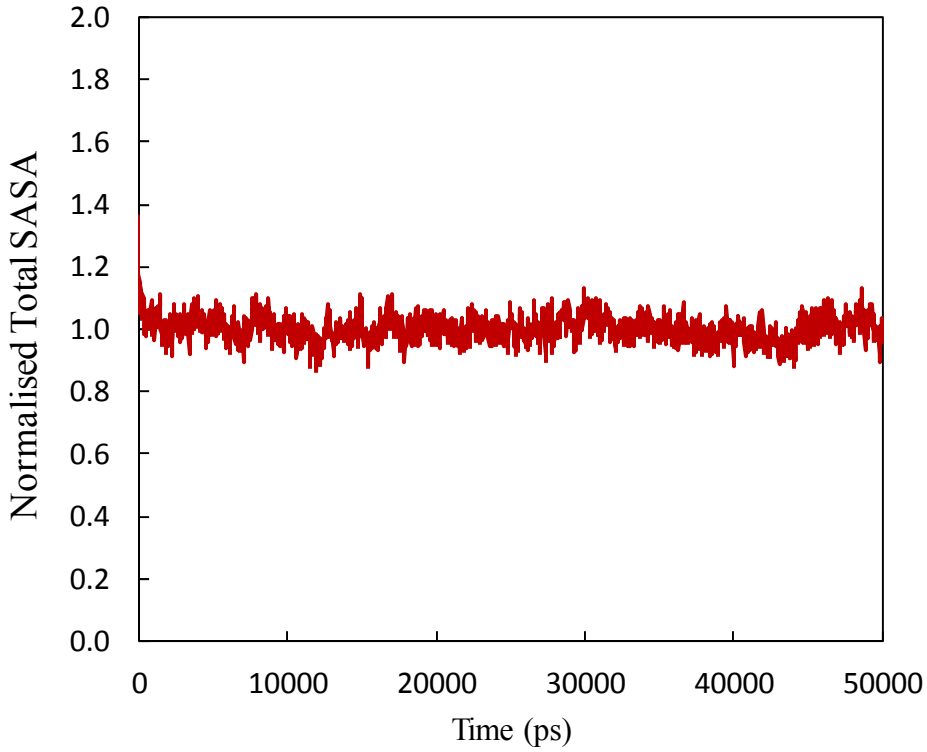

Figure 4-1: Variation of the normalized SASA of the mixed micelle as a function of time.

4.4 Comparison between the Mixture CSMT Model and the Composition-Weighted Average Based Approximate Mixture CSMT Model

To evaluate the applicability of using $g_{tr,CSMT}^{\alpha-avg}$ calculated using the composition-weighted average based mixture CSMT model in lieu of $g_{tr,CSMT}$ calculated using the mixture CSMT model, $g_{tr,CSMT}^{\alpha-avg}$ was compared with $g_{tr,CSMT}$ for various binary mixtures of surfactants. The mixtures of surfactants were chosen such that they satisfy the criteria presented in (i), (ii), and (iii) towards the end of Section 4.2, and that there is available experimental critical micelle concentration (CMC) data for these mixtures to allow comparison with the predicted CMCs. Because, there is not much experimental CMC data for binary mixtures of fluorocarbon-based surfactants (to the best of my knowledge, experimental data CMC is available solely for the binary mixture of lithium perfluorooctanoate and lithium perfluorooctyl sulfonate),[113] binary mixtures of hydrocarbon-based surfactants were used for this study. The specific binary mixtures studied include: (1) a set of mixtures of sodium alkyl sulfates (anionic surfactants) having different number of carbon atoms in the alkyl tail, (2) a set of mixtures of alkyl ammonium chlorides (cationic surfactants) having different number of carbon atoms in the alkyl tail, (3) a mixture of sodium dodecyl sulfate (anionic surfactant) with sodium dodecyl sulfonate (anionic surfactant), (4) a set of mixtures of dodecyl ethoxylates (nonionic surfactants) with different number of ethoxylate units in the surfactant head, (5) a set of mixtures of dodecyl glucoside (nonionic surfactant) and dodecyl ethoxylates (nonionic surfactants) with different number of ethoxylate units in the surfactant head, (6) a set of mixtures of sodium dodecyl sulfate (anionic surfactant) with alkyl ethoxylates (nonionic surfactants) and alkyl glucosides (nonionic surfactants), and (7) a set of mixtures of dodecyl ammonium chlorides (cationic surfactants) with

alkyl ethoxylates (nonionic surfactants) and alkyl glucosides (nonionic surfactants). Surfactant mixtures (1) – (7) above were selected to isolate the effects of the surfactant head, the surfactant tail, and the surfactant charge on $g_{tr,CSMT}$. Specifically, sets (1) and (2) are binary mixtures of surfactants having the same head but different tails, sets (3), (4), and (5) are binary mixtures of surfactants having the same tail but different heads, and sets (6) and (7) are binary mixtures of ionic and nonionic surfactants

For all the binary ionic surfactant mixtures considered in (1), (2), and (3) above, $g_{tr,CSMT}^{\alpha-avg}$ was found to agree very well with $g_{tr,CSMT}$. As an illustration, results for binary mixtures belonging to set (1) above are shown in Figure 4-2. This set includes binary mixtures of sodium decyl sulfate (C10SUL) and: (a) sodium dodecyl sulfate (C12SUL, red), (b) sodium tetradecyl

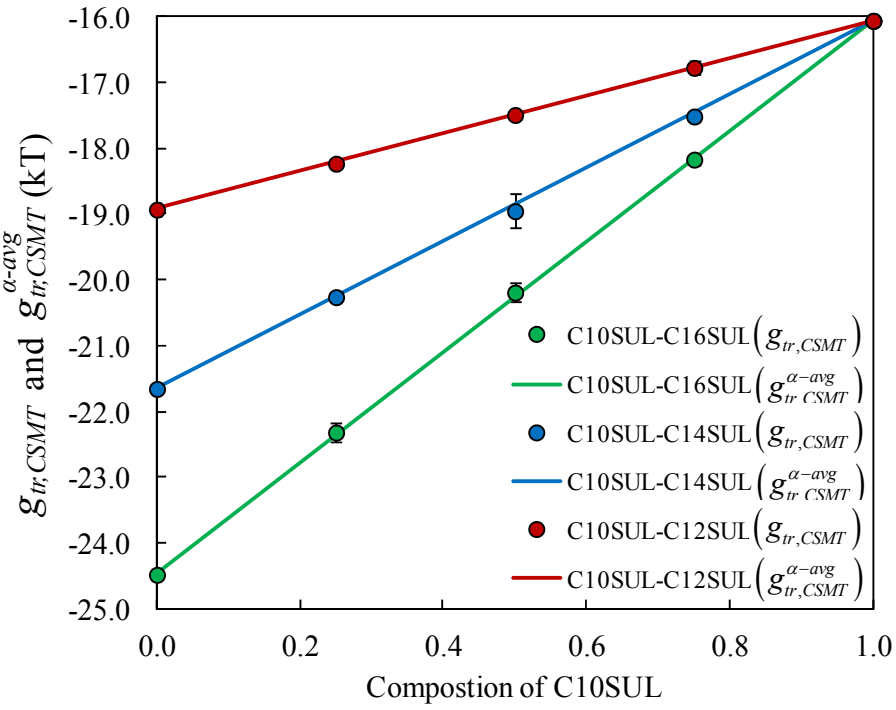

Figure 4-2: Variations of $g_{tr,CSMT}^{\alpha-avg}$ (lines) and $g_{tr,CSMT}$ (filled circles) as a function of micelle composition for a set of binary mixtures of sodium alkyl sulfates.

sulfate (C14SUL, blue), and (c) sodium hexadecyl sulfate (C16SUL, green). Figure 4-2 shows the variation of $g_{tr,CSMT}^{\alpha-avg}$ and $g_{tr,CSMT}$ of mixed micelles as a function of the micelle composition. For the three binary mixtures considered, the filled circles correspond to $g_{tr,CSMT}$, and the solid lines correspond to $g_{tr,CSMT}^{\alpha-avg}$. Note that the error bars shown in Figure 4-2 and the other figures included in this chapter were calculated using a procedure discussed in Section 7.1.16 of the Appendix.

Figure 4-2 shows that the agreement between $g_{tr,CSMT}^{\alpha-avg}$ and $g_{tr,CSMT}$ for the binary mixtures considered is excellent. A similar conclusion can be drawn from Figure 4-3, which shows the variations of $g_{tr,CSMT}^{\alpha-avg}$ and $g_{tr,CSMT}$ as a function of micelle composition in a mixed micelle of C12SUL and sodium dodecyl sulfonate (C12SFN). Note that, relative to Figure 4-2:, the error

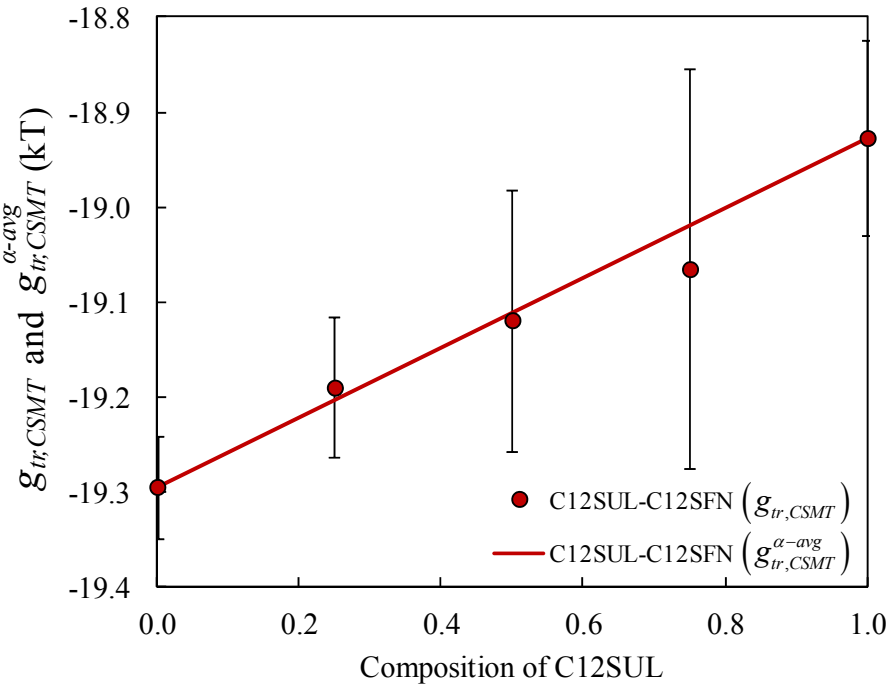

Figure 4-3: Variations of $g_{tr,CSMT}^{\alpha-avg}$ (lines) and $g_{tr,CSMT}$ (filled circles) as a function of micelle composition for a binary mixture of sodium dodecyl sulfate (C12SUL) and sodium dodecyl sulfonate (C12SFN).

bars in Figure 4-3 appear to be very large. However, this is not the case, because the range of the y-axis in Figure 4-3 is only 0.6 *kT*, while that of the y-axis in Figure 4-2: is 9 *kT*. Accordingly, the errors in both figures are actually of the same order of magnitude.

Figure 4-4 shows the variations of $g_{tr,CSMT}^{\alpha-avg}$ and $g_{tr,CSMT}$ as a function of micelle composition for a set of binary mixtures of dodecyl ethoxylates (set (4) above). This set includes binary mixtures of tetraethylene glycol monododecyl ether (C12E4) and: (a) hexaethylene glycol monododecyl ether (C12E6, red), (b) octaethylene glycol monododecyl ether (C12E8, blue), and (c) decaethylene glycol monododecyl ether (C12E10, green). Figure 4-4 shows that, unlike the ionic surfactant mixtures considered in Figures 4-2 and 4-3, for the binary mixtures of the alkyl

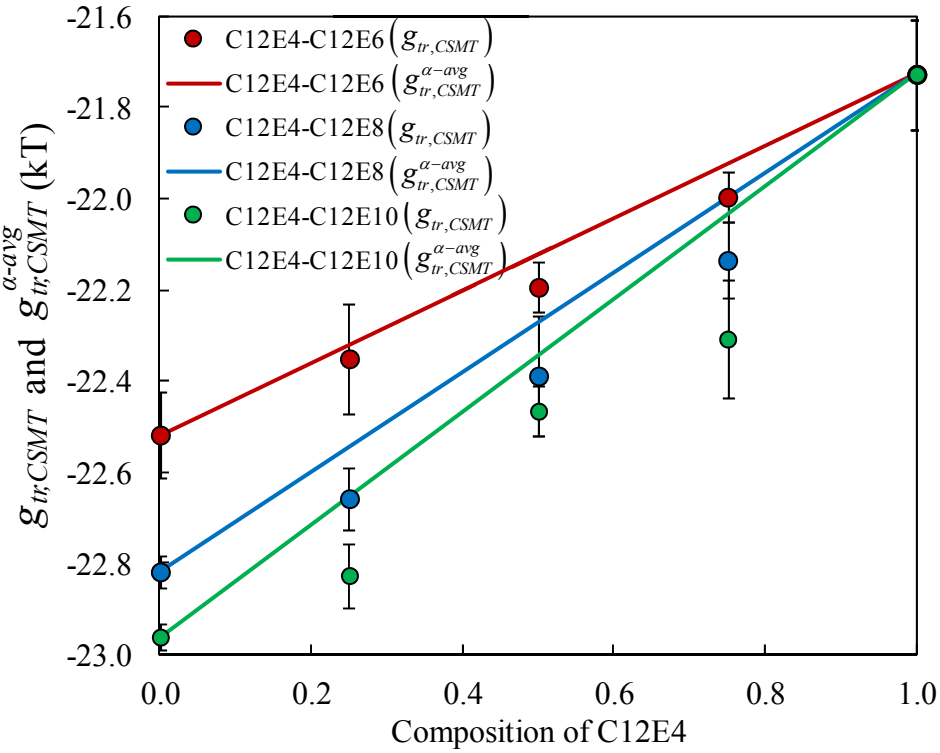

Figure 4-4: Variations of $g_{tr,CSMT}^{\alpha-avg}$ (lines) and $g_{tr,CSMT}$ (filled circles) as a function of micelle composition for a set of binary mixtures of dodecyl ethoxylates.

ethoxylates considered, $g_{tr,CSMT}^{\alpha-avg}$ and $g_{tr,CSMT}$ do not agree well with each other. Instead, $g_{tr,CSMT}^{\alpha-avg}$ is systematically higher than $g_{tr,CSMT}$.

Another important conclusion that can be drawn from Figure 4-4 is that although the four alkyl ethoxylates considered here (C12E4, C12E6, C12E8, and C12E10) have the same dodecyl tail, their $g_{tr,CSMT}$ values are not the same. This can be seen from the points corresponding to a micelle composition of 0 and 1 in Figure 4-4. Specifically, $g_{tr,CSMT}$ of the four surfactants decreases as the number of ethoxylate units in the surfactant head increases. The increase in the number of ethoxylate units makes the surfactant head increasingly flexible which, in turn, allows the ethoxylate head to more effectively shield the micelle core from contact with water. Since the micelle core is hydrophobic, its contact with water is not favorable from a free-energy viewpoint. As a result, better shielding of the micelle core from water leads to a lower $g_{tr,CSMT}$ value. This interesting finding is also reflected in the variation of the degree of hydration, f_i, defined in Eq. (2-38), of the 12-carbon surfactant tails for the four dodecyl ethoxylate surfactants considered (see Figure 4-5). Note that group 1 corresponds to the terminal methyl group in the 12-carbon surfactant tail, and group 12 corresponds to the methylene group adjacent to the ethoxylate head. Examination of Figure 4-5 reveals that as the number of ethoxylate units in the head region increases, the micelle core becomes more dehydrated, as reflected by the lower f_i values. This reduction in hydration of the micelle core in turn results in the observed decrease of $g_{tr,CSMT}$ with increasing ethoxylate head length reported in Figure 4-4. Continuing with the binary mixtures of dodecyl ethoxylates, consider the binary mixture of C12E4 and C12E10. Because C12E10 has a more flexible head than C12E4, the E10 head can shield the micelle core more effectively than the E4 head. Due to the presence of the E10 head in the mixed micelle, the f_i values of the groups in the dodecyl tail of C12E4 are lower in the (C12E4+C12E10) mixed micelle than those in the

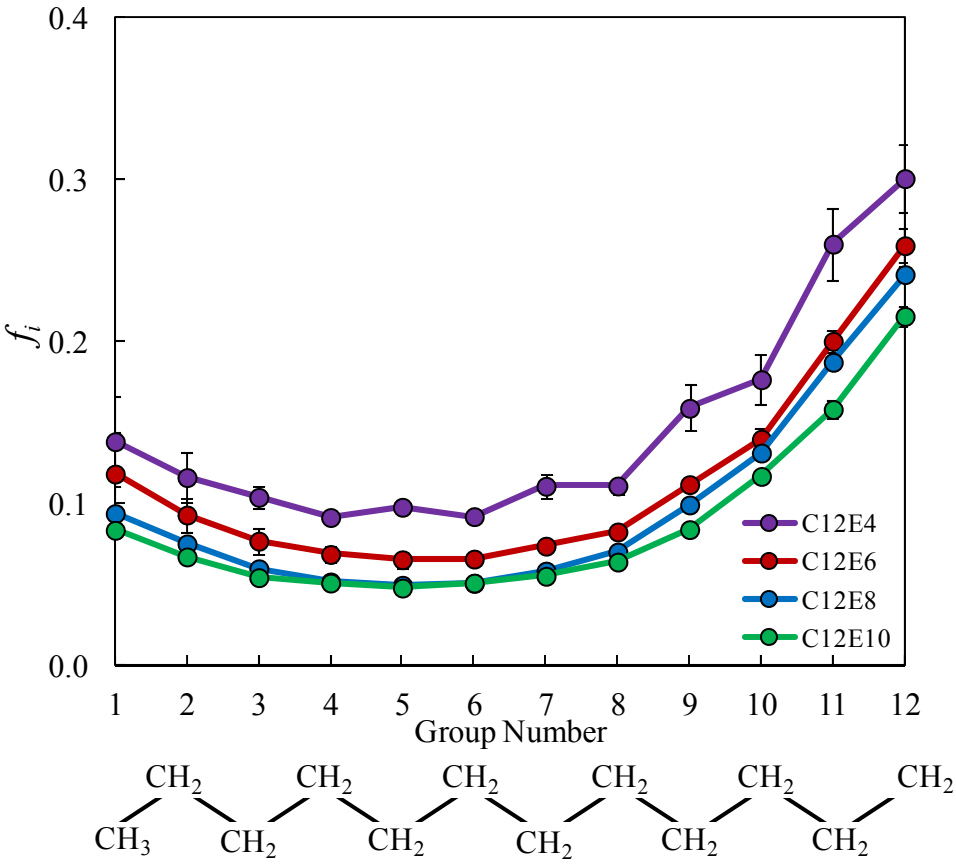

Figure 4-5: Variation of the fractional degree of hydration, f_i, as a function of group number in the 12-carbon tails for the four dodecyl ethoxylates considered (the aggregation numbers of the four simulated dodecyl ethoxylate micelles were the same).

single-component C12E4 micelle. This is reflected in Figure 4-6, which shows the variation of f_i of the 12-carbon tail of C12E4 in the single-component micelle (purple) and in the mixed micelle (red). The observed decrease in f_i results in a decrease in $g_{tr,CSMT}$ for the mixed micelle relative to that of the single-component C12E4 micelle. On the other hand, the f_i values of the groups in the dodecyl tail of C12E10 are higher in the (C12E4+C12E10) mixed micelle than in the single-component C12E10 micelle, due to the presence of the less flexible E4 head. This is also reflected in Figure 4-6. This results in an increase in the $g_{tr,CSMT}$ value of the mixed micelle relative to that of the single-component C12E10 micelle. However, the interactions between C12E4 and C12E10 in the mixed micelle are such that the net effect of mixing the less flexible

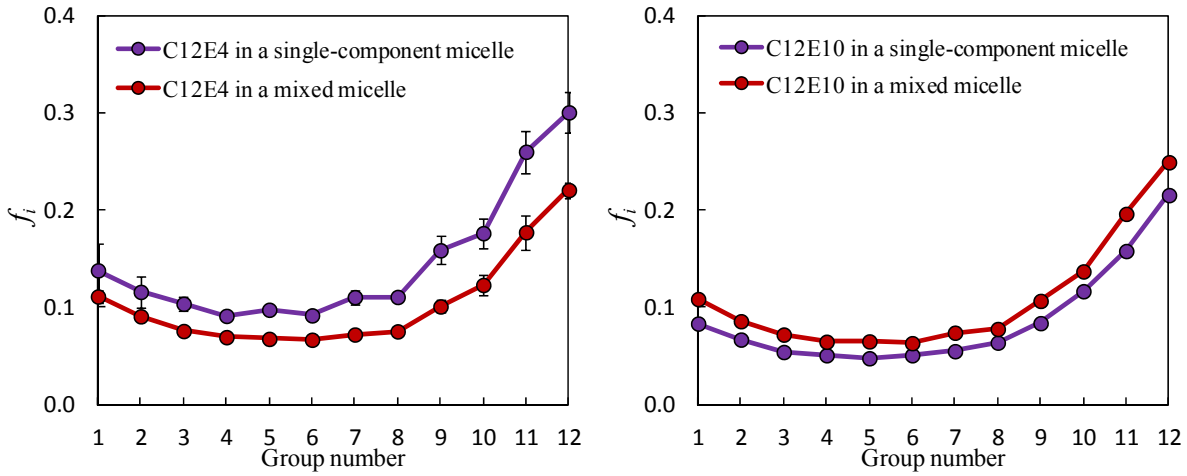

Figure 4-6: Variations of the fractional degree of hydration, f_i, as a function of group number in the 12-carbon tail of C12E4 and C12E10 in a single-component micelle (purple) and in an equimolar (C12E4+C12E10) mixed micelle (red).

E4 head with the more flexible E10 head is a better shielding of the micelle core, thereby leading to a lowering of $g_{tr,CSMT}$. Because $g_{tr,CSMT}^{\alpha-avg}$ does not incorporate any interactions between the surfactants comprising the mixed micelle, it is unable to reproduce the $g_{tr,CSMT}$ values obtained using the mixed-micelle simulation, where these interactions are accounted for. Therefore, the composition-weighted average method does not work well for binary mixtures of ethoxylate surfactants.

Figure 4-7 shows the variations of $g_{tr,CSMT}^{\alpha-avg}$ and $g_{tr,CSMT}$ as a function of micelle composition for binary mixtures in set (5) above. This set includes binary mixtures of dodecyl glucoside and: (a) tetraethylene glycol monododecyl ether (C12E4, purple), and (b) octaethylene glycol monododecyl ether (C12E8, blue). Similar to the results in Figure 4-4, Figure 4-7 shows that $g_{tr,CSMT}^{\alpha-avg}$ (lines) overpredicts $g_{tr,CSMT}$ (filled circles). This can again be attributed to the better shielding of the micelle core by the more flexible ethoxylate heads.

Finally, we consider the case of binary mixtures of ionic and nonionic surfactants.

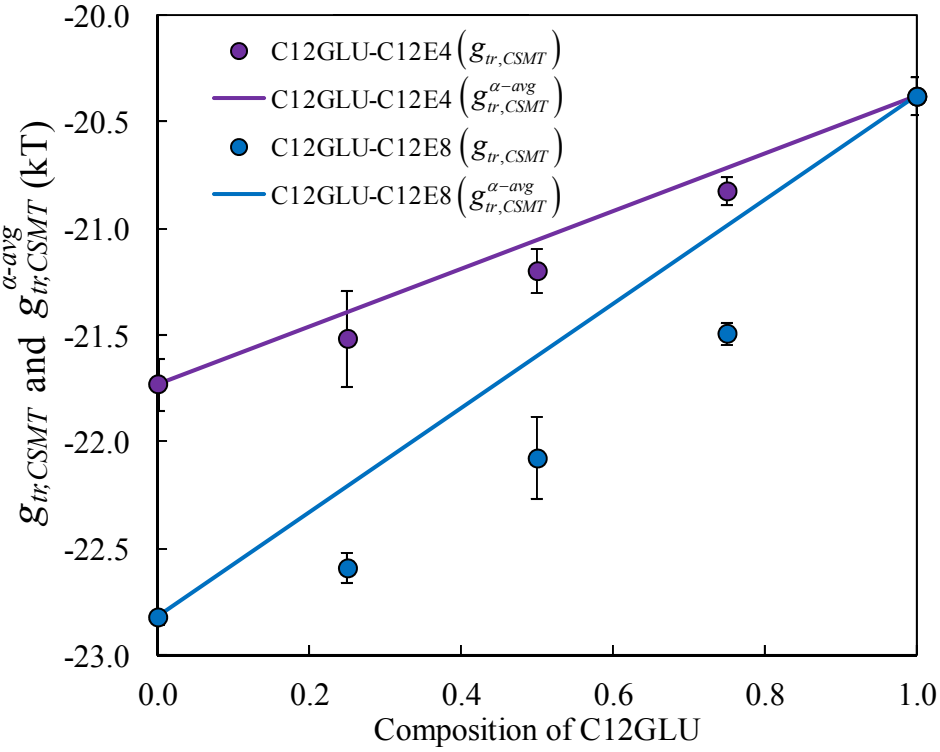

Figure 4-7: Variations of $g_{tr,CSMT}^{\alpha-avg}$ (lines) and $g_{tr,CSMT}$ (filled circles) as a function of micelle composition for a set of binary mixtures of dodecyl ethoxylates and dodecyl glucoside.

Results for the set of binary mixtures of surfactants in set (6) above are shown in Figure 4-8 and Figure 4-9. Figure 4-8 shows the variations of $g_{tr,CSMT}$ and $g_{tr,CSMT}^{\alpha-avg}$ as a function of micelle composition for mixtures of C12SUL with various alkyl ethoxylate surfactants, namely: (1) tetraethylene glycol monooctyl ether (C8E4, green), (2) tetraethylene glycol monodecyl ether (C10E4, red), (3) tetraethylene glycol monododecyl ether (C12E4, purple), and (4) octaethylene glycol monododecyl ether (C12E8, blue). Similar to the other binary mixtures containing alkyl ethoxylates (see Figure 4-4 and Figure 4-7), again, $g_{tr,CSMT}^{\alpha-avg}$ and $g_{tr,CSMT}$ do not agree well with each other. Instead, $g_{tr,CSMT}^{\alpha-avg}$ is systematically higher than $g_{tr,CSMT}$. Again, this can be explained based on the better shielding of the micelle core in the presence of the more flexible ethoxylate heads.

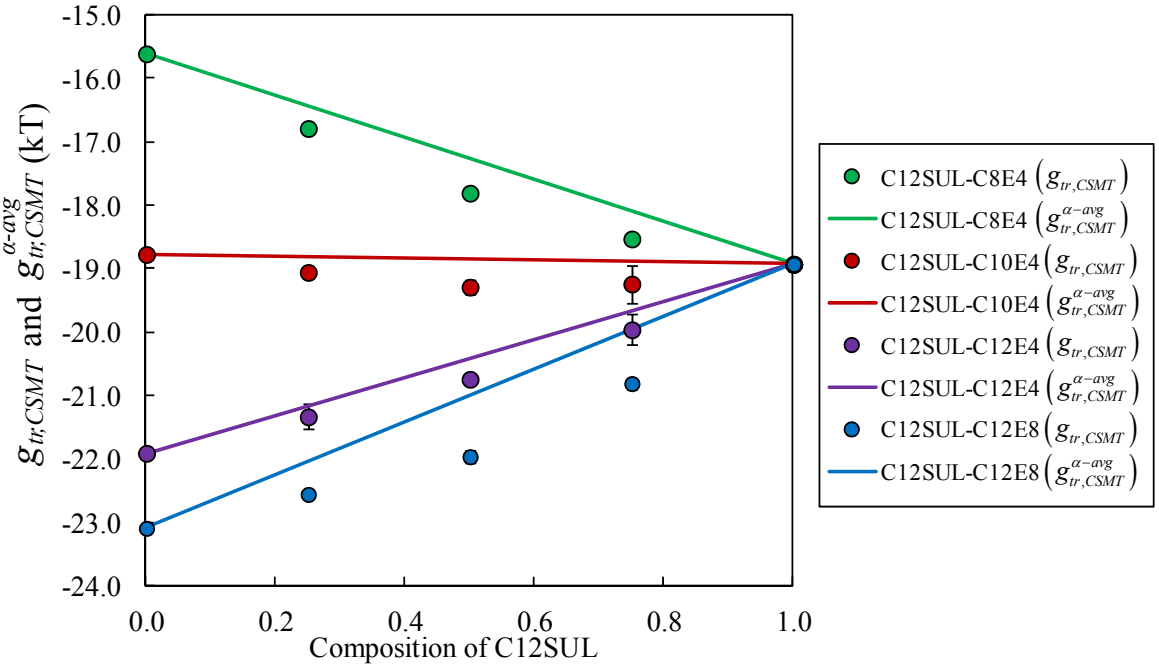

Figure 4-8: Variations of $g_{tr,CSMT}^{\alpha-avg}$ (lines) and $g_{tr,CSMT}$ (filled circles) as a function of micelle composition for a set of binary mixtures of alkyl ethoxylates and sodium dodecyl sulfate.

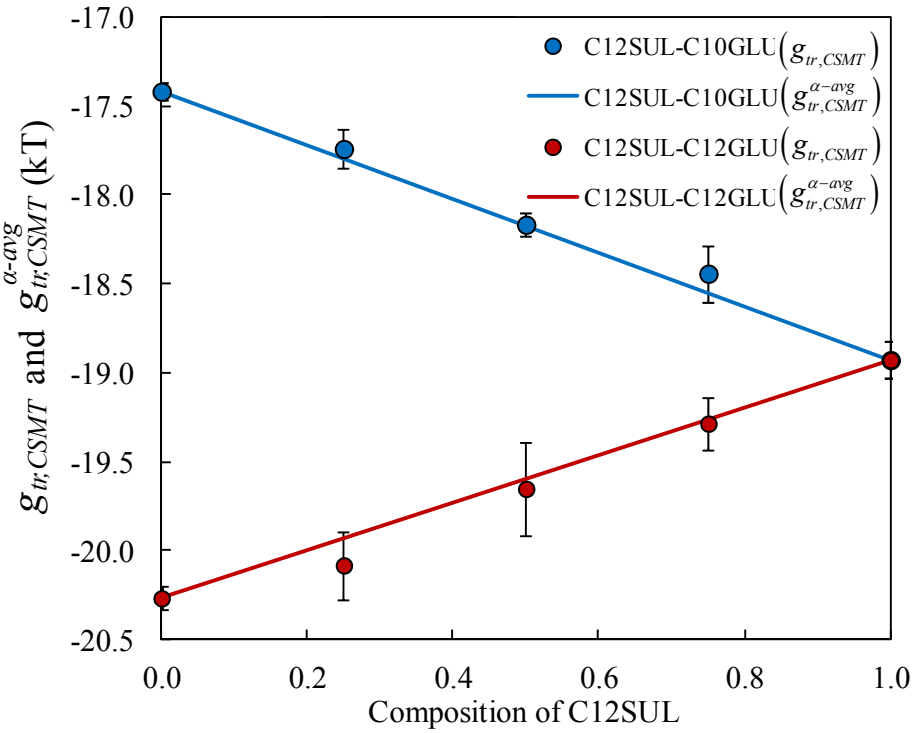

Figure 4-9: Variations of $g_{tr,CSMT}^{approx}$ (lines) and $g_{tr,CSMT}$ (filled circles) as a function of micelle composition for a set of binary mixtures of alkyl glucosides and sodium dodecyl sulfate.

Figure 4-9 shows the variations of $g_{tr,CSMT}^{\alpha-avg}$ and $g_{tr,CSMT}$ as a function of micelle composition for a set of binary mixtures containing C12SUL and alkyl glucosides, including: (1) decyl glucoside (C10GLU, blue), and (2) dodecyl glucoside (C12GLU, red). Unlike the results in Figure 4-8, for the binary mixtures of sodium dodecyl sulfate and alkyl glucosides considered here, $g_{tr,CSMT}^{\alpha-avg}$ and $g_{tr,CSMT}$ agree well with each other. This may reflect the fact that although the glucoside head is relatively big compared to the ionic surfactant head, it is not as flexible as the ethoxylate head to improve the overall shielding of the micelle core. This is also reflected in Figure 4-10 which shows the variations of f_i of the 12-carbon hydrocarbon chains of C12SUL and C12GLU in the single-component micelle (purple) and in the mixed micelle (red). Note that based on the Tanford definition of surfactant head and tail for ionic surfactants, the methylene group connected to the oxygen in C12SUL is considered to be part of the surfactant head. A comparison of Figures 4-6 and 4-10 shows that unlike the case in Figure 4-6, in Figure 4-10, there is no systematic shift in f_i of the surfactant tails in the single-component micelle relative to the mixed micelle. This suggests that the glucoside head does not provide any extra shielding of

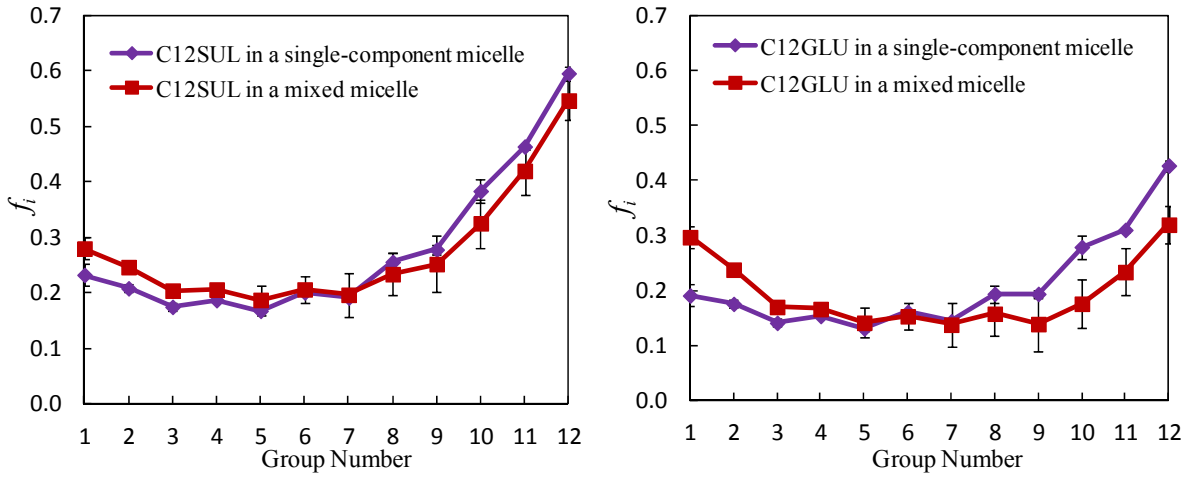

Figure 4-10: Variations of the fractional degree of hydration, f_i, as a function of group number in the 12-carbon hydrocarbon chain of C12SUL and C12GLU in a single-component micelle (purple) and in an equimolar (C12SUL+C12GLU) mixed micelle (red).

the micelle core, which was the case for the ethoxylate head. As a result, $g_{tr,CSMT}^{\alpha-avg}$ and $g_{tr,CSMT}$ agree well with each other in the glucoside case. Note that results which are similar to those presented in Figure 4-8 and Figure 4-9 are obtained when C12SUL is replaced with dodecyl ammonium chloride (results not presented here).

To summarize, based on the comparisons of $g_{tr,CSMT}^{\alpha-avg}$ and $g_{tr,CSMT}$ presented above, one can conclude that $g_{tr,CSMT}^{\alpha-avg}$ works as well as $g_{tr,CSMT}$ for binary mixtures of surfactants where the surfactant heads are small and/or rigid. On the other hand, for binary mixtures containing surfactants with long and flexible heads, like the alkyl ethoxylates, $g_{tr,CSMT}^{\alpha-avg}$ systematically overpredicts $g_{tr,CSMT}$. The observed difference is related to the fact that in a mixed micelle containing alkyl ethoxylates, the long and flexible ethoxylate head is able to interact with the constituent surfactants in a way that improves the shielding of the micelle core from contact with water. While these interactions between the various surfactant species in a mixed micelle are accounted for in calculating $g_{tr,CSMT}$, they are not accounted for in calculating $g_{tr,CSMT}^{\alpha-avg}$. As a result, based on the above findings, caution should be exercised when using $g_{tr,CSMT}^{\alpha-avg}$ in the case of surfactants with long flexible head groups. In the cases where $g_{tr,CSMT}^{\alpha-avg}$ does not mimic $g_{tr,CSMT}$, a quadratic or cubic polynomial fit can be obtained for $g_{tr,CSMT}$ as a function of the micelle composition which can be used in place of g_{tr} in Eq. (2-6).

4.5 Prediction of Micellization Propertied of Various Binary Surfactant Mixtures

To evaluate the predictive ability of the new mixture CSMT model, it was used to predict critical micelle concentrations (CMCs) of various binary mixtures of surfactants and the

predicted CMCs were compared with the experimental ones. Figure 4-11: shows predicted CMCs as a function of solution composition using the CSMT and the MT models for a binary mixture of sodium dodecyl sulfate (C12SUL) and sodium decyl sulfate (C10SUL). Note that $g_{tr,CSMT}^{\alpha-avg}$ was used to make the mixture CSMT CMC predictions. This was done because Figure 4-2 clearly shows that $g_{tr,CSMT}^{\alpha-avg}$ is as good as $g_{tr,CSMT}$ for this particular binary surfactant mixture.

Figure 4-11: shows that the CMCs predicted using the CSMT and the MT models

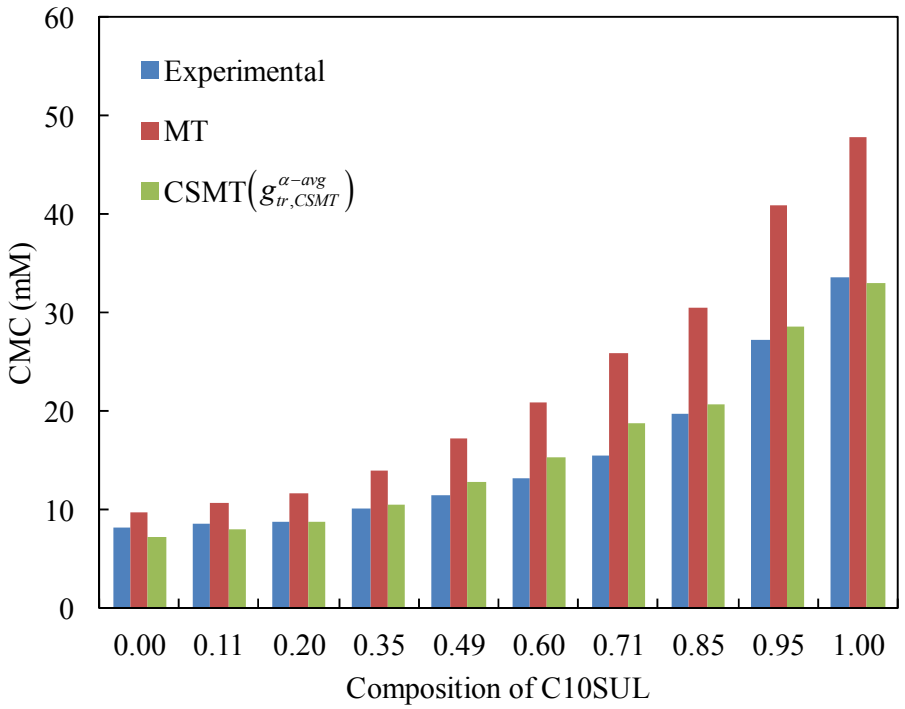

Figure 4-11: Predicted and experimental CMCs vs. solution composition for a binary mixture of sodium decyl sulfate and sodium dodecyl sulfate.

compare very well with the experimental CMCs.[114] All the predicted CMCs are within a factor of 1.7 of the experimental CMCs. The CSMT model does marginally better than the MT model because it better predicts the CMC of sodium decyl sulfate when compared to the MT model.

Figure 4-12 shows predicted CMCs as a function of solution composition using the

CSMT and the MT models for a binary mixture of sodium dodecyl sulfate (C12SUL) and decyl glucoside (C10GLU). The experimental CMCs[115] are also shown for comparison. Similar to the predictions in Figure 4-11:, $g_{tr,CSMT}^{\alpha-avg}$ was used to predict the CMCs because Figure 4-9 shows that for this binary surfactant mixture, $g_{tr,CSMT}^{\alpha-avg}$ is as good as $g_{tr,CSMT}$. Note that for this binary surfactant mixture, the MT model yields marginally better predictions than the CSMT model. This follows because the CMC of decyl glucoside predicted by the MT model is lower than the

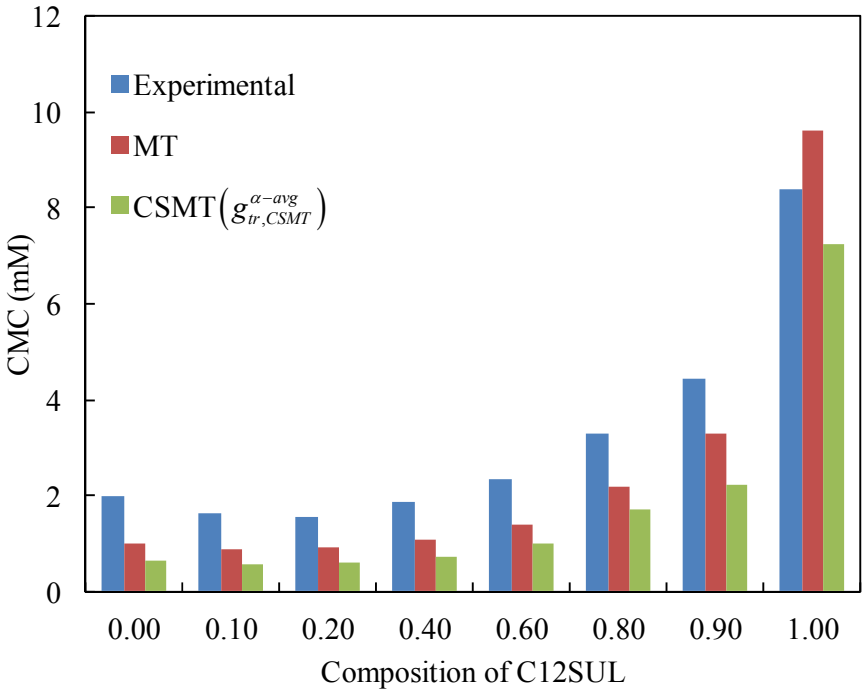

Figure 4-12: Predicted and experimental CMCs vs. solution composition for a binary mixture of sodium dodecyl sulfate and decyl glucoside.

experimental CMC, while the CMC of sodium dodecyl sulfate predicted by the MT model is higher than the experimental CMC. As a result, the CMCs predicted by the MT model at intermediate compositions are quite close to the experimental CMC values. On the other hand, in the case of the CSMT model, the predicted CMCs at the end points are both lower than the experimental CMC values. As a result, the CMCs predicted by the CSMT model at intermediate

compositions are systematically lower than the experimental CMCs. Note that both the MT and the CSMT models predict a minimum in the CMC at a solution composition of 10% C12SUL and 90% C10GLU, while the experimentally observed minimum in the CMC occurs at a solution composition of 20% C12SUL and 80% C10GLU,[115] which is quite close.

In the following three figures, the CMCs predicted using the CSMT and the MT models are compared with experimental CMCs for three binary surfactant mixtures where at least one of the surfactants is an alkyl ethoxylate. Specifically, the three binary mixtures include: (1) a mixture of sodium dodecyl sulfate (C12SUL) and tetraethylene glycol monooctyl ether (C8E4)[116] (see Figure 4-13), (2) a mixture of sodium dodecyl sulfate (C12SUL) and octaethylene glycol monododecyl ether (C12E8) in the presence of 500 mM of NaCl[117] (see Figure 4-14), and (3) a mixture of hexaethylene glycol monododecyl ether(C12E6) and tetraethylene glycol

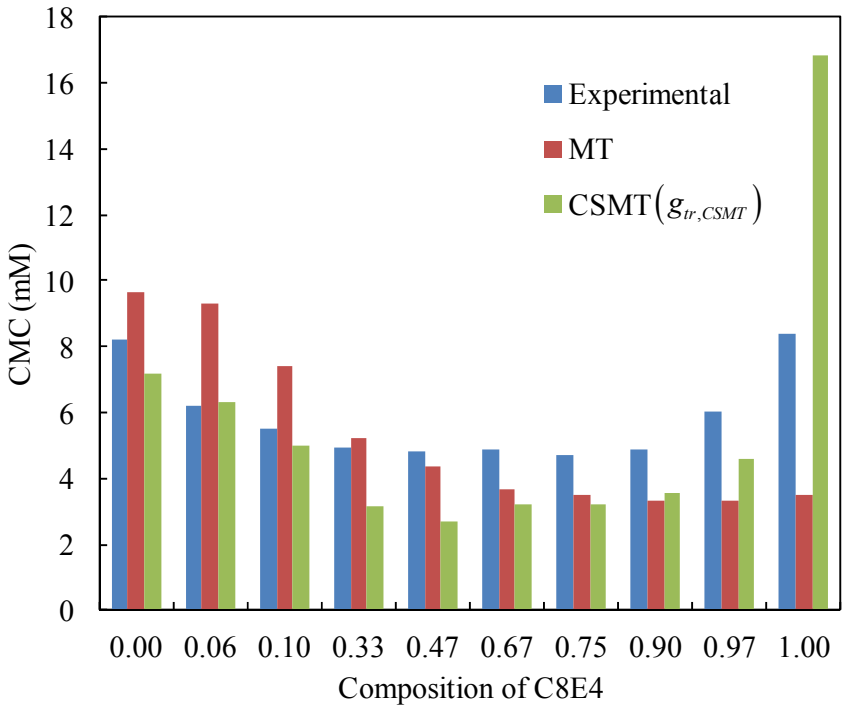

Figure 4-13: Predicted and experimental CMCs vs. solution composition for a binary mixture of sodium dodecyl sulfate and tetraethylene glycol monooctyl ether.

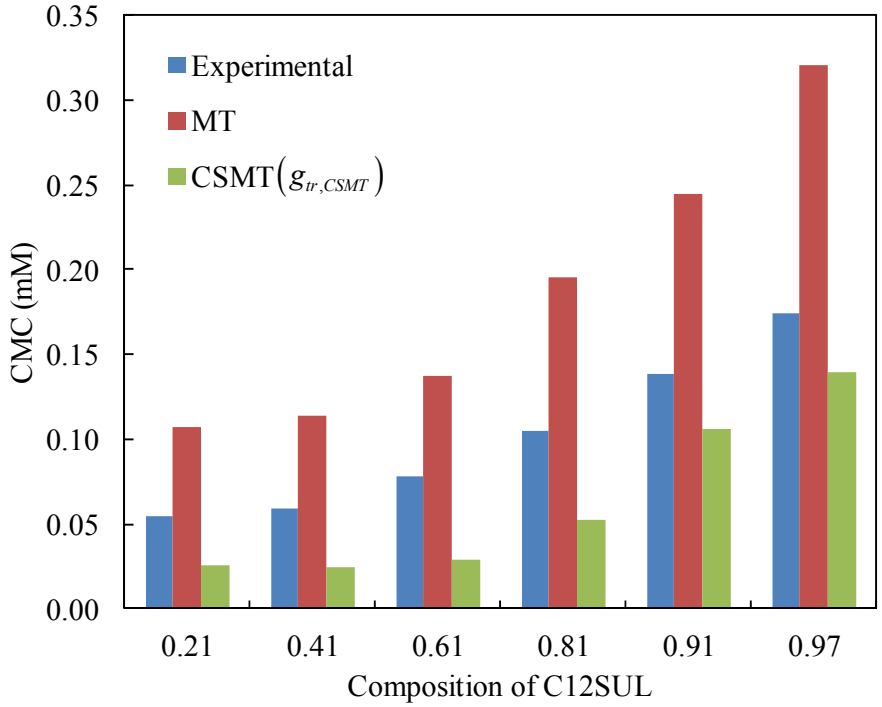

Figure 4-14: Predicted and experimental CMCs vs. solution composition for a binary mixture of sodium dodecyl sulfate and octaethylene glycol monododecyl ether with 500 mM NaCl.

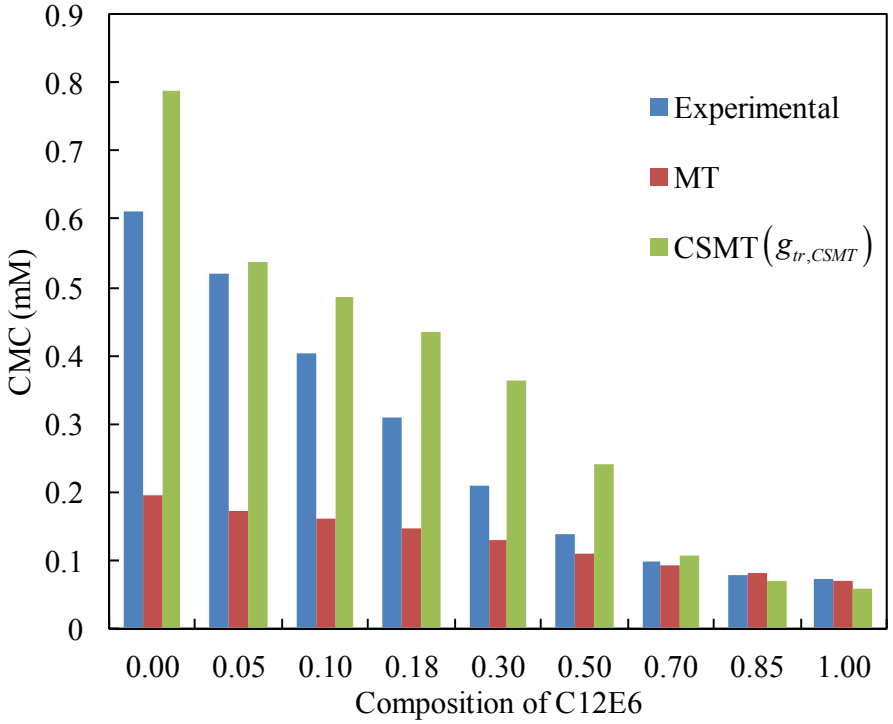

Figure 4-15: Predicted and experimental CMCs vs. solution composition for a binary mixture of tetraethylene glycol monodecyl ether and hexaethylene glycol monododecyl ether.

monodecyl ether (C10E4)[18] (see Figure 4-15). Based on the findings in Section 4.4, it is known that, for binary mixtures containing alkyl ethoxylates, $g_{tr,CSMT}^{\alpha-avg}$ overpredicts relative to $g_{tr,CSMT}$ (see Figure 4-4, Figure 4-7, and Figure 4-8). As a result, $g_{tr,CSMT}$ is utilized to predict the CMCs shown in Figure 4-13, Figure 4-14, and Figure 4-15. To this end, the simulation results were first fitted to analytical polynomials to capture the variation of $g_{tr,CSMT}$ as a function of the micelle composition. Subsequently, these polynomials were used to predict the CMCs. It is noteworthy that for the alkyl ethoxylates considered, different head areas were used for the MT and the CSMT models. The reasons behind this choice, including related calculations, are discussed in Section 7.3 in the Appendix, where values of the molecular descriptors of the various surfactants considered in this thesis are summarized.

Figures 4-13, 4-14, and 4-15 show that, for these three binary surfactant mixtures, the CSMT and the MT models yield very good CMC predictions. At certain compositions, the CMCs predicted by the MT model are better than those predicted by the CSMT model, while for other compositions, the reverse is true. CMCs predicted using both models are, on average, within a factor of 1.5 from the experimental CMC values.

Note that the computational cost associated with making the predictions shown in Figures 4-13, 4-14, and 4-15 (using $g_{tr,CSMT}$) is significantly higher than that associated with making the predictions shown in Figures 4-11 and 4-12 (using $g_{tr,CSMT}^{\alpha-avg}$). To understand the errors in the predicted CMCs resulting from the use of $g_{tr,CSMT}^{\alpha-avg}$ instead of $g_{tr,CSMT}$ for binary mixtures containing surfactants having flexible head groups like those shown in Figures 4-13, 4-14, and 4-15, the CMCs predicted using $g_{tr,CSMT}^{\alpha-avg}$ are compared with the CMCs predicted using $g_{tr,CSMT}$ for a representative case of the binary mixture of sodium dodecyl sulfate and octaethylene glycol

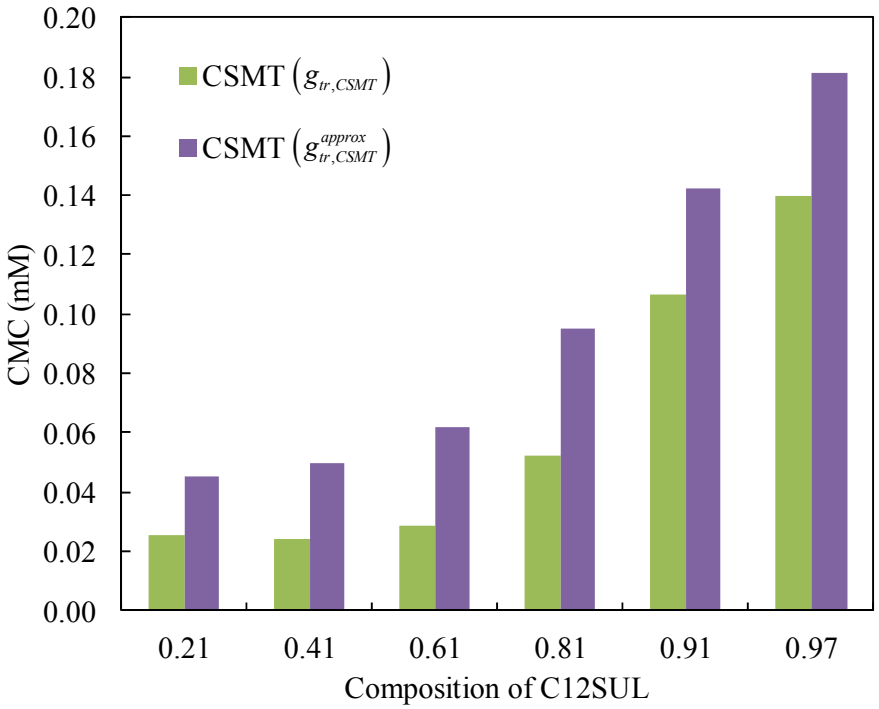

Figure 4-16: Predicted CMC using $g^{\alpha-avg}_{tr,CSMT}$ and $g_{tr,CSMT}$ for a mixture of sodium dodecyl sulfate and octaethylene glycol monododecyl ether

monododecyl ether. The results are presented in Figure 4-16, which shows that the predicted CMC using $g_{tr,CSMT}$ is lower than the predicted CMC using $g^{\alpha-avg}_{tr,CSMT}$. This is due to the fact that $g^{\alpha-avg}_{tr,CSMT}$ is always higher than $g_{tr,CSMT}$, as can be seen in Figures 4-4, 4-7, and 4-8. Indeed, Figure 4-16 shows that, for the C12SUL-C12E8 mixture considered, on average, there is a difference of 0.8 kT between $g^{\alpha-avg}_{tr,CSMT}$ and $g_{tr,CSMT}$. An examination of Figure 4-16 shows that, on average, the CMCs predicted using $g^{\alpha-avg}_{tr,CSMT}$ are a factor of 2 higher than the CMCs predicted using $g_{tr,CSMT}$. Note that in free-energy units, a factor of 2 is equal to ln(2) = 0.7 kT (free energy ~ ln(CMC)), which is very close to the average difference between $g^{\alpha-avg}_{tr,CSMT}$ and $g_{tr,CSMT}$ (0.8 kT). Therefore, by quantifying the difference between $g^{\alpha-avg}_{tr,CSMT}$ and $g_{tr,CSMT}$, one can quantify the expected error in the predicted CMCs if one used $g^{\alpha-avg}_{tr,CSMT}$, which is computationally cheaper than using $g_{tr,CSMT}$.

To decide between using the mixture CSMT model or the composition-weighted average based mixture CSMT model, one can perform an equimolar mixed-micelle simulation and evaluate the difference between $g_{tr,CSMT}^{\alpha-avg}$ and $g_{tr,CSMT}$. Based on this difference, one can quantify the expected error in the predicted CMC if $g_{tr,CSMT}^{\alpha-avg}$ is used instead of $g_{tr,CSMT}$, and decide accordingly which model to use.

Finally, the mixture CSMT model was used to predict the CMCs of the only binary mixture of fluorocarbon-based surfactants for which experimental data is available in the literature, namely, a binary mixture of lithium perfluorooctyl sulfonate (LiPFOS) and lithium perfluorooctanoate (LiPFO).[113] First, Figure 4-17 compares $g_{tr,CSMT}$ and $g_{tr,CSMT}^{\alpha-avg}$ for the binary mixture of lithium perfluorooctyl sulfonate (LiPFOS) and lithium perfluorooctanoate (LiPFO).

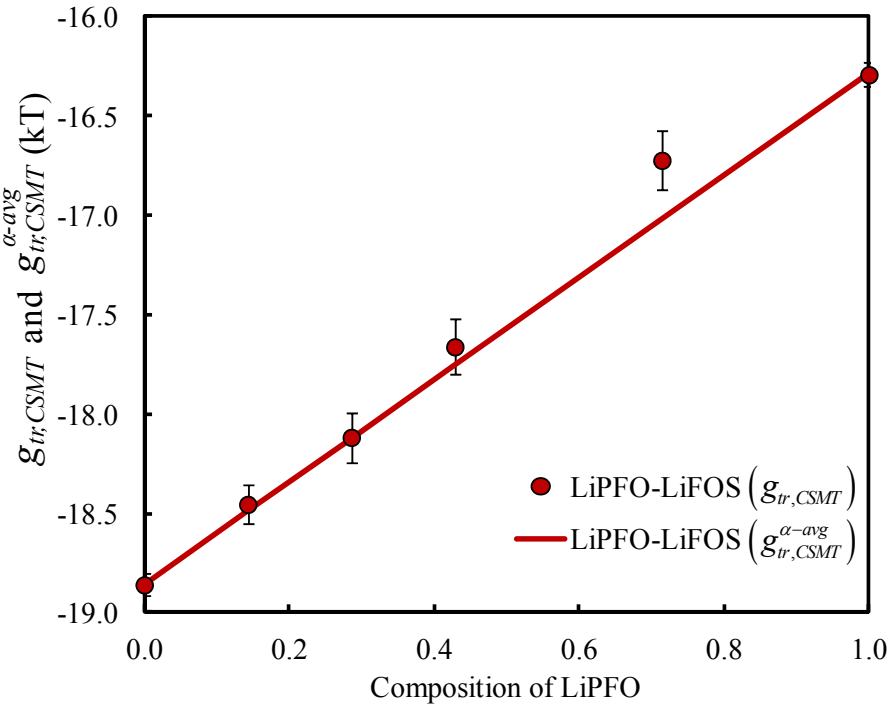

Figure 4-17: Variations of $g_{tr,CSMT}^{approx}$ (lines) and $g_{tr,CSMT}$ (filled circles) as a function of micelle composition for a binary mixture of lithium perfluorooctyl sulfonate (LiPFOS) and lithium perfluorooctanoate (LiPFO).

The figure clearly suggests that $g_{tr,CSMT}^{\alpha-avg}$ (red solid line) compares very well with $g_{tr,CSMT}$ calculated from the mixed-micelle simulation (red filled circles). Subsequently, the mixture CSMT and MT models were used to predict the mixture CMC. A comparison of the predicted and the experimental CMC values is presented in Figure 4-18. Similar to the predictions for the other binary mixtures presented in this section, the CMCs predicted using the CSMT and the MT models shown in Figure 4-18 compare very well with the experimental CMCs.[113] All the predicted CMCs are within a factor of 1.5 of the experimental CMCs. This is considered excellent agreement in the context of the MT and the CSMT models because the critical micelle concentration has an exponential dependence on the free energy of micellization (see Eq. (2-41)), which is the quantity that is actually modeled.[39] Therefore, even a small error in the predicted free energy of micellization can lead to a significant error in the predicted critical micelle concentration.

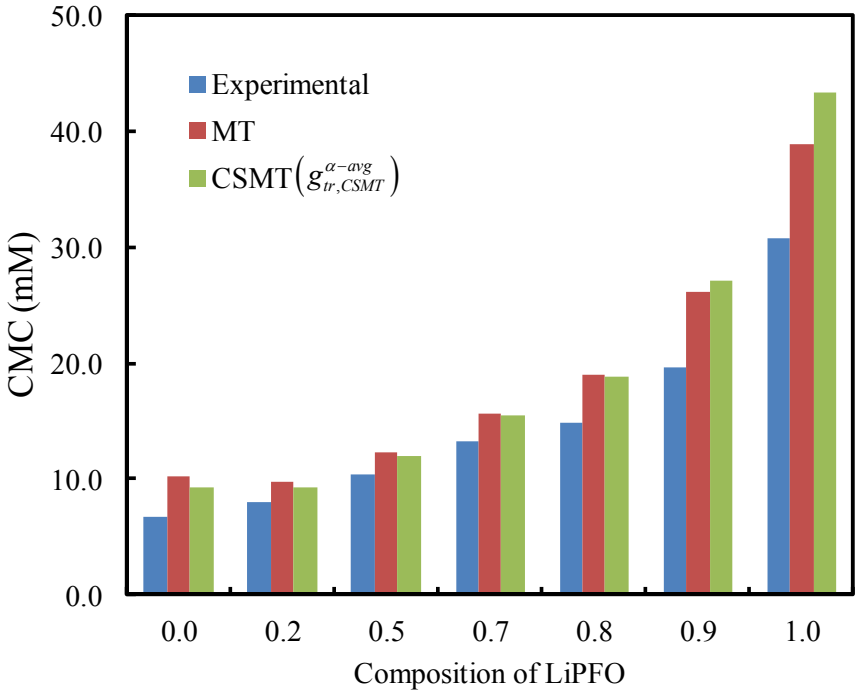

Figure 4-18: Predicted and experimental CMCs vs. solution composition for a binary mixture of lithium perfluorooctyl sulfonate (LiPFOS) and lithium perfluorooctanoate (LiPFO).

Moreover, it is important to recognize that the main motivation behind developing the mixture CSMT framework is not only to predict the micellization behavior of mixtures of *simple* surfactants, but also to predict the micellization behavior of mixtures of surfactants possessing complex chemical architectures, including branched and aromatic surfactants, which cannot be modeled using the traditional MT framework. The work presented here aims at building the foundation for the mixture CSMT framework, while ensuring that it predicts the micellization behavior of relatively simple surfactant mixtures accurately. Now that this has been established, the new mixture CSMT framework can be used to predict the micellization behavior of surfactant mixtures that cannot be modeled using the traditional MT framework.

4.6 Conclusions

In summary, in this chapter, a computer-simulation-molecular-thermodynamic (CSMT) framework was developed to predict the micellization behavior of surfactant mixtures. To overcome the difficulty in implementing the CSMT framework due to the computational costs associated with simulating mixed micelles at several compositions, an approximation to calculate $g_{tr,CSMT}$, referred to as $g_{tr,CSMT}^{\alpha-avg}$, was implemented. This approximation uses only information from the simulated single-component surfactant micelles for each of the constituent surfactants comprising the mixture. The approximation was tested for a variety of binary surfactant mixtures, and it was found to work very well for all the binary surfactant mixtures considered, except for those containing alkyl ethoxylate surfactants. The difference between $g_{tr,CSMT}^{\alpha-avg}$ and $g_{tr,CSMT}$ in the context of mixtures containing alky ethoxylate surfactants was attributed to the interactions between the surfactant molecules resulting from the flexible nature of the ethoxylate heads. CMC predictions made using the mixture CSMT model and the MT model were compared with the experimental CMCs for various binary mixtures of linear surfactants. The

predictions made using the MT model were found to be as good as the predictions made using the CSMT model for the binary mixtures of linear surfactants considered here. By demonstrating the applicability of the mixture CSMT model in the case of mixtures of simple surfactants, I have laid the foundation for the use of the mixture CSMT framework to model mixtures of surfactants that have a complex chemical architecture (for example, branched and aromatic surfactants), and are therefore not amenable to traditional MT modeling.

In the next chapter, I develop an MT model for binary mixtures of fluorocarbon-based and hydrocarbon-based surfactants. These surfactant mixtures are very different from those considered in this chapter because the fluorocarbon surfactant tails and the hydrocarbon surfactant tails mix nonideally. This nonideal mixing can lead to unconventional micellization behavior, including the coexistence of fluorocarbon-rich and fluorocarbon-poor mixed micelles.

Chapter 5

Modeling the Micellization Behavior of Binary Mixtures of Fluorocarbon-Based and Hydrocarbon-Based Surfactants

5.1 Introduction

The special properties of fluorocarbon-based surfactants, discussed in Section 1.1, make them far superior than their hydrocarbon counterparts, resulting in their widespread use in paints, polishes, floor waxes, adhesives, fire-fighting foams,[5] and emulsion polymerization.[5] However, as discussed in Section 1.2, the downside of using fluorinated surfactants is that due to their chemical inertness and thermal stability, they are not biodegradable,[5] and hence, are potentially toxic.[10, 118] Concerns about the bioaccumulation and toxicity of fluorinated surfactants have prompted a search for alternative surfactant formulations which minimize the use of fluorocarbon-based surfactants. To this end, an interesting strategy involves mixing fluorocarbon-based surfactants with other environmentally-benign surfactants, such as, hydrocarbon-based surfactants. In addition to reducing the fluorocarbon content of the surfactant

formulation, mixing fluorocarbon-based and hydrocarbon-based surfactants also reduces the cost of the surfactant formulation because fluorocarbon-based surfactants are much more expensive than their hydrocarbon counterparts.[5]

It is well known that fluorocarbons and hydrocarbons interact non-ideally, with their mixtures exhibiting positive enthalpies of mixing.[119] As a result, mixtures of fluorocarbon-based and hydrocarbon-based surfactants have received considerable academic attention, because they can exhibit significant deviations from the ideal-solution behavior. For example, for the binary mixture of sodium perfluorooctanoate (SPFO) and sodium decyl sulfate (SDeS), Mukerjee and Yang found that the experimental CMCs, measured using electrical conductance, were not very different from the CMCs calculated by assuming complete demixing of micelles. This led them to suggest that mixing of SPFO with SDeS leads to the coexistence SPFO micelles and SDeS micelles.[120] Aratono et al. concluded that, for certain solution compositions, mixing SPFO and SDeS leads to the coexistence of two types of mixed micelles: one rich in SPFO and the other rich in SDeS.[121] Aratono et al. arrived at this conclusion based on a thermodynamic treatment of their experimentally-measured surface tension data.[121] For the same system, Shinoda and Nomura[122] used the Regular Solution Theory (RST) to model the experimental data reported by Mukerjee and Yang,[120] and found that the RST interaction parameter was less than 2.0. Similar to the case of mixing in a binary solution, Shinoda and Nomura showed that for a binary mixture of surfactants, an interaction parameter that is smaller than 2.0 implies no demixing of micelles, that is, the existence of only one type of mixed micelle in solution.[122] Therefore, they concluded that the SPFO-SDeS binary mixture resulted in only one type of SPFO-SDeS mixed micelle. Kamogawa and Tajima also arrived at the same conclusion by measuring the electron-spin resonance (ESR) correlation times for certain spin probes in the mixed-micellar system

consisting of SPFO and SDeS at 25^0C in the absence of salt.[123] Interestingly, using nuclear-magnetic resonance spectroscopy, Nordstierna et al. concluded that the experimental measurements can be explained by assuming demixing within the mixed micelle.[124] In other words, the experimental data can be rationalized by assuming that only one type of mixed micelle exists with a fluorocarbon compartment and a hydrocarbon compartment within the micelle. In view of the above, it is clear that, for the same binary surfactant mixture, use of different methods has led to very different conclusions, with some studies suggesting the existence of one type of mixed micelle, and others suggesting the coexistence of two types of micelles. This follows because there is no direct experimental method to verify the existence of two types of mixed micelles, and all the conclusions were reached based on indirect evidence.

While there have been many experimental studies on the micellization behavior of mixtures of fluorocarbon-based and hydrocarbon-based surfactants, relatively little effort has been devoted to theoretically understand the micellization behavior of these interesting surfactant mixtures. To the best of my knowledge, Nagarajan's molecular-thermodynamic (MT) model is the only one that was developed to predict the micellization properties of mixtures of fluorocarbon-based and hydrocarbon-based surfactants.[83] With this in mind, in this chapter, I present a theoretical framework to model the micellization behavior of mixtures of fluorocarbon-based and hydrocarbon-based surfactants. Like Nagarajan's model, the model presented here is also based on a MT description of the micellization process, because as explained in Chapter 2, the MT framework provides useful insight on the roles played by the constituent surfactants in the mixture, including the surfactant head and tail, as well as on the effect of the solvent, the ions, and other solution conditions, on the micellization process.

In this chapter, the MT framework, originally developed by Puvvada and Blankschtein,[17] and subsequently advanced by several others[18, 19, 26, 39, 82, 99] (as discussed in Chapter 2), is generalized to allow predictions of micellization properties of mixtures of fluorocarbon-based and hydrocarbon-based surfactants. In particular, the new MT framework allows predictions of the coexistence of two types of micelles in solution, as has been observed experimentally. In addition, the new MT framework can be used to predict CMCs, micelle shapes, sizes, aggregation numbers, compositions, and degrees of counterion binding. Most importantly, the new MT framework provides a theoretical basis to identify the conditions for which mixing fluorocarbon-based and hydrocarbon-based surfactants leads to the coexistence of two types of mixed micelles. In addition to the clear fundamental relevance, the coexistence of two types of micelles can be very useful practically. Indeed, one can design surfactant formulations to generate materials with hierarchical or multimodal pore architectures for optimized transport and size selectivity.[125, 126] Note that the MT framework presented here does not model inhomogeneous micelles with compartmentalization within the micelle. This will be briefly discussed in the next chapter (see Section 6.2.3).

Theoretical details of the MT framework as they pertain to mixtures of fluorocarbon-based and hydrocarbon-based surfactants are presented in Section 5.2. These include modifications to the packing free energy, g_{pack}, to the mixing free energy, g_{mix}, as well as modifications in the method discussed in Section 2.5 to calculate micellization properties. The main improvements in the new MT framework, as compared to that developed by Nagarajan,[83] are also discussed in Section 5.2. Following the theoretical details, Section 5.3 demonstrates the model's ability to predict the coexistence of two types of mixed micelles in solution. This is done by predicting the micelle population distributions for three hypothetical binary mixtures of

surfactants. Finally in Section 5.4, the new framework is used to predict various micellization properties, including mixture CMCs, micelle population distributions, and optimal micelle compositions, for various mixtures of fluorocarbon-based and hydrocarbon-based surfactants. These predictions are also compared with the corresponding experimental measurements.

5.2 MT Framework for Mixtures of Fluorocarbon-Based and Hydrocarbon-Based Surfactants

5.2.1 Packing Free Energy of Mixtures of Fluorocarbon and Hydrocarbon Tails

The packing free energy per molecule, g_{pack}, is the free-energy penalty associated with the restructuring of an oil drop such that it mimics the micelle core (with the surfactant's head tail connection tethered at the interface). As discussed in Section 2.3, g_{pack} for a micelle of a given shape and size is calculated based on the mean-field, statistical-mechanical method pioneered by Ben-Shaul et al.[34] For the case of binary mixtures of surfactants, g_{pack} is a function of both the micelle composition and the micelle shape and size. Therefore, for each micelle shape and size, g_{pack} is calculated for all micelle compositions using the method described in Section 2.3.[21] For every micelle shape, size, and composition, this is done by sampling all the chain conformations for both surfactants. The generated packing data for each shape is then converted into polynomials that relate the packing free energy to the micelle size and the micelle composition. These polynomial functions are subsequently used to calculate the free energy of micellization, g_{mic}, the CMC, and other micellization properties.[21] The packing polynomials for various mixtures of fluorocarbon and hydrocarbon tails considered in this thesis are reported in Section 7.2 in the Appendix.

In the context of the packing free energy, the size of the micelle core (that is, the radius for spheres and infinite cylinders, and the half thickness for infinite bilayers) is limited by the maximum extension length of the surfactant tail, because the micelle core cannot have voids. However, in the case of a mixed-micelle core formed by surfactants having different tail lengths, the maximum size of the micelle core becomes a function of the micelle composition. Nagarajan, in his MT framework, assumed that the maximum size of the mixed-micelle core, r_{max}, is equal to a volume-fraction based weighted average of the maximum lengths of the constituent surfactant tails. Specifically, he assumed that:[83]

$$r_{max} = \phi_1 l_{tail,1} + \phi_2 l_{tail,2} \tag{5-1}$$

where ϕ_1 and ϕ_2 are the volume fractions of components 1 and 2, and $l_{tail,1}$ and $l_{tail,2}$ are the tail lengths of surfactants 1 and 2, respectively. Because our method to calculate g_{pack} (see Section 2.3) explicitly involves calculating the packing free energy at different micelle compositions, shapes, and sizes, one can actually infer the functional dependence of the maximum micelle-core size on the micelle composition without making the simplifying assumption made by Nagarajan. As an illustration, Figure 5-1 shows plots of the variation of r_{max} as a function of the composition of the longer-tail in binary mixtures of C_6F_{13} and $C_{10}H_{21}$ packed in infinite bilayers, infinite cylinders, and spheres. To understand the effect of the surfactant tail lengths, Figure 5-2 shows plots of the variation of r_{max} as a function of the composition of the longer-tail surfactant, for spherical micelles formed by three binary mixtures: (i) C_7F_{15} and C_8H_{17}, (ii) C_6F_{13} and C_9H_{19}, and (iii) C_6F_{13} and $C_{10}H_{21}$. The reported r_{max} values (shown as red circles in Figures 5-1 and 5-2) correspond to the maximum size of the micelle core for which g_{pack} could be calculated without violating the uniform density packing constraint (see Eq. (2-21) in Section 2.3). Note that for every shape, g_{pack} is calculated for discrete values of size (typically at intervals of 0.5 Å) and

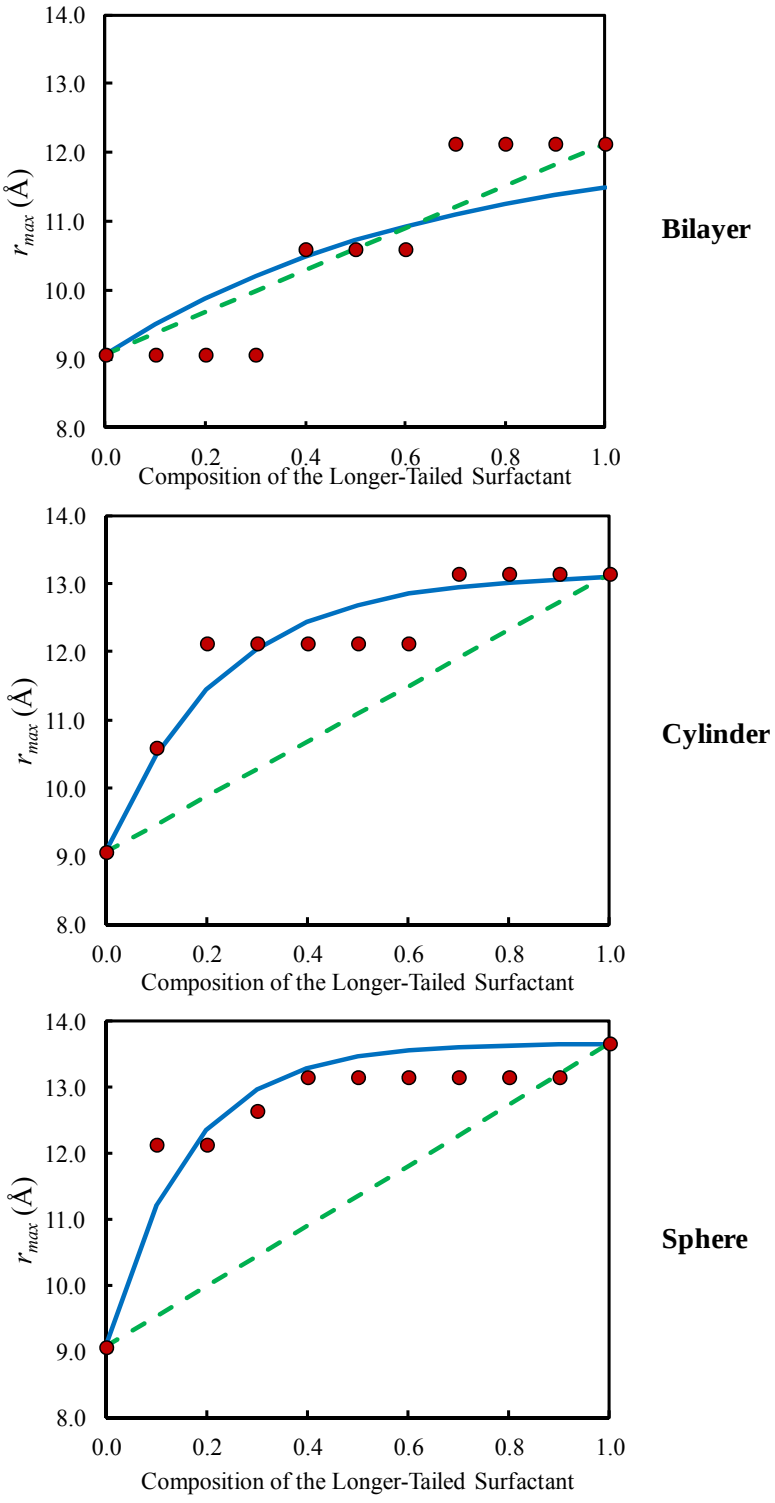

Figure 5-1: Plots showing the variation of r_{max} of a mixed-micelle core formed by C_6F_{13} and $C_{10}H_{21}$ surfactant tails, as a function of the composition of the longer-tailed surfactant for infinite bilayer-like, infinite cylindrical, and spherical micelle cores. The red circles represent the actual r_{max} values, the dashed green line represents r_{max} calculated using Eq. (5-1), and the solid blue line represents r_{max} calculated using Eq. (5-2).

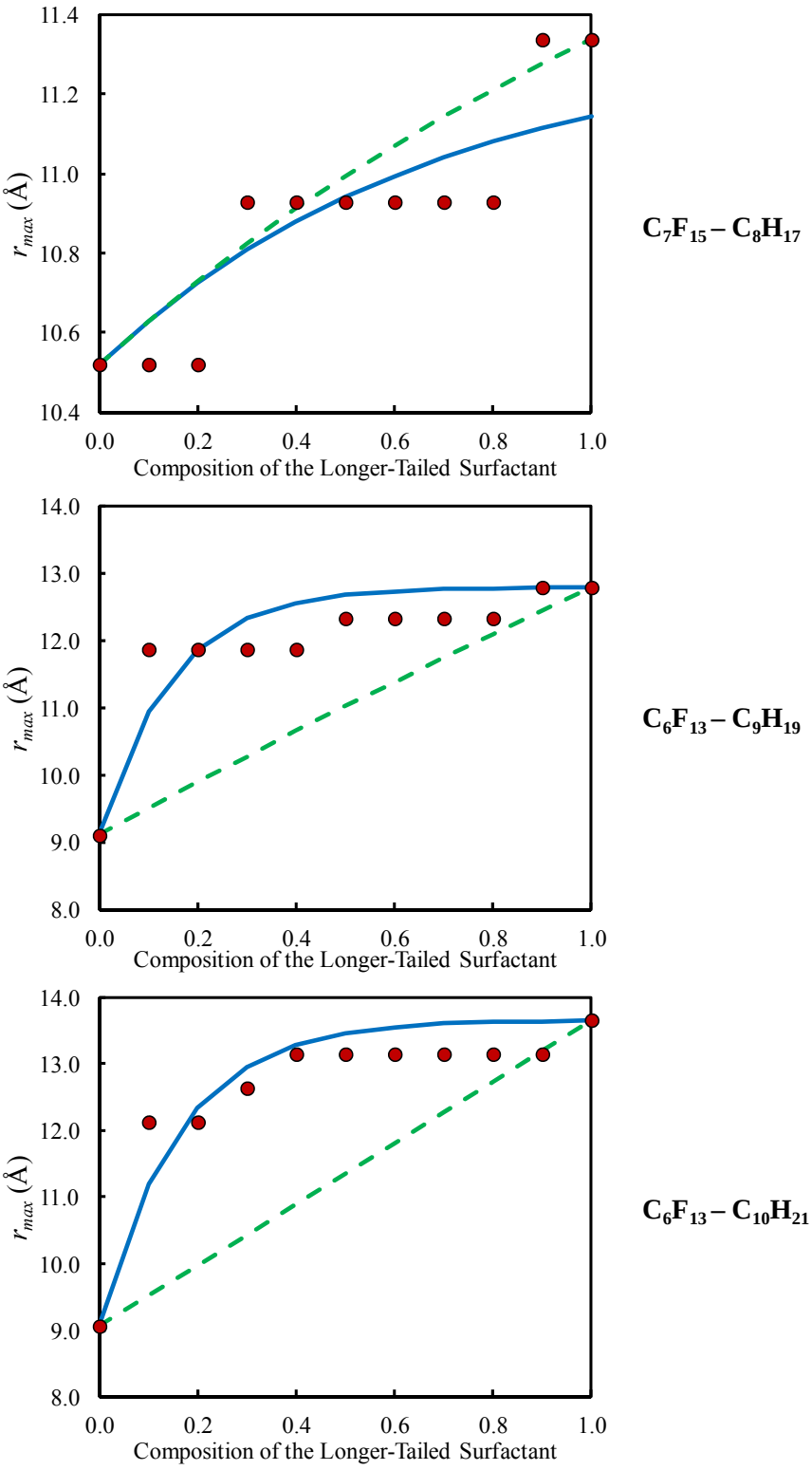

Figure 5-2: Plots showing the variation of r_{max} of a spherical mixed-micelle core as a function of the composition of the longer-tailed surfactant for three binary mixtures of fluorocarbon-based and hydrocarbon-based surfactants. The red filled circles represent the actual r_{max} values, the dashed green line represents r_{max} calculated using Eq. (5-1), and the solid blue line represents r_{max} calculated using Eq. (5-2).

composition (typically at intervals of 0.1). Therefore, the red circles shown in Figures 5-1 and 5-2 do not vary continuously. To obtain a continuous curve, g_{pack} would have to be calculated at smaller intervals of sizes and compositions.

Figure 5-1 shows that, for cylindrical and spherical micelle cores, r_{max} starts at $r_{max,short}$, the maximum tail length of the shorter tail, when the composition of the longer tail is 0.0, and rapidly increases to $r_{max,long}$, the maximum tail length of the longer tail, well before the composition of the longer tail is 1.0. Similarly, Figure 5-2 shows that when the difference between $r_{max,short}$ and $r_{max,long}$ is large, r_{max} starts at $r_{max,short}$, when the composition of the longer tail is 0.0, and rapidly increases to $r_{max,long}$ well before the composition of the longer tail is 1.0. Based on these observations, the following functional form can be used to relate r_{max} to α_{long}, the composition of the longer tail:

$$r_{max} = r_{max,short} + \left(r_{max,long} - r_{max,short}\right)\left(1 - e^{-\alpha_{long}/\alpha_0}\right) \tag{5-2}$$

where α_0 is a parameter used to fit the data. Values of the fitting parameter, α_0, for various binary surfactant mixtures are tabulated in the packing polynomial tables in Section 7.2 in the Appendix. Figures 5-1 and 5-2 also compare the r_{max} values, calculated using Eq. (5-1) [green dashed line] and Eq. (5-2) [blue solid curve], with the actual r_{max} values, calculated using the actual packing data (red circles). As expected, the functional form in Eq. (5-2) works best for cylindrical and spherical micelle cores, and for cases when the difference between $r_{max,short}$ and $r_{max,long}$ is large. On the other hand, Eq. (5-1)[83] systematically underpredicts the maximum micelle-core size for these cases. For bilayers, as well as for cases when the difference between $r_{max,short}$ and $r_{max,long}$ is small, Eq. (5-2) does not work as well, while Eq. (5-1) works better. This difference in the behavior of r_{max} for the different micelle-core shapes is due to the difference in

the volume distribution in the three micelle-core shapes. Indeed, bilayers have a uniform distribution of volume, while cylinders and spheres have more volume near the periphery than in the center. Compared to cylindrical and spherical micelles, bilayer-like micelles are not that commonly encountered micelle shapes. Therefore, Eq. (5-2) was used to determine the maximum micelle-core size.

5.2.2 Enthalpy of Mixing

The primary reason for the coexistence of two types of micelles in mixtures of fluorocarbon-based and hydrocarbon-based surfactants is the positive enthalpy of mixing exhibited by mixtures of fluorocarbons and hydrocarbons. As discussed in Eq. (2-35) in Section 2.3, the enthalpic contribution to the free energy of mixing was neglected because the surfactant tails in mixtures of hydrocarbon-based surfactants are expected to behave ideally. However, the same cannot be assumed for the surfactant tails in mixtures of fluorocarbon-based and hydrocarbon-based surfactants.

In any model aimed at predicting the micellization properties of binary mixtures of fluorocarbon-based and hydrocarbon-based surfactants, it is imperative to accurately model the enthalpy of mixing between the fluorocarbon-tails and the hydrocarbon-tails. Early attempts to model mixtures of fluorocarbons and hydrocarbons utilized the Regular Solution Theory (RST), along with the commonly used mixing rules, to model the interaction parameter quantifying the interactions between two different types of molecules. Unfortunately, this did not yield satisfactory results.[119] Specifically, it was found that the geometric-mean mixing rule to estimate the unlike interaction parameter yielded values which are higher than those required to accurately predict the mixture properties.[119] More sophisticated models, based on the Statistical

Associating Fluid Theory (SAFT),[127] were also utilized to predict the phase behavior of mixtures of fluorocarbons and hydrocarbons.[128-130] These models confirmed the findings by other researchers that the unlike interaction energy has to be about 10% smaller than that predicted by the geometric-mean mixing rule for the model to accurately predict the experimental data. It then follows that the departure from the geometric-mean mixing rule needs to be accounted for in any model used to properly quantify the enthalpic interactions between fluorocarbons and hydrocarbons.

With the above in mind, we have used the RST to model the non-ideal interactions between the fluorocarbon and the hydrocarbon tails, because of its simple mathematical form and broad applicability to non-polar mixtures. However, because of the challenge associated with the estimation of the interaction parameter discussed above, we estimated this parameter based on experimental phase equilibrium data for mixtures of fluorocarbons and hydrocarbons, instead of implementing commonly-used mixing rules. Recall that, in the RST, the enthalpy of mixing, ΔH_{mix}, of a binary solution is given by:

$$\Delta H_{mix} = A_{mix}\phi_1\phi_2 V \tag{5-3}$$

where A_{mix} is the interaction parameter between component 1 and 2, ϕ_1 and ϕ_2 are the volume fractions of components 1 and 2, respectively, and V is the solution volume. Using Eq. (5-3) and Eq. (2-35), the free energy of mixing per molecule, g_{mix}, for mixtures of fluorocarbon-based and hydrocarbon-based surfactants can be written as follows:

$$g_{mix} = kT\left(\sum_i \ln\left(\frac{\alpha_{n,i}}{1+\beta_n}\right) + \beta_n \ln\left(\frac{\beta_n}{1+\beta_n}\right)\right) + A_{mix}\phi_1\phi_2\left(\sum_i \alpha_{n,i} v_{tail,i}\right) \tag{5-4}$$

where the extensive solution volume, V, in Eq. (5-3) is replaced by the intensive average tail volume, which is the volume of the micelle core on a per molecule basis, to obtain the mixing free energy per molecule. The value of A_{mix} was calculated based on the values reported in several experimental studies involving mixtures of fluorocarbons and hydrocarbons.[119, 131-135] In these studies, the values of A_{mix} for mixtures of fluorocarbons and hydrocarbons having 5-8 carbon atoms were calculated based on measurements of vapor-liquid equilibiurm,[133] liquid-liquid equilibrium,[131, 133] calorimetry data,[132] consolute temperatures,[131] and infinite-dilution activity coefficients.[135] The value of A_{mix} was found to vary as a function of temperature and of the number of carbon atoms in the fluorocarbon and the hydrocarbon constituents. Specifically, the A_{mix} values were found to vary between 6.6 cal/cm^3 and 9.8 cal/cm^3, for temperatures varying between 10^0C and 50^0C and number of carbon atoms in the fluorocarbon and the hydrocarbon chains varying between 5 and 8. Note that this variation in A_{mix} is indeed significant. However, in the absence of quality data characterizing the effect of the hydrocarbon chain length, the fluorocarbon chain length, and the temperature, an average, constant value of A_{mix} = 7.16 cal/cm^3 was used in the calculations reported here.

5.2.3 Prediction of Micellization Properties

In Section 2.5, I presented a method to calculate micellization properties, such as the critical micelle concentration (CMC), the micelle shape, the micelle size, the micelle composition, and the degree of counterion binding. This method was based on calculating the set of micelle characteristics that correspond to the lowest free energy of micellization, and consequently, to the highest concentration of micelles in the surfactant solution. The method presented in Section 2.5 to calculate micellization properties assumes that the micelle population distribution is unimodal. However, in the case of mixtures of fluorocarbon-based and

hydrocarbon-based surfactants, the micelle population distribution can be bimodal, yielding two local maxima. As a result, the method presented in Section 2.5 needs to be modified to accurately predict CMCs and other micelle characteristics.

Recall that the CMC is defined as the surfactant concentration that marks the onset of aggregate formation (see Section 2.5). In addition to the definition proposed in Section 2.5, which involves calculating the minimum value of the free energy of micellization, other CMC definitions have been proposed to predict CMCs. For example, Tanford defined the CMC as the surfactant concentration at which 5% of the surfactant molecules are in micellar form and the remaining 95 % are in monomeric form.[1] Ruckenstein and Nagarajan defined the CMC as the concentration of surfactant at which the micelle population distribution, defined in Eq. (2-5) as a function of the aggregation number, shows a point of inflection.[136] In the context of the MT model for mixtures of fluorocarbon-based and hydrocarbon-based surfactants, implementing the method introduced by Ruckenstein and Nagarajan to determine the CMCs is much more complicated than implementing the CMC definition introduced by Tanford. This follows because the Tanford method does not require derivatives of the micelle population distribution for its implementation. Therefore, to simplify calculations, we adopted Tanford's definition to predict CMCs for the systems considered. Note that other micelle characteristics, including micelle shapes, sizes, compositions, and degrees of counterion binding, can be predicted by first determining whether the micelle population distribution is unimodal or bimodal. Specifically, if the micelle population distribution is found to be unimodal, then, the optimal micelle corresponds to the micelle with the highest population. On the other hand, if the micelle population distribution is found to be bimodal, then, the characteristics of the two types of micelles correspond to the two peaks in the micelle population distribution.

The micelle population distribution is computed by calculating the concentration of each type of micelle that can exist in solution. For each aggregation number, the concentrations of various micelles spanning micelle compositions between 0.0 and 1.0 and degrees of counterion binding between 0.0 and 1.0 are calculated. In the case of spherical micelles, the aggregation number uniquely determines the size of the micelle. However, in the case of spherocylindrical and discoidal micelles, the aggregation number alone is not sufficient to determine the size of these micelles. For example, in the case of a spherocylindrical micelle, each micelle aggregation number corresponds to a set of infinitely many combinations of the cylinder radii and lengths.

The population of all possible types of micelles is calculated to evaluate what fraction of the added surfactant remains in micellar form. This information is needed in order to solve the mass balance equations, Eqs. (2-3) and (2-4). Specifically, for each aggregation number, the population of micelles is integrated over three independent variables: (i) the micelle composition, (ii) the degree of counterion binding, and (iii) the micelle radius or width for spherocylinders and discs, respectively. The integration is carried out numerically using the trapezoidal rule. Note that the integrals over all three variables are finite, because the micelle composition and the degree of counterion binding vary between 0.0 and 1.0, and the micelle radius and thickness in the case of spherocylinders and discs, respectively, is limited by r_{max} [see Eq. (5-2)].

Another important consideration in calculating the micelle population distribution involves determining the upper limit on the aggregation number. For spherical micelles, the aggregation number is limited by r_{max} [see Eq. (5-2)]. However, spherocylindrical and discoidal micelles can theoretically grow indefinitely in one and two dimensions, respectively. Nevertheless, from an entropic standpoint, the micelles cannot grow indefinitely. As a result, the population of micelles will eventually become negligible beyond some threshold aggregation

number. Because there is no theoretical way to a priori estimate this threshold aggregation number, it is estimated in the process of calculating the population of micelles of different aggregation numbers. Specifically, starting from the lowest aggregation number, set at 6 here (this choice does not significantly affect the model predictions), the contribution of micelles of each aggregation number, in increasing order, is calculated and added to compute the concentration of surfactant molecules in micellar form. This addition is concluded when the following criterion is met: the contribution of micelles of the ten largest aggregation numbers, towards the population of micelles, is less than 1% of the maximum contribution by any aggregation number. In other words, if the sum of the population of micelles with aggregation numbers n, n+1, n+2, …., n+9 is less than 1% of the population of micelles with aggregation number m, where m is the aggregation number with the largest population of micelles, then, the population of micelles with an aggregation number higher than $n+9$ is ignored. Note that the idea behind choosing the ten largest aggregation numbers is to select a sufficiently large number such that no significant portion of the micelle population distribution is neglected.

5.2.4 Salient New Features

In addition to the difference in the calculation of the maximum micelle-core size for mixtures of surfactants presented in Section 5.2.1, there are several other differences between the MT framework for mixtures of fluorocarbon-based and hydrocarbon-based surfactants presented here and the MT framework developed by Nagarajan.[83] For example, the method used to calculate the packing free energy, g_{pack}, in the MT framework presented here, is very different from that used by Nagarajan,[83] which is based on the model developed by Nagarajan and Ruckenstein.[16] The equivalent of g_{pack} in the MT framework developed by Nagarajan and Ruckenstein (NR) is referred to as the deformation free energy of the surfactant tail. In the NR

model, the method to calculate the deformation free energy utilizes an approach which is similar to the theory developed by Semenov[137] for block copolymers by using a lattice representation. This approach yields convenient analytical expressions in terms of various parameters, including the lattice size and the chain length.[16, 83] Consequently, the NR model is much easier to implement than the model for g_{pack} presented in Sections 2.3 and 5.2.1. However, it is not clear if the theory for polymeric chains is applicable for the shorter surfactant tails considered. In addition, this model does not account for the different energies associated with the different conformations of the surfactant tail. In other words, information about the difference in rigidity of the fluorocarbon tails compared to that of the hydrocarbon tails is neglected in calculating the deformation free energy. Similarly, the difference in the geometrical properties of the fluorocarbon tail and the hydrocarbon tail, including the volume of the tail, is not accounted for. As a result, the behavior of the deformation free energy as a function of the micelle size and composition is very different from the behavior of the packing free energy discussed in Sections 2.3 and 5.2.1.

Other new features in the MT framework presented here include: (i) accounting for counterion binding, and (ii) incorporating the effect of curvature on the interfacial tension. The NR model[16, 83] does not account for counterion binding. As a result, it severely affects the calculation of the electrostatic free energy and the steric free energy presented in Section 2.3. In addition, the NR model does not account for the effect of curvature on the calculation of interfacial tensions. This, in turn, can have a significant effect on the calculation of the interfacial free energy, because the micelle cores are small in size. As a result, they have a high curvature, for which the interfacial tension is known to deviate from its value for a flat (zero curvature) interface.[27, 29]

5.3 Model Predictions for Hypothetical Binary Surfactant Mixtures

The MT framework for mixtures of fluorocarbon-based and hydrocarbon-based surfactants presented in this chapter was used to predict the critical micelle concentrations (CMCs) and micelle population distributions of three hypothetical binary surfactant mixtures. In particular, the model's ability to predict bimodal micelle population distributions was tested. The three hypothetical surfactant mixtures include:

1. A binary mixture consisting of two identical 7-carbon fluorocarbon-based nonionic surfactants having a head area of 60 $Å^2$ (typical of a glucamide head).
2. The binary mixture in 1 above with added hypothetical antagonistic enthalpic interactions between the surfactant tails. The enthalpic interactions are calculated using Eq. (5-3) with A_{mix} = 7.16 cal/cm^3.
3. The binary mixture in 2 above, but with the nonionic head of one of the two surfactants replaced by an ionic sulfonate head.

The resulting micelle population distributions at different solution compositions, α, (shown at the top of each plot), for mixtures 1, 2, and 3 above are shown in Figure 5-3, Figure 5-4, and Figure 5-5, respectively. Specifically, for each solution composition, the relative micelle population distribution is plotted as a function of the aggregation number, n, and the micelle composition, α_{mic}. The relative micelle population is calculated by dividing the micelle concentration calculated using Eq. (2-5) by the highest micelle concentration. As a result, the micelle with the highest concentration has a relative population of 1. Note that all the surface plots presented in this chapter are smoothened surface plots, and do not represent the raw data obtained from Eq. (2-5).

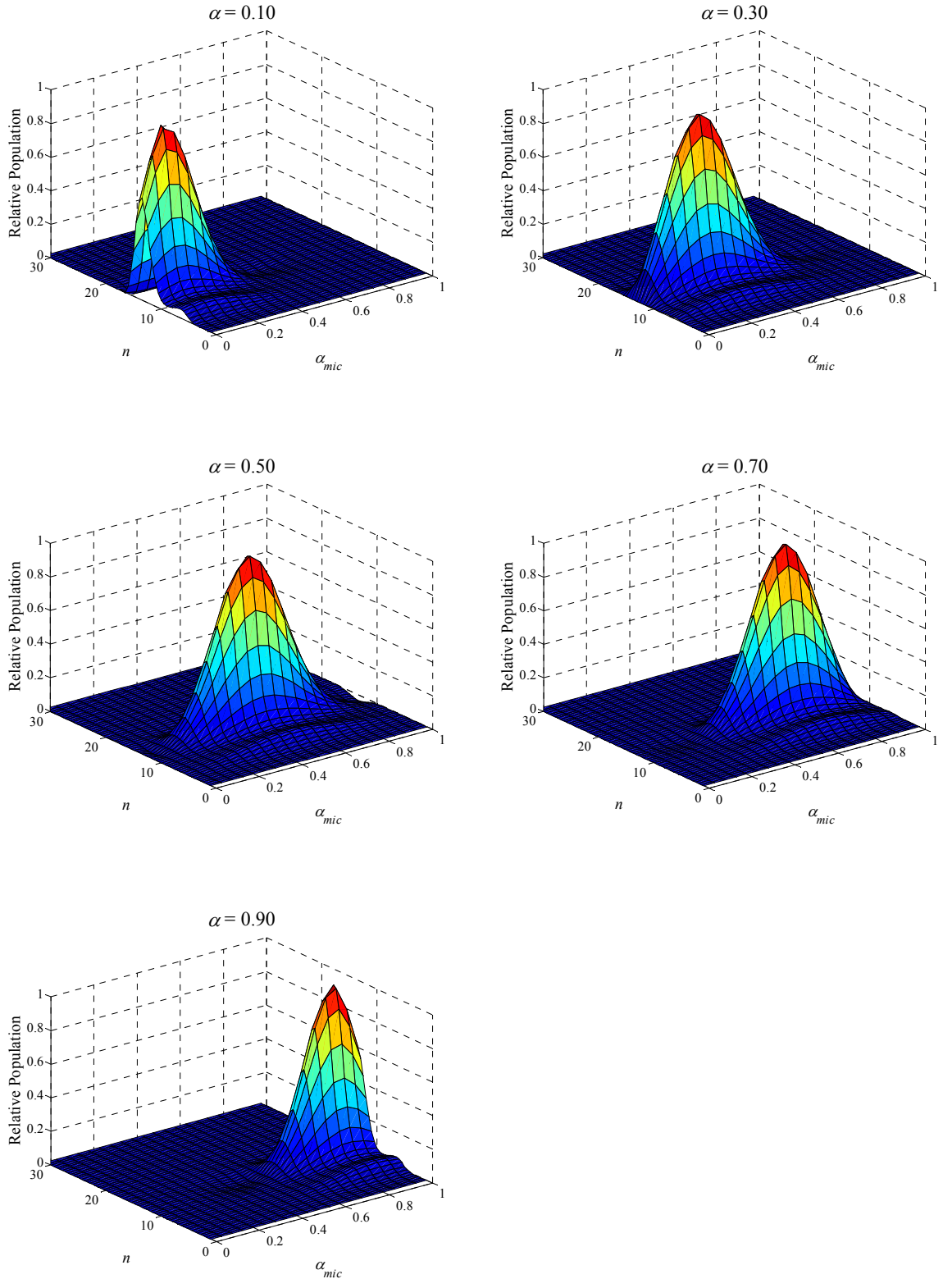

Figure 5-3: Relative micelle population distribution for the hypothetical binary mixture 1 consisting of two identical 7-carbon fluorocarbon-based nonionic surfactants having a head area of 60 Å^2.

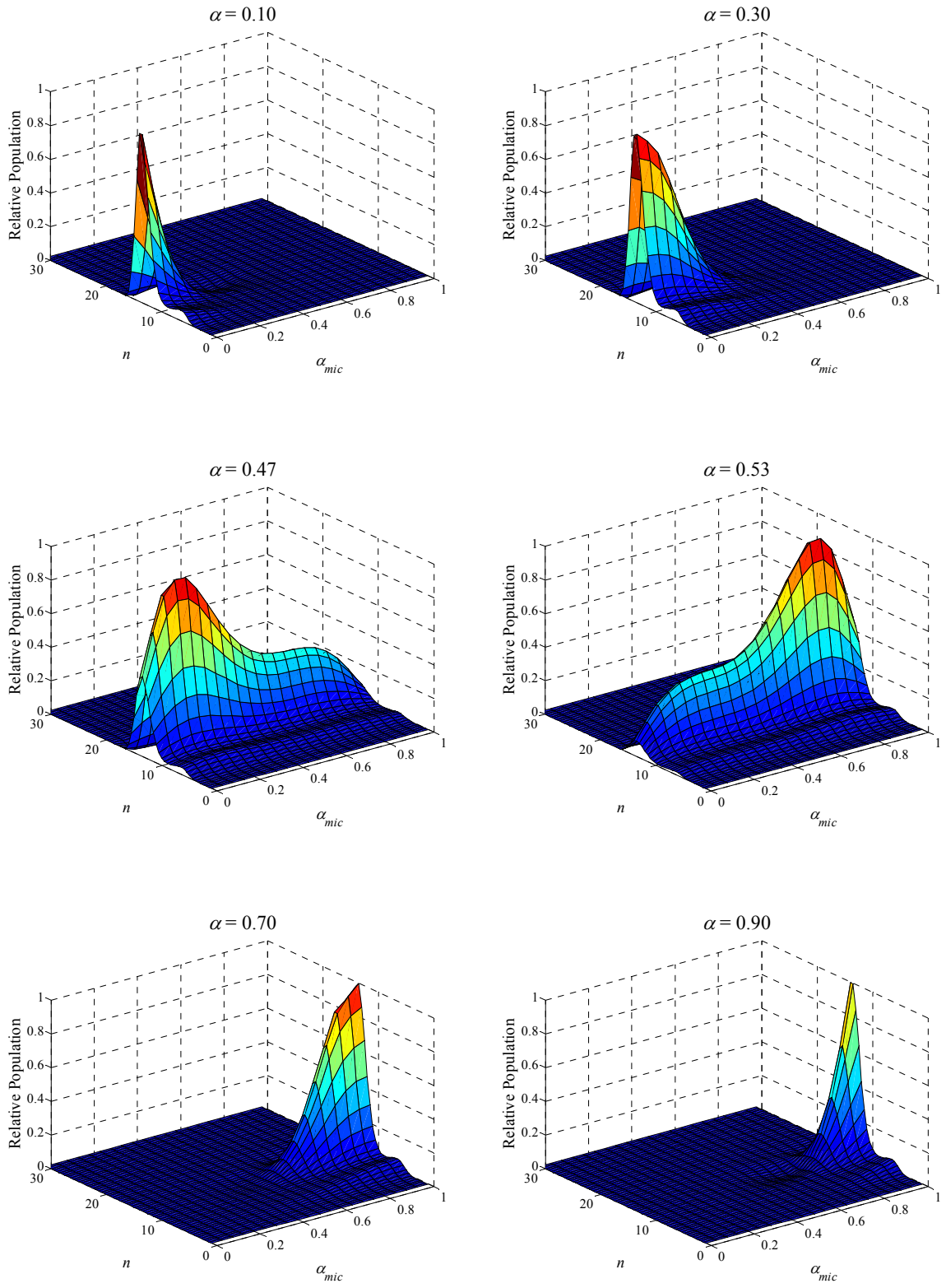

Figure 5-4: Relative micelle population distribution for the hypothetical binary mixture 2 consisting of two identical 7-carbon fluorocarbon-based nonionic surfactants having a head area of 60 Å^2, and a hypothetical enthalpy of mixing given by Eq. (5-3) with A_{mix} = 7.16 cal/cm^3.

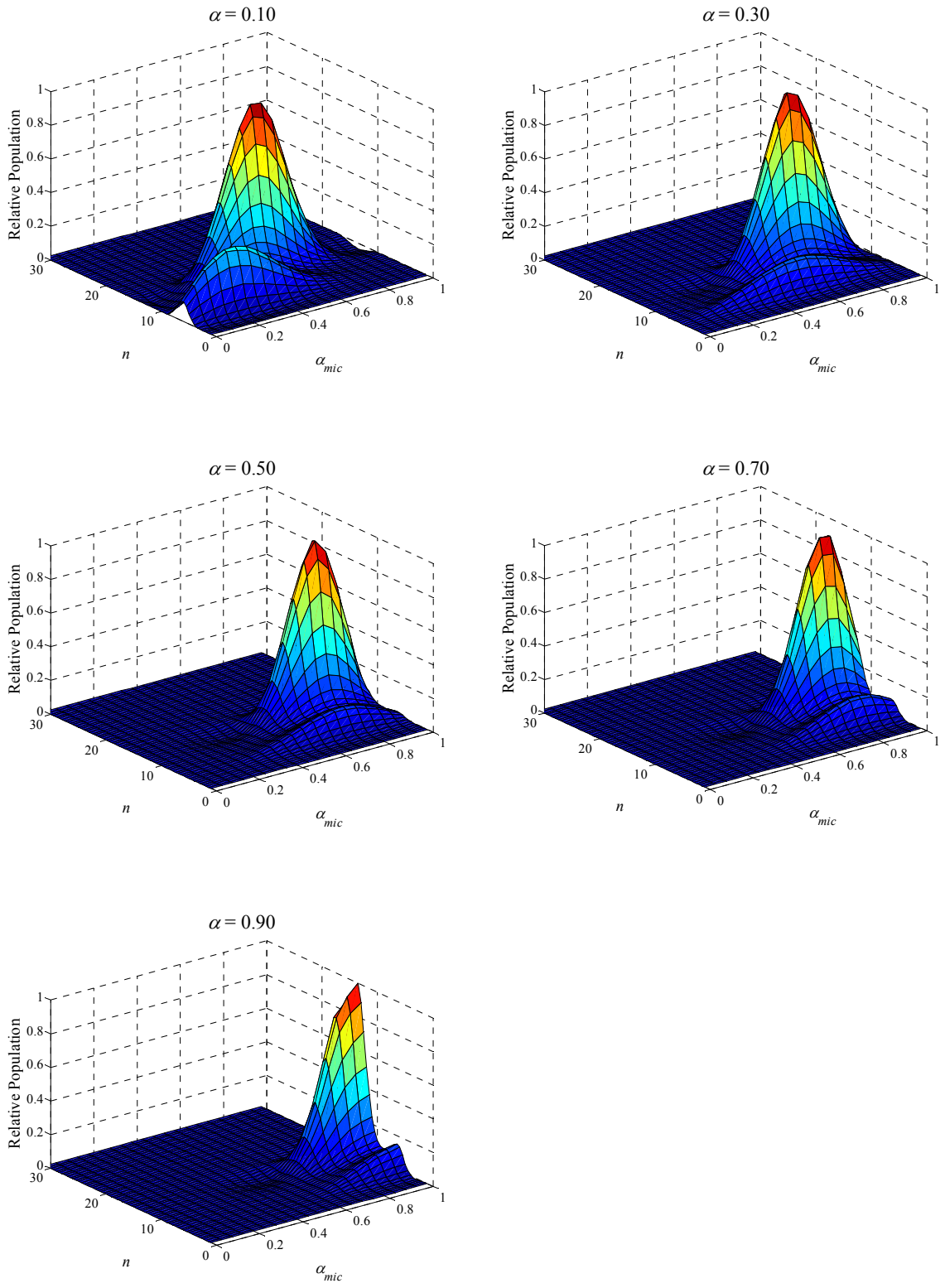

Figure 5-5: Relative micelle population distribution for the hypothetical binary mixture 3 consisting of two 7-carbon fluorocarbon-based surfactants with a hypothetical enthalpy of mixing given by Eq. (5-3) with A_{mix} = 7.16 cal/cm^3. One of the surfactants has a sulfonate head and the other has an uncharged head with a head area of 60 Å^2. Note that α and α_{mic} correspond to the composition of the nonionic surfactant.

The micelle population distribution for mixture 1 is presented in Figure 5-3. Figure 5-3 shows that as the solution composition increases, the peak of the micelle population distribution moves along the micelle composition axis, such that the composition of the micelle with the highest population, $\alpha_{mic,peak}$, is equal to the solution composition, α (this will be quantified more clearly in Figure 5-9). This follows because for this particular hypothetical binary surfactant mixture, both surfactants have identical tendencies to micellize. In addition, the micelle population distribution remains unimodal for the entire solution composition range. This follows because there are no antagonistic interactions between the two surfactants considered. As a result, the entropic contribution to mixing dominates, and there is no enthalpic driving force to form two types of micelles.

By artificially imposing a positive enthalpy of mixing on binary mixture 1, the micelle population distribution for binary mixture 2, shown in Figure 5-4, is very different from that corresponding to binary mixture 1, shown in Figure 5-3. Indeed, unlike the micelle population distribution in Figure 5-3, the micelle population distribution in Figure 5-4 shows bimodality at α = 0.5. This follows because when the micelle composition approaches 0.5, from a free-energy viewpoint, it is beneficial to form two types of micelles: one rich in surfactant 1 and the other rich in surfactant 2, instead of forming a single type of a well-mixed micelle which would result in an increased enthalpy of mixing, and hence, in a larger free energy of micellization. Note that the peaks associated with the bimodal micelle population distribution shown in Figure 5-4 are not very sharp. This indicates that the chosen magnitude of the enthalpy of mixing is quite weak. In Figure 5-6, g_{mix} for mixture 2 is plotted as a function of the volume fraction of one of the surfactants. The red curve corresponds to A_{mix} = 7.16 cal/cm^3, as discussed in Section 5.2.2. The difference between the local maximum and the local minima for the red curve is only 0.03 kT,

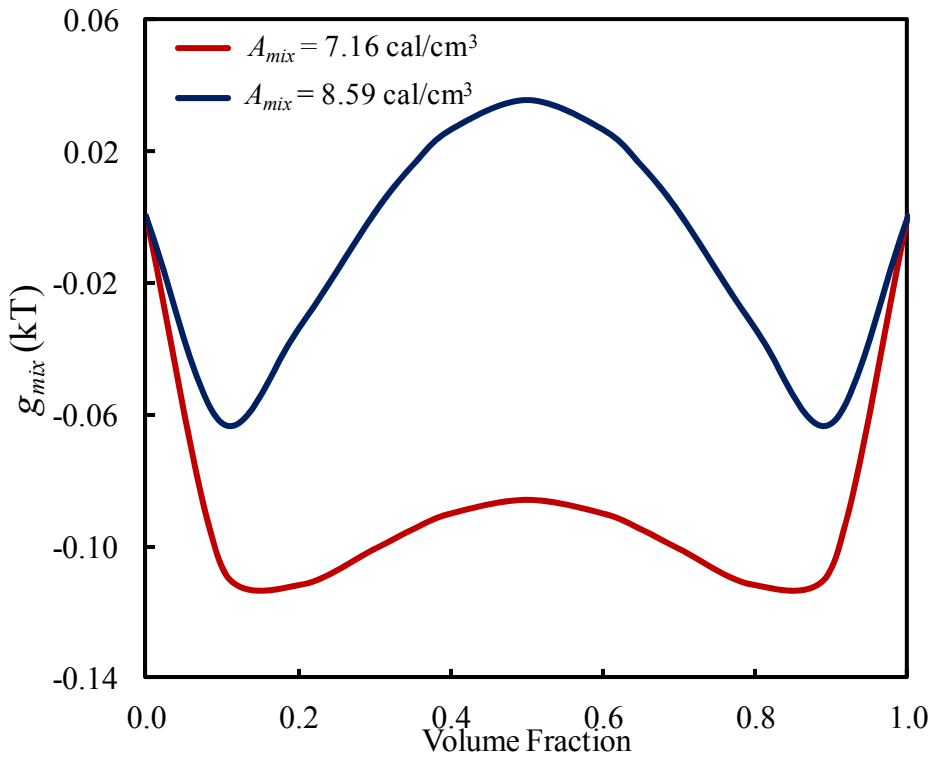

Figure 5-6: Variation of the free energy of mixing of a binary mixture of 7-carbon fluorocarbon-based nonionic surfactants with an enthalpy of mixing given by Eq. (5-3), for different values of A_{mix}.

which indicates that the two minima are quite shallow. Upon increasing A_{mix} by 20% to 8.59 cal/cm^3, which is close to the maximum value of A_{mix} reported in Section 5.2.2, the difference between the local maximum and the local minima for the dark blue curve increases by more than a factor of two, which indicates an increase in the depth of the minima.

The effect of increasing A_{mix} on the micelle population distribution formed by the hypothetical binary mixture 2 is shown in Figure 5-7. Both plots in Figure 5-7 correspond to a solution composition of 0.5. Figure 5-7 clearly shows that an increase in A_{mix} results in: (i) a narrowing of the peaks in the micelle population distribution and (ii) an increase in the difference between the micelle compositions corresponding to the two peaks of the micelle population distribution. This is a direct consequence of the change in g_{mix} due to the change in A_{mix}.

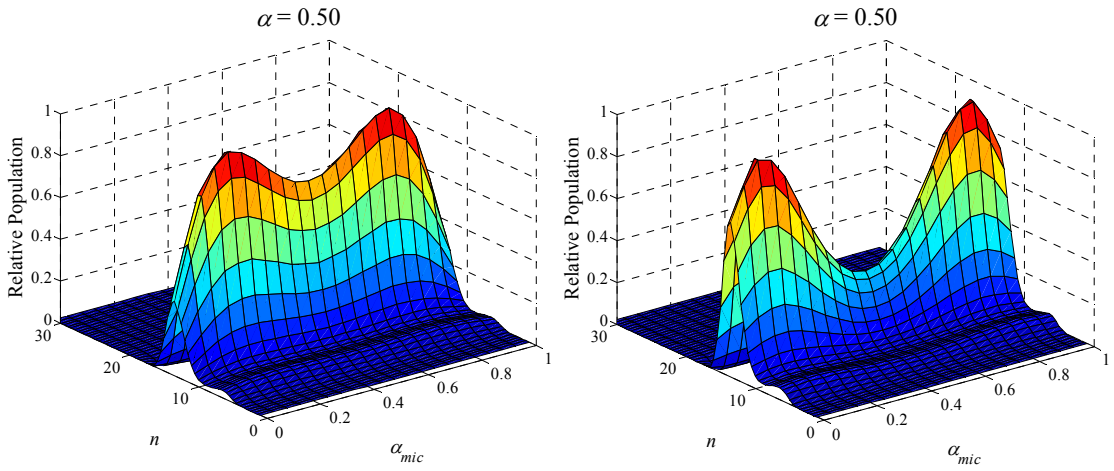

Figure 5-7: Relative micelle population distribution for the hypothetical binary mixture consisting of two identical 7-carbon fluorocarbon-based nonionic surfactants having a head area of 60 Å^2, and a hypothetical enthalpy of mixing given by Eq. (5-3). The plot on the left corresponds to A_{mix} = 7.16 cal/cm^3 and the plot on the right corresponds to A_{mix} = 8.19 cal/cm^3.

The micelle population distribution of the final hypothetical binary mixture 3 is shown in Figure 5-5. Recall that, in mixture 3, one of the surfactants has a charged sulfonate head and the other has an uncharged head with a head area of 60 Å^2. In addition, mixture 3 has a hypothetical enthalpy of mixing given by Eq. (5-3) with A_{mix} = 7.16 cal/cm^3. Figure 5-5 shows that, similar to Figure 5-3, as the solution composition increases, the peak of the micelle population distribution moves along the micelle composition axis, and remains unimodal over the entire solution composition range, in spite of the positive enthalpy of mixing between the surfactant tails. This follows because although the surfactant tails do not like to mix with each other, the ionic surfactant heads prefer to mix with the nonionic surfactant heads to reduce the net charge on the micelle in order to reduce the charging free energy discussed in Section 2.3. In this case, the synergy resulting from mixing of the surfactant heads is greater than the antagonism resulting from mixing of the surfactant tails. This, in turn, produces a micelle population distribution that remains unimodal over the entire solution composition range. Another important aspect of Figure 5-5 is that, unlike Figure 5-3, the micelle composition corresponding to the peak of the micelle

population distribution does not coincide with the solution composition (this is more clearly shown in Figure 5-9). This follows because the two surfactants comprising binary mixture 3 are not identical, as was the case for the two surfactants comprising binary mixture 1. In the case of binary mixture 3, the nonionic surfactant has a higher tendency to micellize than the ionic surfactant. Therefore, the resulting micelle typically contains more of the nonionic surfactant, while the monomers contain more of the ionic surfactant. Note that, in Figure 5-5, α and α_{mic} correspond to the composition of the nonionic surfactant.

The predicted CMCs as a function of α for the three hypothetical mixtures considered here are shown in Figure 5-8. Figure 5-8 shows that the CMC of binary mixture 1 (the red circles) remains constant throughout the solution composition range. This follows because the two surfactants comprising the binary mixture have the same tendency to micellize. For mixture 2 (the blue circles), the CMC exhibits a maximum at $\alpha = 0.5$. This is a direct result of the positive

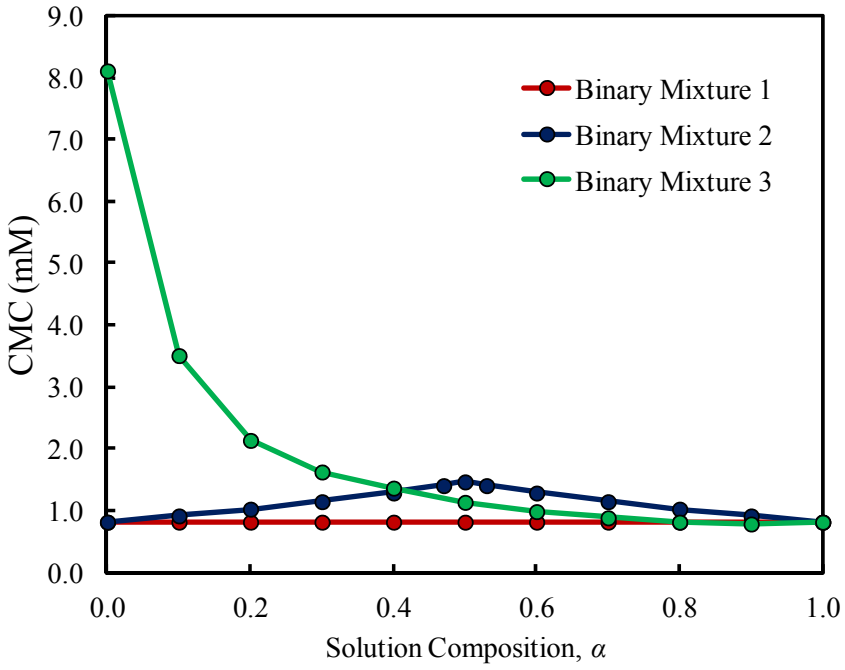

Figure 5-8: Predicted mixture CMCs as a function of solution composition, α, for the three hypothetical binary mixtures considered here.

enthalpy of mixing associated with binary mixture 2. The CMC shows a maximum at α = 0.5 because the two surfactants are identical and the enthalpy of mixing in Eq. (5-3) is symmetric This behavior is absent in the case of mixture 3 (the green circles) because the antagonistic effect of the enthalpy of mixing is overcome by the synergism in the head region due to mixing of the ionic and the nonionic surfactant heads. Note that the CMC of the ionic surfactant (corresponding to α = 0.0 in the green curve in Figure 5-8) is higher than that of the nonionic surfactant (at α = 1.0) due to the additional electrostatic free-energy contribution to the micellization free energy in the case of ionic surfactants (see Section 2.3). Figure 5-9 shows the variation of the composition of the micelle with the highest population, referred to as the optimal micelle composition, $\alpha_{mic,peak}$, as a function of the solution composition, α, for the three hypothetical binary surfactant mixtures considered here. Note that the various points in Figure 5-9 do not vary smoothly because the micelle population was calculated for micelle

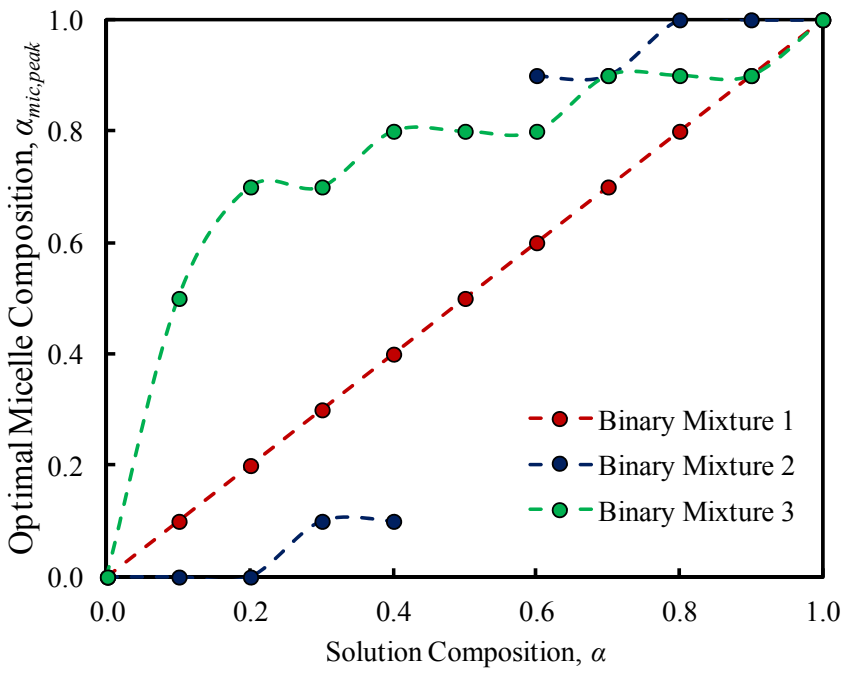

Figure 5-9: Variation of the optimal micelle composition, $\alpha_{mic,peak}$, as a function of the solution composition, α, for the three hypothetical binary mixtures considered here. Note that the various dashed curves are drawn to guide the eye.

compositions at intervals of 0.1. To obtain a smoother plot, the micelle population distribution has to be calculated for micelle compositions at intervals which are smaller than 0.1.

As expected, the optimal micelle composition for binary mixture 1 perfectly tracks the solution composition, as was shown in Figure 5-3, as well as by the red circles in Figure 5-9. For mixture 2, Figure 5-9 only shows the composition of the optimal micelle in the unimodal region of the micelle population distribution. As a result, no points are shown for $0.4 \leq \alpha \leq 0.6$, for which the micelle population distribution is bimodal (see Figure 5-4). For mixture 2, the optimal micelle composition remains smaller than, or equal to, 0.1 for $0 \leq \alpha \leq 0.4$. When $\alpha \geq 0.6$, the optimal micelle composition increases dramatically to values higher than, or equal to, 0.9. This results from the positive enthalpy of mixing between the surfactant tails which discourages mixing of the tails. For mixture 3, the optimal micelle composition varies smoothly between $\alpha = 0$ and $\alpha = 1$ (see the green circles in Figure 5-9). Note that the green circles in Figure 5-9 consistently lie above the red circles. This indicates that, for all α values, the micelles are richer in the nonionic surfactant, while the monomers are richer in the ionic surfactant. This is because the nonionic surfactant has a higher tendency to micellize due to its lower CMC (see Figure 5-8).

5.4 Model Predictions for Mixtures of Fluorocarbon-Based and Hydrocarbon-Based Surfactants

The results in Section 5.3 clearly demonstrate that the MT framework presented in this chapter is capable of predicting the coexistence of two types of micelles in solution. Next, to demonstrate the applicability of this framework to mixtures of fluorocarbon-based and hydrocarbon-based surfactants, in this section, the MT model predictions of CMCs, micelle compositions, and micelle population distributions are compared with available experimental data for various mixtures of fluorocarbon-based and hydrocarbon-based surfactants.

5.4.1 Binary Mixture of Lithium Perfluorooctyl Sulfonate (LiPFOS) and Octyl Glucoside (OG)

Figure 5-10 shows the micelle population distribution for the binary mixture of lithium perfluorooctyl sulfonate (LiPFOS) and octyl glucoside (OG) at various solution compositions. Note that all the micelle population distribution plots shown in this section correspond to A_{mix} = 7.16 cal/cm^3, unless otherwise specified (see Section 5.2.2). Figure 5-10 shows that the micelle population distribution remains unimodal over the entire solution composition range. This indicates that the synergism resulting from mixing of the ionic sulfonate heads and the nonionic glucoside heads is greater than the antagonism resulting from the positive enthalpy of mixing between the heptyl fluorocarbon tails (note that for an ionic surfactant, the carbon connected to the surfactant head is considered to be part of the surfactant head[1]) and the octyl hydrocarbon tails [see Eq. (5-3)].

Figures 5-11 and 5-12 compare the predicted CMCs and the predicted micelle compositions for the binary mixture of LiPFOS and OG with the available experimental values, respectively.[138] The MT framework accurately predicts the qualitative trends for both the mixture CMC and the micelle composition. Quantitatively, the predicted CMCs are within a factor of 1.5 of the experimental CMCs, which is viewed as excellent agreement, because the CMC has an exponential dependence on the free energy of micellization, g_{mic}, which is the quantity that is actually modeled in the MT framework. As a result, a small error in g_{mic} can result in a significant error in the CMC. This important point has been emphasized in Section 4.5.

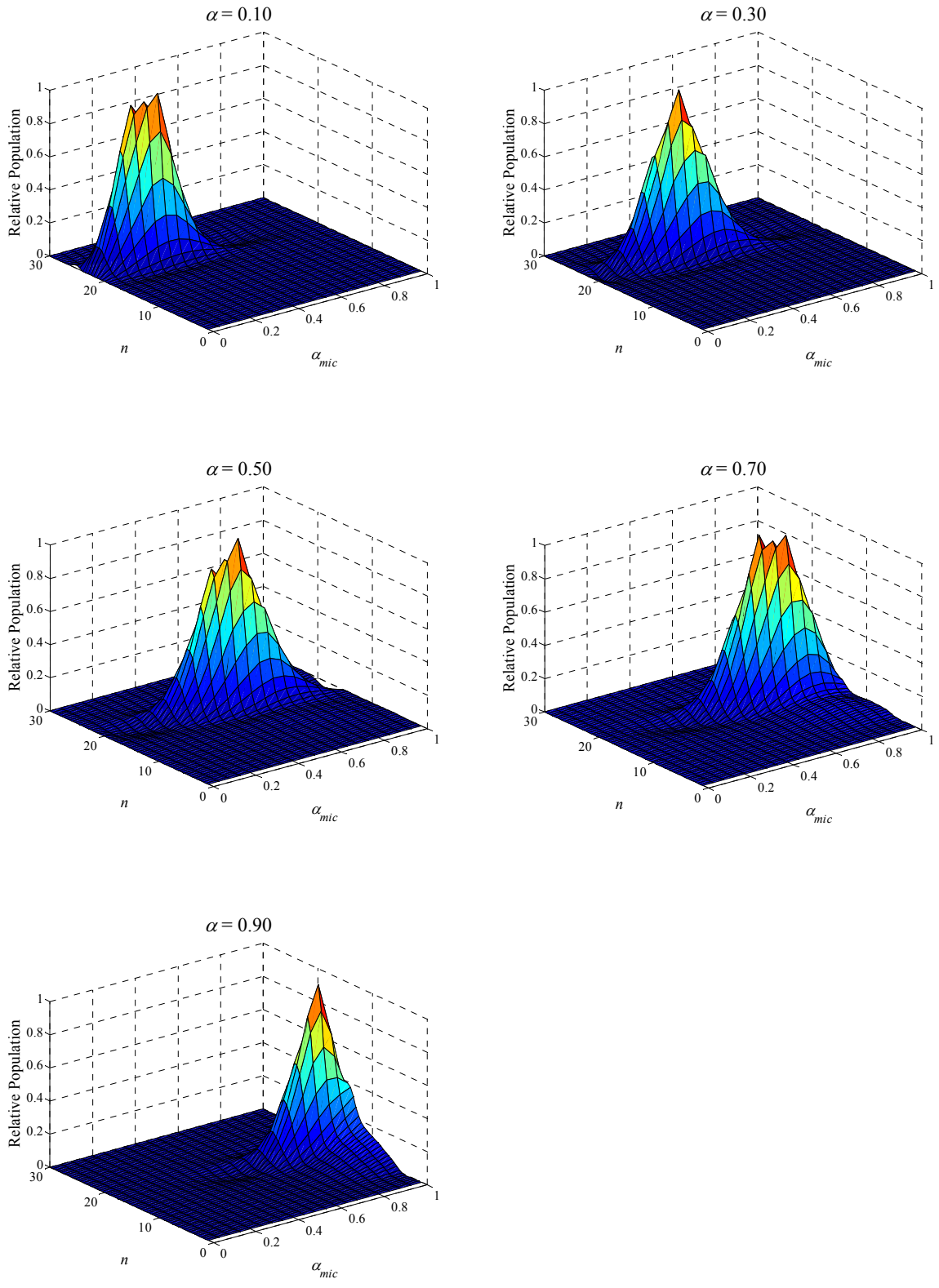

Figure 5-10: Relative micelle population distribution for the binary mixture of lithium perfluorooctyl sulfonate (LiPFOS) and octyl glucoside (OG). Note that the micelle composition, α_{mic}, and the solution composition, α, correspond to the composition of LiPFOS.

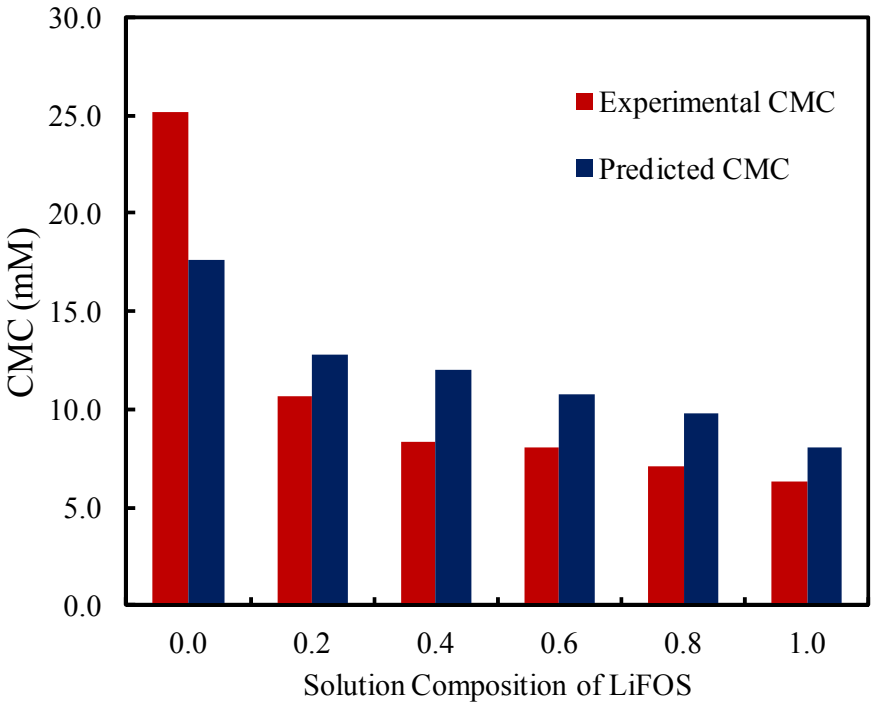

Figure 5-11: Predicted and experimental CMCs vs. solution composition for a binary mixture of lithium perfluorooctyl sulfonate (LiPFOS) and octyl glucoside (OG).

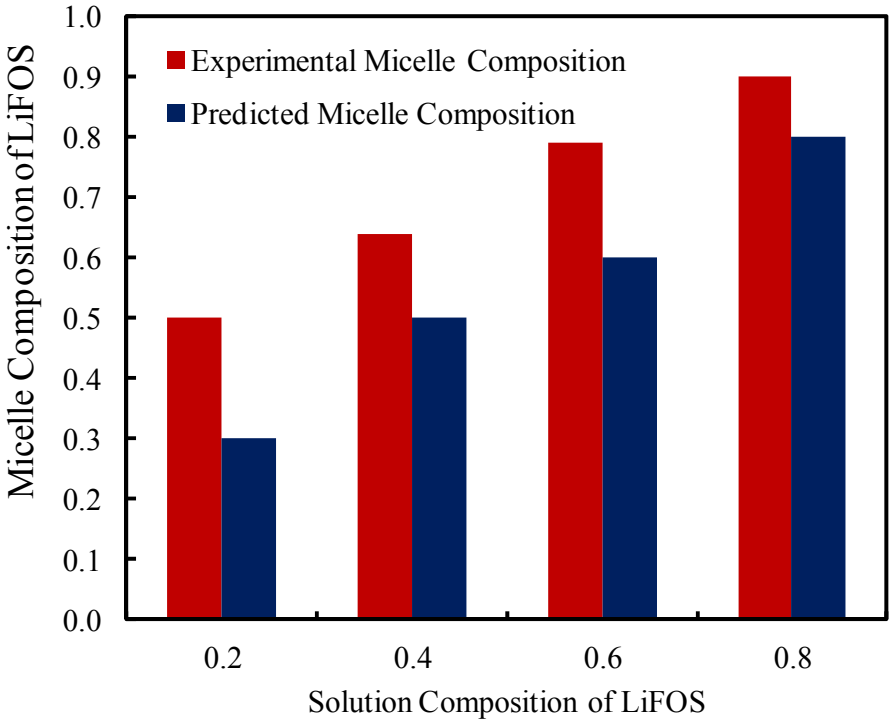

Figure 5-12: Predicted and experimental micelle compositions vs. solution composition for a binary mixture of lithium perfluorooctyl sulfonate (LiPFOS) and octyl glucoside (OG).

The MT framework predictions of the composition of LiPFOS in the micelle are systematically lower than the experimental values (see Figure 5-12). To understand this trend, consider Figure 5-11 which shows that the CMC of LiPFOS (at $\alpha = 1.0$) is lower than that of OG (at $\alpha = 0.0$). This indicates that LiPFOS has a higher tendency to micellize relative to that of OG. As a result, the micelles are richer in LiPFOS, while the monomers are richer in OG. This behavior is reflected in both the experimental and the predicted values of the optimal micelle composition of LiPFOS, which is always higher than, or equal to, the solution composition of LiPFOS (see Figure 5-12). In Figure 5-11, the MT framework underpredicts the CMC of OG (at $\alpha = 0.0$), while it overpredicts the CMC of LiPFOS (at $\alpha = 1.0$). As a result, the difference between the predicted CMCs of OG and LiPFOS is lower than the difference between the experimental CMCs of OG and LiPFOS. Accordingly, the tendency of LiPFOS to micellize relative to that of OG predicted by the MT framework is not as high as that based on the experimental data. This is the reason behind the systematic underprediction of the micelle composition of LiPFOS shown in Figure 5-12.

5.4.2 Binary Mixture of Sodium Perfluorooctanoate (SPFO) and Sodium Decyl Sulfate (SDeS)

Figure 5-13 shows the micelle population distribution for the binary mixture of sodium perfluorooctanoate (SPFO) and sodium decyl sulfate (SDeS) at various solution compositions, α. Figure 5-13 shows that the micelle population distribution remains unimodal over the entire solution composition range, but becomes very broad for $0.4 \leq \alpha \leq 0.5$. This indicates that the enthalpic antagonism between the surfactant tails characterized by $A_{mix} = 7.16$ cal/cm^3 is not sufficiently strong to lead to the formation of two distinct types of micelles. This conclusion agrees with the conclusions reached by Shinoda and Nomura[122] and by Kamogawa and

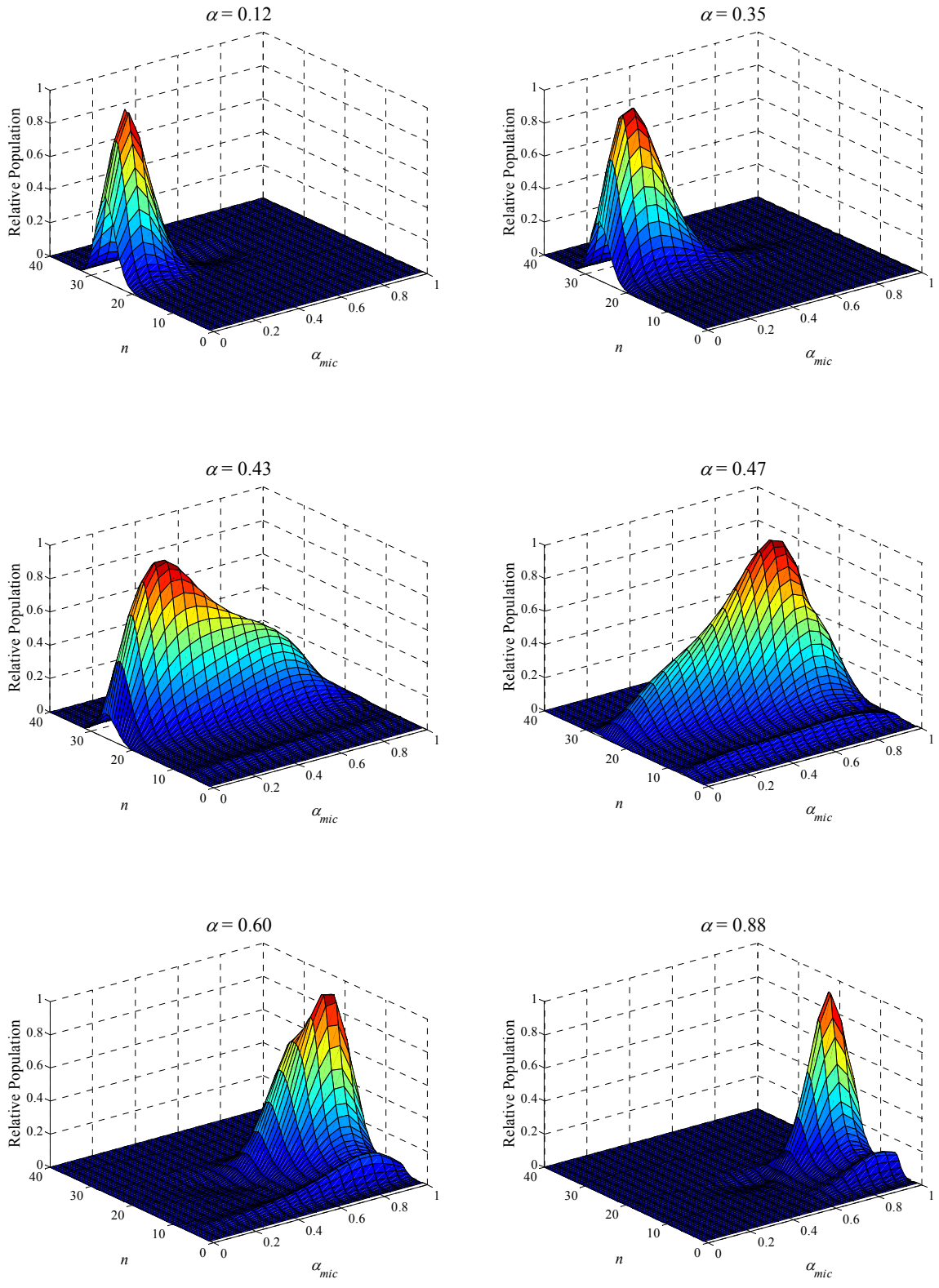

Figure 5-13: Relative micelle population distribution for the binary mixture of sodium perfluorooctanoate (SPFO) and sodium decyl sulfate (SDeS). Note that the micelle composition, α_{mic}, and the solution composition, α, correspond to the composition of SPFO.

Tajima.[123] However, it does not agree with the conclusions reached by Mukerjee and Yang[120] and by Aratono et al.[121] who concluded that this binary surfactant mixture resulted in the coexistence of two types of micelles. It is interesting to note that by increasing the enthalpic interaction parameter A_{mix} by 20 %, from 7.16 cal/cm^3 to 8.59 cal/cm^3, which is close to the maximum value of A_{mix} observed for mixtures of hydrocarbons and fluorocarbons, as described in Section 5.2.2, two peaks clearly emerge in the micelle population distribution, as illustrated in Figure 5-14, and as suggested by Aratono et al.[121]

Figures 5-14 and 5-7 indicate that the predicted micelle population distribution strongly depends on the magnitude of the enthalpic interaction parameter used. In the predictions shown, the value of A_{mix} used is an average calculated based on the available experimental data for mixtures of fluoroalkanes and alkanes of various lengths and measured at various temperatures, as discussed in Section 5.2.2. Based on the results in Figure 5-14, it is clear that the ability of the MT framework to predict micelle population distributions will benefit greatly from a more accurate estimation of the enthalpic interaction parameter, A_{mix}.

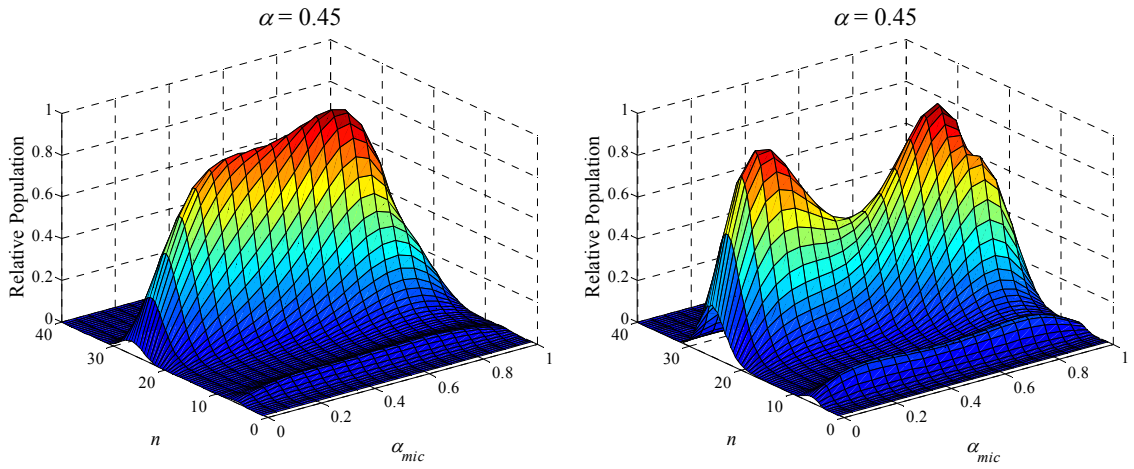

Figure 5-14: Relative micelle population distribution for the binary mixture of sodium perfluorooctanoate (SPFO) and sodium decyl sulfate (SDeS). The plot on the left corresponds to A_{mix} = 7.16 cal/cm^3 and the plot on the right corresponds to A_{mix} = 8.59 cal/cm^3

Figure 5-15 compares the predicted and the experimental CMCs as a function of the solution composition of SPFO, α_{SPFO}, for the binary mixture of SPFO and SDeS.[121] The MT framework accurately predicts the qualitative trends in the mixture CMC. Quantitatively, the predicted CMCs are within a factor of 1.3 of the experimental CMCs, which is viewed as excellent agreement, as discussed in Sections 4.5 and 5.4.1. The MT framework predicts a maximum in the CMC at α_{SPFO} = 0.40, while the experimental maximum is observed at α_{SPFO} = 0.50. Note that the experimental CMCs of SPFO (31.2 mM) and SDeS (31.3 mM) are very close to each other, which results in the experimentally observed maximum at 0.50. On the other hand, the MT framework predicts that the CMC of SPFO (25.7 mM) is lower than that of SDeS (32.8 mM). As a result, the predicted maximum in the CMC occurs at a solution composition that is richer in SPFO, rather than at an equimolar solution composition.

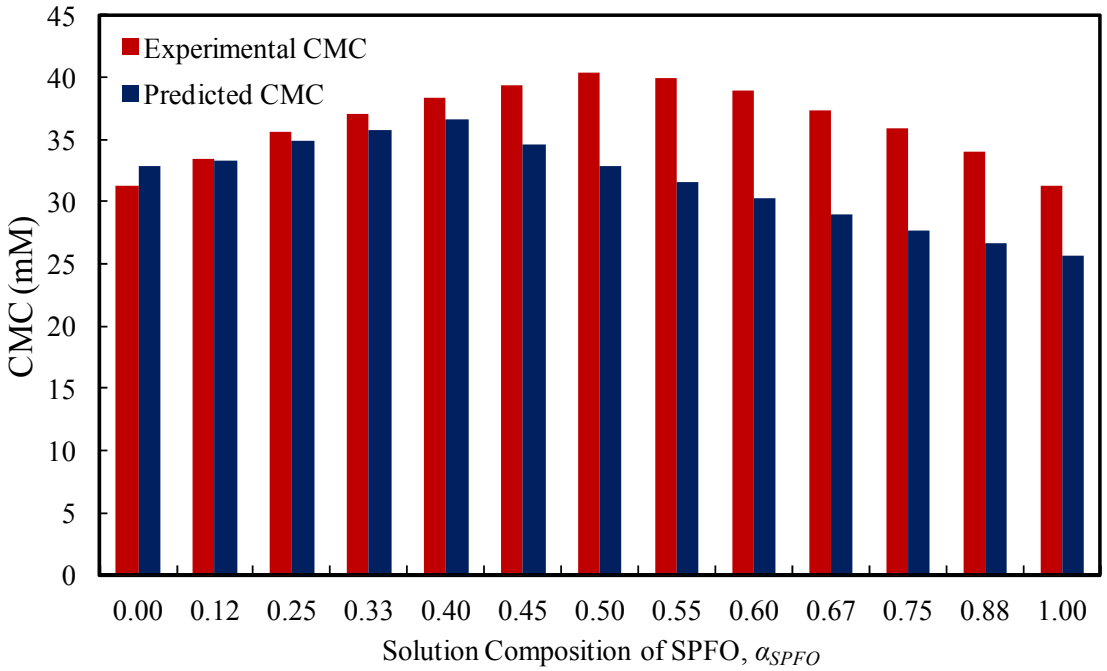

Figure 5-15: Predicted and experimental CMCs vs. solution composition of SPFO, α_{SPFO}, for a binary mixture of sodium perfluorooctanoate (SPFO) and sodium decyl sulfate (SDeS).

5.4.3 Binary Mixture of Sodium Perfluorooctanoate (SPFO) and Sodium Dodecyl Sulfate (SDS)

Figure 5-16 shows the micelle population distribution for the binary mixture of sodium perfluorooctanoate (SPFO) and sodium dodecyl sulfate (SDS) for various solution compositions, α. The micelle population distribution in Figure 5-16 shows some indication of bimodality at α = 0.845. Upon increasing the value of A_{mix} by 20%, from 7.16 cal/cm^3 to 8.59 cal/cm^3, the micelle population distribution does indeed become bimodal for $0.83 \leq \alpha \leq 0.89$. This again indicates that A_{mix} = 7.16 cal/cm^3 is not sufficiently high to clearly observe two distinct types of micelles, as was the case for the binary mixture of SPFO and SDeS discussed in Section 5.4.2

Figure 5-17 compares the predicted and the experimental CMCs as a function of α_{SPFO} for the binary mixture of SPFO and SDS.[139] Quantitatively, the predicted CMCs are within a factor of 2.0 of the experimental CMCs which is viewed as very good agreement, as explained in Sections 4.5 and 5.4.1. However, Figure 5-17 shows that qualitatively, the MT framework does not predict the maximum observed in the experimental CMC data at α_{SPFO} = 0.91. Instead, the CMC is predicted to plateau at $0.84 \leq \alpha \leq 0.96$, and then increase again. The maximum in the CMC observed by Sugihara et al.[139] is absent in the mixture CMCs calculated by Kamrath and Franses[140] using the differential conductance data of Mukerjee and Yang.[120] However, the absence of the maximum may be attributed to fewer number of solution compositions at which the CMC was calculated. Note that although the MT framework predicts bimodality in the micelle population distribution, the predicted mixture CMC does not show a maximum even when A_{mix} is increased by 20%, from 7.16 cal/cm^3 to 8.59 cal/cm^3. This indicates that A_{mix} would have to be increased significantly to predict a maximum in the CMC for this mixture. This is probably because SDS has a CMC that is much lower than that of SPFO due to a lower transfer

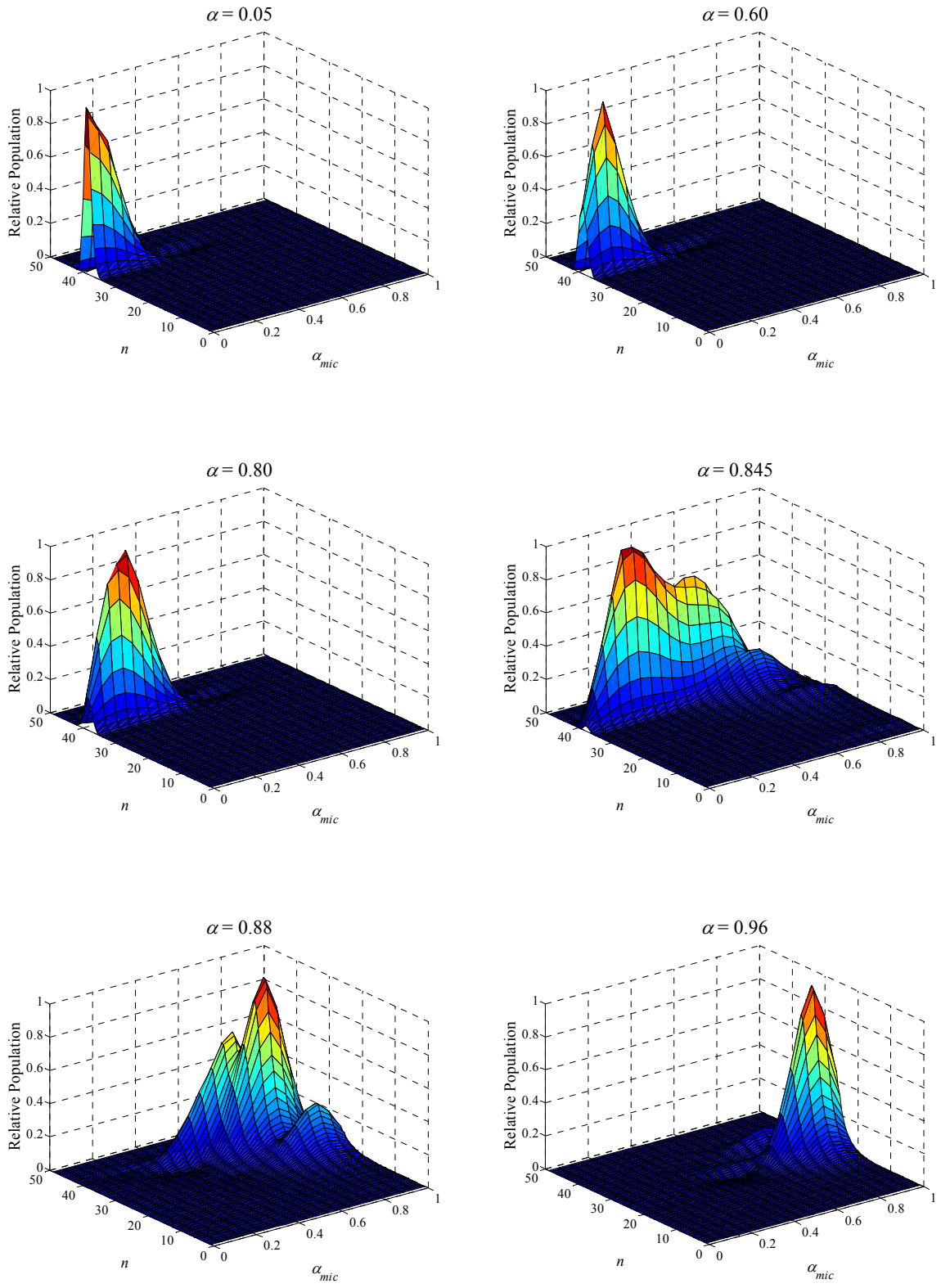

Figure 5-16: Relative micelle population distribution for the binary mixture of sodium perfluorooctanoate (SPFO) and sodium dodecyl sulfate (SDS). Note that the micelle composition, α_{mic}, and the solution composition, α, correspond to the composition of SPFO.

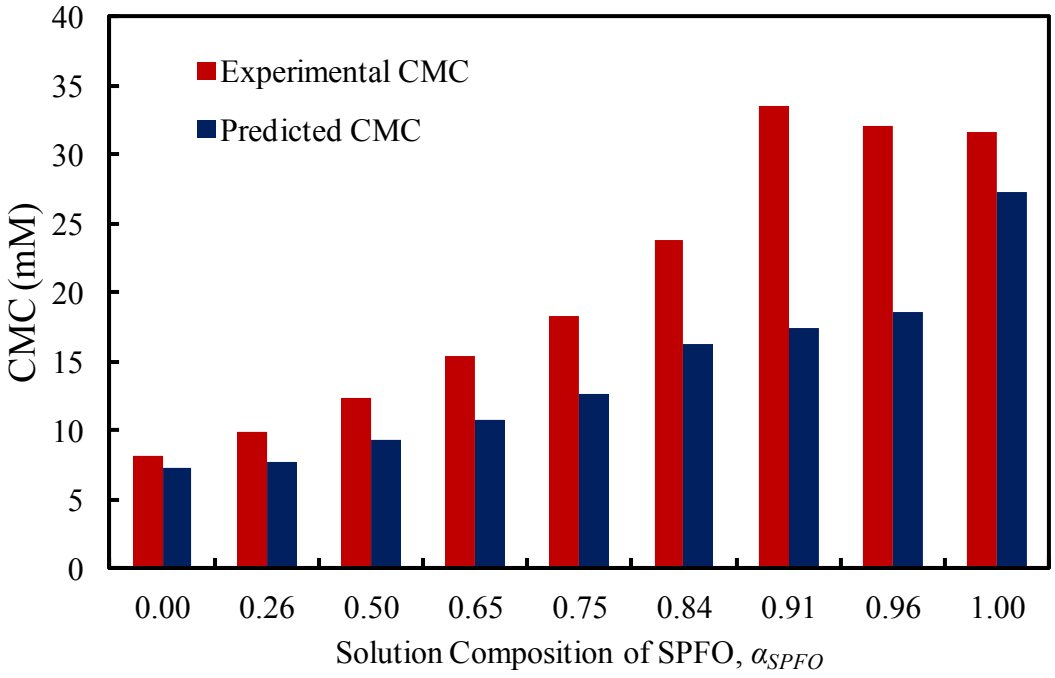

Figure 5-17: Predicted and experimental CMCs vs. solution composition of SPFO, α_{SPFO}, for a binary mixture of sodium perfluorooctanoate (SPFO) and sodium dodecyl sulfate (SDS).

free energy [refer to Eqs. (2-8) and (2-10)]. Upon adding a small amount of SDS to SPFO, while the mixing free energy goes up, the transfer free energy goes down thereby reducing the CMC.

5.4.4 Binary Mixture of Sodium Perfluorooctanoate (SPFO) and Sodium Dodecanoate (SDO)

Figure 5-18 shows the micelle population distribution for the binary mixture of sodium perfluorooctanoate (SPFO) and sodium dodecanoate (SDO) at various solution compositions, α. The micelle population distribution in Figure 5-18 remains unimodal over the entire solution composition range, but becomes very broad at α = 0.70. This indicates that the antagonism between the surfactant tails is not sufficiently high to result in the coexistence of two types of micelles. This conclusion agrees with the conclusions reached by Pedone et al.[141] and Caponetti et al.[142] that the binary mixture of SPFO and SDO does not demix. However, it does not agree

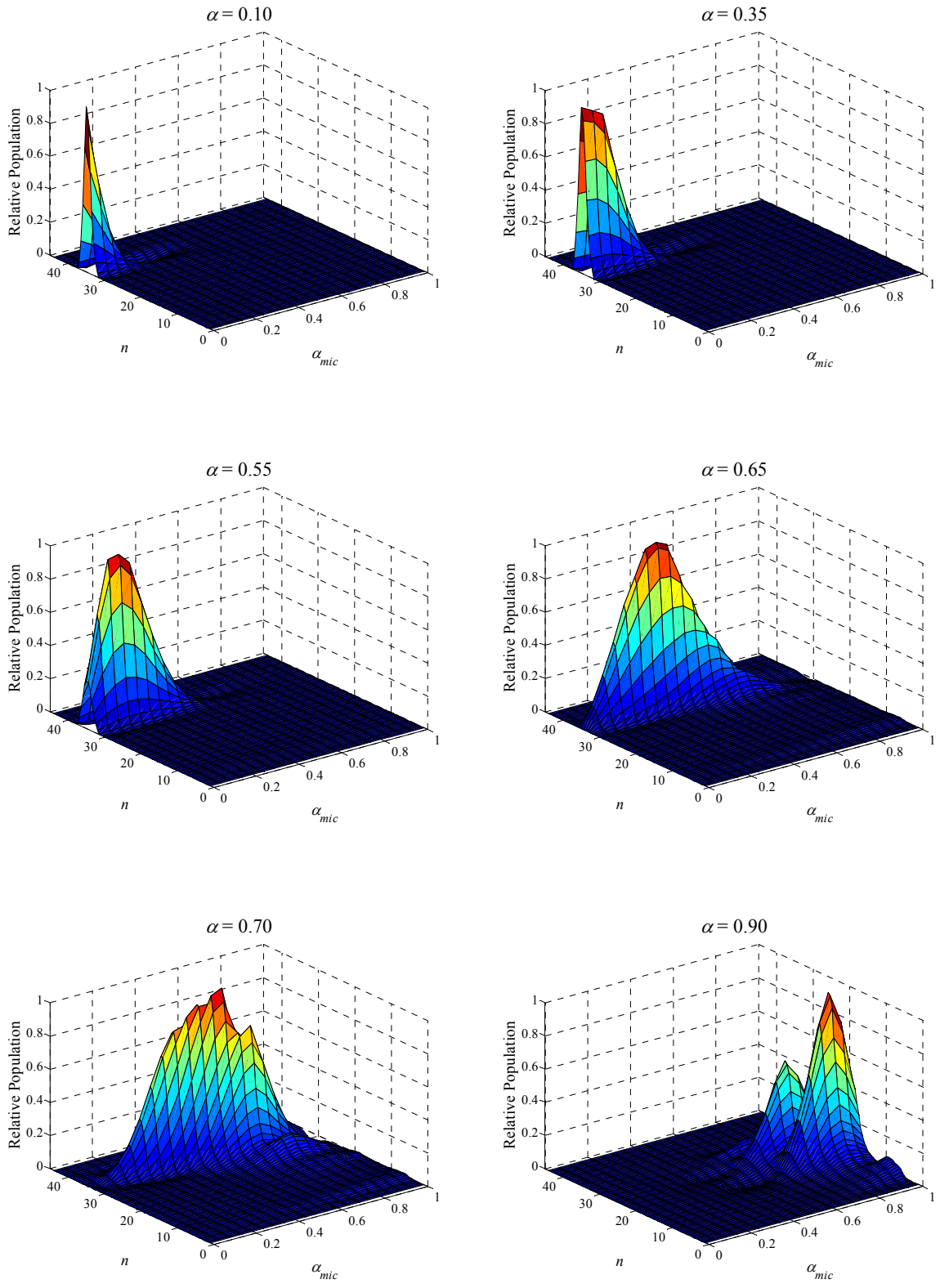

Figure 5-18: Relative micelle population distribution for the binary mixture of sodium perfluorooctanoate (SPFO) and sodium dodecanoate (SDO). Note that the micelle composition, α_{mic}, and the solution composition, α, correspond to the composition of SPFO.

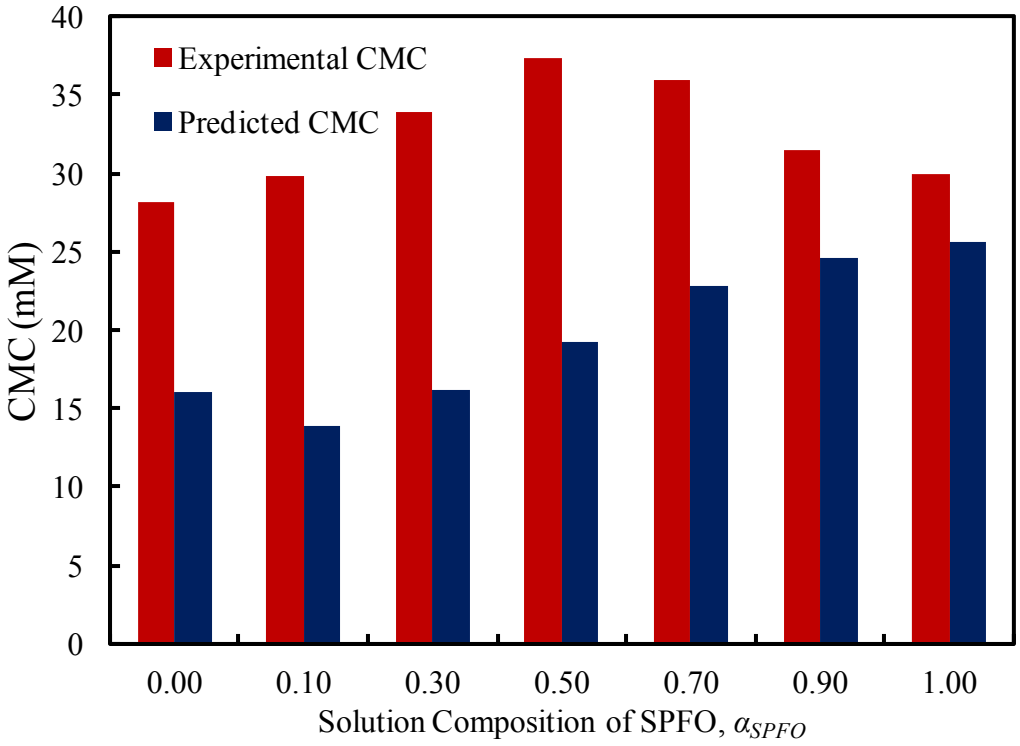

Figure 5-19: Predicted and experimental CMCs vs. solution composition of SPFO, α_{SPFO}, for a binary mixture of sodium perfluorooctanoate (SPFO) and sodium dodecanoate (SDO).

with the conclusions reached by Mukerjee and Yang,[120] who claimed that the binary mixture of SPFO and SDO results in the coexistence of two types of micelles. Figure 5-19 compares the predicted and the experimental CMCs[143] for the binary mixture of SPFO and SDO. Quantitatively, the predicted CMCs are within a factor of 2.2 of the experimental CMCs, which is viewed as very good agreement, as discussed in Sections 4.5 and 5.4.1. However, qualitatively, the MT framework does not predict the maximum in the CMC observed in the experimental data at $\alpha_{SPFO} = 0.5$ (see Figure 5-19). The primary reason behind the absence of the maximum in the predicted CMC is the underprediction of the CMC of SDO by the MT framework.[143] Based on the experimental CMC data shown in Figure 5-19, SPFO and SDO have similar CMCs, and therefore, exhibit similar tendencies to micellize. However, in the context of the MT framework predictions, SDO exhibits a higher tendency to micellize relative to that of

SPFO. To better understand this observation, consider the experimental and predicted CMC values for a set of fluorocarbon-based and hydrocarbon-based surfactants shown in Table 5-1. The table compares the CMCs of two carboxylate surfactants ($C_{11}H_{23}COONa$ and $C_8F_{17}COONa$) with those of analogous sulfonate surfactants ($C_{11}H_{23}SO_3Na$ and $C_8F_{17}SO_3Na$) having the same tails. The MT framework predicts that the CMCs of the carboxylate surfactants are lower than those of the corresponding sulfonate surfactants because the carboxylate head has a smaller head area than the sulfonate head (see Table 7-1). However, the experimental trends are opposite, that is, the experimental CMCs of the carboxylate surfactants are higher than those of the corresponding sulfonate surfactants. This result suggests that the carboxylate head is not accurately modeled in the MT framework. The discrepancy is more severe in the case of hydrocarbon-based carboxylate surfactants, because the difference between the experimental CMCs of $C_{11}H_{23}COONa$ (28.1 mM)[143] and $C_{11}H_{23}SO_3Na$ (17 mM)[144] is 11.1 mM, while that between $C_{11}H_{23}SO_3Na$ (17 mM)[144] and $C_{11}H_{23}SO_4Na$ (16 mM),[145] an analogous surfactant with a sulfate head, is only 1 mM. Note that although the predicted CMC of SDO is within a factor of 1.75 of the experimental value, which is viewed as very good agreement (see Sections 4.5 and 5.4.1), to accurately predict qualitative trends of surfactant mixtures, it is necessary to accurately predict the qualitative behavior of the CMCs of the individual surfactant components.

Table 5-1: Predicted and Experimental CMCs for fluorocarbon-based and hydrocarbon-based surfactants.

Name	**$C_{11}H_{23}COONa$**	**$C_{11}H_{23}SO_3Na$**		**$C_8F_{17}COONa$**	**$C_8F_{17}SO_3Na$**
Tail Type	Hydrocarbon	Hydrocarbon		Fluorocarbon	Fluorocarbon
n_{tail}	10	10		7	7
Head	$COO+CH_2$	SO_3+CH_2		$COO+CF_2$	SO_3+CF_2
Predicted CMC	16.1 mM	21.3 mM		6.6 mM	7.6 mM
Experimental CMC	28.1 mM[143]	17.0 mM[144]		11.0 mM[146]	8.0 mM[5]

The precise cause behind the discrepancy in the predicted and experimental CMCs of SDO is unclear. The nature of hydrogen bonding associated with the alkyl carboxylate can be one reason, because the hydrogen bonds formed with the sulfonate head can be different than those formed with the carboxylate heads.[147] In addition, the nature of the group connected to the carboxylic acid plays an important role in its protonation properties, which may help explain the difference in behavior of the CMCs of the hydrocarbon-based carboxylate surfactants relative to the fluorocarbon-based carboxylate surfactants.

5.5 Conclusions

In summary, in this chapter, I presented a molecular-thermodynamic framework to predict the micellization properties of mixtures of fluorocarbon-based and hydrocarbon-based surfactants. The framework includes modifications to the packing free energy, g_{pack}, as well the inclusion of an enthalpy of mixing contribution in the mixing free energy, g_{mix}, using the Regular Solution Theory. The framework presented here is able to predict the coexistence of two types of mixed micelles in solution, including the resulting micelle population distributions, CMCs, and optimal micelle compositions, which compare well with the experimental values for various binary mixtures of fluorocarbon-based and hydrocarbon-based surfactants. Prediction of the micelle population distribution is affected greatly by the value of the enthalpic interaction parameter, A_{mix}, used. As a result, the model predictions would become much more reliable if an accurate estimate of A_{mix} could be obtained. The CMCs predicted by the MT framework developed in this chapter compare well with the experimental CMCs for the binary mixtures of LiPFOS and OG and of SPFO and SDeS. On the other hand, the MT framework was unable to fully predict some aspects of the experimental mixture CMC data for the binary mixtures of

SPFO and SDS and of SPFO and SDO. Possible reasons for these results were discussed in Sections 5.4.3 and 5.4.4.

The work presented in Chapters 3, 4, and 5 can be extended in a number of interesting directions to further advance our understanding of the micellization behavior of fluorocarbon-based surfactants and associated surfactant formulations. A discussion of some of the interesting topics that were not addressed in this thesis is presented in the next Chapter.

Chapter 6

Thesis Summary and Future Research Directions

6.1 Thesis Summary

The goal of this thesis was to theoretically model, at the molecular level, various aspects associated with the micellization behavior of fluorocarbon-based surfactants and their mixtures in order to gain an understanding of the roles played by the surfactant chemical structure (polar head and nonpolar tail) in the micellization process. This understanding, in turn, aids in the rational design of surfactant formulations for various applications. To meet the thesis goal, several important challenges associated with modeling the micellization behavior of fluorocarbon-based surfactants were addressed. The knowledge gained is generally applicable to the theoretical modeling of surfactant micellization.

In Chapter 3, models to calculate the free energy of micellization of discoidal and biaxial ellipsoidal micelles (which are both important micelle shapes in the context of fluorocarbon-based surfactants) were developed. These models are significantly more complex than the corresponding models for spheres, cylinders, and bilayers. Indeed, unlike these regular shapes,

discs and biaxial ellipsoids have a position-dependent curvature. Consequently, the effect of curvature on the interfacial free energy, the packing free energy, the steric free energy, and the electrostatic free energy was explicitly incorporated in order to develop models for the free energy of micellization of discoidal and biaxial ellipsoidal micelles (referred to in this thesis as the curvature-corrected model). The importance of incorporating the position-dependent curvature in the free-energy models was demonstrated by comparing the Curvature-Corrected (CC) model with a model developed by Srinivasan and Blankschtein (SB), in which the effect of curvature was not explicitly accounted for. The comparison between the CC and SB models presented in Section 3.7 shows that the SB model significantly overpredicts the free energy of micellization relative to the CC model, clearly demonstrating the importance of the CC model.

The CC model was also used to evaluate the feasibility of forming biaxial ellipsoidal micelles. In the literature on micelle shapes, there has been some controversy about the shape of globular micelles. While many experimental studies claim that some surfactants under certain solution conditions form ellipsoidal micelles,[52-54, 61] several theoretical studies have refuted this premise based on arguments related to the packing criterion,[63] the surface area per molecule,[66] and the high curvature[57, 58] associated with the ellipsoidal micelle shape. However, none of these conclusions were based on a rigorous theoretical study of ellipsoidal micelles that incorporates the effect of the position-dependent curvature on the free energy of micelle formation. Using the CC model developed in Chapter 3, in Section 3.8, I showed that contrary to the conclusions reached in previous theoretical studies, the biaxial ellipsoidal shape is indeed a feasible micelle shape.

In Chapter 4, I developed a computer-simulation-molecular-thermodynamic (CSMT) framework to predict the micellization behavior of surfactant mixtures. This framework blends

microstructural details obtained from molecular-dynamics simulations of surfactant micelles and monomers with the well-established MT framework, and allows better quantification of the hydrophobic effect through $g_{tr,CSMT}$. However, using the CSMT framework to predict micellization properties of surfactant mixtures is computationally very expensive, because it requires carrying out multiple mixed-micelle simulations at various micelle compositions. To overcome this difficulty, an approximation to calculate $g_{tr,CSMT}$, referred to as $g_{tr,CSMT}^{\alpha-avg}$, was developed. Specifically, $g_{tr,CSMT}^{\alpha-avg}$ is calculated as a micelle-composition based weighted average of the transfer free energies calculated from the simulated single-component surfactant micelles for each of the surfactants comprising the mixture. $g_{tr,CSMT}^{\alpha-avg}$ was compared with $g_{tr,CSMT}$ for several binary surfactant mixtures, and was found to work very well for all the binary surfactant mixtures considered, except for those containing alkyl ethoxylate surfactants. The observed discrepancy in the context of mixtures containing alky ethoxylate surfactants was attributed to the interactions between the surfactant molecules resulting from the flexible nature of the ethoxylate heads. This flexibility allows the ethoxylate heads to shield the micelle core from water better than other surfactant heads. CMC predictions made using the mixture CSMT model and the MT model compared very well with the experimental CMCs for various binary mixtures of linear surfactants. By demonstrating the applicability of the mixture CSMT model in the case of binary mixtures of simple surfactants, I have laid the foundation for the use of the mixture CSMT framework to model mixtures of surfactants that have a more complex chemical architecture (for example, branched and aromatic surfactants), and are therefore not amenable to traditional MT modeling.

In Chapter 5, a molecular-thermodynamic framework to predict the micellization properties of mixtures of fluorocarbon-based and hydrocarbon-based surfactants was developed.

Due to the enthalpic interactions between the fluorocarbon tails and the hydrocarbon tails, these surfactant mixtures can result in the coexistence of two types of mixed micelles in solution: one rich in the fluorocarbon-based surfactants and the other rich in the hydrocarbon-based surfactant. Accordingly, the MT framework was modified to include an enthalpy of mixing contribution, which was modeled using the Regular Solution Theory. The ability of the MT framework to predict the coexistence of two types of mixed micelles in solution was demonstrated in Section 5.3. In addition, the MT framework predictions of micelle population distributions, CMCs, and optimal micelle compositions were compared with the corresponding experimental values for various mixtures of fluorocarbon-based and hydrocarbon-based surfactants. It was found that the predictions of the population distribution of micelles are significantly affected by the value of the interaction parameter, A_{mix}, used to calculate the enthalpy of mixing. Therefore, it was concluded that the MT framework predictions would become more reliable if a better estimate of A_{mix} can be obtained.

6.2 Future Research Directions

6.2.1 Improving the Modeling of Discoidal and Biaxial Ellipsoidal Micelles

In Chapter 3, curvature-corrected models for the interfacial free energy, the packing free energy, the steric free energy, and the electrostatic free energy were discussed. Of the four free energies, only the interfacial free energy can be evaluated using analytical expressions [see Eqs. (3-41), (3-42), (3-43), and (3-50)]. The steric free energy can be calculated using numerical integration, as described in Eqs. (3-72) and (3-76). Numerical integration of Eqs. (3-72) and (3-76) using the Gauss quadrature technique is also not very computationally intensive, because it only requires evaluating the integrand for several values of the variable of integration. On the other hand, calculating the packing free energy, g_{pack}, and the charging component of the

electrostatic free energy, g_{ch}, is computationally very expensive. As discussed in Section 3.4, to calculate g_{pack}, all internal conformations of the surfactant tail have to be evaluated for 500 different external conformations at various locations on the discoidal or the ellipsoidal micelle surface (see Figure 3-9). The total number of internal tail conformations, even for a short 6-carbon fluorocarbon tail, is $3^4 = 81$ (there are a total of 4 rotatable bonds and each rotatable bond can take three states). Based on the recipe given in Section 3.4.1 to calculate the packing free energy of the 6-carbon fluorocarbon tail packed in a discoidal micelle with $b = b' = 8.0$ Å, all the 81 tail conformations have to be evaluated at 16 different locations on the discoidal surface. Accounting for the 500 external conformations for each internal tail conformation pinned at each of the 16 locations, the total number of terms in the summation in Eq. (3-52) equals 81x16x500 = 648000! Additionally, the uniform density constraint in Eq. (3-52) has to be satisfied for a total of 54 cells (see Figure 3-11). Based on these numbers, it is clear that evaluating g_{pack} for a single-surfactant tail packed in discs or biaxial ellipsoids of a variety of sizes represents a computationally intensive task. Therefore, it would be beneficial if a simpler method of calculating g_{pack} can be developed. While the method developed in Section 3.4 is based on a mean-field statistical mechanical method, other approaches, like Monte Carlo-based methods[47, 148], can also be considered, because they may be computationally less expensive. A faster method would be particularly important for surfactants having a larger number of carbon atoms in the tail (for example, commercial hydrocarbon-based surfactants). This follows because an increase in the number of carbons in the surfactant tail by 1, increases the total number of internal tail conformations by a factor of 3. In addition, it increases the size of the micelle, which in turn increases the number of cells and the number of locations at which all the tail conformations need to be sampled.

Similar to g_{pack}, the calculation of g_{ch} using the method discussed in Section 3.6 is also computationally very intensive. This follows because the method involves numerically solving a set of partial differential equations for a variety of micelle sizes, micelle surface charges, and solution ionic strengths. The interpolation table used to generate the results presented in Section 3.7 has close to 1400 points, and is applicable only for single monovalent surfactants having an associated monovalent counterion. For other surfactant systems, including divalent surfactants such as phosphate surfactants,[149, 150] divalent counterions, or mixtures of surfactants, the interpolation table would have to be regenerated, which represents a very expensive task. Therefore, developing a simpler method to calculate g_{elec} will prove very useful. In this regard, several authors have presented solutions to the Poisson-Boltzmann equation which are valid under a variety of simplifying conditions. These include: (i) Aoi's study of the properties of the solution to the linearized Poisson-Boltzmann equation (valid for low electric potentials) for biaxial ellipsoids using spheroidal functions,[151] (ii) Yoon and Kim's[152] and Hsu and Liu's[153, 154] derivations of the exact solution to the linearized Poisson-Boltzmann equation valid for low electric potentials for biaxial ellipsoids using spheroidal wavefunctions, and (iii) Hsu and Liu's derivation of a perturbation-method based solution to the Poisson-Boltzmann equation for biaxial ellipsoids valid for moderately thick double layers.[155] In the case of a torus, Cade used a perturbation method to solve problems in electrostatics,[156] while Andrews introduced a method based on separation of variables to solve the Laplace equation in toroidal coordinates.[157] Simplifying the calculations of g_{pack} and g_{ch} will allow use of the CC model to predict the micelle shapes of several longer-tailed hydrocarbon-based surfactants for which experimental data is available.[52-54]

6.2.2 Modeling of Surfactant Mixtures using the Mixture CSMT Framework

In Section 4.5, I showed that the mixture CSMT framework discussed in Chapter 4 is able to predict CMCs of binary mixtures of linear surfactants. However, the main motivation for developing the mixture CSMT framework is to use it to model surfactant mixtures that are not amenable to traditional MT modeling. Such mixtures may contain aromatic surfactants, branched surfactants, or gemini surfactants.

The mixture CSMT framework is essential to model these more complex surfactant mixtures, because it is challenging to identify the head and tails groups in these surfactants by visual inspection. For example, in the case of linear alkyl benzene sulfonates, it is not clear what part of the benzene ring, if any, is part of the surfactant head. Recently, the CSMT framework for single surfactant systems was used to identify the heads and tails of various linear, branched, and aromatic surfactants.[47] It is possible that for surfactant mixtures, the head and tail identifications of the various surfactants comprising the micelle is a function of the micelle composition. Therefore, the next steps in the development of the mixture CSMT framework include: (i) Identifying the heads and the tails for mixtures of linear surfactants, and then evaluating how the identification behaves for various types of surfactant mixtures, similar to the study presented in Section 4.4. (ii) Comparing $g_{tr,CSMT}^{\alpha-avg}$ with $g_{tr,CSMT}$ for binary mixtures of more complex surfactants. If one can show that $g_{tr,CSMT}^{\alpha-avg}$ compares well with $g_{tr,CSMT}$ for a particular set of surfactant mixtures, then, mixed-micelle simulations would not be needed to predict the micellization properties of these mixtures. (iii) Predicting the micellization properties of mixtures of more complex surfactants, including comparing these with experimental data. In the absence of experimental data, a design of experiments can be carried out to measure micellization properties, including CMCs, of a well-chosen set of binary surfactant mixtures (similar to the set

considered in Section 4.4) that would aid in identifying the reasons behind any discrepancy observed between the model predictions and the experimental data.

6.2.3 Modeling Inhomogeneous Mixed Micelles

Experimental studies of mixtures of fluorocarbon-based and hydrocarbon-based surfactants have shown that while certain mixtures yield a single type of mixed micelle in solution, other mixtures result in the coexistence of two types of micelles in solution: one rich in fluorocarbon-based surfactant and the other rich in hydrocarbon-based surfactant. Based on these observations, in Chapter 5, an MT framework capable of modeling the coexistence of different types of micelles was developed. This MT framework is not able to predict inhomogeneity within a micelle, that is, a mixed micelle consisting of a fluorocarbon compartment and a hydrocarbon compartment. The existence of such an inhomogeneous micelle was hypothesized by Nordstierna et al. to explain their nuclear-magnetic resonance spectroscopy data.[124] It would indeed be interesting to theoretically evaluate the feasibility of forming inhomogeneous micelles by comparing its free energy relative to the free energies associated with forming a well-mixed micelle or with the coexistence of a fluorocarbon-rich and a hydrocarbon-rich micelle.

Modeling inhomogeneous micelles will involve the appropriate calculations of the interfacial free energy, the packing free energy, the steric free energy, and the electrostatic free energy. The interfacial, the packing, and the steric free energies can be calculated by modifying the calculations discussed in Section 3.3, 3.4, and 3.5, respectively. However, instead of the curvature varying with position, the surfactant properties, including the tail volume, the tail length, and the head area will vary with position. Therefore, position-dependent surfactant properties would have to be incorporated in the free-energy models in a manner similar to the incorporation of the position-dependent curvature. An additional interfacial free-energy

contribution associated with the interface between the hydrocarbon compartment and the fluorocarbon compartment within the micelle core would have to be added to the model (if there are only two compartments. If there are more than two compartments, then, free energies associated with forming all the interfaces, as well as with the mixing of the different compartments, would need to be accounted for). This contribution would depend on the interfacial tension between the hydrocarbon and the fluorocarbon tails, as well as on the surface area of the internal interface. By formulating a model for the free energy of micellization of an inhomogeneous micelle, the feasibility of forming such a micelle can be theoretically evaluated by comparing the predicted populations of inhomogeneous micelles, homogeneous mixed micelles, and fluorocarbon-rich and hydrocarbon-rich mixed micelles calculated using Eq. (2-5).

6.2.4 Potential Replacements for Traditional Fluorocarbon-Based Surfactants

One of the goals of this thesis was to gain a molecular-level understanding of the micellization behavior of traditional fluorocarbon-based surfactants, as well as to exploit this understanding to model surfactant mixtures where the use of traditional fluorocarbon-based surfactants is reduced. While mixing fluorocarbon-based surfactants with hydrocarbon-based surfactants represents an interesting strategy to reduce the fluorine content of the surfactant formulation, it does not eliminate the use of the traditional fluorocarbon-based surfactants. Some of the potential replacements for traditional fluorocarbon-based surfactants include: (i) hybrid surfactants with a fluorocarbon chain and a hydrocarbon chain linked together by a common hydrophilic head,[158-162] (ii) partially-fluorinated surfactants,[163-166] and (iii) fluorinated surfactants with intermittent ether linkages along the fluorocarbon chain.[159, 160]

There are several challenges associated with modeling the surfactants listed in (i), (ii), and (iii) above. The biggest challenge is the lack of experimental solubility and interfacial

tension data for the surfactant tails. For example, in the case of the hybrid surfactants in (i) above, it is not clear whether the solubility of the hybrid tail is equal to the sum of the solubilities of the individual fluorocarbon and hydrocarbon tails. Experimental solubility data for fluorocarbon chains with intermittent ether linkages is not available. Accurate experimental solubility data is essential to predict CMCs, because the solubility is a quantitative measure of the hydrophobic effect, which is the main contribution to the free energy of micellization. With this in mind, a systematic experimental study of the solubility of these novel surfactant tails would be extremely beneficial in the context of modeling their micellization behavior. Development of theories capable of predicting the solubilities of such complex surfactant tails will also be useful. The other serious challenge in modeling these novel surfactants is associated with the evaluation of the packing free energy. Indeed, the packing free energy will have to be generalized to account for two tails in the case of the hybrid surfactants in (i) above. In addition, new RIS models, associated with the heterogeneous surfactant tails in (ii) and (iii) above, would have to be included to calculate the corresponding packing free energies. Development of a micellization framework capable of predicting the micellization properties of such novel surfactants and their mixtures would be very useful, because the framework predictions can guide surfactant formulators in synthesizing and characterizing those surfactants which exhibit optimal properties.

6.2.5 Experimental Measurements for Validating Theoretical Predictions

Experimental measurements of micellization properties, including CMCs, micelle population distributions, micelle aggregations numbers, micelle shapes, micelle sizes, and micelle compositions are extremely important to validate theoretical predictions. Often, the experimental data available in the literature reports measurements for a wide variety of

surfactants having different head and tail groups. To gain a better understanding of any shortcomings of the theoretical modeling, including the effect of the surfactant structure on micellization behavior, it is beneficial to have experimental data for a carefully-chosen set of surfactants (similar to the set considered in Section 4.4). This should aid in identifying the reasons behind any discrepancy observed between the model predictions and the experimental data.

In the context of the theoretical modeling of biaxial ellipsoidal micelle shapes, experimental measurements of the micelle shapes and sizes of a variety of surfactants including: (i) a set of nonionic surfactants having the same head (for example a glucoside head) and different number of carbon atoms in the tail, (ii) a set of nonionic surfactants having the same tail but different heads (glucoside and maltoside heads, or ethoxylated heads with different number of ethoxylate units), and (iii) a set of ionic surfactants having the same tail but different heads (carboxylate head, sulfate head, trimethyl ammonium head, etc.), would be useful to understand the effect of the surfactant head and tail on the micellization behavior and validate the model predictions made in Section 3.8.1. Experimental measurements that are useful in the context of the mixture CSMT framework were discussed in Section 6.2.2. Finally, in the context of the theoretical modeling of mixtures of fluorocarbon-based and hydrocarbon-based surfactants, it is essential to obtain a reliable estimate of the interaction parameter, A_{mix}, as a function of temperature and the fluorocarbon and hydrocarbon chain lengths, to further improve the predictions of micelle population distributions. Phase equilibrium measurements for several binary mixtures of fluorocarbons and hydrocarbons having different number of carbon atoms will aid in obtaining a reliable estimate of A_{mix}. In addition, as discussed in Section 5.1, conclusions about the unimodality or the bimodality of the micelle population distributions are

based on indirect evidence. The development of experimental methods to reliably determine the unimodality and bimodality of micelle population distributions would improve our understating of the micellization behavior of mixtures of fluorocarbon-based and hydrocarbon-based surfactants.

Chapter 7

Appendix

7.1 Mathematical Derivations and Proofs

7.1.1 Differential Volume of a Discoidal Micelle

The Jacobian matrix for the parameterization of the semi-toroidal rim of a discoidal micelle shown in Eq. (3-14) is given by:

$$J=\begin{bmatrix} \frac{\partial x}{\partial r} & \frac{\partial x}{\partial u} & \frac{\partial x}{\partial v} \\ \frac{\partial y}{\partial r} & \frac{\partial y}{\partial u} & \frac{\partial y}{\partial v} \\ \frac{\partial z}{\partial r} & \frac{\partial z}{\partial u} & \frac{\partial z}{\partial v} \end{bmatrix}=\begin{bmatrix} \cos v\cos u & -\left(b+r\cos v\right)\sin u & -r\sin v\cos u \\ \cos v\sin u & \left(b+r\cos v\right)\cos u & -r\sin v\sin u \\ \sin v & 0 & r\cos v \end{bmatrix} \tag{7-1}$$

$$\begin{aligned} \left|J\right| &= \cos v\cos u\cdot\left(\left(b+r\cos v\right)\cos u\cdot r\cos v-0\right) \\ &\quad +\left(b+r\cos v\right)\sin u\cdot\left(\cos v\sin u\cdot r\cos v+r\sin v\sin u\cdot\sin v\right) \\ &\quad -r\sin v\cos u\left(0-\left(b+r\cos v\right)\cos u\cdot\sin v\right) \\ &= r\left(b+r\cos v\right) \end{aligned} \tag{7-2}$$

Substituting Eq. (7-2) in Eq. (3-12) yields:

$$dV=dxdydz=r\cdot\left(b+r\cos v\right)drdudv \tag{7-3}$$

which is the result obtained in Eq. (3-15)

7.1.2 Differential Area and Mean Curvature of a Discoidal Micelle using the First and Second Fundamental Forms

To evaluate the first fundamental form for a discoidal micelle, we first evaluate x_1 and x_2, defined in Eq. (3-1), and their inner product, g_{ij}, defined in Eq. (3-4), for the surface parameterization given in Eq. (3-16) as follows:

$$x_1 = \frac{\partial \overline{x}}{\partial u} = \left(\left(b + b'\cos v\right)\left(-\sin u\right), \left(b + b'\cos v\right)\cos u, 0\right) \tag{7-4}$$

$$x_2 = \frac{\partial \overline{x}}{\partial v} = \left(-b'\sin v\cos u, -b'\sin v\sin u, b'\cos v\right) \tag{7-5}$$

$$g_{11} = \left\langle x_1, x_1 \right\rangle = \left(b + b'\cos v\right)^2 \left(\left(-\sin u\right)^2 + \cos^2 v\right) = \left(b + b'\cos v\right)^2 \tag{7-6}$$

$$g_{12} = g_{21} = \left\langle x_1, x_2 \right\rangle = b'\left(b + b'\cos v\right)\left(-\sin u \cdot \left(-\sin v\cos u\right) - \cos u \cdot \sin v\sin u\right) = 0 \tag{7-7}$$

$$g_{22} = \left\langle x_2, x_2 \right\rangle = b'^2 \left(\sin^2 v\cos^2 u + \sin^2 v\sin^2 u + \cos^2 v\right) = b'^2 \tag{7-8}$$

$$g = \begin{bmatrix} g_{11} & g_{12} \\ g_{21} & g_{22} \end{bmatrix} = \begin{bmatrix} \left(b + b'\cos v\right)^2 & 0 \\ 0 & b'^2 \end{bmatrix} \tag{7-9}$$

Substituting Eq. (7-9) in Eq. (3-5) yields:

$$dA = \sqrt{|g|}\,dudv = b'\left(b + b'\cos v\right)dudv \tag{7-10}$$

The following equations show the steps needed to obtain an expression for the mean curvature of the surface of the semi-toroidal rim based on the recipe introduced in Section 3.2.

$$n = \frac{x_1 \times x_2}{\left|x_1 \times x_2\right|}$$

$$= \frac{\left((-\sin u)\cdot(-\sin v \sin u)\cdot \hat{k} + (-\sin u)\cdot \cos v \cdot \left(-\hat{j}\right) + \cos u \cdot (-\sin v \cos u)\cdot \left(-\hat{k}\right) + \cos u \cdot \cos v \cdot \hat{i}\right)}{\left(\cos^2 u \cos^2 v + \sin^2 u \cos^2 v + \left(\sin v \cos^2 u + \sin v \sin^2 u\right)^2\right)} \tag{7-11}$$
$$= \left(\cos v \cos u, \cos v \sin u, \sin v\right)$$

$$x_{11} = \frac{\partial^2 \overline{x}}{\partial u^2} = \left(-\left(b + b' \cos v\right)\cos u, -\left(b + b' \cos v\right)\sin u, 0\right) \tag{7-12}$$

$$x_{12} = x_{21} = \frac{\partial^2 \overline{x}}{\partial u \partial v} = \left(b' \sin v \sin u, -b' \sin v \cos u, 0\right) \tag{7-13}$$

$$x_{22} = \frac{\partial^2 \overline{x}}{\partial v^2} = \left(-b' \cos v \cos u, -b' \cos v \sin u, -b' \sin v\right) \tag{7-14}$$

$$\begin{aligned} L_{11} &= \left\langle x_{11}, n \right\rangle = -\left(b + b' \cos v\right)\left(\cos u \cdot \cos v \cos u + \sin u \cdot \cos v \sin u + 0\right) \\ &= -\left(b + b' \cos v\right)\cos v \end{aligned} \tag{7-15}$$

$$\begin{aligned} L_{12} = L_{21} &= \left\langle x_{12}, n \right\rangle = b'\left(\sin v \sin u \cdot \cos v \cos u - \sin v \cos u \cdot \cos v \sin u + 0\right) \\ &= 0 \end{aligned} \tag{7-16}$$

$$\begin{aligned} L_{22} &= \left\langle x_{22}, n \right\rangle = -b'\left(\cos v \cos u \cdot \cos v \cos u + \cos v \sin u \cdot \cos v \sin u + \sin v \cdot \sin v\right) \\ &= -b' \end{aligned} \tag{7-17}$$

$$g^{-1} = \frac{1}{b'^2\left(b + b' \cos v\right)^2}\begin{bmatrix} b'^2 & 0 \\ 0 & \left(b + b' \cos v\right)^2 \end{bmatrix} \tag{7-18}$$

$$L_1^1 = L_{11} g^{11} + L_{21} g^{21} = -\cos v\left(b + b' \cos v\right)\cdot \frac{1}{\left(b + b' \cos v\right)^1} + 0 = \frac{-\cos v}{\left(b + b' \cos v\right)} \tag{7-19}$$

$$L_2^2 = L_{12} g^{12} + L_{22} g^{22} = 0 - b' \cdot \frac{1}{b'^1} = -\frac{1}{b'} \tag{7-20}$$

$$c = \frac{1}{2}\left(L_1^1 + L_2^2\right) = \frac{1}{2}\left(\frac{-\cos v}{b + b' \cos v} - \frac{1}{b'}\right) = -\frac{1}{2b'}\left(\frac{b + 2b' \cos v}{b + b' \cos v}\right) \tag{7-21}$$

7.1.3 Differential Volume of a Biaxial Ellipsoidal Micelle

The Jacobian matrix for the parameterization of the biaxial ellipsoid shown in Eq. (3-20) is given by:

$$J = \begin{bmatrix} \frac{\partial x}{\partial r} & \frac{\partial x}{\partial u} & \frac{\partial x}{\partial v} \\ \frac{\partial y}{\partial r} & \frac{\partial y}{\partial u} & \frac{\partial y}{\partial v} \\ \frac{\partial z}{\partial r} & \frac{\partial z}{\partial u} & \frac{\partial z}{\partial v} \end{bmatrix} = \begin{bmatrix} p\cos u\sin v & -pr\sin u\sin v & pr\cos u\cos v \\ p\sin u\sin v & pr\cos u\sin v & pr\sin u\cos v \\ q\cos v & 0 & -qr\sin v \end{bmatrix} \tag{7-22}$$

$$\begin{aligned} |J| &= p\cos u\sin v\cdot\left(pr\cos u\sin v\cdot\left(-qr\sin v\right)-0\right) \\ &\quad + pr\sin u\sin v\cdot\left(p\sin u\sin v\cdot\left(-qr\sin v\right)-pr\sin u\cos v\cdot q\cos v\right) \\ &\quad + pr\cos u\cos v\cdot\left(0-pr\cos u\sin v\cdot q\cos v\right) \\ &= -p^2qr^2\sin v \end{aligned} \tag{7-23}$$

Substituting Eq. (7-23) in (3-12) yields:

$$dV = dxdydz = p^2qr^2\sin v drdudv \tag{7-24}$$

It should be noted that the absolute value of the determinant of the Jacobian is used to calculate the differential volume.

7.1.4 Differential Area and Mean Curvature of a Biaxial Ellipsoidal Micelle using the First and Second Fundamental Forms

To evaluate the first fundamental form, we first evaluate x_1 and x_2, defined in Eq. (3-1), and their inner product, g_{ij}, defined in Eq. (3-4), for the surface parameterization given in Eq. (3-20) as follows:

$$x_1 = \frac{\partial \overline{x}}{\partial u} = \left(-p\sin u\sin v, p\cos u\sin v, 0\right) \tag{7-25}$$

$$x_2 = \frac{\partial \overline{x}}{\partial v} = \left(p\cos u\cos v, p\sin u\cos v, -q\sin v\right) \tag{7-26}$$

$$g_{11} = \left\langle x_1, x_1 \right\rangle = p^2\sin^2 u\sin^2 v + p^2\cos^2 u\sin^2 v = p^2\sin^2 v \tag{7-27}$$

$$g_{12} = g_{21} = \left\langle x_1, x_2 \right\rangle = \left(-p\sin u\sin v\right)\cdot p\cos u\cos v + p\cos u\sin v\cdot p\sin u\cos v + 0 = 0 \tag{7-28}$$

$$g_{22} = \langle x_2, x_2 \rangle = p^2 \cos^2 u \cos^2 v + p^2 \sin^2 u \cos^2 v + q^2 \sin^2 v = p^2 \cos^2 v + q^2 \sin^2 v \tag{7-29}$$

$$g = \begin{bmatrix} g_{11} & g_{12} \\ g_{21} & g_{22} \end{bmatrix} = \begin{bmatrix} p^2 \sin^2 v & 0 \\ 0 & p^2 \cos^2 v + q^2 \sin^2 v \end{bmatrix} \tag{7-30}$$

Substituting Eq. (7-30) in Eq. (3-5) yields:

$$dA = \sqrt{|g|}\, du dv = p \sin v \sqrt{p^2 \cos^2 v + q^2 \sin^2 v}\, du dv \tag{7-31}$$

The following equations show the steps required to obtain an expression for the mean curvature of a biaxial ellipsoidal surface based on the recipe introduced in Section 3.2.

$$n = \frac{x_1 \times x_2}{|x_1 \times x_2|} = \frac{-(q \sin v \cos u, q \sin v \sin u, p \cos v)}{\sqrt{p^2 \cos^2 v + q^2 \sin^2 v}} \tag{7-32}$$

$$x_{11} = \frac{\partial^2 \overline{x}}{\partial u^2} = (-p \sin v \cos u, -p \sin v \sin u, 0) \tag{7-33}$$

$$x_{12} = x_{21} = \frac{\partial^2 \overline{x}}{\partial u \partial v} = (-p \cos v \sin u, p \cos v \cos u, 0) \tag{7-34}$$

$$x_{22} = \frac{\partial^2 \overline{x}}{\partial v^2} = (-p \sin v \cos u, -p \sin v \sin u, -q \cos v) \tag{7-35}$$

$$\begin{aligned} L_{11} = \langle x_{11}, n \rangle &= \frac{p \sin v \cos u \cdot pq \sin^2 v \cos u + p \sin v \sin u \cdot pq \sin^2 v \sin u + 0}{p \sin v \sqrt{p^2 \cos^2 v + q^2 \sin^2 v}} \\ &= \frac{pq \sin^2 v}{\sqrt{p^2 \cos^2 v + q^2 \sin^2 v}} \end{aligned} \tag{7-36}$$

$$\begin{aligned} L_{12} = L_{21} = \langle x_{12}, n \rangle &= \frac{p \cos v \sin u \cdot pq \sin^2 v \cos u - p \cos v \cos u \cdot pq \sin^2 v \sin u + 0}{p \sin v \sqrt{p^2 \cos^2 v + q^2 \sin^2 v}} \\ &= 0 \end{aligned} \tag{7-37}$$

$$\begin{aligned} L_{22} = \langle x_{22}, n \rangle &= \frac{p \sin v \cos u \cdot pq \sin^2 v \cos u + p \sin v \sin u \cdot pq \sin^2 v \sin u + p^2 \sin v \cos v \cdot q \cos v}{p \sin v \sqrt{p^2 \cos^2 v + q^2 \sin^2 v}} \\ &= \frac{pq}{\sqrt{p^2 \cos^2 v + q^2 \sin^2 v}} \end{aligned} \tag{7-38}$$

$$g^{-1} = \frac{1}{p^2 \sin^2 v\left(p^2 \cos^2 v + q^2 \sin^2 v\right)} \begin{bmatrix} p^2 \cos^2 v + q^2 \sin^2 v & 0 \\ 0 & p^2 \sin^2 v \end{bmatrix} \tag{7-39}$$

$$L_1^1 = L_{11} g^{11} + L_{21} g^{21} = \frac{pq \sin^2 v}{\sqrt{p^2 \cos^2 v + q^2 \sin^2 v}} \cdot \frac{1}{p^2 \sin^2 v} = \frac{q}{p} \cdot \frac{1}{\sqrt{p^2 \cos^2 v + q^2 \sin^2 v}} \tag{7-40}$$

$$\begin{aligned} L_2^2 &= L_{12} g^{12} + L_{22} g^{22} = 0 + \frac{pq}{\sqrt{p^2 \cos^2 v + q^2 \sin^2 v}} \cdot \frac{1}{p^2 \cos^2 v + q^2 \sin^2 v} \\ &= \frac{pq}{\left(p^2 \cos^2 v + q^2 \sin^2 v\right)^{3/2}} \end{aligned} \tag{7-41}$$

$$\begin{aligned} c &= \frac{1}{2}\left(L_1^1 + L_2^2\right) = \frac{1}{2}\left(\frac{q}{p\left(p^2 \cos^2 v + q^2 \sin^2 v\right)^{1/2}} + \frac{pq}{\left(p^2 \cos^2 v + q^2 \sin^2 v\right)^{3/2}} \right) \\ &= \frac{1}{2}\left(\frac{q\left(p^2 \cos^2 v + q^2 \sin^2 v\right) + p^2 q}{p\left(p^2 \cos^2 v + q^2 \sin^2 v\right)^{3/2}} \right) \end{aligned} \tag{7-42}$$

7.1.5 Interfacial Free Energy of a Discoidal Micelle

The mathematical details of the evaluation of the integral in Eq. (3-40) are given below:

$$\begin{aligned} &\int_{v=-\pi/2}^{v=\pi/2} \left(\frac{b + 2b'\cos v}{b + b'\cos v}\right)\left(\frac{bb'^2}{2} + \frac{b'^3}{3}\cos v\right) dv = \int_{v=-\pi/2}^{v=\pi/2} \left(\frac{2b + 2b'\cos v - b}{b + b'\cos v}\right)\left(\frac{3bb'^2 + 2b'^3 \cos v}{6}\right) dv \\ &= \int_{v=-\pi/2}^{v=\pi/2} \left(\frac{3bb'^2 + 2b'^3 \cos v}{3}\right) - \left(\frac{b}{b + b'\cos v}\right)\left(\frac{3bb'^2 + 2b'^3 \cos v}{6}\right) dv \\ &= bb'^2 \pi + \frac{4b'^3}{3} - \int_{v=-\pi/2}^{v=\pi/2} \left(\frac{b}{b + b'\cos v}\right)\left(\frac{2bb'^2 + 2b'^3 \cos v + bb'^2}{6}\right) dv \\ &= bb'^2 \pi + \frac{4b'^3}{3} - \int_{v=-\pi/2}^{v=\pi/2} \left[\left(\frac{bb'^2}{3}\right) + \left(\frac{b^2 b'^2}{6\left(b + b'\cos v\right)}\right)\right] dv \\ &= bb'^2 \pi + \frac{4b'^3}{3} - \frac{bb'^2 \pi}{3} - \int_{v=-\pi/2}^{v=\pi/2} \left(\frac{b^2 b'^2}{6\left(b + b'\cos v\right)}\right) dv = \frac{V}{\pi} - \frac{bb'^2 \pi}{3} - \int_{v=-\pi/2}^{v=\pi/2} \left(\frac{b^2 b'^2}{6\left(b + b'\cos v\right)}\right) dv \end{aligned} \tag{7-43}$$

The integral in (7-43) is evaluated as follows:

$$\int_{-\pi/2}^{\pi/2} \frac{1}{(b+b'\cos v)}\,dv = \int_{-\pi/2}^{\pi/2} \frac{1}{\left(b\left(\sin^2 v/2 + \cos^2 v/2\right) + b'\left(\cos^2 v/2 - \sin^2 v/2\right)\right)}\,dv$$
$$= \int_{-\pi/2}^{\pi/2} \frac{1}{\left((b-b')\sin^2 v/2 + (b+b')\cos^2 v/2\right)}\,dv = \int_{-\pi/2}^{\pi/2} \frac{\sec^2 v/2}{\left((b-b')\tan^2 v/2 + (b+b')\right)}\,dv \tag{7-44}$$
$$= \int_{-\pi/2}^{\pi/2} \frac{\sec^2 v/2}{(b+b')\left(\frac{(b-b')}{(b+b')}\tan^2 v/2 + 1\right)}\,dv$$

For $b > b'$, the integral in Eq. (7-44) is readily evaluated by making the following substitutions:

$$p = \sqrt{\frac{b-b'}{b+b'}}\tan\frac{v}{2} \tag{7-45}$$

and

$$dp = \sqrt{\frac{b-b'}{b+b'}}\sec^2(v/2)\cdot\frac{1}{2}\,dv \tag{7-46}$$

Substituting Eqs. (7-45) and (7-46) in Eq. (7-44) yields:

$$\frac{1}{(b+b')}\int_{-\pi/2}^{\pi/2} \frac{\sec^2 v/2}{\left(\frac{(b-b')}{(b+b')}\tan^2 v/2 + 1\right)}\,dv = \frac{2}{(b+b')\sqrt{\frac{(b-b')}{(b+b')}}}\int_{-\sqrt{(b-b')/(b+b')}}^{\sqrt{(b-b')/(b+b')}} \frac{dp}{\left(p^2+1\right)}$$
$$= \frac{2}{(b+b')\sqrt{\frac{(b-b')}{(b+b')}}}\left(\tan^{-1}\sqrt{\frac{(b-b')}{(b+b')}} - \tan^{-1}\left(-\sqrt{\frac{(b-b')}{(b+b')}}\right)\right) = \frac{4}{(b+b')\sqrt{\frac{(b-b')}{(b+b')}}}\tan^{-1}\sqrt{\frac{(b-b')}{(b+b')}} \tag{7-47}$$

Substituting Eq. (7-47) in Eq. (7-44) and subsequently in the integral in Eq. (3-40) yields:

$$g_{int}=\frac{\sigma_0}{n}\left(A-2\pi\delta\left(b\pi+4b'\right)-a_0 n+2\pi a_0\frac{n}{V}\left(\frac{\delta}{b'}\right)\left(\begin{array}{l}\dfrac{V}{\pi}-\dfrac{bb'^2\pi}{3}\\ -\dfrac{b^2b'^2}{6}\left(\dfrac{4\tan^{-1}\sqrt{\dfrac{(b-b')}{(b+b')}}}{(b+b')\sqrt{\dfrac{(b-b')}{(b+b')}}}\right)\end{array}\right)\right) \tag{7-48}$$

$$g_{int}=\sigma_0\left(a-a_0-2\pi\delta\left(b\pi+4b'\right)\frac{a}{A}+\frac{2a_0\delta}{b'}-\left(\frac{2\pi a_0 bb'\delta}{3V}\right)\left(\pi+\left(\frac{2b\tan^{-1}\sqrt{\dfrac{(b-b')}{(b+b')}}}{(b+b')\sqrt{\dfrac{(b-b')}{(b+b')}}}\right)\right)\right)$$

which is the result obtained in Eq. (3-41).

For $b<b'$, a new variable q can be defined as follows:

$$q=\sqrt{\frac{b'-b}{b'+b}}\tan\frac{v}{2} \tag{7-49}$$

and

$$dq=\sqrt{\frac{b'-b}{b'+b}}\sec^2\left(v/2\right)\cdot\frac{1}{2}dv \tag{7-50}$$

Substituting Eqs.(7-49) and (7-50) in Eq. (7-44) yields:

$$\begin{aligned}\frac{1}{(b+b')}\int_{-\pi/2}^{\pi/2}\frac{\sec^2 v/2}{\left(\dfrac{(b-b')}{(b+b')}\tan^2 v/2+1\right)}dv&=\frac{2}{(b+b')\sqrt{\dfrac{(b'-b)}{(b+b')}}}\int_{-\sqrt{(b'-b)/(b+b')}}^{\sqrt{(b'-b)/(b+b')}}\frac{dq}{\left(1-q^2\right)}\\ =\frac{1}{(b+b')\sqrt{\dfrac{(b'-b)}{(b+b')}}}\left(\ln\left(\frac{1+\sqrt{\dfrac{b'-b}{b'+b}}}{1-\sqrt{\dfrac{b'-b}{b'+b}}}\right)-\ln\left(\frac{1-\sqrt{\dfrac{b'-b}{b'+b}}}{1+\sqrt{\dfrac{b'-b}{b'+b}}}\right)\right)&=\frac{2}{(b+b')\sqrt{\dfrac{(b'-b)}{(b+b')}}}\ln\left(\frac{1+\sqrt{\dfrac{b'-b}{b'+b}}}{1-\sqrt{\dfrac{b'-b}{b'+b}}}\right)\end{aligned} \tag{7-51}$$

Substituting Eq. (7-51) in Eq. (7-44) and subsequently in the integral in Eq. (3-40) yields:

$$g_{int}=\frac{\sigma_0}{n}\left(A-2\pi\delta\left(b\pi+4b'\right)-a_0n+2\pi a_0\frac{n}{V}\left(\frac{\delta}{b'}\right)\left(\begin{array}{l}\frac{V}{\pi}-\frac{bb'^2\pi}{3}\\-\frac{b^2b'^2}{6}\left(\frac{2\left(\ln\left(1+\sqrt{\frac{b'-b}{b'+b}}\right)-\ln\left(1-\sqrt{\frac{b'-b}{b'+b}}\right)\right)}{\left(b+b'\right)\sqrt{\frac{\left(b'-b\right)}{\left(b+b'\right)}}}\right)\end{array}\right)\right) \tag{7-52}$$

$$g_{int}=\sigma_0\left(a-a_0-2\pi\delta\left(b\pi+4b'\right)\frac{a}{A}+\frac{2a_0\delta}{b'}-\left(\frac{2\pi a_0bb'\delta}{3V}\right)\left(\pi+\left(\frac{b\left(\ln\left(1+\sqrt{\frac{b'-b}{b'+b}}\right)-\ln\left(1-\sqrt{\frac{b'-b}{b'+b}}\right)\right)}{\left(b+b'\right)\sqrt{\frac{\left(b-b'\right)}{\left(b+b'\right)}}}\right)\right)\right)$$

which is identical to Eq. (3-42).

If $b=b'$, the integral in Eq. (7-44) reduces to:

$$\int_{-\pi/2}^{\pi/2}\frac{\sec^2 v/2}{\left(b+b'\right)}dv=\frac{2}{\left(b+b'\right)}\left(\tan\pi/4-\tan\left(-\pi/4\right)\right)=\frac{4}{\left(b+b'\right)} \tag{7-53}$$

Substituting Eq. (7-53) in Eq. (7-44) and subsequently in the integral in Eq. (3-40) yields:

$$g_{int}\left(b=b'\right)=\sigma_0\left(a-a_0-a\frac{2\pi\delta\left(b\pi+4b'\right)}{A}+a_0\left(\frac{2\delta}{b'}\right)-a_0\frac{2\pi bb'\delta}{3V}\left(\pi+\frac{2b}{\left(b+b'\right)}\right)\right) \tag{7-54}$$

which is identical to Eq. (3-43)

7.1.6 Limiting Cases for the Interfacial Free Energy of a Discoidal Micelle

To verify the validity of the g_{int} expressions in Eqs. (3-41) - (3-43), consider the following limiting cases:

1. The torus becomes a sphere. This corresponds to the case $b = 0$ and $A = 4\pi b'^2$. Taking these limits in Eq. (3-42) yields:

$$g_{int} = \sigma_0 \left(a - a_0 - a\frac{2\pi\delta\left(0+4b'\right)}{4\pi b'^2} + a_0\left(\frac{2\delta}{b'}\right) - a_0 \cdot 0 \left(\pi + \lim_{b\to 0} \frac{b}{\left(0+b'\right)\sqrt{\frac{\left(b'-0\right)}{\left(b'+0\right)}}} \ln\left(\frac{1+\sqrt{\frac{\left(b'-0\right)}{\left(b'+0\right)}}}{1-\sqrt{\frac{\left(b'-b\right)}{\left(b'+b\right)}}} \right) \right) \right)$$
$$= \sigma_0 \left(a - a_0 - a\frac{2\delta}{b'} + a_0\left(\frac{2\delta}{b'}\right) \right) = \sigma_0 \left(a - a_0\right)\left(1 - 2\frac{\delta}{b'}\right) \tag{7-55}$$

which is identical to the g_{int} expression utilized for a spherical micelle of radius b'.

2. The torus is a cylinder. This corresponds to the case when $b\to\infty$, $A = (1/2)2\pi b'(2\pi b)$, and $V = (1/2)\pi b'^2(2\pi b)$. Note that the factor of one half in the expressions for A and V account for the fact that the cylinder is actually a hemi-cylinder because the rim is a semi-toroidal rim and the height of the cylinder is equal to the inner circumference of the semi-toroidal rim which is equal to $2\pi b$. Using the expressions for A and V and taking the limit $b\to\infty$ in Eq. (3-41) yields:

$$g_{int} = \sigma_0 \left(a - a_0 - a\frac{2\pi\delta\left(b\pi\right)}{2\pi^2 bb'} + a_0\left(\frac{2\delta}{b'}\right) - a_0\frac{2\pi bb'\delta}{3\pi^2 bb'^2} \left(\pi + \frac{2b}{\left(b\right)\sqrt{\frac{\left(b\right)}{\left(b\right)}}} \tan^{-1}\sqrt{\frac{\left(b\right)}{\left(b\right)}} \right) \right) \tag{7-56}$$
$$= \sigma_0 \left(a - a_0 - a\frac{\delta}{b'} + a_0\left(\frac{2\delta}{b'}\right) - a_0\frac{2\delta}{3b'}\left(1+\frac{1}{2}\right) \right) = \sigma_0 \left(a - a_0\right)\left(1 - \frac{\delta}{b'}\right)$$

which is identical to the g_{int} expression utilized for a cylindrical micelle of radius b'.

7.1.7 Total Surface Area of a Biaxial Ellipsoidal Micelle

The integral in Eq. (3-48) is evaluated separately for $p > q$ and $p < q$. For $p > q$, the following substitutions are made:

$$t = \sqrt{p^2 - q^2}\cos v \tag{7-57}$$

and

$$dt = -\sqrt{p^2 - q^2}\sin v dv \tag{7-58}$$

Substituting Eqs. (7-57) and (7-58) in the integral in Eq. (3-48) yields:

$$A = 2\pi p \int_{v=0}^{v=\pi} \sin v \sqrt{\left(p^2 - q^2\right)\cos^2 v + q^2}\, dv = \frac{-2\pi p}{\sqrt{\left(p^2 - q^2\right)}} \int_{t=\sqrt{\left(p^2-q^2\right)}}^{t=-\sqrt{\left(p^2-q^2\right)}} \sqrt{t^2 + q^2}\, dt$$

$$A = \frac{2\pi p}{\sqrt{\left(p^2 - q^2\right)}} \int_{t=-\sqrt{\left(p^2-q^2\right)}}^{t=\sqrt{\left(p^2-q^2\right)}} \sqrt{t^2 + q^2}\, dt \tag{7-59}$$

The integral in Eq. (7-59) is evaluated using integration by parts as follows:

$$\int \sqrt{t^2 + q^2}\, dt = t \cdot \sqrt{t^2 + q^2} - \int \frac{t}{\sqrt{t^2 + q^2}} \cdot t dt = t\sqrt{t^2 + q^2} - \int \left(\frac{t^2 + q^2}{\sqrt{t^2 + q^2}} - \frac{q^2}{\sqrt{t^2 + q^2}} \right) dt$$

$$= t\sqrt{t^2 + q^2} - \int \sqrt{t^2 + q^2}\, dt + \int \frac{q^2}{\sqrt{t^2 + q^2}} dt \tag{7-60}$$

$$\Rightarrow 2\int \sqrt{t^2 + q^2}\, dt = t\sqrt{t^2 + q^2} + \int \frac{q^2}{\sqrt{t^2 + q^2}} dt$$

To evaluate the integral on the right-hand side of Eq. (7-60), the following substitutions are made:

$$t = q\tan\theta \tag{7-61}$$

and

$$dt = q\sec^2\theta d\theta \tag{7-62}$$

Substituting Eqs. (7-61) and (7-62) in the integral in Eq. (7-60) yields:

$$\int \frac{q^2}{\sqrt{t^2+q^2}}dt = \int \frac{q^2 \cdot q\sec^2\theta}{\sqrt{q^2\tan^2\theta+q^2}}d\theta = \int \frac{q^3\sec^2\theta}{q\left|\sec\theta\right|}d\theta$$
$$= \int q^2\left|\sec\theta\right|d\theta = q^2\ln\left|\sec\theta+\tan\theta\right| = q^2\ln\left|\sqrt{1+\left(t/q\right)^2}+t/q\right| \tag{7-63}$$

One can verify that in the interval of integration, $-\sqrt{p^2-q^2} < q\tan\theta < \sqrt{p^2-q^2}$, $\sec\theta$ is always positive, and as a result, $\left|\sec\theta\right|$ can be replaced by $\sec\theta$. Substituting Eq. (7-63) in Eq. (7-60), and the subsequent result in Eq. (7-59) yields:

$$A = \frac{2\pi p}{\sqrt{\left(p^2-q^2\right)}}\int_{t=-\sqrt{\left(p^2-q^2\right)}}^{t=\sqrt{\left(p^2-q^2\right)}}\sqrt{t^2+q^2}dt\int\sqrt{t^2+q^2}dt = \frac{t}{2}\sqrt{t^2+q^2}+\frac{1}{2}\int\frac{q^2}{\sqrt{t^2+q^2}}dt$$
$$= \left(t/2\right)\sqrt{t^2+q^2}+\left(q^2/2\right)\ln\left|t/q+\sqrt{1+\left(t/q\right)^2}\right|+\frac{C_1}{2}$$
$$= \frac{2\pi p}{\sqrt{\left(p^2-q^2\right)}}\left(\frac{t}{2}\sqrt{t^2+q^2}+\frac{1}{2}\int\frac{q^2}{\sqrt{t^2+q^2}}dt\right)\Bigg|_{t=-\sqrt{\left(p^2-q^2\right)}}^{t=\sqrt{\left(p^2-q^2\right)}}$$
$$= \frac{2\pi p}{\sqrt{\left(p^2-q^2\right)}}\left(\left(t/2\right)\sqrt{t^2+q^2}+\left(q^2/2\right)\ln\left|t/q+\sqrt{1+\left(t/q\right)^2}\right|\right)\Bigg|_{t=-\sqrt{\left(p^2-q^2\right)}}^{t=\sqrt{\left(p^2-q^2\right)}}$$
$$= \frac{2\pi p}{\sqrt{\left(p^2-q^2\right)}}\left(p\sqrt{\left(p^2-q^2\right)}+\left(q^2/2\right)\ln\left|\frac{\frac{\sqrt{\left(p^2-q^2\right)}}{q}+\sqrt{1+\frac{p^2-q^2}{q^2}}}{-\frac{\sqrt{\left(p^2-q^2\right)}}{q}+\sqrt{1+\frac{p^2-q^2}{q^2}}}\right|\right)$$
$$= \frac{2\pi p}{\sqrt{\left(p^2-q^2\right)}}\left(p\sqrt{\left(p^2-q^2\right)}+\left(q^2/2\right)\ln\left|\frac{p/q+\sqrt{\left(p/q\right)^2-1}}{p/q-\sqrt{\left(p/q\right)^2-1}}\cdot\frac{p/q+\sqrt{\left(p/q\right)^2-1}}{p/q+\sqrt{\left(p/q\right)^2-1}}\right|\right)$$

$$= \frac{2\pi p}{\sqrt{\left(p^2 - q^2\right)}} \left(p\sqrt{\left(p^2 - q^2\right)} + q^2 \ln \left| {p}/{q} + \sqrt{\left({p}/{q}\right)^2 - 1} \right| \right)$$

$$= 2\pi pq \left({p}/{q} + \frac{\ln \left| {p}/{q} + \sqrt{\left({p}/{q}\right)^2 - 1} \right|}{\sqrt{\left({p}/{q}\right)^2 - 1}} \right) \tag{7-64}$$

which is identical to the expression in Eq. (3-48).

For $p < q$, the integral in Eq. (3-48) is evaluated by following a procedure similar to that followed for $p > q$. The variable of integration, v, in Eq. (3-48) is replaced by t defined below:

$$t = \sqrt{q^2 - p^2} \cos v \tag{7-65}$$

and

$$dt = -\sqrt{q^2 - p^2} \sin v dv \tag{7-66}$$

Substituting Eqs. (7-65) and (7-66) in the integral in Eq. (3-48) yields:

$$A = 2\pi p \int_{v=0}^{v=\pi} \sin v \sqrt{\left(p^2 - q^2\right)\cos^2 v + q^2}\, dv = \frac{-2\pi p}{\sqrt{\left(q^2 - p^2\right)}} \int_{t=\sqrt{\left(q^2-p^2\right)}}^{t=-\sqrt{\left(q^2-p^2\right)}} \sqrt{q^2 - t^2}\, dt$$

$$= \frac{2\pi p}{\sqrt{\left(q^2 - p^2\right)}} \int_{t=-\sqrt{\left(q^2-p^2\right)}}^{t=\sqrt{\left(q^2-p^2\right)}} \sqrt{q^2 - t^2}\, dt \tag{7-67}$$

The integral in Eq. (7-67) is evaluated using integration by parts as follows:

$$\int \sqrt{q^2 - t^2}\, dt = t \cdot \sqrt{q^2 - t^2} - \int \frac{-t}{\sqrt{q^2 - t^2}} \cdot t dt = t\sqrt{q^2 - t^2} - \int \left(\frac{q^2 - t^2}{\sqrt{q^2 - t^2}} - \frac{q^2}{\sqrt{q^2 - t^2}} \right) dt$$

$$= t\sqrt{q^2 - t^2} - \int \sqrt{q^2 - t^2}\, dt + \int \frac{q^2}{\sqrt{q^2 - t^2}} dt$$

$$\Rightarrow 2\int\sqrt{q^2-t^2}\,dt = t\sqrt{q^2-t^2}+\int\frac{q^2}{\sqrt{q^2-t^2}}dt \tag{7-68}$$

To evaluate the integral on the right-hand side of Eq. (7-68), the following substitutions are made:

$$t = q\sin\theta \tag{7-69}$$

and

$$dt = q\cos\theta d\theta \tag{7-70}$$

Substituting Eqs. (7-69) and (7-70) in the integral in Eq. (7-68) yields:

$$\begin{aligned}\int\frac{q^2}{\sqrt{q^2-t^2}}dt &= \int\frac{q^2\cdot q\cos\theta}{\sqrt{q^2-q^2\sin^2\theta}}d\theta = \int\frac{q^3\cos\theta}{q\left|\cos\theta\right|}d\theta = \int q^2 d\theta = q^2\theta \\ &= q^2\sin^{-1}\left(t/q\right)\end{aligned} \tag{7-71}$$

One can verify that in the interval of integration, $-\sqrt{q^2-p^2} < q\sin\theta < \sqrt{q^2-p^2}$, $\cos\theta$ is always positive, and as a result, $\cos\theta/\left|\cos\theta\right|$ can be replaced by 1. Substituting Eq. (7-71) in Eq. (7-68), and the subsequent result in Eq. (7-67) yields:

$$\begin{aligned}A &= \frac{2\pi p}{\sqrt{q^2-p^2}}\int_{t=-\sqrt{q^2-p^2}}^{t=\sqrt{q^2-p^2}}\sqrt{q^2-t^2}\,dt\int\sqrt{q^2-t^2}\,dt = \left(t/2\right)\sqrt{q^2-t^2}+\left(1/2\right)\int\frac{q^2}{\sqrt{q^2-t^2}}dt \\ &= \left(t/2\right)\sqrt{q^2-t^2}+\left(q^2/2\right)\sin^{-1}\left(t/q\right)+C' \\ &= \frac{2\pi p}{\sqrt{q^2-p^2}}\left(\left(t/2\right)\sqrt{q^2-t^2}+\left(1/2\right)\int\frac{q^2}{\sqrt{q^2-t^2}}dt\right)\Bigg|_{t=-\sqrt{q^2-p^2}}^{t=\sqrt{q^2-p^2}} \\ &= \frac{2\pi p}{\sqrt{q^2-p^2}}\left(\left(t/2\right)\sqrt{q^2-t^2}+\left(q^2/2\right)\sin^{-1}\left(t/q\right)\right)\Bigg|_{t=-\sqrt{q^2-p^2}}^{t=\sqrt{q^2-p^2}}\end{aligned}$$

$$= \frac{2\pi p}{\sqrt{q^2 - p^2}} \left(p\sqrt{q^2 - p^2} + q^2 \sin^{-1} \frac{\sqrt{q^2 - p^2}}{q} \right)$$
$$= 2\pi pq \left(\left(p/q \right) + \frac{\sin^{-1} \sqrt{1 - \left(p/q \right)^2}}{\sqrt{1 - \left(p/q \right)^2}} \right) \tag{7-72}$$

which is identical to the expression in Eq. (3-48).

7.1.8 Interfacial Free Energy of a Biaxial Ellipsoidal Micelle

The first and second integrals in Eq. (3-50) are similar to the integrals used to evaluate the area and the volume of an ellipsoid presented in Eqs. (3-48) and (3-49). Therefore, in this section, mathematical details regarding the evaluation of the remaining integrals are discussed. The following equations present the evaluation of the remaining four integrals for $p > q$:

1.

$$\int_{v=0}^{v=\pi} \frac{qp\delta}{w} \sin v dv = \int_{v=0}^{v=\pi} \frac{qp\delta}{p^2 \cos^2 v + q^2 \sin^2 v} \sin v dv$$
$$= \int_{v=0}^{v=\pi} \frac{qp\delta}{\left(p^2 - q^2 \right) \cos^2 v + q^2} \sin v dv \tag{7-73}$$

Substituting Eqs. (7-57) and (7-58) in Eq. (7-73) yields:

$$\int_{v=0}^{v=\pi} \frac{qp\delta}{\left(p^2 - q^2 \right) \cos^2 v + q^2} \sin v dv = \frac{-qp\delta}{\sqrt{\left(p^2 - q^2 \right)}} \int_{t=\sqrt{\left(p^2 - q^2 \right)}}^{t=-\sqrt{\left(p^2 - q^2 \right)}} \frac{1}{t^2 + q^2} dt$$
$$= \frac{qp\delta}{\sqrt{\left(p^2 - q^2 \right)}} \cdot \frac{1}{q} \tan^{-1} \left(t/q \right) \Bigg|_{t=-\sqrt{\left(p^2 - q^2 \right)}}^{t=\sqrt{\left(p^2 - q^2 \right)}} = \frac{2p\delta}{\sqrt{\left(p^2 - q^2 \right)}} \tan^{-1} \left(\frac{\sqrt{\left(p^2 - q^2 \right)}}{q} \right) \tag{7-74}$$

2.

$$\int_{v=0}^{v=\pi} \frac{q\delta}{p} \sin v dv = \frac{2q\delta}{p} \tag{7-75}$$

3.

$$\begin{aligned} \int_{v=0}^{v=\pi} a_0 \frac{n}{V} \frac{q^2 p^2 \delta}{3w^{3/2}} \sin v dv &= \int_{v=0}^{v=\pi} a_0 \frac{n}{V} \frac{q^2 p^2 \delta}{3\left(p^2 \cos^2 v + q^2 \sin^2 v\right)^{3/2}} \sin v dv \\ &= \int_{v=0}^{v=\pi} a_0 \frac{n}{V} \frac{q^2 p^2 \delta}{3\left(\left(p^2 - q^2\right)\cos^2 v + q^2\right)^{3/2}} \sin v dv \end{aligned} \tag{7-76}$$

Substituting Eqs. (7-57) and (7-58) in Eq. (7-76) yields:

$$\int_{v=0}^{v=\pi} a_0 \frac{n}{V} \frac{q^2 p^2 \delta}{3\left(\left(p^2 - q^2\right)\cos^2 v + q^2\right)^{3/2}} \sin v dv = a_0 \frac{nq^2 p^2 \delta}{3V\sqrt{\left(p^2 - q^2\right)}} \int_{t=-\sqrt{\left(p^2-q^2\right)}}^{t=\sqrt{\left(p^2-q^2\right)}} \frac{1}{\left(t^2 + q^2\right)^{3/2}} dt \tag{7-77}$$

To evaluate the integral in Eq. (7-77), the following substitutions are made:

$$t = q \tan\theta \tag{7-78}$$

and

$$dt = q \sec^2 \theta d\theta \tag{7-79}$$

Substituting Eqs. (7-78) and (7-79) in the integral in Eq. (7-77) yields:

$$\begin{aligned} &\int \frac{1}{\left(t^2 + q^2\right)^{3/2}} dt = \int \frac{q \sec^2 \theta}{\left(q^2 \tan^2 \theta + q^2\right)^{3/2}} d\theta = \int \frac{q \sec^2 \theta}{q^3 \left|\sec^3 \theta\right|} d\theta = \int \frac{\left|\cos\theta\right|}{q^2} d\theta = \int \frac{\cos\theta}{q^2} d\theta \\ &= \frac{\sin\theta}{q^2} = \left(1/q^2\right) \sin\left(\tan^{-1}\left(t/q\right)\right) = \left(1/q^2\right) \sin\left(\sin^{-1}\left(\frac{t}{\sqrt{t^2 + q^2}}\right)\right) = \left(1/q^2\right) \frac{t}{\sqrt{t^2 + q^2}} + C_3 \end{aligned} \tag{7-80}$$

One can verify that in the interval of integration, $-\sqrt{p^2-q^2} < q\sin\theta < \sqrt{p^2-q^2}$, $\cos\theta$ is always positive. This allows one to replace $|\cos\theta|$ by $\cos\theta$. Substituting Eq. (7-80) in Eq. (7-77), and the subsequent result in Eq. (7-76) yields:

$$\int_{v=0}^{v=\pi} a_0 \frac{n}{V} \frac{q^2 p^2 \delta}{3\left(\left(p^2-q^2\right)\cos^2 v + q^2\right)^{3/2}} \sin v dv = a_0 \frac{nq^2 p^2 \delta}{3V\sqrt{\left(p^2-q^2\right)}} \int_{t=-\sqrt{\left(p^2-q^2\right)}}^{t=\sqrt{\left(p^2-q^2\right)}} \frac{1}{\left(t^2+q^2\right)^{3/2}} dt$$

$$= a_0 \frac{nq^2 p^2 \delta}{3V\sqrt{\left(p^2-q^2\right)}} \cdot \frac{1}{q^2} \cdot \frac{t}{\sqrt{t^2+q^2}} \Bigg|_{t=-\sqrt{\left(p^2-q^2\right)}}^{t=\sqrt{\left(p^2-q^2\right)}} = a_0 \frac{np^2 \delta}{3V\sqrt{\left(p^2-q^2\right)}} \frac{2\sqrt{\left(p^2-q^2\right)}}{p} \tag{7-81}$$

$$= a_0 \frac{2np\delta}{3V}$$

4.

$$\int_{v=0}^{v=\pi} a_0 \frac{n}{V} \frac{q^2\delta}{3w^{1/2}} \sin v dv = \int_{v=0}^{v=\pi} a_0 \frac{n}{V} \frac{q^2\delta}{3\left(p^2\cos^2 v + q^2 \sin^2 v\right)^{1/2}} \sin v dv$$

$$= \int_{v=0}^{v=\pi} a_0 \frac{n}{V} \frac{q^2\delta}{3\left(\left(p^2-q^2\right)\cos^2 v + q^2\right)^{1/2}} \sin v dv \tag{7-82}$$

Substituting Eqs. (7-57) and (7-58) in Eq. (7-82) yields:

$$\int_{v=0}^{v=\pi} a_0 \frac{n}{V} \frac{q^2\delta}{3\left(\left(p^2-q^2\right)\cos^2 v + q^2\right)^{1/2}} \sin v dv = a_0 \frac{nq^2\delta}{3V\sqrt{\left(p^2-q^2\right)}} \int_{t=-\sqrt{\left(p^2-q^2\right)}}^{t=\sqrt{\left(p^2-q^2\right)}} \frac{1}{\left(t^2+q^2\right)^{1/2}} dt \tag{7-83}$$

Using the result in Eq. (7-63), the integral in Eq. (7-83) can be evaluated as follows:

$$a_0 \frac{nq^2\delta}{3V\sqrt{\left(p^2-q^2\right)}} \int_{t=-\sqrt{\left(p^2-q^2\right)}}^{t=\sqrt{\left(p^2-q^2\right)}} \frac{1}{\left(t^2+q^2\right)^{1/2}} dt = a_0 \frac{nq^2\delta}{3V\sqrt{\left(p^2-q^2\right)}} \ln\left| \left(t/q\right) + \sqrt{1+\left(t/q\right)^2} \right|_{t=-\sqrt{\left(p^2-q^2\right)}}^{t=\sqrt{\left(p^2-q^2\right)}}$$

$$= a_0 \frac{2nq^2\delta}{3V\sqrt{\left(p^2-q^2\right)}} \ln\left| p/q + \sqrt{\left(p/q\right)^2-1} \right| \tag{7-84}$$

Substituting Eqs. (3-48), (3-49), (7-74), (7-75), (7-81), and (7-84) in Eq. (3-50) yields:

$$g_{int} = \frac{2\pi\sigma_0 p}{n} \left(\begin{array}{l} \int_{v=0}^{v=\pi} w^{1/2} \sin v dv - \int_{v=0}^{v=\pi} a_0 \frac{n}{V}\frac{pq}{3} \sin v dv - \int_{v=0}^{v=\pi} \frac{qp\delta}{w} \sin v dv - \int_{v=0}^{v=\pi} \frac{q\delta}{p} \sin v dv \\ + \int_{v=0}^{v=\pi} a_0 \frac{n}{V}\frac{q^2p^2\delta}{3w^{3/2}} \sin v dv + \int_{v=0}^{v=\pi} a_0 \frac{n}{V}\frac{q^2\delta}{3w^{1/2}} \sin v dv \end{array} \right)$$

$$= \frac{\sigma_0}{n} \left(\begin{array}{l} A - a_0 n - \frac{4\pi p^2\delta}{\sqrt{p^2-q^2}} \tan^{-1}\left(\frac{\sqrt{p^2-q^2}}{q}\right) - 4\pi q\delta \\ + a_0 \frac{4\pi np^2\delta}{3V} + a_0 \frac{4\pi nq^2 p\delta}{3V\sqrt{p^2-q^2}} \ln\left| p/q + \sqrt{\left(p/q\right)^2-1} \right| \end{array} \right)$$

$$= \frac{\sigma_0}{n} \left(A - na_0 - 4\pi q\delta \left(\frac{\left(p/q\right)^2}{\sqrt{\left(p/q\right)^2-1}} \tan^{-1}\sqrt{\left(p/q\right)^2-1} + 1 \right) + \frac{4\pi npq\delta}{3V} a_0 \left(\frac{p}{q} + \frac{\ln\left| p/q + \sqrt{\left(p/q\right)^2-1} \right|}{\sqrt{\left(p/q\right)^2-1}} \right) \right)$$

$$= \frac{\sigma_0}{n} \left(A - na_0 - 4\pi q\delta \left(\frac{\left(p/q\right)^2}{\sqrt{\left(p/q\right)^2-1}} \tan^{-1}\sqrt{\left(p/q\right)^2-1} + 1 \right) + \frac{4\pi npq\delta}{3V} a_0 \frac{A}{2\cancel{\pi pq}} \right)$$

$$g_{int} = \sigma_0 \left(a - a_0 - \frac{4\pi q\delta}{n} \left(\frac{\left(p/q\right)^2}{\sqrt{\left(p/q\right)^2-1}} \tan^{-1}\sqrt{\left(p/q\right)^2-1} + 1 \right) + \frac{2\delta A}{3V} a_0 \right) \tag{7-85}$$

which is identical to the expression in Eq. (3-50).

A similar analysis is carried out to evaluate the integral in Eq. (3-50) for $p < q$. In Eq. (3-50), the first two integrals, like in the case of $p > q$, are similar to the integrals shown in Eqs. (3-48) and (3-49), respectively. The remaining four integrals are evaluated as follows:

1. Substituting Eqs. (7-65) and (7-66) in Eq. (7-73) yields:

$$\int_{v=0}^{v=\pi} \frac{qp\delta}{\left(p^2-q^2\right)\cos^2 v+q^2}\sin v dv = \frac{-qp\delta}{\sqrt{\left(q^2-p^2\right)}} \int_{t=\sqrt{\left(q^2-p^2\right)}}^{t=-\sqrt{\left(q^2-p^2\right)}} \frac{1}{q^2-t^2}dt$$

$$= \frac{qp\delta}{\sqrt{\left(q^2-p^2\right)}} \int_{t=-\sqrt{\left(q^2-p^2\right)}}^{t=\sqrt{\left(q^2-p^2\right)}} \frac{1}{2q}\frac{q-t+q+t}{(q-t)(q+t)}dt = \frac{p\delta}{2\sqrt{\left(q^2-p^2\right)}} \int_{t=-\sqrt{\left(q^2-p^2\right)}}^{t=\sqrt{\left(q^2-p^2\right)}} \frac{1}{(q+t)}+\frac{1}{(q-t)}dt$$

$$= \frac{p\delta}{2\sqrt{\left(q^2-p^2\right)}} \ln\left|\frac{q+t}{q-t}\right|_{-\sqrt{\left(q^2-p^2\right)}}^{\sqrt{\left(q^2-p^2\right)}} = \frac{2p\delta}{2\sqrt{\left(q^2-p^2\right)}} \ln\left|\frac{q+\sqrt{\left(q^2-p^2\right)}}{q-\sqrt{\left(q^2-p^2\right)}}\cdot\frac{q+\sqrt{\left(q^2-p^2\right)}}{q+\sqrt{\left(q^2-p^2\right)}}\right| \quad (7\text{-}86)$$

$$= \frac{p\delta}{\sqrt{\left(q^2-p^2\right)}} \ln\left|\frac{\left(q+\sqrt{\left(q^2-p^2\right)}\right)^2}{q^2-\left(\sqrt{q^2-p^2}\right)^2}\right| = \frac{2p\delta}{\sqrt{\left(q^2-p^2\right)}} \ln\left|q/p+\sqrt{\left(q/p\right)^2-1}\right|$$

2.

$$\int_{v=0}^{v=\pi} \frac{q\delta}{p}\sin v dv = \frac{2q\delta}{p} \quad (7\text{-}87)$$

3. Substituting Eqs. (7-65) and (7-66) in Eq. (7-76) yields:

$$\int_{v=0}^{v=\pi} a_0\frac{n}{V}\frac{q^2p^2\delta}{3\left(\left(p^2-q^2\right)\cos^2 v+q^2\right)^{3/2}}\sin v dv = a_0\frac{nq^2p^2\delta}{3V\sqrt{\left(q^2-p^2\right)}} \int_{t=-\sqrt{\left(q^2-p^2\right)}}^{t=\sqrt{\left(q^2-p^2\right)}} \frac{1}{\left(q^2-t^2\right)^{3/2}}dt \quad (7\text{-}88)$$

To evaluate the integral in Eq. (7-88), the following substitutions are made:

$$t = q\sin\theta \quad (7\text{-}89)$$

and

$$dt = q\cos\theta \tag{7-90}$$

Substituting Eqs. (7-89) and (7-90) in the integral in Eq. (7-88) yields:

$$\int \frac{1}{\left(q^2 - t^2\right)^{3/2}} dt = \int \frac{q\cos\theta}{\left(q^2 - q^2\sin^2\theta\right)^{3/2}} d\theta = \int \frac{q\cos\theta}{q^3\left|\cos^3\theta\right|} d\theta = \frac{1}{q^2}\int \sec^2\theta d\theta = \frac{1}{q^2}\tan\theta$$
$$= \frac{1}{q^2}\frac{t}{\sqrt{q^2 - t^2}} \tag{7-91}$$

In the interval of integration, $-\sqrt{q^2 - p^2} < q\sin\theta < \sqrt{q^2 - p^2}$, $\cos\theta$ is always positive. Therefore, $\cos\theta/\left|\cos\theta\right|$ is replaced by 1. Substituting Eq. (7-91) in Eq. (7-88) yields:

$$a_0 \frac{nq^2p^2\delta}{3V\sqrt{\left(q^2 - p^2\right)}} \int_{t=-\sqrt{\left(q^2-p^2\right)}}^{t=\sqrt{\left(q^2-p^2\right)}} \frac{1}{\left(q^2 - t^2\right)^{3/2}} dt = a_0 \frac{nq^2p^2\delta}{3V\sqrt{\left(q^2 - p^2\right)}} \cdot \frac{1}{q^2} \cdot \frac{t}{\sqrt{q^2 - t^2}} \Bigg|_{t=-\sqrt{\left(q^2-p^2\right)}}^{t=\sqrt{\left(q^2-p^2\right)}}$$
$$= a_0 \frac{np^2\delta}{3V\sqrt{\left(q^2 - p^2\right)}} \frac{2\sqrt{\left(q^2 - p^2\right)}}{p} = a_0 \frac{2np\delta}{3V} \tag{7-92}$$

4. Substituting Eqs. (7-65) and (7-66) in Eq. (7-82) yields:

$$\int_{v=0}^{v=\pi} a_0 \frac{n}{V} \frac{q^2\delta}{3\left(\left(p^2 - q^2\right)\cos^2 v + q^2\right)^{1/2}} \sin v dv = a_0 \frac{nq^2\delta}{3V\sqrt{\left(q^2 - p^2\right)}} \int_{t=-\sqrt{\left(q^2-p^2\right)}}^{t=\sqrt{\left(q^2-p^2\right)}} \frac{1}{\left(q^2 - t^2\right)^{1/2}} dt \tag{7-93}$$

Using the result in Eq. (7-71), the integral in Eq. (7-93) can be evaluated as follows:

$$a_0 \frac{nq^2\delta}{3V\sqrt{\left(q^2-p^2\right)}} \int_{t=-\sqrt{\left(q^2-p^2\right)}}^{t=\sqrt{\left(q^2-p^2\right)}} \frac{1}{\left(q^2-t^2\right)^{1/2}} dt = a_0 \frac{nq^2\delta}{3V\sqrt{\left(q^2-p^2\right)}} \sin^{-1}\frac{t}{q}\Bigg|_{t=-\sqrt{\left(q^2-p^2\right)}}^{t=\sqrt{\left(q^2-p^2\right)}}$$
$$= a_0 \frac{2nq^2\delta}{3V\sqrt{\left(q^2-p^2\right)}} \sin^{-1}\frac{\sqrt{\left(q^2-p^2\right)}}{q} \tag{7-94}$$

Substituting Eqs. (3-48), (3-49), (7-86), (7-87), (7-92), and (7-94) in Eq. (3-50) yields:

$$g_{int} = \int_{v=0}^{v=\pi}\int_{u=0}^{u=2\pi} \frac{\sigma_0 p \sin v}{n}\left(1-\frac{q}{p}\frac{p^2+w}{w^{3/2}}\delta\right)\left(w^{1/2}-a_0\frac{n}{V}\frac{pq}{3}\right)dudv$$
$$= \frac{2\pi\sigma_0 p}{n}\left(\begin{array}{l}\int_{v=0}^{v=\pi} w^{1/2}\sin v dv - \int_{v=0}^{v=\pi} a_0\frac{n}{V}\frac{pq}{3}\sin v dv - \int_{v=0}^{v=\pi}\frac{qp\delta}{w}\sin v dv - \int_{v=0}^{v=\pi}\frac{q\delta}{p}\sin v dv \\ + \int_{v=0}^{v=\pi} a_0\frac{n}{V}\frac{q^2p^2\delta}{3w^{3/2}}\sin v dv + \int_{v=0}^{v=\pi} a_0\frac{n}{V}\frac{q^2\delta}{3w^{1/2}}\sin v dv\end{array}\right)$$
$$= \frac{\sigma_0}{n}\left(\begin{array}{l}A - a_0 n - \frac{4\pi p^2\delta}{\sqrt{\left(q^2-p^2\right)}}\ln\left|{}^{q}\!/_{p} + \sqrt{\left({}^{q}\!/_{p}\right)^2-1}\right| - 4\pi q\delta \\ + a_0\frac{4\pi np^2\delta}{3V} + a_0\frac{4\pi nq^2 p\delta}{3V\sqrt{\left(q^2-p^2\right)}}\sin^{-1}\sqrt{1-\left({}^{p}\!/_{q}\right)^2}\end{array}\right)$$
$$= \frac{\sigma_0}{n}\left(A - na_0 - 4\pi q\delta\left(\frac{\left({}^{p}\!/_{q}\right)^2}{\sqrt{1-\left({}^{p}\!/_{q}\right)^2}}\ln\left|{}^{q}\!/_{p} + \sqrt{\left({}^{q}\!/_{p}\right)^2-1}\right| + 1\right) + \frac{4\pi npq\delta}{3V}a_0\left(\frac{p}{q} + \frac{\sin^{-1}\sqrt{1-\left({}^{p}\!/_{q}\right)^2}}{\sqrt{1-\left({}^{p}\!/_{q}\right)^2}}\right)\right)$$
$$= \sigma_0\left(a - a_0 - \frac{4\pi q\delta}{n}\left(\frac{\left({}^{p}\!/_{q}\right)^2}{\sqrt{1-\left({}^{p}\!/_{q}\right)^2}}\ln\left|{}^{q}\!/_{p} + \sqrt{\left({}^{q}\!/_{p}\right)^2-1}\right| + 1\right) + \frac{4\pi pq\delta}{3V}a_0\frac{A}{2\pi pq}\right) \tag{7-95}$$
$$= \sigma_0\left(a - a_0 - \frac{4\pi q\delta}{n}\left(\frac{\left({}^{p}\!/_{q}\right)^2}{\sqrt{1-\left({}^{p}\!/_{q}\right)^2}}\ln\left|{}^{q}\!/_{p} + \sqrt{\left({}^{q}\!/_{p}\right)^2-1}\right| + 1\right) + \frac{2\delta A}{3V}a_0\right)$$

which is identical to the expression in Eq. (3-50).

7.1.9 Limiting Cases for the Interfacial Free Energy of a Biaxial Ellipsoidal Micelle

To verify the validity of the g_{int} expressions in Eq. (3-50), consider the limiting case $p = q$ when the ellipsoid becomes a sphere. Taking this limit for the equation corresponding to the oblate ellipsoidal micelle in Eq. (3-50) yields:

$$\begin{aligned} g_{int} &= \sigma_0\left(a-a_0-\frac{4\pi p\delta}{n}\left(\left(p/p\right)^2\lim_{q\to p}\frac{\tan^{-1}\sqrt{\left(p/q\right)^2-1}}{\sqrt{\left(p/q\right)^2-1}}+1\right)+\frac{2\delta\left(4\pi p^2\right)}{3\left(\frac{4}{3}\pi p^3\right)}a_0\right) \\ &= \sigma_0\left(a-a_0-\frac{4\pi p\delta}{n}(1+1)+\left(2\delta/p\right)a_0\right)=\sigma_0\left(a-a_0-\frac{8\pi p\delta}{n}\frac{A}{A}+\left(2\delta/p\right)a_0\right) \\ &= \sigma_0\left(a-a_0-\frac{8\pi p\delta}{4\pi p^2}a+2a_0\left(\delta/p\right)\right)=\sigma_0\left(a-a_0\right)\left(1-2\left(\delta/p\right)\right) \end{aligned} \tag{7-96}$$

which is identical to the g_{int} expression utilized for a spherical micelle of radius p.

Taking the limit $p = q$, for the equation corresponding to the oblate ellipsoidal micelle in Eq. (3-50) yields:

$$g_{int} = \sigma_0\left(a-a_0-\frac{4\pi p\delta}{n}\left(\left(p/p\right)^2\lim_{q\to p}\frac{\ln\left|q/p+\sqrt{\left(q/p\right)^2-1}\right|}{\sqrt{1-\left(p/q\right)^2}}+1\right)+\frac{2\delta\left(4\pi p^2\right)}{3\left(\frac{4}{3}\pi p^3\right)}a_0\right) \tag{7-97}$$

The limit in Eq. (7-97) is evaluated using L'Hôpital's rule as follows:

$$\lim_{q/p\to 1}\frac{\ln\left|q/p+\sqrt{\left(q/p\right)^2-1}\right|}{\sqrt{1-\left(p/q\right)^2}}=\lim_{q/p\to 1}\frac{\frac{d}{d\left(q/p\right)}\left(\ln\left|q/p+\sqrt{\left(q/p\right)^2-1}\right|\right)}{\frac{d}{d\left(q/p\right)}\left(\sqrt{1-\left(p/q\right)^2}\right)}$$

$$= \lim_{q/p\to 1} \frac{\left(q/p + \sqrt{\left(q/p\right)^2 - 1}\right)^{-1}\left(1 + \dfrac{q/p}{\sqrt{\left(q/p\right)^2 - 1}}\right)}{\dfrac{-p/q}{\sqrt{1-\left(p/q\right)^2}} \cdot \dfrac{-1}{\left(q/p\right)^2}} = \lim_{q/p\to 1}\left(q/p\right)^2 = 1 \tag{7-98}$$

Substituting the limit obtained in Eq. (7-98) in Eq. (7-97) yields:

$$\begin{aligned} g_{int} &= \sigma_0\left(a - a_0 - \frac{4\pi p\delta}{n}(1+1) + \frac{2\delta}{p}a_0\right) = \sigma_0\left(a - a_0 - \frac{8\pi p\delta}{n}\cdot\frac{A}{A} + 2a_0\left(\delta/p\right)\right) \\ &= \sigma_0\left(a - a_0\right)\left(1 - 2\left(\delta/p\right)\right) \end{aligned} \tag{7-99}$$

which is again identical to the g_{int} expression utilized for a spherical micelle of radius p.

7.1.10 Volume of a Cell to Calculate g_{pack} of a Biaxial Ellipsoidal Micelle

The integral in Eq. (3-67) can be evaluated as follows:

$$2\pi p_n^2 q_n \int_{\theta_{n,k-1}}^{\theta_{n,k}} \frac{1}{3}\left(1 - \left(\left(\frac{p_{n-1}}{p_n}\right)^2 + \frac{\left(\dfrac{p_{n-1}}{p_n}\right)^2 - \left(\dfrac{q_{n-1}}{q_n}\right)^2}{\left(\dfrac{p_n q_{n-1}}{q_n p_{n-1}}\right)^2 \tan^2 v + 1}\right)^{\frac{3}{2}}\right)\sin v\,dv$$

$$= \frac{2\pi p_n^2 q_n}{3}\left(\cos\theta_{n,k-1} - \cos\theta_{n,k} - \int_{\theta_{n,k-1}}^{\theta_{n,k}} \left(\frac{\left(\dfrac{q_{n-1}}{q_n}\right)^2 \tan^2 v + \left(\dfrac{p_{n-1}}{p_n}\right)^2 + \left(\dfrac{q_{n-1}}{q_n}\right)^2 - \left(\dfrac{p_{n-1}}{p_n}\right)^2}{\left(\dfrac{p_n q_{n-1}}{q_n p_{n-1}}\right)^2 \tan^2 v + 1}\right)^{\frac{3}{2}} \sin v\,dv\right)$$

$$= \frac{2\pi p_n^2 q_n}{3}\left(\cos\theta_{n,k-1} - \cos\theta_{n,k} - \int_{\theta_{n,k-1}}^{\theta_{n,k}} \left(\frac{q_{n-1}}{q_n}\right)^3 \left|\sec^3 v\right| \left(\left(\frac{p_n q_{n-1}}{q_n p_{n-1}}\right)^2 \tan^2 v + 1\right)^{-\frac{3}{2}} \sin v\,dv\right)$$

$$= \frac{2\pi p_n^2 q_n}{3}\left(\cos\theta_{n,k-1} - \cos\theta_{n,k} - \int_{\theta_{n,k-1}}^{\theta_{n,k}} \left(\frac{q_{n-1}}{q_n}\right)^3 \sec^2 v \tan v \left(\left(\frac{p_n q_{n-1}}{q_n p_{n-1}}\right)^2 \tan^2 v + 1 \right)^{-\frac{3}{2}} dv \right) \quad (7\text{-}100)$$

The integral in Eq. (7-100) can be evaluated by making the following substitutions:

$$t = 1 + \left(\frac{p_n q_{n-1}}{q_n p_{n-1}}\right)^2 \tan^2 v \quad (7\text{-}101)$$

and

$$dt = \left(\frac{p_n q_{n-1}}{q_n p_{n-1}}\right)^2 2\tan v \sec^2 v \quad (7\text{-}102)$$

Substituting Eqs. (7-101) and (7-102) in Eq. (7-100) yields:

$$\frac{2\pi p_n^2 q_n}{3}\left(\cos\theta_{n,k-1} - \cos\theta_{n,k} - \int_{1+\left(\frac{p_n q_{n-1}}{q_n p_{n-1}}\right)^2 \tan^2\theta_{n,k-1}}^{1+\left(\frac{p_n q_{n-1}}{q_n p_{n-1}}\right)^2 \tan^2\theta_{n,k}} \left(\frac{q_{n-1}}{q_n}\right)^3 \frac{t^{-3/2}}{2\left(\frac{p_n q_{n-1}}{q_n p_{n-1}}\right)^2} dt \right)$$

$$= \frac{2\pi p_n^2 q_n}{3}\left(\cos\theta_{n,k-1} - \cos\theta_{n,k} + \left(\frac{q_{n-1}}{q_n}\right)\left(\frac{p_{n-1}}{p_n}\right)^2 \left(\left(1 + \left(\frac{p_n q_{n-1}}{q_n p_{n-1}}\right)^2 \tan^2\theta_{n,k}\right)^{-1/2} - \left(1 + \left(\frac{p_n q_{n-1}}{q_n p_{n-1}}\right)^2 \tan^2\theta_{n,k-1}\right)^{-1/2} \right) \right) \quad (7\text{-}103)$$

which is identical to Eq. (3-67)

7.1.11 Interpolation Scheme to Calculate the Charging Free Energy

For a regular grid, the interpolation scheme introduced in Section 3.6 is equivalent to the multilinear interpolation scheme. Consider the application of the interpolation scheme presented in Section 3.6 using an interpolation table which is a regular grid. Specifically, when all the points in the interpolation table are arranged in a five-dimensional space, they form a regular 5-D rectangular grid with no missing points. In such a grid, the 32 nearest neighbors for any given

point will form a regular polyhedron, where each face is perpendicular to every other face with which it has a common edge (that is, the 4-dimensional version of a 2 dimensional edge). This is easily visualized in a three-dimensional analog of the five-dimensional regular grid as shown in Figure 7-1. In such a case, each vertex of the regular polyhedron formed by the nearest neighbors is characterized by the values of the five variables, where each variable can take one of only two values (3 and 7 for variable 1 in the example shown in Figure 7-1). Note that for an irregular grid, this need not be true.

Let (a,b,c,d,e) denote the 5-dimensional point at which one desires to find the surface electric potential using the interpolation scheme. In addition, let the 32 nearest-neighbor grid points be denoted by $\left(a^{X_1},b^{X_2},c^{X_3},d^{X_4},e^{X_5}\right)$, where superscripts X_1, X_2, X_3, X_4, and X_5 are equal to either +1 or -1. A superscript of +1 denotes the high value of the variable, while a superscript of -1 denotes the low value. For example, for variable 1 in Figure 7-1, a superscript of +1 corresponds to 7, and a superscript of -1 corresponds to 3. For such a grid, the weights corresponding to the point $\left(a^{X_1},b^{X_2},c^{X_3},d^{X_4},e^{X_5}\right)$ in the multilinear interpolation scheme is given by:

$$wt_{\left(a^{X_1},b^{X_2},c^{X_3},d^{X_4},e^{X_5}\right)}=\frac{\left|a-a^{-X_1}\right|\cdot\left|b-b^{-X_2}\right|\cdot\left|c-c^{-X_3}\right|\cdot\left|d-d^{-X_4}\right|\cdot\left|e-e^{-X_5}\right|}{\left(a^{+1}-a^{-1}\right)\cdot\left(b^{+1}-b^{-1}\right)\cdot\left(c^{+1}-c^{-1}\right)\cdot\left(d^{+1}-d^{-1}\right)\cdot\left(e^{+1}-e^{-1}\right)} \tag{7-104}$$

For the interpolation scheme described in Section 3.6, the weight corresponding to the point $\left(a^{X_1},b^{X_2},c^{X_3},d^{X_4},e^{X_5}\right)$ is given by:

$$wt_{\left(a^{X_1},b^{X_2},c^{X_3},d^{X_4},e^{X_5}\right)}=\frac{\left|a-a^{X_1}\right|^{-1}\cdot\left|b-b^{X_2}\right|^{-1}\cdot\left|c-c^{X_3}\right|^{-1}\cdot\left|d-d^{X_4}\right|^{-1}\cdot\left|e-e^{X_5}\right|^{-1}}{\sum_{X_1,X_2,X_3,X_4,X_5}^{-1,+1}\left|a-a^{X_1}\right|^{-1}\cdot\left|b-b^{X_2}\right|^{-1}\cdot\left|c-c^{X_3}\right|^{-1}\cdot\left|d-d^{X_4}\right|^{-1}\cdot\left|e-e^{X_5}\right|^{-1}} \quad (7\text{-}105)$$

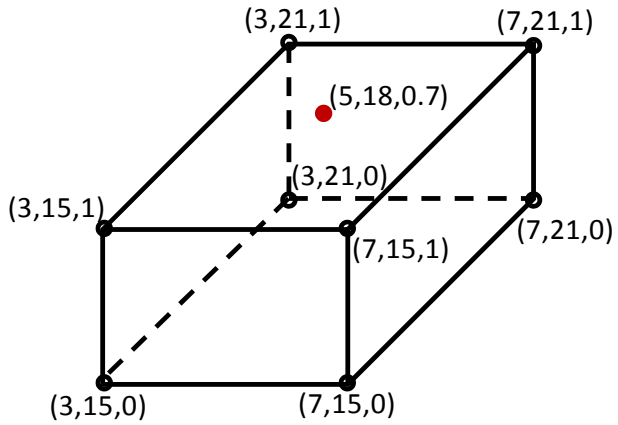

Figure 7-1: A schematic of the regular polyhedron formed by the 8 nearest neighbors of the point shown in red.

where the denominator is introduced so that all the weights add up to 1. To prove the equivalence of the two weighting schemes shown in Eqs. (7-104) and (7-105), we simplify Eq. (7-105) as follows:

$$wt_{\left(a^{X_1},b^{X_2},c^{X_3},d^{X_4},e^{X_5}\right)}=\frac{\left|a-a^{X_1}\right|^{-1}\cdot\left|b-b^{X_2}\right|^{-1}\cdot\left|c-c^{X_3}\right|^{-1}\cdot\left|d-d^{X_4}\right|^{-1}\cdot\left|e-e^{X_5}\right|^{-1}}{\sum_{X_1,X_2,X_3,X_4,X_5}^{-1,+1}\left|a-a^{X_1}\right|^{-1}\cdot\left|b-b^{X_2}\right|^{-1}\cdot\left|c-c^{X_3}\right|^{-1}\cdot\left|d-d^{X_4}\right|^{-1}\cdot\left|e-e^{X_5}\right|^{-1}}$$

$$=\frac{\left|a-a^{X_1}\right|^{-1}\cdot\left|b-b^{X_2}\right|^{-1}\cdot\left|c-c^{X_3}\right|^{-1}\cdot\left|d-d^{X_4}\right|^{-1}\cdot\left|e-e^{X_5}\right|^{-1}}{\left(\left(1/\left(e-e^{-1}\right)+1/\left(e^{+1}-e\right)\right)\cdot\sum_{X_1,X_2,X_3,X_4}^{-1,+1}\left|a-a^{X_1}\right|^{-1}\cdot\left|b-b^{X_2}\right|^{-1}\cdot\left|c-c^{X_3}\right|^{-1}\cdot\left|d-d^{X_4}\right|^{-1}\right)}$$

$$=\frac{\left|a-a^{X_1}\right|^{-1}\cdot\left|b-b^{X_2}\right|^{-1}\cdot\left|c-c^{X_3}\right|^{-1}\cdot\left|d-d^{X_4}\right|^{-1}\cdot\left|e-e^{X_5}\right|^{-1}}{\left(\left(e^{+1}-e\right)^{-1}\left(e-e^{-1}\right)^{-1}\left(e^{+1}-e^{-1}\right)\cdot\sum_{X_1,X_2,X_3,X_4}^{-1,+1}\left|a-a^{X_1}\right|^{-1}\cdot\left|b-b^{X_2}\right|^{-1}\cdot\left|c-c^{X_3}\right|^{-1}\cdot\left|d-d^{X_4}\right|^{-1}\right)}$$

$$
\begin{aligned}
&= \frac{\left|a-a^{X_1}\right|^{-1}\cdot\left|b-b^{X_2}\right|^{-1}\cdot\left|c-c^{X_3}\right|^{-1}\cdot\left|d-d^{X_4}\right|^{-1}\cdot\left|e-e^{X_5}\right|^{-1}}{\left(\begin{array}{l}\left(e^{+1}-e\right)^{-1}\cdot\left(e-e^{-1}\right)^{-1}\left(e^{+1}-e^{-1}\right)\\ \cdot\sum\limits_{X_1,X_2,X_3}^{-1,+1}\left|a-a^{X_1}\right|^{-1}\cdot\left|b-b^{X_2}\right|^{-1}\cdot\left|c-c^{X_3}\right|^{-1}\cdot\left(1/\left(d-d^{-1}\right)+1/\left(d^{+1}-d\right)\right)\end{array}\right)}\\
&= \frac{\left|a-a^{X_1}\right|^{-1}\cdot\left|b-b^{X_2}\right|^{-1}\cdot\left|c-c^{X_3}\right|^{-1}\cdot\left|d-d^{X_4}\right|^{-1}\cdot\left|e-e^{X_5}\right|^{-1}}{\left(\begin{array}{l}\left(e^{+1}-e\right)^{-1}\cdot\left(e-e^{-1}\right)^{-1}\left(e^{+1}-e^{-1}\right)\cdot\left(d^{+1}-d\right)^{-1}\cdot\left(d-d^{-1}\right)^{-1}\left(d^{+1}-d^{-1}\right)\\ \cdot\sum\limits_{X_1,X_2,X_3}^{-1,+1}\left|a-a^{X_1}\right|^{-1}\cdot\left|b-b^{X_2}\right|^{-1}\cdot\left|c-c^{X_3}\right|^{-1}\end{array}\right)}\\
&= \frac{\left|a-a^{X_1}\right|^{-1}\cdot\left|b-b^{X_2}\right|^{-1}\cdot\left|c-c^{X_3}\right|^{-1}\cdot\left|d-d^{X_4}\right|^{-1}\cdot\left|e-e^{X_5}\right|^{-1}}{\left(\begin{array}{l}\left(e^{+1}-e\right)^{-1}\cdot\left(e-e^{-1}\right)^{-1}\left(e^{+1}-e^{-1}\right)\cdot\left(d^{+1}-d\right)^{-1}\cdot\left(d-d^{-1}\right)^{-1}\left(d^{+1}-d^{-1}\right)\\ \left(c^{+1}-c\right)^{-1}\cdot\left(c-c^{-1}\right)^{-1}\left(c^{+1}-c^{-1}\right)\cdot\left(b^{+1}-b\right)^{-1}\cdot\left(b-b^{-1}\right)^{-1}\left(b^{+1}-b^{-1}\right)\\ \cdot\left(a^{+1}-a\right)^{-1}\cdot\left(a-a^{-1}\right)^{-1}\left(a^{+1}-a^{-1}\right)\end{array}\right)}\\
&= \frac{\cancel{\left|a-a^{X_1}\right|^{-1}}\cdot\cancel{\left|b-b^{X_2}\right|^{-1}}\cdot\cancel{\left|c-c^{X_3}\right|^{-1}}\cdot\cancel{\left|d-d^{X_4}\right|^{-1}}\cdot\cancel{\left|e-e^{X_5}\right|^{-1}}}{\left(\begin{array}{l}\cancel{\left|e-e^{X_5}\right|^{-1}}\cdot\left|e-e^{-X_5}\right|^{-1}\cdot\left(e^{+1}-e^{-1}\right)\cdot\cancel{\left|d-d^{X_4}\right|^{-1}}\cdot\left|d-d^{-X_4}\right|^{-1}\cdot\left(d^{+1}-d^{-1}\right)\\ \cdot\cancel{\left|c-c^{X_3}\right|^{-1}}\cdot\left|c-c^{-X_3}\right|^{-1}\cdot\left(c^{+1}-c^{-1}\right)\cdot\cancel{\left|b-b^{X_2}\right|^{-1}}\cdot\left|b-b^{-X_2}\right|^{-1}\cdot\left(b^{+1}-b^{-1}\right)\\ \cdot\cancel{\left|a-a^{X_1}\right|^{-1}}\cdot\left|a-a^{-X_1}\right|^{-1}\cdot\left(a^{+1}-a^{-1}\right)\end{array}\right)}\\
&= \frac{\left|a-a^{-X_1}\right|\cdot\left|b-b^{-X_2}\right|\cdot\left|c-c^{-X_3}\right|\cdot\left|d-d^{-X_4}\right|\cdot\left|e-e^{-X_5}\right|}{\left(e^{+1}-e^{-1}\right)\cdot\left(d^{+1}-d^{-1}\right)\cdot\left(c^{+1}-c^{-1}\right)\cdot\left(b^{+1}-b^{-1}\right)\cdot\left(a^{+1}-a^{-1}\right)}
\end{aligned}
\tag{7-106}
$$

Equation (7-106) is identical to Eq. (7-104). Hence, we have proved that the weighting scheme presented in Section 3.6 is identical to that for a multilinear interpolation scheme, if the interpolation table forms a regular grid with no missing entries.

7.1.12 Laplace and Gradient Operators for the Discoidal Coordinate System

The Laplace operator for the parameterization introduced in Eq. (3-14) can be calculated by substituting Eq. (3-14) in Eq. (3-78) as follows:

$$h_r = \left|\left(\cos v\cos u, \cos v\sin u, \sin v\right)\right| = \left(\cos^2 v\cos^2 u + \cos^2 v\sin^2 u + \sin^2 v\right)^{1/2} \\ = 1 \tag{7-107}$$

$$h_v = \left|\left(-r\sin v\cos u, -r\sin v\sin u, r\cos v\right)\right| = r\left(\sin^2 v\cos^2 u + \sin^2 v\sin^2 u + \cos^2 v\right)^{1/2} \\ = r \tag{7-108}$$

$$h_u = \left|\left(-\left(b + r\cos v\right)\sin u, \left(b + r\cos v\right)\cos u, 0\right)\right| = \left(b + r\cos v\right)\left(\sin^2 u + \cos^2 u\right)^{1/2} \\ = \left(b + r\cos v\right) \tag{7-109}$$

Substituting Eqs. (7-107) - (7-109) in Eq. (3-77) and (3-79) yields:

$$\nabla^2\psi = \frac{1}{1\times r\times\left(b + r\cos v\right)}\left(\frac{\partial}{\partial r}\left(\frac{r\left(b + r\cos v\right)}{b}\frac{\partial\psi}{\partial r}\right) + \frac{\partial}{\partial v}\left(\frac{\left(b + r\cos v\right)\times 1}{r}\frac{\partial\psi}{\partial v}\right) + \frac{\partial}{\partial u}\left(\frac{1\times r}{b + r\cos v}\frac{\partial\psi}{\partial u}\right)\right) \tag{7-110}$$

and

$$\nabla\psi = \frac{\partial\psi}{\partial r}\hat{r} + \frac{1}{r}\frac{\partial\psi}{\partial v}\hat{v} + \frac{\dfrac{\partial\psi}{\partial u}}{b + r\cos v}\hat{u} \tag{7-111}$$

which are identical to Eqs. (3-80) and (3-83), respectively.

7.1.13 Linearization of the Poisson-Boltzmann Equation

The nonlinear Poisson-Boltzmann equation in Eq. (3-92) can be linearized as follows:

$$\left(\xi^4\frac{\partial^2\overline{\psi}}{\partial\xi^2} + \left(\frac{\xi^4 b}{\left(\xi b + b'_{charge}\cos v\right)}\right)\frac{\partial\overline{\psi}}{\partial\xi} + \xi^2\frac{\partial^2\overline{\psi}}{\partial v^2} - \left(\frac{\xi^2 b'_{charge}\sin v}{\left(\xi b + b'_{charge}\cos v\right)}\right)\frac{\partial\overline{\psi}}{\partial v}\right)$$

$$= -\frac{\left(\kappa b'_{charge}\right)^2\sum_i I_{i,0}z_i\exp\left(-z_i\overline{\psi}\right)}{\sum_i I_{i,0}z_i^2} = -\frac{\left(\kappa b'_{charge}\right)^2\sum_i I_{i,0}z_i\left(1 - z_i\overline{\psi}\right)}{\sum_i I_{i,0}z_i^2}$$

$$= -\frac{\left(\kappa b'_{charge}\right)^2\left(\sum_i I_{i,0}z_i - \sum_i I_{i,0}z_i^2\overline{\psi}\right)}{\sum_i I_{i,0}z_i^2} = -\frac{\left(\kappa b'_{charge}\right)^2\left(0 - \sum_i I_{i,0}z_i^2\overline{\psi}\right)}{\sum_i I_{i,0}z_i^2}$$

$$= \left(\kappa b'_{charge}\right)^2 \overline{\psi} \tag{7-112}$$

which is identical to Eq. (3-108).

7.1.14 Laplace and Gradient Operators for the Prolate Ellipsoidal Coordinate System

The Laplace operator for the parameterization introduced in Eq. (3-109) can be calculated by substituting Eq. (3-109) in Eq. (3-78) as follows:

$$\begin{aligned} h_\xi &= \left|\left(f\cosh\xi\sin v\cos u, f\cosh\xi\sin v\sin u, f\sinh\xi\cos v\right)\right| \\ &= f\left(\cosh^2\xi\sin^2 v\cos^2 u + \cosh^2\xi\sin^2 v\sin^2 u + \sinh^2\xi\cos^2 v\right)^{1/2} \\ &= f\left(\cosh^2\xi\sin^2 v + \sinh^2\xi\cos^2 v\right)^{1/2} = f\left(\left(1+\sinh^2\xi\right)\sin^2 v + \sinh^2\xi\left(1-\sin^2 v\right)\right)^{1/2} \\ &= f\left(\sin^2 v + \sinh^2\xi\right)^{1/2} \end{aligned} \tag{7-113}$$

$$\begin{aligned} h_v &= \left|\left(f\sinh\xi\cos v\cos u, f\sinh\xi\cos v\sin u, -f\cosh\xi\sin v\right)\right| \\ &= f\left(\sinh^2\xi\cos^2 v\cos^2 u + \sinh^2\xi\cos^2 v\sin^2 u + \cosh^2\xi\sin^2 v\right)^{1/2} \\ &= f\left(\sinh^2\xi\cos^2 v + \cosh^2\xi\sin^2 v\right)^{1/2} = f\left(\sin^2 v + \sinh^2\xi\right)^{1/2} \end{aligned} \tag{7-114}$$

$$\begin{aligned} h_u &= \left|\left(-f\sinh\xi\sin v\sin u, f\sinh\xi\sin v\cos u, 0\right)\right| \\ &= f\left(\sinh^2\xi\sin^2 v\sin^2 u + \sinh^2\xi\sin^2 v\cos^2 u\right)^{1/2} \\ &= f\sinh\xi\sin v \end{aligned} \tag{7-115}$$

Substituting Eqs. (7-113) - (7-115) in Eq. (3-77) and (3-79) yields:

$$\nabla^2\psi = \frac{1}{f^3\left(\sin^2 v + \sinh^2\xi\right)\sinh\xi\sin v}\left(\begin{aligned} &\frac{\partial}{\partial\xi}\left(f\sinh\xi\sin v\frac{\partial\psi}{\partial\xi}\right) + \frac{\partial}{\partial v}\left(f\sinh\xi\sin v\frac{\partial\psi}{\partial v}\right) \\ &+ \frac{\partial}{\partial u}\left(\frac{\sinh\xi\sin v}{f\left(\sin^2 v + \sinh^2\xi\right)}\frac{\partial\psi}{\partial u}\right) \end{aligned}\right) \tag{7-116}$$

and

$$\nabla\psi = \frac{1}{f\left(\sin^2 v + \sinh^2 \xi\right)^{1/2}} \frac{\partial \psi}{\partial \xi} \hat{\xi} + \frac{1}{f\left(\sin^2 v + \sinh^2 \xi\right)^{1/2}} \frac{\partial \psi}{\partial v} \hat{v} + \frac{\frac{\partial \psi}{\partial u}}{f \sin v \sinh \xi} \hat{u} \quad (7\text{-}117)$$

which are identical to Eqs. (3-111) and (3-112), respectively.

7.1.15 CC Model vs SB Model for the Steric Free Energy of Discoidal Micelles

In Section 3.7.3, the systematic difference between the CC model and the SB model, in the context of the steric free energy, was attributed to the fact that the average of logarithmic terms is smaller than the logarithm of the average of the terms. The proof, which builds on the fact that arithmetic mean is greater than the geometric mean, is shown below:

$$\begin{aligned} &\frac{1}{n}\sum_{i=1}^{n} x_i \geq \left(\prod_{i=1}^{n} x_i\right)^{1/n} \Rightarrow \ln\left(\frac{1}{n}\sum_{i=1}^{n} x_i\right) \geq \ln\left(\left(\prod_{i=1}^{n} x_i\right)^{1/n}\right) \Rightarrow \ln\langle x_i\rangle \geq \frac{1}{n}\ln\left(\prod_{i=1}^{n} x_i\right) \\ &\Rightarrow \ln\langle x_i\rangle \geq \frac{1}{n}\sum_{i=1}^{n} \ln x_i \Rightarrow \ln\langle x_i\rangle \geq \langle \ln x_i\rangle \end{aligned} \quad (7\text{-}118)$$

7.1.16 Calculation of the Error in Modeling $g_{tr,CSMT}$

The errors associated with counting the number of hydrating contacts and with calculating the solvent accessible surface area were obtained using the block-averaging technique.[46, 105] The block-averaging technique yields errors in the fractional degree of hydration, f_i, and in the solvent accessible surface areas, $SASA_i$ and $SASA_{core}$, which are used to calculate the root-mean square error in $g_{tr,CSMT}$. Substituting Eqs. (4-2) and (4-4) in Eq. (2-40) yields:

$$\begin{aligned} g_{tr,CSMT} &= \sum_j \alpha_j \sum_{i_j} \left(1 - f_{i_j}\right) g_{tr,i_j} + \sum_j \alpha_j \sum_{c_j} f_{c_j} \cdot SASA_{c_j} \left(\frac{\sigma_{mix}\left(A_{core} - \sum_j N_j a_{0,j}\right)}{\left(SASA_{core} - \sum_j N_j a_{0,j}\right)} - \frac{-g_{tr,c_j}}{SASA_{c_j}} \right) - \hat{g}_{int} \\ &= \sum_j \alpha_j \left[\sum_{c_j} \left(1 - f_{c_j}\right) g_{tr,c_j} + \sum_{i_j \neq c_j} \left(1 - f_{i_j}\right) g_{tr,i_j} + \sum_{c_j} f_{c_j} \cdot SASA_{c_j} \frac{\sigma_{mix}\left(A_{core} - \sum_j N_j a_{0,j}\right)}{\left(SASA_{core} - \sum_j N_j a_{0,j}\right)} + f_{c_j} g_{tr,c_j} \right] - \hat{g}_{int} \end{aligned}$$

$$= \sum_j \alpha_j \left[\sum_{c_j} g_{tr,c_j} + \sum_{i_j \neq c_j} \left(1 - f_{i_j}\right) g_{tr,i_j} + \sum_{c_j} f_{c_j} \cdot SASA_{c_j} \frac{\sigma_{mix}\left(A_{core} - \sum_j N_j a_{0,j}\right)}{\left(SASA_{core} - \sum_j N_j a_{0,j}\right)} \right] - \hat{g}_{int} \tag{7-119}$$

Let the error in the variable x be denoted by Δx. Accounting solely for the errors from the simulations, that is, for errors arising from the calculation of f_i, $SASA_i$, and $SASA_{core}$, the error in the calculated $g_{tr,CSMT}$ is given by:

$$\begin{aligned}
\Delta g_{tr,CSMT} &= \sum_j \alpha_j \left[\sum_{c_j} \left(\Delta g_{tr,icore_j}\right)^2 + \sum_{i_j \neq c_j} \left(\Delta\left(\left(1 - f_{i_j}\right) g_{tr,i_j}\right)\right)^2 + \sum_{c_j} \left(\Delta\left(f_{c_j} \cdot SASA_{c_j} \frac{\sigma_{mix}\left(A_{core} - \sum_j N_j a_{0,j}\right)}{\left(SASA_{core} - \sum_j N_j a_{0,j}\right)} \right) \right)^2 \right] + \left(\Delta g_{int}\right)^2 \\
&= \sum_j \alpha_j \left[0 + \sum_{i_j \neq c_j} \left(g_{tr,i_j} \Delta f_{i_j}\right)^2 + \sum_{c_j} \left(\sigma_{mix}\left(A_{core} - \sum_j N_j a_{0,j}\right) \Delta\left(\frac{f_{c_j} \cdot SASA_{c_j}}{\left(SASA_{core} - \sum_j N_j a_{0,j}\right)} \right) \right)^2 \right] + 0 \\
&= \sum_j \alpha_j \left[\sum_{i_j \neq c_j} \left(g_{tr,i_j} \Delta f_{i_j}\right)^2 + \sum_{c_j} \left(\sigma_{mix}\left(A_{core} - \sum_j N_j a_{0,j}\right) \Delta\left(\frac{f_{c_j} \cdot SASA_{c_j}}{\left(SASA_{core} - \sum_j N_j a_{0,j}\right)} \right) \right)^2 \right]
\end{aligned} \tag{7-120}$$

$$\left(\frac{\Delta\left(\frac{f_{c_j} \cdot SASA_{c_j}}{SASA_{core} - \sum_j N_j a_{0,j}} \right)}{\frac{f_{c_j} \cdot SASA_{c_j}}{SASA_{core} - \sum_j N_j a_{0,j}}} \right)^2 = \left(\frac{\Delta f_{c_j}}{f_{c_j}} \right)^2 + \left(\frac{\Delta SASA_{c_j}}{SASA_{c_j}} \right)^2 + \left(\frac{\Delta\left(SASA_{core} - \sum_j N_j a_{0,j} \right)}{SASA_{core} - \sum_j N_j a_{0,j}} \right)^2$$

$$= \left(\frac{\Delta f_{c_j}}{f_{c_j}} \right)^2 + \left(\frac{\Delta SASA_{c_j}}{SASA_{c_j}} \right)^2 + \left(\frac{\Delta SASA_{core}}{SASA_{core} - \sum_j N_j a_{0,j}} \right)^2 \tag{7-121}$$

Substituting Eq. (7-121) in Eq. (7-120) yields the error in $g_{tr,CSMT}$.

7.2 Packing Polynomials

The packing polynomials used to calculate the packing free energy for the surfactants considered in this thesis are listed in this section. The polynomial function is specific to the surfactant tail, or to be surfactant tail mixture, as well as to the micelle shape. For a single surfactant system packed in one of the three regular shapes, namely, spheres, infinite cylinders, or infinite bilayers, the polynomial is of the form:

$$g_{pack} = \sum_{n=0}^{6} a_n \left(r / r_{rel} \right)^n \tag{7-122}$$

where r is the half-thickness in the case of an infinite bilayer, and is the radius in the case of an infinite cylinder or a sphere, r_{rel} is a length parameter, and a_n are the polynomial coefficients. The upper and lower limits on r are r_{max} and r_{min}, respectively.

For the biaxial ellipsoidal case or for the discoidal case, the polynomial is a function of two size variables, since two parameters are required to uniquely define their size. Therefore, the polynomial is of the form:

$$g_{pack,prolate} = \sum_{j=0}^{4} \sum_{i=0}^{4} a_{ij} \left(p / p_{rel} \right)^i \left(q / p_{rel} \right)^j \tag{7-123}$$

$$g_{pack,oblate} = \sum_{j=0}^{4} \sum_{i=0}^{4} a_{ij} \left(q / q_{rel} \right)^i \left(p / q_{rel} \right)^j \tag{7-124}$$

$$g_{pack,disc} = \sum_{j=0}^{6} \sum_{i=0}^{6} a_{ij} \left(b' / r_{rel} \right)^i \left(b / q_{rel} \right)^j \tag{7-125}$$

where p and q are the two semi-axis lengths as shown in Figure 3-2, b and b' are the size variables associated with a discoidal micelle as shown in Figure 3-1 p_{rel}, q_{rel}, and r_{rel} are length

parameters, and a_{ij} are the polynomial coefficients. In the case of a prolate ellipsoid, an oblate ellipsoid, and a disc, the upper limits on p, q, and b' are p_{max}, q_{max}, and b'_{max}, respectively, and the lower limits on p, q, and b' are p_{min}, q_{min}, and b'_{min}, respectively. In addition, the polynomial has been fitted using data for aspect ratios varying between $(q/p)_{min}$ and $(q/p)_{max}$, for prolate ellipsoids, $(p/q)_{min}$ and $(p/q)_{max}$, for oblate ellipsoids, and $(b/b')_{min}$ and $(b/b')_{max}$, for discs. All the polynomial coefficients, parameters, and limits introduced above are listed in the parameter table.

For the case of binary mixtures of surfactants forming spherical, cylindrical, and bilayer-like micelles, the polynomial is a function of r and the micelle composition of the surfactant with the shorter tail, α. Therefore, the polynomial is of the form:

$$g_{pack} = \sum_{j=0}^{2} \sum_{i=0}^{4} a_{ij} \left(r / r_{rel} \right)^{i} \alpha^{j} \tag{7-126}$$

where a_{ij} are the polynomial coefficients. In addition, the parameter α_0, and the limits $r_{max,short}$ and $r_{max,long}$ introduced in Section 5.2.1, are also tabulated along with the coefficient table. Note that to minimize the number of parameters, r_{rel} in Eq. (7-126) is chosen to be $r_{max,short}$.

7.2.1 Packing Polynomials for Single Fluorocarbon Tails in Spheres, Cylinders, and Bilayers

n_c	Shape	r_{min} (Å)	r_{max} (Å)	r_{rel} (Å)	a_0	a_1	a_2	a_3	a_4	a_5	a_6
5	Bilayer	2.6	7.4	6.5	24.86	-186.7	611.9	-1046	982.4	-482.9	98.22
5	Cylinder	2.6	7.9	6.5	39.90	-267.0	790.7	-1252	1112	-525.2	103.3
5	Sphere	2.6	7.9	6.5	132.8	-893.2	2568	-3937	3379	-1537	288.9
6	Bilayer	3.1	9.1	7.8	6.955	-31.75	71.31	-72.36	28.21	0.0	0.0
6	Cylinder	3.1	9.1	7.8	44.44	-295.8	861.5	-1331	1145	-520.7	98.10
6	Sphere	3.1	9.1	7.8	115.6	-737.4	2009	-2908	2346	-998.3	175.1
7	Bilayer	3.2	10.1	9.1	31.83	-264.0	959.9	-1857	2012	-1159	278.2
7	Cylinder	3.2	10.5	9.1	20.48	-99.77	214.8	-227.3	115.3	-21.72	0.0
7	Sphere	3.2	10.5	9.1	160.1	-1130	3416	-5520	4993	-2390	472.1

n_c is the number of carbon atoms in the fluorocarbon tail

7.2.2 Packing Polynomials for Single Hydrocarbon Tails in Spheres, Cylinders, and Bilayers

n_c	Shape	r_{min} (Å)	r_{max} (Å)	r_{rel} (Å)	a_0	a_1	a_2	a_3	a_4	a_5	a_6
6	Bilayer	2.7	8.2	7.7	7.667	-37.53	89.98	-94.78	38.68	0.0	0.0
6	Cylinder	2.7	9.1	7.7	20.32	-111.0	274.8	-338.6	204.1	-47.53	0.0
6	Sphere	2.7	9.1	7.7	117.1	-846.8	2616	-4279	3887	-1856	364.1
8	Bilayer	3.6	10.5	9.7	6.653	-29.46	68.48	-73.36	31.08	0.0	0.0
8	Cylinder	3.6	10.5	9.7	15.40	-66.26	128.6	-113.1	37.60	0.0	0.0
8	Sphere	3.6	11.3	9.7	165.9	-1310	4420	-7927	7932	-4191	912.9
9	Bilayer	4.0	11.4	10.9	6.479	-28.57	67.58	-74.29	32.59	0.0	0.0
9	Cylinder	4.0	12.3	10.9	12.35	-47.55	87.47	-74.49	24.47	0.0	0.0
9	Sphere	4.0	12.3	10.9	62.39	-367.4	917.3	-1143	703.2	-170.4	0.0
10	Bilayer	4.5	12.1	11.1	7.313	-31.45	69.26	-70.16	28.09	0.0	0.0
10	Cylinder	4.5	13.2	11.1	12.86	-47.03	82.10	-66.40	20.67	0.0	0.0
10	Sphere	4.5	13.7	11.1	88.300	-574.5	1635	-2482	2106	-942.6	173.9
11	Bilayer	4.9	13.4	12.8	7.381	-33.23	76.95	-82.43	35.17	0.0	0.0
11	Cylinder	4.9	13.9	12.8	13.80	-54.54	101.3	-86.71	28.50	0.0	0.0
11	Sphere	4.9	14.5	12.8	110.9	-814.8	2593	-4391	4140	-2056	420.0
12	Bilayer	5.4	13.9	13.3	7.071	-29.96	66.93	-69.61	29.07	0.0	0.0
12	Cylinder	5.4	15.2	13.3	12.73	-46.36	81.62	-67.04	21.36	0.0	0.0
12	Sphere	5.4	15.8	13.3	48.95	-259.6	600.9	-699.4	403.9	-91.95	0.0

n_c is the number of carbon atoms in the hydrocarbon tail.

7.2.3 Packing Polynomials for Surfactant Tails in Biaxial Ellipsoidal Micelles and Discoidal Micelles

a. 5-Carbon Fluorocarbon Tail

Shape: Prolate Ellipsoid

Parameter Table

p_{min}	2.6152 Å
p_{max}	7.6822 Å
p_{rel}	6.5380 Å
$(q/p)_{min}$	1.0
$(q/p)_{max}$	3.0

Coefficient Table

	1	q/p_{rel}	$(q/p_{rel})^2$	$(q/p_{rel})^3$	$(q/p_{rel})^4$
1	89.72	-174.75	131.18	-32.67	0.0
p/p_{rel}	-380.56	752.49	-555.73	137.12	0.0
$(p/p_{rel})^2$	623.67	-1214.52	880.30	-214.69	0.0
$(p/p_{rel})^3$	-452.59	865.63	-615.97	148.39	0.0
$(p/p_{rel})^4$	122.06	-229.27	160.41	-38.18	0.0

Shape: Oblate Ellipsoid

Parameter Table

q_{min}	2.6152 Å
q_{max}	7.6822 Å
q_{rel}	6.5380 Å
$(p/q)_{min}$	1.0
$(p/q)_{max}$	3.0

Coefficient Table

	1	p/q_{rel}	$(p/q_{rel})^2$	$(p/q_{rel})^3$	$(p/q_{rel})^4$
1	75.6089	-286.36	389.62	-218.18	43.21
q/q_{rel}	-213.37	949.83	-1379.95	804.65	-164.25
$(q/q_{rel})^2$	197.42	-1126.90	1795.54	-1099.75	232.25
$(q/q_{rel})^3$	-41.73	538.55	-1004.59	657.60	-144.61
$(q/q_{rel})^4$	-14.98	-76.84	200.43	-144.59	33.42

b. 6-Carbon Fluorocarbon Tail

Shape: Prolate Ellipsoid

Parameter Table

p_{min}	3.1140 Å
p_{max}	8.8069 Å
p_{rel}	7.7851 Å
$(q/p)_{min}$	1.0
$(q/p)_{max}$	4.0

Coefficient Table

	1	q/p_{rel}	$(q/p_{rel})^2$	$(q/p_{rel})^3$	$(q/p_{rel})^4$
1	81.18	-122.77	80.97	-18.65	0.0
p/p_{rel}	-354.69	529.76	-339.43	78.21	0.0
$(p/p_{rel})^2$	610.28	-869.89	536.69	-122.88	0.0
$(p/p_{rel})^3$	-470.11	638.66	-377.90	85.59	0.0
$(p/p_{rel})^4$	135.53	-175.99	99.766	-22.28	0.0

Shape: Oblate Ellipsoid

Parameter Table

q_{min}	3.1140 Å
q_{max}	9.1475 Å
q_{rel}	7.7851 Å
$(p/q)_{min}$	1.0
$(p/q)_{max}$	4.0

Coefficient Table

	1	p/q_{rel}	$(p/q_{rel})^2$	$(p/q_{rel})^3$	$(p/q_{rel})^4$
1	92.38	-233.27	237.37	-106.58	17.60
q/q_{rel}	-362.89	896.24	-888.73	397.97	-66.62
$(q/q_{rel})^2$	577.51	-1343.28	1275.46	-562.17	94.74
$(q/q_{rel})^3$	-418.01	915.66	-826.37	355.19	-59.93
$(q/q_{rel})^4$	113.57	-236.27	202.79	-84.52	14.22

Shape: Disc

Parameter Table

b'_{min}	3.1140 Å
b'_{max}	8.4463 Å
r_{rel}	7.7851 Å
$(b/b')_{min}$	1.0
$(b/b')_{max}$	5.0

Coefficient Table

	1	b/r_{rel}	$(b/r_{rel})^2$	$(b/r_{rel})^3$	$(b/r_{rel})^4$	$(b/r_{rel})^5$	$(b/r_{rel})^6$
1	75.9	-481.4	1205	-1434	924.8	-315	44.0
b'/r_{rel}	-395	2804	-7085	8314	-5350	1851	-267
$(b'/r_{rel})^2$	795	-6542	16946	-19666	12643	-4469	670
$(b'/r_{rel})^3$	-643	7562	-20792	24044	-15514	5646	-886
$(b'/r_{rel})^4$	6.28	-4257	13484	-15784	10321	-3918	651
$(b'/r_{rel})^5$	270	863.4	-4175	5128	-3469	1406	-252
$(b'/r_{rel})^6$	-107	51.94	418.6	-602.8	444.3	-201	40.0

c. 7-Carbon Fluorocarbon Tail

Shape: Prolate Ellipsoid

Parameter Table

p_{min}	3.1915 Å
p_{max}	10.4865 Å
p_{rel}	9.1187 Å
$(q/p)_{min}$	1.0
$(q/p)_{max}$	3.0

Coefficient Table

	1	q/p_{rel}	$(q/p_{rel})^2$	$(q/p_{rel})^3$	$(q/p_{rel})^4$
1	115.73	-257.14	221.73	-65.10	0.0
p/p_{rel}	-501.98	1106.46	-932.18	272.74	0.0
$(p/p_{rel})^2$	855.72	-1814.32	1478.33	-428.00	0.0
$(p/p_{rel})^3$	-657.89	1335.06	-1045.8	297.93	0.0
$(p/p_{rel})^4$	190.48	-370.12	277.98	-77.59	0.0

Shape: Oblate Ellipsoid

Parameter Table

q_{min}	3.1915 Å
q_{max}	10.4865 Å
q_{rel}	9.1187 Å
$(p/q)_{min}$	1.0
$(p/q)_{max}$	3.0

Coefficient Table

	1	p/q_{rel}	$(p/q_{rel})^2$	$(p/q_{rel})^3$	$(p/q_{rel})^4$
1	141.44	-499.73	698.15	-430.48	96.49
q/q_{rel}	-531.42	1833.84	-2538.34	1591.38	-366.55
$(q/q_{rel})^2$	832.83	-2664.73	3541.67	-2220.97	522.41
$(q/q_{rel})^3$	-619.05	1811.20	-2254.12	1389.31	-331.30
$(q/q_{rel})^4$	178.55	-481.09	552.87	-329.25	78.95

d. 6-Carbon Hydrocarbon Tail

Shape: Prolate Ellipsoid

Parameter Table

p_{min}	2.6811 Å
p_{max}	9.1158 Å
p_{rel}	7.6603 Å
$(q/p)_{min}$	1.0
$(q/p)_{max}$	4.0

Coefficient Table

	1	q/p_{rel}	$(q/p_{rel})^2$	$(q/p_{rel})^3$	$(q/p_{rel})^4$
1	62.44	-97.64	62.33	-13.63	0.0
p/p_{rel}	-282.64	444.97	-270.49	57.66	0.0
$(p/p_{rel})^2$	508.77	-771.82	444.59	-91.63	0.0
$(p/p_{rel})^3$	-406.28	594.37	-325.35	64.64	0.0
$(p/p_{rel})^4$	119.90	-169.86	88.91	-17.03	0.0

Shape: Oblate Ellipsoid

Parameter Table

q_{min}	2.6811 Å
q_{max}	9.1158 Å
q_{rel}	7.6603 Å
$(p/q)_{min}$	1.0
$(p/q)_{max}$	4.0

Coefficient Table

	1	p/q_{rel}	$(p/q_{rel})^2$	$(p/q_{rel})^3$	$(p/q_{rel})^4$
1	59.36	-168.30	186.33	-87.85	14.83
q/q_{rel}	-223.12	647.48	-705.9	332.52	-56.69
$(q/q_{rel})^2$	349.43	-975.67	1027.00	-476.70	81.45
$(q/q_{rel})^3$	-247.99	666.40	-673.77	305.69	-52.05
$(q/q_{rel})^4$	64.615	-170.13	166.54	-73.70	12.468

7.2.4 Packing Polynomials for Binary Mixtures of Surfactants in Spheres, Cylinders, and Bilayers

a. Packing Polynomial for a Binary Mixture of Octyl and Undecyl Hydrocarbon Tails

Shape: Bilayer

Parameter Table

$n_{c,short}$	8
$n_{c,long}$	11
r_{min}	4.9 Å
$r_{max,short}$	10.6 Å
$r_{max,long}$	13.4 Å
α_0	0.333

Coefficient Table

	1	α	α^2
1	0.4312	-5.984	-0.4666
r/r_{rel}	8.970	22.96	8.185
$(r/r_{rel})^2$	-16.34	-28.41	-23.58
$(r/r_{rel})^3$	9.328	11.01	18.62
$(r/r_{rel})^4$	0.0	0.0	0.0

Shape: Cylinder

Parameter Table

$n_{c,short}$	8
$n_{c,long}$	11
r_{min}	4.9 Å
$r_{max,short}$	11.1 Å
$r_{max,long}$	13.9 Å
α_0	0.101

Coefficient Table

	1	α	α^2
1	6.214	-1.094	0.0
r/r_{rel}	-8.207	0.2906	0.0
$(r/r_{rel})^2$	4.124	1.031	0.0
$(r/r_{rel})^3$	0.0	0.0	0.0
$(r/r_{rel})^4$	0.0	0.0	0.0

Shape: Sphere

Parameter Table

$n_{c,short}$	8
$n_{c,long}$	11
r_{min}	4.9 Å
$r_{max,short}$	11.1 Å
$r_{max,long}$	14.5 Å
α_0	0.150

Coefficient Table

	1	α	α^2
1	30.64	-19.21	0.0
r/r_{rel}	-110.7	79.15	0.0
$(r/r_{rel})^2$	169.6	-126.7	0.0
$(r/r_{rel})^3$	-117.0	89.87	0.0
$(r/r_{rel})^4$	30.21	-23.48	0.0

b. Packing Polynomials for a Binary Mixture of Nonyl and Undecyl Hydrocarbon Tails

Shape: Bilayer

Parameter Table

$n_{c,short}$	9
$n_{c,long}$	11
r_{min}	4.9 Å
$r_{max,short}$	11.1 Å
$r_{max,long}$	13.4 Å
α_0	0.242

Coefficient Table

	1	α	α^2
1	0.2712	-6.620	3.250
r/r_{rel}	10.16	28.55	-12.27
$(r/r_{rel})^2$	-19.07	-40.51	12.88
$(r/r_{rel})^3$	11.25	18.90	-2.736
$(r/r_{rel})^4$	0.0	0.0	0.0

Shape: Cylinder

Parameter Table

$n_{c,short}$	9
$n_{c,long}$	11
r_{min}	4.9 Å
$r_{max,short}$	12.2 Å
$r_{max,long}$	13.9 Å
α_0	0.116

Coefficient Table

	1	α	α^2
1	6.224	-0.7810	0.0
r/r_{rel}	-9.114	0.3210	0.0
$(r/r_{rel})^2$	5.122	0.7168	0.0
$(r/r_{rel})^3$	0.0	0.0	0.0
$(r/r_{rel})^4$	0.0	0.0	0.0

Shape: Sphere

Parameter Table

$n_{c,short}$	9
$n_{c,long}$	11
r_{min}	4.9 Å
$r_{max,short}$	12.2 Å
$r_{max,long}$	14.5 Å
α_0	0.131

Coefficient Table

	1	α	α^2
1	30.66	-13.32	0.0
r/r_{rel}	-122.1	59.01	0.0
$(r/r_{rel})^2$	206.1	-100.7	0.0
$(r/r_{rel})^3$	-156.5	75.52	0.0
$(r/r_{rel})^4$	44.48	-20.69	0.0

c. Packing Polynomials for a Binary Mixture of Decyl and Undecyl Hydrocarbon Tails

Shape: Bilayer

Parameter Table

$n_{c,short}$	10
$n_{c,long}$	11
r_{min}	4.9 Å
$r_{max,short}$	12.2 Å
$r_{max,long}$	13.4 Å
α_0	0.355

Coefficient Table

	1	α	α^2
1	-0.2644	-0.9448	0.0
r/r_{rel}	13.70	4.880	0.0
$(r/r_{rel})^2$	-26.81	-9.433	0.0
$(r/r_{rel})^3$	16.69	6.415	0.0
$(r/r_{rel})^4$	0.0	0.0	0.0

Shape: Cylinder

Parameter Table

$n_{c,short}$	10
$n_{c,long}$	11
r_{min}	4.9 Å
$r_{max,short}$	13.4 Å
$r_{max,long}$	13.9 Å
α_0	0.267

Coefficient Table

	1	α	α^2
1	6.243	-0.3587	0.0
r/r_{rel}	-10.06	0.0217	0.0
$(r/r_{rel})^2$	6.240	0.5340	0.0
$(r/r_{rel})^3$	0.0	0.0	0.0
$(r/r_{rel})^4$	0.0	0.0	0.0

Shape: Sphere

Parameter Table

$n_{c,short}$	10
$n_{c,long}$	11
r_{min}	4.9 Å
$r_{max,short}$	13.4 Å
$r_{max,long}$	14.5 Å
α_0	0.278

Coefficient Table

	1	α	α^2
1	30.48	-6.374	0.0
r/r_{rel}	-131.9	28.38	0.0
$(r/r_{rel})^2$	241.7	-47.47	0.0
$(r/r_{rel})^3$	-199.4	33.70	0.0
$(r/r_{rel})^4$	61.52	-8.254	0.0

d. Packing Polynomials for a Binary Mixture of Decyl and Dodecyl Hydrocarbon Tails

Shape: Bilayer

Parameter Table

$n_{c,short}$	10
$n_{c,long}$	12
r_{min}	5.4 Å
$r_{max,short}$	12.1 Å
$r_{max,long}$	13.9 Å
α_0	0.262

Coefficient Table

	1	α	α^2
1	-0.4975	-0.1822	0.0
r/r_{rel}	13.59	1.695	0.0
$(r/r_{rel})^2$	-23.82	-6.122	0.0
$(r/r_{rel})^3$	13.32	5.914	0.0
$(r/r_{rel})^4$	0.0	0.0	0.0

Shape: Cylinder

Parameter Table

$n_{c,short}$	10
$n_{c,long}$	12
r_{min}	5.4 Å
$r_{max,short}$	13.3 Å
$r_{max,long}$	15.2 Å
α_0	0.262

Coefficient Table

	1	α	α^2
1	6.315	-0.7817	0.0
r/r_{rel}	-9.407	0.5029	0.0
$(r/r_{rel})^2$	5.390	0.5075	0.0
$(r/r_{rel})^3$	0.0	0.0	0.0
$(r/r_{rel})^4$	0.0	0.0	0.0

Shape: Sphere

Parameter Table

$n_{c,short}$	10
$n_{c,long}$	12
r_{min}	5.4 Å
$r_{max,short}$	13.3 Å
$r_{max,long}$	15.8 Å
α_0	0.231

Coefficient Table

	1	α	α^2
1	28.13	-11.03	0.0
r/r_{rel}	-109.5	49.96	0.0
$(r/r_{rel})^2$	183.3	-80.45	0.0
$(r/r_{rel})^3$	-139.0	59.15	0.0
$(r/r_{rel})^4$	39.54	-15.79	0.0

e. Packing Polynomials for a Binary Mixture of Undecyl and Dodecyl Hydrocarbon Tails

Shape: Bilayer

Parameter Table

$n_{c,short}$	11
$n_{c,long}$	12
r_{min}	5.4 Å
$r_{max,short}$	13.3 Å
$r_{max,long}$	13.9 Å
α_0	0.268

Coefficient Table

	1	α	α^2
1	0.4684	-1.440	0.0
r/r_{rel}	10.40	7.290	0.0
$(r/r_{rel})^2$	-22.15	-13.09	0.0
$(r/r_{rel})^3$	14.75	8.166	0.0
$(r/r_{rel})^4$	0.0	0.0	0.0

Shape: Cylinder

Parameter Table

$n_{c,short}$	11
$n_{c,long}$	12
r_{min}	5.4 Å
$r_{max,short}$	13.9 Å
$r_{max,long}$	15.2 Å
α_0	0.280

Coefficient Table

	1	α	α^2
1	6.329	-0.3745	0.0
r/r_{rel}	-9.913	0.2019	0.0
$(r/r_{rel})^2$	5.990	0.3006	0.0
$(r/r_{rel})^3$	0.0	0.0	0.0
$(r/r_{rel})^4$	0.0	0.0	0.0

Shape: Sphere

Parameter Table

$n_{c,short}$	11
$n_{c,long}$	12
r_{min}	5.4 Å
$r_{max,short}$	14.6 Å
$r_{max,long}$	15.2 Å
α_0	0.159

Coefficient Table

	1	α	α^2
1	29.69	-7.189	0.0
r/r_{rel}	-129.7	36.16	0.0
$(r/r_{rel})^2$	242.5	-69.09	0.0
$(r/r_{rel})^3$	-205.1	58.06	0.0
$(r/r_{rel})^4$	65.06	-17.81	0.0

f. Packing Polynomials for a Binary Mixture of Perfluorohexyl Fluorocarbon Tail and Nonyl Hydrocarbon Tail

Shape: Bilayer

Parameter Table

$n_{c,short}$	6
$n_{c,long}$	9
r_{min}	4.0 Å
$r_{max,short}$	8.6 Å
$r_{max,long}$	11.4 Å
α_0	0.615

Coefficient Table

	1	α	α^2
1	-0.6454	-0.3282	0.0
r/r_{rel}	12.76	2.686	0.0
$(r/r_{rel})^2$	-20.22	-9.547	0.0
$(r/r_{rel})^3$	10.11	8.512	0.0
$(r/r_{rel})^4$	0.0	0.0	0.0

Shape: Cylinder

Parameter Table

$n_{c,short}$	6
$n_{c,long}$	9
r_{min}	4.0 Å
$r_{max,short}$	9.1 Å
$r_{max,long}$	12.3 Å
α_0	0.330

Coefficient Table

	1	α	α^2
1	6.098	-1.593	0.0
r/r_{rel}	-8.035	1.044	0.0
$(r/r_{rel})^2$	4.008	0.5285	0.0
$(r/r_{rel})^3$	0.0	0.0	0.0
$(r/r_{rel})^4$	0.0	0.0	0.0

Shape: Sphere

Parameter Table

$n_{c,short}$	6
$n_{c,long}$	9
r_{min}	4.0 Å
$r_{max,short}$	9.1 Å
$r_{max,long}$	12.8 Å
α_0	0.145

Coefficient Table

	1	α	α^2
1	32.84	-16.19	0.0
r/r_{rel}	-116.9	60.56	0.0
$(r/r_{rel})^2$	172.6	-85.77	0.0
$(r/r_{rel})^3$	-113.8	53.00	0.0
$(r/r_{rel})^4$	27.93	-11.74	0.0

g. Packing Polynomials for a Binary Mixture of Perfluorohexyl Fluorocarbon Tail and Decyl Hydrocarbon Tail

Shape: Bilayer

Parameter Table

$n_{c,short}$	6
$n_{c,long}$	10
r_{min}	4.5 Å
$r_{max,short}$	9.1 Å
$r_{max,long}$	12.1 Å
α_0	0.645

Coefficient Table

	1	α	α^2
1	0.5987	-11.27	0.3035
r/r_{rel}	7.404	43.54	7.541
$(r/r_{rel})^2$	-12.67	-55.89	-26.07
$(r/r_{rel})^3$	6.759	23.30	20.93
$(r/r_{rel})^4$	0.0	0.0	0.0

Shape: Cylinder

Parameter Table

$n_{c,short}$	6
$n_{c,long}$	10
r_{min}	4.5 Å
$r_{max,short}$	9.1 Å
$r_{max,long}$	13.2 Å
α_0	0.230

Coefficient Table

	1	α	α^2
1	6.117	-2.168	1.286
r/r_{rel}	-7.300	2.496	-4.177
$(r/r_{rel})^2$	3.383	-1.106	3.579
$(r/r_{rel})^3$	0.0	0.0	0.0
$(r/r_{rel})^4$	0.0	0.0	0.0

Shape: Sphere

Parameter Table

$n_{c,short}$	6
$n_{c,long}$	10
r_{min}	4.5 Å
$r_{max,short}$	9.1 Å
$r_{max,long}$	13.7 Å
α_0	0.160

Coefficient Table

	1	α	α^2
1	17.71	-9.689	0.0
r/r_{rel}	-37.28	21.49	0.0
$(r/r_{rel})^2$	30.75	-17.25	0.0
$(r/r_{rel})^3$	-8.518	4.758	0.0
$(r/r_{rel})^4$	0.0	0.0	0.0

h. Packing Polynomials for a Binary Mixture of Perfluorohexyl Fluorocarbon Tail and Undecyl Hydrocarbon Tail

Shape: Bilayer

Parameter Table

$n_{c,short}$	6
$n_{c,long}$	11
r_{min}	4.9 Å
$r_{max,short}$	8.9 Å
$r_{max,long}$	13.4 Å
α_0	0.725

Coefficient Table

	1	α	α^2
1	0.1159	-9.854	4.153
r/r_{rel}	8.390	35.53	-8.045
$(r/r_{rel})^2$	-12.16	-42.80	-4.666
$(r/r_{rel})^3$	5.634	16.40	11.14
$(r/r_{rel})^4$	0.0	0.0	0.0

Shape: Cylinder

Parameter Table

$n_{c,short}$	6
$n_{c,long}$	11
r_{min}	4.9 Å
$r_{max,short}$	8.9 Å
$r_{max,long}$	13.9 Å
α_0	0.194

Coefficient Table

	1	α	α^2
1	6.201	-2.215	1.157
r/r_{rel}	-6.628	2.139	-3.740
$(r/r_{rel})^2$	2.761	-0.9304	3.265
$(r/r_{rel})^3$	0.0	0.0	0.0
$(r/r_{rel})^4$	0.0	0.0	0.0

Shape: Sphere

Parameter Table

$n_{c,short}$	6
$n_{c,long}$	11
r_{min}	4.9 Å
$r_{max,short}$	8.9 Å
$r_{max,long}$	14.5 Å
α_0	0.091

Coefficient Table

	1	α	α^2
1	17.06	-9.155	0.0
r/r_{rel}	-31.58	17.14	0.0
$(r/r_{rel})^2$	23.18	-11.95	0.0
$(r/r_{rel})^3$	-5.745	2.981	0.0
$(r/r_{rel})^4$	0.0	0.0	0.0

i. Packing Polynomials for a Binary Mixture of Perfluoroheptyl Fluorocarbon Tail and Octyl Hydrocarbon Tail

Shape: Bilayer

Parameter Table

$n_{c,short}$	7
$n_{c,long}$	8
r_{min}	3.6 Å
$r_{max,short}$	10.1 Å
$r_{max,long}$	10.1 Å
α_0	1.000

Coefficient Table

	1	α	α^2
1	6.313	8.964	0.0
r/r_{rel}	-28.38	-65.38	0.0
$(r/r_{rel})^2$	68.62	168.7	0.0
$(r/r_{rel})^3$	-76.91	-186.7	0.0
$(r/r_{rel})^4$	34.28	74.84	0.0

Shape: Cylinder

Parameter Table

$n_{c,short}$	7
$n_{c,long}$	8
r_{min}	3.6 Å
$r_{max,short}$	10.5 Å
$r_{max,long}$	10.9 Å
α_0	0.890

Coefficient Table

	1	α	α^2
1	5.984	-0.1165	0.0
r/r_{rel}	-10.11	-0.6915	0.0
$(r/r_{rel})^2$	6.524	0.5994	0.0
$(r/r_{rel})^3$	0.0	0.0	0.0
$(r/r_{rel})^4$	0.0	0.0	0.0

Shape: Sphere

Parameter Table

$n_{c,short}$	7
$n_{c,long}$	8
r_{min}	3.6 Å
$r_{max,short}$	10.5 Å
$r_{max,long}$	11.3 Å
α_0	0.200

Coefficient Table

	1	α	α^2
1	69.69	27.78	0.0
r/r_{rel}	-442.5	-203.0	0.0
$(r/r_{rel})^2$	1177	585.9	0.0
$(r/r_{rel})^3$	-1555	-843.8	0.0
$(r/r_{rel})^4$	1012	603.9	0.0
$(r/r_{rel})^5$	-258.9	-171.1	0.0

7.3 Molecular Descriptors of Surfactants

The molecular descriptors associated with the MT modeling of a surfactant includes: (i) the surfactant tail volume, v_{tail}, (ii) the surfactant tail length, l_{tail}, (iii) the shielding area, a_0, (iv) the interfacial tension between the tail phase and water, σ_o, (v) the tolman length, δ, (vi) the head area, a_h, (vii) the head length, h_l, (viii) the distance of the charge from the head-tail junction, d_{charge}, and (ix) the radius of the counterion, r_{ion}. Equations to calculate the values of descriptors (i) – (v) are presented in Section 2.3. The values of the remaining descriptors are listed in Table 7-1.

Note that the head areas, a_h, for the alkyl ethoxylates in Table 7-1 are only used in the MT framework. All the other molecular descriptors are used in both the MT and the CSMT frameworks. Note that the head areas of the alkyl ethoxylates in Table 7-1 are not used with the CSMT model because these were specifically derived for the MT model.[17] The head area was calculated as the ratio of the head volume and the head length. The head volume, v_{head}, is proportional to the number of ethoxylate units, j. The head length was calculated using concepts from scaling theories of polymers which yielded $a_{h,j} = a_{h,0}\ (j)^{0.8}$. The parameter $a_{h,0}$ was fitted to yield reasonable agreement between the predicted and the experimental CMC of C12E6.[17] Since the transfer free energy of the alkyl ethoxylates in the MT framework is significantly different from that in the CSMT framework (for example, the transfer free energy of C12E6 is -19.95 kT in the MT framework and -22.52 kT in the CSMT framework), the a_h values were recalculated for the CSMT framework.

To calculate a_h for alkyl ethoxylates, a procedure similar to the one described above was followed. In our approach, the head volume, v_{head}, is proportional to j, similar to what was used

by Puvvada and Blankschtein in deriving their equation for $a_{h,j}$ shown above.[17] However, the length of the ethoxylate head was calculated based on the study by Sarmoria and Blankschtein.[167]. Using the data presented by Sarmoria and Blankschtein,[167] one can show that the head length of PEO chains is proportional to $j^{0.53}$, for j varying between 4 and 10. Therefore, the head area of the ethoxylate head, $a_{h,j}$, is proportional to $j^1/j^{0.53} = j^{0.47}$, i.e., $a_{h,j} = a_{h,i}\,(j/i)^{0.47}$. By varying $a_{h,6}$, the CMC predicted using the CSMT framework can be matched to the experimental CMC for C12E6. This yields a value of $a_{h,6}$ = 65.3 Å^2, which was subsequently used to make predictions using the CSMT framework.

Table 7-1: Molecular Descriptors of the Surfactants Considered.

	a_h (Å^2)	h_l (Å)	d_{charge} (Å)	r_{ion} (Å)
C10SUL	24.9	4.29	2.89	2.18
C12SUL	24.9	4.29	2.89	2.18
C10GLU	40.0	-	-	-
C8E4	28.3	-	-	-
C12E8	52.9	-	-	-
C12E6	42.0	-	-	-
C10E4	28.3	-	-	-
LiPFOS	29.8	3.55	2.15	2.43
OG	40.0	-	-	-
SPFO	29.8	4.31	2.91	2.18
SDO	21.0	4.31	2.91	2.18

Bibliography

1. Tanford, C., *The Hydrophobic Effect: Formation of Micelles and Biological Membranes*. John Wiley & Sons, Inc.: 1980.
2. Rosen, M. J., *Surfactants and Interfacial Phenomena*. John Wiley & Sons, Inc.: 2004.
3. Bryce, H. G., Industrial and utilitarian aspects of fluorine chemistry. In *Fluorine Chemistry*, Simons, J. H., Ed. Academic Press: 1964; Vol. 5.
4. Coltharp, K. A.; Franses, E. I., Equilibrium and dynamic surface tension behavior of aqueous soaps: Sodium octanoate and sodium dodecanoate (sodium laurate). *Colloids Surf., A* **1996,** *108* (2-3), 225-242.
5. Kissa, E., *Fluorinated Surfactants*. Marcel Dekker: 1994; Vol. 50.
6. Simons, J. H.; Brice, T. J., Fluorocarbon Chemistry. In *Fluorine Chemistry*, Simons, J. H., Ed. Academic Press: 1964; Vol. 5.
7. Carraway, E. R.; Schlautman, M. A.; An, Y.-J., Solubilization of polycyclic aromatic hydrocarbons by perfluorinated surfactant micelles. *Water Res.* **2002,** *36* (1), 300-308.
8. Shinoda, K.; Nakagawa, T.; Tamamushi, B.-I.; Isemura, T., *Colloidal Surfactants: Some Physiochemical Properties*. Academic Press, Inc. : 1963.
9. Harkins, W. D., A general theory of the mechanism of emulsion polymerization. *J. Am. Chem. Soc.* **1947,** *69* (6), 1428-1444.
10. Hekster, F. M.; Laane, R. W. P. M.; de Voogt, P., Environmental and toxicity effects of perfluoroalkylated substances. *Reviews of Environmental Contamination and Toxicology, Vol 179* **2003,** *179*, 99-121.
11. Upham, B. L.; Deocampo, N. D.; Wurl, B.; Trosko, J. E., Inhibition of gap junctional intercellular communication by perfluorinated fatty acids is dependent on the chain length of the fluorinated tail. *Int. J. Cancer* **1998,** *78* (4), 491-495.
12. Wang, K.; Karlsson, G.; Almgren, M.; Asakawa, T., Aggregation behavior of cationic fluorosurfactants in water and salt solutions. A cryoTEM survey. *J. Phys. Chem. B* **1999,** *103* (43), 9237-9246.

13. Al-Anber, Z. A.; Avalos, J. B.; Mackie, A. D., Prediction of the critical micelle concentration in a lattice model for amphiphiles using a single-chain mean-field theory. *J. Chem. Phys.* **2005,** *122* (10).
14. de Bruijn, V. G.; van den Broeke, L. J. P.; Leermakers, F. A. M.; Keurentjes, J. T. F., Self-consistent-field analysis of poly(ethylene oxide)-poly(propylene oxide)-poly(ethylene oxide) surfactants: Micellar structure, critical micellization concentration, critical micellization temperature, and cloud point. *Langmuir* **2002,** *18* (26), 10467-10474.
15. Brodskaya, E. N., Computer simulations of micellar systems. *Colloid J.* **2012,** *74* (2), 154-171.
16. Nagarajan, R.; Ruckenstein, E., Theory of surfactant self-assembly: A predictive molecular thermodynamic approach. *Langmuir* **1991,** *7* (12), 2934-2969.
17. Puvvada, S.; Blankschtein, D., Molecular-Thermodynamic Approach to Predict Micellization, Phase-Behavior and Phase-Separation of Micellar Solutions .1. Application to Nonionic Surfactants. *J. Chem. Phys.* **1990,** *92* (6), 3710-3724.
18. Puvvada, S.; Blankschtein, D., Theoretical and Experimental Investigations of Micellar Properties of Aqueous-Solutions Containing Binary-Mixtures of Nonionic Surfactants. *J. Phys. Chem.* **1992,** *96* (13), 5579-5592.
19. Shiloach, A.; Blankschtein, D., Prediction of critical micelle concentrations and synergism of binary surfactant mixtures containing zwitterionic surfactants. *Langmuir* **1997,** *13* (15), 3968-3981.
20. Goldsipe, A.; Blankschtein, D., Molecular-thermodynamic theory of micellization of multicomponent surfactant mixtures: 2. pH-sensitive surfactants. *Langmuir* **2007,** *23* (11), 5953-5962.
21. Shiloach, A.; Blankschtein, D., Predicting micellar solution properties of binary surfactant mixtures. *Langmuir* **1998,** *14* (7), 1618-1636.
22. Blankschtein, D.; Thurston, G. M.; Benedek, G. B., Theory of Phase Separation in Micellar Solutions. *Phys. Rev. Lett.* **1985,** *54* (9), 955-958.
23. Nagarajan, R., Modeling Solution Entropy in the Theory of Micellization. *Colloids Surf. Physicochem. Eng. Aspects* **1993,** *71* (1), 39-64.

24. Blankschtein, D.; Thurston, G. M.; Benedek, G. B., Phenomenological Theory of Equilibrium Thermodynamic Properties and Phase-Separation of Micellar Solutions. *J. Chem. Phys.* **1986,** *85* (12), 7268-7288.
25. Kabalnov, A. S.; Makarov, K. N.; Shcherbakova, O. V., Solubility of Fluorocarbons in Water as a Key Parameter Determining Fluorocarbon Emulsion Stability. *J. Fluorine Chem.* **1990,** *50* (3), 271-284.
26. Srinivasan, V.; Blankschtein, D., Prediction of conformational characteristics and micellar solution properties of fluorocarbon surfactants. *Langmuir* **2005,** *21* (4), 1647-1660.
27. Tolman, R. C., The effect of droplet size on surface tension. *J. Chem. Phys.* **1949,** *17* (3), 333-337.
28. Srinivasan, V. Theoretical modeling of micellization and solubilization in ionic surfactant systems. Doctoral, Massachusetts Institute of Technology, Cambridge, 2003.
29. Tolman, R. C., Consideration of the Gibbs theory of surface tension. *J. Chem. Phys.* **1948,** *16* (8), 758-774.
30. Lin, S. A Computer Simulation and Molecular-Thermodynamic Framework to Model the Micellization of Ionic Branched Surfactants in Aqueous Solution Massachusetts Institute of Technology, Cambridge, MA, USA, 2008.
31. Puvvada, S. Theoretical and experimental studies of micellization and phase behavior of aqueous solutions of single and mixed surfactants. Massachusetts Institute of Technology, Cambridge, MA, USA, 1992.
32. Aveyard, R.; Briscoe, B. J.; Chapman, J., Adhesion at Alkane/Water and Ester/Water Interfaces. *J. Chem. Soc., Faraday Trans. I* **1972,** *68* (589), 10-&.
33. Nostro, P. L.; Chen, S. H., Aggregation of a Semifluorinated N-Alkane in Perfluorooctane. *J. Phys. Chem.* **1993,** *97* (24), 6535-6540.
34. Ben-Shaul, A.; Szleifer, I.; Gelbart, W. M., Chain Organization and Thermodynamics in Micelles and Bilayers .I. Theory. *J. Chem. Phys.* **1985,** *83* (7), 3597-3611.
35. Flory, P. J., *Statistical Mechanics of Chain Molecules*. Wiley-Interscience: New York, 1969.
36. Mattice, W. L., Suter, U. W., *Conformational Theory of Large Molecules: The Rotational Isomeric State Model in Macromolecular Systems*. Wiley: New York, 1994.

37. Bates, T. W.; Stockmayer, W. H., Conformational Properties of Isolated Polytetrafluoroethylene Chains. *J. Chem. Phys.* **1966,** *45* (6), 2321-2322.

38. Szleifer, I.; Benshaul, A.; Gelbart, W. M., Chain Statistics in Micelles and Bilayers - Effects of Surface-Roughness and Internal Energy. *J. Chem. Phys.* **1986,** *85* (9), 5345-5358.

39. Srinivasan, V.; Blankschtein, D., Effect of counterion binding on micellar solution behavior: 1. Molecular-thermodynamic theory of micellization of ionic surfactants. *Langmuir* **2003,** *19* (23), 9932-9945.

40. Bockris, J. O. M.; Reddy, A. K. N., *Modern Electrochemistry*. Plenum Press: New York, 1970; Vol. 1.

41. Halliday, D., Resnick, R., Walker, J. , *Fundamentals of Physcis*. John Wiley & Sons, Inc: 2011.

42. Ohshima, H.; Healy, T. W.; White, L. R., Accurate Analytic Expressions for the Surface-Charge Density Surface-Potential Relationship and Double-Layer Potential Distribution for a Spherical Colloidal Particle. *J. Colloid Interface Sci.* **1982,** *90* (1), 17-26.

43. Goldsipe, A. Molecular-Thermodynamic theories of micellization of multicomponent surfactant mixtures and of pH-sensitive surfactants. Doctoral Thesis, Massachusetts Institute of Technology, Cambridge, 2006.

44. Stephenson, B. C.; Beers, K. J.; Blankschtein, D., Quantifying the hydrophobic effect. 3. A computer simulation-molecular-thermodynamic model for the micellization of ionic and zwitterionic surfactants in aqueous solution. *J. Phys. Chem. B* **2007,** *111* (5), 1063-1075.

45. Stephenson, B. C.; Goldsipe, A.; Beers, K. J.; Blankschtein, D., Quantifying the hydrophobic effect. 1. A computer simulation-molecular-thermodynamic model for the self-assembly of hydrophobic and amphiphilic solutes in aqueous solution. *J. Phys. Chem. B* **2007,** *111* (5), 1025-1044.

46. Stephenson, B. C.; Goldsipe, A.; Beers, K. J.; Blankschtein, D., Quantifying the hydrophobic effect. 2. A computer simulation-molecular-thermodynamic model for the micellization of nonionic surfactants in aqueous solution. *J. Phys. Chem. B* **2007,** *111* (5), 1045-1062.

47. Mendenhall, J. D. Theoretical and Simulations-Based Modeling of Micellization in Linear and Branched Surfactant Systems. Massachusetts Institute of Technology, Cambridge, 2012.
48. Reynolds, J. A.; Gilbert, D. B.; Tanford, C., Empirical Correlation between Hydrophobic Free-Energy and Aqueous Cavity Surface-Area. *Proceedings of the National Academy of Sciences of the United States of America* **1974,** *71* (8), 2925-2927.
49. Lee, B.; Richards, F. M., Interpretation of Protein Structures - Estimation of Static Accessibility. *J. Mol. Biol.* **1971,** *55* (3), 379-&.
50. Iijima, H.; Kato, T.; Yoshida, H.; Imai, M., Small-angle X-ray and neutron scattering from dilute solutions of cesium perfluorooctanoate. Micellar growth along two dimensions. *J. Phys. Chem. B* **1997,** *102* (6), 990-995.
51. Holmes, M. C.; Reynolds, D. J.; Boden, N., Concentration-temperature dependence of the size and shape of the micelles in the cesium pentadecafluorooctanoate/water system. *J. Phys. Chem.* **1987,** *91* (20), 5257-5262.
52. Kawaguchi, T.; Hamanaka, T.; Kito, Y.; Machida, H., Structural Studies of a Homologous Series of Alkyl Sucrose Ester Micelle by X-Ray-Scattering. *J. Phys. Chem.* **1991,** *95* (9), 3837-3846.
53. Caetano, W., Gelamo, E. L., Tabak, M., Itri, R., Chlorpromazine and sodium dodecyl sulfate mixed micelles investigated by small angle X-ray scattering. *J. Colloid Interface Sci.* **2002,** *248* (1), 149-157.
54. Sarkar, B., Lam, S., Alexandridis, P., Micellization of alkyl-propoxy-ethoxylate surfactants in water-polar organic solvent mixtures. *Langmuir* **2010,** *26* (13), 10532-10540.
55. Millman, R. S., Parker, G. D., *Elements of Differential Geometry*. Prentice-Hall: Englewood Cliffs, N. J. , 1977.
56. Gibbs, J. W., *The Collected Works of J. Willard Gibbs*. Longmans, Green and Co. : New York, 1928; Vol. 1.
57. Taddei, G., Relative Stability of Micellar Forms. *J. Chem. Soc., Faraday Trans.* **1993,** *89* (11), 1749-1751.
58. Taddei, G., Micelle Form and Stability. *Colloid. Polym. Sci.* **1994,** *272* (10), 1300-1305.

59. Ivory, J., A new series for the rectification of the ellipse. *Transactions of the Royal Society of Edinburgh* **1796,** *4* (II), 177-190.
60. Iijima, H.; Koyama, S.; Fujio, K.; Uzu, Y., NMR study of the transformation of perfluorinated surfactant solutions. **1997**.
61. Tanford, C., Nozaki, Y., Rohde, M. F., Size and shape of globular micelles formed in aqueous solution by n-alkyl polyoxyethylene ethers. *J. Phys. Chem.* **1977,** *81* (16), 1555-1560.
62. Clint, J. H., *Surfactant aggregation*. Chapman and Hall: New York, 1992.
63. Israelachvili, J. N.; Mitchell, D. J.; Ninham, B. W., Theory of Self-Assembly of Hydrocarbon Amphiphiles into Micelles and Bilayers. *Journal of the Chemical Society, Faraday Transactions 2* **1976,** *72*, 1525-1568.
64. Tartar, H. V., A Theory of the structure of the micelles of normal paraffin-chain salts in aqueous solution. *J. Phys. Chem.* **1955,** *59* (12), 1195-1199.
65. Tanford, C., Micelle shape and size. *J. Phys. Chem.* **1972,** *76* (21), 3020-3024.
66. Leibner, J. E.; Jacobus, J., Charged Micelle Shape and Size. *J. Phys. Chem.* **1977,** *81* (2), 130-135.
67. Halle, B., Landgren, M., Jonsson, B., The shape of ionic micelles. *J. Phys.* **1988,** *49* (7), 1235-1259.
68. Borkovec, M., Phenomenological Theories of Globular Microemulsions. *Adv. Colloid Interface Sci.* **1992,** *37* (3-4), 195-217.
69. Hill, R. M., *Applications of Surfactant Mixtures*. Marcel Dekker: New York, 1993; Vol. 46.
70. Holland, P. M.; Rubingh, D. N., *Mixed Surfactant Systems: An overview*. American Chemical Society: Washington DC, 1992.
71. Clint, J. H., Micellization of Mixed Nonionic Surface-Active Agents. *J. Chem. Soc., Faraday Trans. I* **1975,** *71* (6), 1327-1334.
72. Holland, P. M.; Rubingh, D. N., Nonideal Multicomponent Mixed Micelle Model. *J. Phys. Chem.* **1983,** *87* (11), 1984-1990.
73. Hao, L. S.; Deng, Y. T.; Zhou, L. S.; Ye, H.; Nan, Y. Q.; Hu, P., Mixed Micellization and the Dissociated Margules Model for Cationic/Anionic Surfactant Systems. *J. Phys. Chem. B* **2012,** *116* (17), 5213-5225.

74. Georgiev, G. S., Markov chain model of mixed surfactant systems .1. New expression for the non ideal interaction parameter. *Colloid. Polym. Sci.* **1996,** *274* (1), 49-58.
75. Zaldivar, M.; Larson, R. G., Lattice Monte Carlo simulations of dilute mixed micelles. *Langmuir* **2003,** *19* (24), 10434-10442.
76. Gharibi, H.; Hashemianzadeh, S. M.; Razavizadeh, B. M., Determination of interaction parameters of mixed surfactant system using a Monte Carlo simulation technique. *Colloids Surf., A* **2002,** *196* (1), 31-38.
77. Rodriguez-Guadarrama, L. A.; Ramanathana, S.; Mohanty, K. K.; Vasquez, V., Molecular modeling of binary mixtures of amphiphiles in a lattice solution. *Fluid Phase Equilib.* **2004,** *226*, 27-36.
78. Poorgholami-Bejarpasi, N.; Hashemianzadeh, M.; Mousavi-Khoshdel, S. M.; Sohrabi, B., Investigation of the mixing behavior of surfactants by lattice Monte Carlo simulation. *J. Mol. Model.* **2010,** *16* (9), 1499-1508.
79. Davis, J. R.; Panagiotopoulos, A. Z., Micellization and phase separation in binary amphiphile mixtures. *Mol. Phys.* **2009,** *107* (22), 2359-2366.
80. Nagarajan, R., Molecular Theory for Mixed Micelles. *Langmuir* **1985,** *1* (3), 331-341.
81. Goldsipe, A.; Blankschtein, D., Molecular-thermodynamic theory of micellization of multicomponent surfactant mixtures: 1. Conventional (pH-insensitive) surfactants. *Langmuir* **2007,** *23* (11), 5942-5952.
82. Shiloach, A.; Blankschtein, D., Measurement and prediction of ionic/nonionic mixed micelle formation and growth. *Langmuir* **1998,** *14* (25), 7166-7182.
83. Nagarajan, R., Micellization of binary surfactant mixtures: Theory. In *Mixed Surfactant Systems*, Holland, P. M.; Rubingh, D. N., Eds. American Chemical Society: Washington DC, 1992; Vol. 501.
84. Liu, X. Y., Molecular modeling for nonideal mixing of amphiphilic molecules and applications to ionic surfactant/salt solutions. *Langmuir* **2002,** *18* (1), 14-25.
85. Bruce, C. D.; Berkowitz, M. L.; Perera, L.; Forbes, M. D. E., Molecular dynamics simulation of sodium dodecyl sulfate micelle in water: Micellar structural characteristics and counterion distribution. *J. Phys. Chem. B* **2002,** *106* (15), 3788-3793.
86. Bogusz, S.; Venable, R. M.; Pastor, R. W., Molecular dynamics simulations of octyl glucoside micelles: Structural properties. *J. Phys. Chem. B* **2000,** *104* (23), 5462-5470.

87. Tieleman, D. P.; van der Spoel, D.; Berendsen, H. J. C., Molecular dynamics simulations of dodecylphosphocholine micelles at three different aggregate sizes: Micellar structure and chain relaxation. *J. Phys. Chem. B* **2000,** *104* (27), 6380-6388.

88. Garde, S.; Yang, L.; Dordick, J. S.; Paulaitis, M. E., Molecular dynamics simulation of C8E5 micelle in explicit water: structure and hydrophobic solvation thermodynamics. *Mol. Phys.* **2002,** *100* (14), 2299-2306.

89. Pool, R.; Bolhuis, P. G., Accurate free energies of micelle formation. *J. Phys. Chem. B* **2005,** *109* (14), 6650-6657.

90. Mohanty, S.; Davis, H. T.; McCormick, A. V., Complementary use of simulations and free energy models for CTAB/NaSal systems. *Langmuir* **2001,** *17* (22), 7160-7171.

91. Jusufi, A.; LeBard, D. N.; Levine, B. G.; Klein, M. L., Surfactant Concentration Effects on Micellar Properties. *J. Phys. Chem. B* **2012,** *116* (3), 987-991.

92. Jusufi, A.; Sanders, S.; Klein, M. L.; Panagiotopoulos, A. Z., Implicit-Solvent Models for Micellization: Nonionic Surfactants and Temperature-Dependent Properties. *J. Phys. Chem. B* **2011,** *115* (5), 990-1001.

93. Levine, B. G.; LeBard, D. N.; DeVane, R.; Shinoda, W.; Kohlmeyer, A.; Klein, M. L., Micellization Studied by GPU-Accelerated Coarse-Grained Molecular Dynamics. *Journal of Chemical Theory and Computation* **2011,** *7* (12), 4135-4145.

94. Sanders, S. A.; Sammalkorpi, M.; Panagiotopoulos, A. Z., Atomistic Simulations of Micellization of Sodium Hexyl, Heptyl, Octyl, and Nonyl Sulfates. *J. Phys. Chem. B* **2012,** *116* (8), 2430-2437.

95. Yakovlev, D. S.; Boek, E. S., Molecular dynamics simulations of mixed cationic/anionic wormlike micelles. *Langmuir* **2007,** *23* (12), 6588-6597.

96. Ferreira, M. L.; Sierra, M. B.; Morini, M. A.; Rodriguez, J. L.; Minardi, R.; Schulz, P. C., Explanation of Experimental Results of Mixed Micelles of Homologous Surfactants through a Mm2 Bidimensional Modeling. *J. Phys. Chem. B* **2010,** *114* (46), 14924-14933.

97. Stephenson, B. C.; Stafford, K. A.; Beers, K. J.; Blankschtein, D., Application of computer simulation free-energy methods to compute the free energy of micellization as a function of micelle composition. 1. Theory. *J. Phys. Chem. B* **2008,** *112* (6), 1634-1640.

98. Stephenson, B. C.; Stafford, K. A.; Beers, K. J.; Blankschtein, D., Application of computer simulation free-energy methods to compute the free energy of micellization as a function of micelle composition. 2. Implementation. *J. Phys. Chem. B* **2008,** *112* (6), 1641-1656.

99. Goldsipe, A.; Blankschtein, D., Modeling counterion binding in ionic-nonionic and ionic-zwitterionic binary surfactant mixtures. *Langmuir* **2005,** *21* (22), 9850-9865.

100. Hess, B.; Kutzner, C.; van der Spoel, D.; Lindahl, E., GROMACS 4: Algorithms for highly efficient, load-balanced, and scalable molecular simulation. *Journal of Chemical Theory and Computation* **2008,** *4* (3), 435-447.

101. Van der Spoel, D.; Lindahl, E.; Hess, B.; Groenhof, G.; Mark, A. E.; Berendsen, H. J. C., GROMACS: Fast, flexible, and free. *J. Comput. Chem.* **2005,** *26* (16), 1701-1718.

102. Jorgensen, W. L.; Maxwell, D. S.; TiradoRives, J., Development and testing of the OPLS all-atom force field on conformational energetics and properties of organic liquids. *J. Am. Chem. Soc.* **1996,** *118* (45), 11225-11236.

103. Jorgensen, W. L.; Tiradorives, J., The Opls Potential Functions for Proteins - Energy Minimizations for Crystals of Cyclic-Peptides and Crambin. *J. Am. Chem. Soc.* **1988,** *110* (6), 1657-1666.

104. Lopes, J. N. C.; Padua, A. A. H.; Shimizu, K., Molecular force field for ionic liquids IV: Trialkylimidazolium and alkoxycarbonyl-imidazolium cations; alkylsulfonate and alkylsulfate anions. *J. Phys. Chem. B* **2008,** *112* (16), 5039-5046.

105. Anderson, P. M.; Wilson, M. R., Developing a force field for simulation of poly(ethylene oxide) based upon ab initio calculations of 1,2-dimethoxyethane. *Mol. Phys.* **2005,** *103* (1), 89-97.

106. Berendsen, H. J. C.; Grigera, J. R.; Straatsma, T. P., The Missing Term in Effective Pair Potentials. *J. Phys. Chem.* **1987,** *91* (24), 6269-6271.

107. van der Spoel, D.; Lindahl, E.; Hess, B.; van Buuren, A. R.; Apol, E.; Meulenhoff, P. J.; Tieleman, D. P.; Sijbers, A. L. T. M.; Feenstra, K. A.; van Drunen, R.; Berendsen, H. J. C., *Gromacs User Manual version 4.5.4*. Uppsala University, Sweden, 2010.

108. Darden, T.; York, D.; Pedersen, L., Particle Mesh Ewald - an N.Log(N) Method for Ewald Sums in Large Systems. *J. Chem. Phys.* **1993,** *98* (12), 10089-10092.

109. Essmann, U.; Perera, L.; Berkowitz, M. L.; Darden, T.; Lee, H.; Pedersen, L. G., A Smooth Particle Mesh Ewald Method. *J. Chem. Phys.* **1995,** *103* (19), 8577-8593.

110. Deserno, M.; Holm, C., How to mesh up Ewald sums. I. A theoretical and numerical comparison of various particle mesh routines. *J. Chem. Phys.* **1998,** *109* (18), 7678-7693.

111. Bussi, G.; Donadio, D.; Parrinello, M., Canonical sampling through velocity rescaling. *J. Chem. Phys.* **2007,** *126* (1).

112. Berendsen, H. J. C.; Postma, J. P. M.; Vangunsteren, W. F.; Dinola, A.; Haak, J. R., Molecular-Dynamics with Coupling to an External Bath. *J. Chem. Phys.* **1984,** *81* (8), 3684-3690.

113. Yoda, K.; Tamori, K.; Esumi, K.; Meguro, K., Critical Micelle Concentrations of Fluorocarbon Surfactant Mixtures in Aqueous-Solution. *J. Colloid Interface Sci.* **1989,** *131* (1), 282-283.

114. Mysels, K. J.; Otter, R. J., Conductivity of Mixed Sodium Decyl and Dodecyl Sulfates - Composition of Mixed Micelles. *Journal of Colloid Science* **1961,** *16* (5), 462-&.

115. Bergstrom, M.; Jonsson, P.; Persson, M.; Eriksson, J. C., A model-independent evaluation of experimental data, and comparison with theory, of synergistic effects in mixtures of an ionic and a nonionic surfactant. *Langmuir* **2003,** *19* (26), 10719-10725.

116. Matsubara, H.; Muroi, S.; Kameda, M.; Ikeda, N.; Ohta, A.; Aratono, M., Interaction between ionic and nonionic surfactants in the adsorbed film and micelle. 3. Sodium dodecyl sulfate and tetraethylene glycol monooctyl ether. *Langmuir* **2001,** *17* (25), 7752-7757.

117. Hua, X. Y.; Rosen, M. J., Synergism in Binary-Mixtures of Surfactants .1. Theoretical-Analysis. *J. Colloid Interface Sci.* **1982,** *90* (1), 212-219.

118. Kennedy, G. L.; Butenhoff, J. L.; Olsen, G. W.; O'Connor, J. C.; Seacat, A. M.; Perkins, R. G.; Biegel, L. B.; Murphy, S. R.; Farrar, D. G., The toxicology of perfluorooctanoate. *Crit. Rev. Toxicol.* **2004,** *34* (4), 351-384.

119. Scott, R. L., The anomalous behavior of fluorocarbon solutions. *J. Phys. Chem.* **1957,** *62*, 136-145.

120. Mukerjee, P.; Yang, A. Y. S., Nonideality of Mixing of Micelles of Fluorocarbon and Hydrocarbon Surfactants and Evidence of Partial Miscibility from Differential Conductance Data. *J. Phys. Chem.* **1976,** *80* (12), 1388-1390.

121. Aratono, M.; Ikeguchi, M.; Takiue, T.; Ikeda, N.; Motomura, K., Thermodynamic Study on the Miscibility of Sodium Perfluorooctanoate and Sodium Decyl Sulfate in the Adsorbed Film and Micelle. *J. Colloid Interface Sci.* **1995,** *174* (1), 156-161.

122. Shinoda, K.; Nomura, T., Miscibility of Fluorocarbon and Hydrocarbon Surfactants in Micelles and Liquid-Mixtures - Basic Studies of Oil Repellent and Fire Extinguishing Agents. *J. Phys. Chem.* **1980,** *84* (4), 365-369.

123. Kamogawa, K.; Tajima, K., Distinctive Behavior of the Esr Correlation Times of Doxyl Spin Probes in Mixed Micellar Solutions of Hydrocarbon and Fluorocarbon Surfactants. *J. Phys. Chem.* **1993,** *97* (37), 9506-9512.

124. Nordstierna, L.; Furo, I.; Stilbs, P., Mixed micelles of fluorinated and hydrogenated surfactants. *J. Am. Chem. Soc.* **2006,** *128* (20), 6704-6712.

125. Xing, R.; Lehmler, H. J.; Knutson, B. L.; Rankin, S. E., Synthesis and Tuning of Bimodal Mesoporous Silica by Combined Hydrocarbon/Fluorocarbon Surfactant Templating. *Langmuir* **2009,** *25* (11), 6486-6492.

126. Groenewolt, M.; Antonietti, M.; Polarz, S., Mixed micellar phases of nonmiscible surfactants: Mesoporous silica with bimodal pore size distribution via the nanocasting process. *Langmuir* **2004,** *20* (18), 7811-7819.

127. GilVillegas, A.; Galindo, A.; Whitehead, P. J.; Mills, S. J.; Jackson, G.; Burgess, A. N., Statistical associating fluid theory for chain molecules with attractive potentials of variable range. *J. Chem. Phys.* **1997,** *106* (10), 4168-4186.

128. McCabe, C.; Galindo, A.; Gil-Villegas, A.; Jackson, G., Predicting the high-pressure phase equilibria of binary mixtures of perfluoro-n-alkanes plus n-alkanes using the SAFT-VR approach. *J. Phys. Chem. B* **1998,** *102* (41), 8060-8069.

129. Morgado, P.; McCabe, C.; Filipe, E. J. M., Modelling the phase behaviour and excess properties of alkane plus perfluoroalkane binary mixtures with the SAFT-VR approach. *Fluid Phase Equilib.* **2005,** *228*, 389-393.

130. de Melo, M. J. P.; Dias, A. M. A.; Blesic, M.; Rebelo, L. P. N.; Vega, L. F.; Coutinho, J. A. P.; Marrucho, I. M., Liquid-liquid equilibrium of (perfluoroalkane + alkane) binary mixtures. *Fluid Phase Equilib.* **2006,** *242* (2), 210-219.

131. Kyle, B. G.; Reed, T. M., Free Energy Relations in Fluorocarbon-Hydrocarbon Systems. *J. Am. Chem. Soc.* **1958,** *80* (23), 6170-6177.

132. Williamson, A. G.; Scott, R. L., Heats of Mixing of Non-Electrolyte Solutions .2. Perfluoro-N-Heptane and Isooctane and Perfluoro-N-Hexane and N-Hexane. *J. Phys. Chem.* **1961,** *65* (2), 275-&.

133. Duce, C.; Tine, M. R.; Lepori, L.; Matteoli, E., VLE and LLE of perfluoroalkane plus alkane mixtures. *Fluid Phase Equilib.* **2002,** *199* (1-2), 197-212.

134. Duce, C.; Tine, M. R.; Lepori, L.; Matteoli, E.; Marongiu, B.; Piras, A., A comparative study of thermodynamic properties of binary mixtures containing perfluoroalkanes. *J. Therm. Anal. Calorim.* **2008,** *92* (1), 145-154.

135. Dobrjakov, Y. G.; Balashova, I. M.; Maurer, G., Experimental results for the limiting activity coefficients in some binary and ternary mixtures of organic components. *J. Chem. Eng. Data* **2000,** *45* (2), 185-193.

136. Ruckenstein, E.; Nagarajan, R., Critical Micelle Concentration - Transition Point for Micellar Size Distribution. *J. Phys. Chem.* **1975,** *79* (24), 2622-2626.

137. Semenov, A. N., Contribution to the theory of microphase layering in block-copolymer melts. *Soviet Physics JETP* **1985,** *61* (4), 733-742.

138. Esumi, K.; Arai, T.; Takasugi, K., Mixed micellar properties of octyl-beta-D-glucoside and lithium perfluorooctane sulfonate. *Colloids Surf., A* **1996,** *111* (3), 231-234.

139. Sugihara, G., Nakamura, D., Okawauchi, M., Sakai, S., Kuriyama, K., Tanaka, M., Pressure effect on micelle formation of mixed systems of sodium perfluorooctanoate with hydrocarbon surfactants - sodium dodecyl sulfate and sodium decyl sulfate. *Fukuoka University Science Reports* **1987,** *17* (2), 31-40.

140. Kamrath, R. F.; Franses, E. I., Thermodynamics of Mixed Micellization - Pseudo-Phase Separation Models. *Industrial & Engineering Chemistry Fundamentals* **1983,** *22* (2), 230-239.

141. Pedone, L.; Martino, D. C.; Caponetti, E.; Floriano, M. A.; Triolo, R., Determination of the composition of mixed hydrogenated and fluorinated micelles by small angle neutron scattering. *J. Phys. Chem. B* **1997,** *101* (46), 9525-9531.

142. Caponetti, E.; Martino, D. C.; Floriano, M. A.; Triolo, R., Fluorinated, Protonated, and Mixed Surfactant Solutions - a Small-Angle Neutron-Scattering Study. *Langmuir* **1993,** *9* (5), 1193-1200.

143. DeLisi, R.; Inglese, A.; Milioto, S.; Pellerito, A., Demixing of mixed micelles. Thermodynamics of sodium perfluorooctanoate sodium dodecanoate mixtures in water. *Langmuir* **1997,** *13* (2), 192-202.

144. Roscigno, P.; Paduano, L.; D'Errico, G.; Vitagliano, V., On the presumed specific interaction of anionic surfactants with nonionic polymers. Aqueous solution of sodium alkylsulfonate in the presence of poly(vinylpyrrolidone): An "excluded volume" effect. *Langmuir* **2001,** *17* (15), 4510-4518.

145. Mukerjee, P.; Mysels, K. J., *Critical Micelle Concentrations of Aqueous Surfactant Systems*. United States Government: Washington D. C., 1971.

146. Nakano, T. Y.; Sugihara, G.; Nakashima, T.; Yu, S. C., Thermodynamic study of mixed hydrocarbon/fluorocarbon surfactant system by conductometric and fluorimetric techniques. *Langmuir* **2002,** *18* (23), 8777-8785.

147. Pirard, B.; Baudoux, G.; Durant, F., A Database Study of Intermolecular Nh-Center-Dot-Center-Dot-Center-Dot-O Hydrogen-Bonds for Carboxylates, Sulfonates and Monohydrogen Phosphonates. *Acta Crystallographica Section B-Structural Science* **1995,** *51*, 103-107.

148. Allen, M. P.; Tildesley, D. J., *Computer Simulation of Liquids*. Oxford University Press: New York, 2002.

149. Cooper, R. S., Anionic Phosphate Surfactants. *J. Am. Oil Chem. Soc.* **1963,** *40* (11), 642-&.

150. Hagslatt, H.; Soderman, O.; Jonsson, B., Divalent Surfactants - Experimental Results and Theoretical Modeling of Surfactant Water Phase-Equilibria. *Langmuir* **1994,** *10* (7), 2177-2187.

151. Aoi, T., On Spheroidal Functions. *J. Phys. Soc. Jpn.* **1955,** *10* (2), 130-141.

152. Yoon, B. J.; Kim, S., Electrophoresis of Spheroidal Particles. *J. Colloid Interface Sci.* **1989,** *128* (1), 275-288.

153. Hsu, J. P.; Liu, B. T., Exact solution to the linearized Poisson-Boltzmann equation for spheroidal surfaces. *J. Colloid Interface Sci.* **1996,** *178* (2), 785-788.

154. Hsu, J. P.; Liu, B. T., Solution to the linearized Poisson-Boltzmann equation for a spheroidal surface under a general surface condition. *J. Colloid Interface Sci.* **1996,** *183* (1), 214-222.

155. Hsu, J. P.; Liu, B. T., Electrostatic potential distribution for spheroidal surfaces in symmetric electrolyte solutions. *J. Colloid Interface Sci.* **1997,** *192* (2), 481-489.

156. Cade, R., Perturbation Method for Solving Torus Problems in Electrostatics. *Journal of the Institute of Mathematics and Its Applications* **1978,** *21* (3), 265-284.

157. Andrews, M., Alternative separation of Laplace's equation in toroidal coordinates and its application to electrostatics. *J. Electrostatics* **2006,** *64* (10), 664-672.

158. Dupont, A.; Eastoe, J.; Martin, L., Hybrid fluorocarbon-hydrocarbon CO2-philic surfactants. 2. Formation and properties of water-in-CO2 microemulsions. *Langmuir* **2004,** *20* (23), 9960-9967.

159. Acosta, E. J.; Taylor, C. K. Mixed fluoroalkyl-alkyl surfactants. US8263670 B2, Sep 11, 2012, 2012.

160. Taylor, C. K.; Michalczyk, M. J.; Acosta, E. J. Mixed fluoroalkyl-alkyl surfactants. US 7728163 B2, 2010.

161. Hisatomi, M.; Abe, M.; Yoshino, N.; Lee, S.; Nagadome, S.; Sugihara, G., Thermodynamic study on surface adsorption and micelle formation of a hybrid anionic surfactant in water by surface tension (drop volume) measurements. *Langmuir* **2000,** *16* (4), 1515-1521.

162. Ito, A.; Sakai, H.; Kondo, Y.; Yoshino, N.; Abe, M., Micellar solution properties of fluorocarbon-hydrocarbon hybrid surfactants. *Langmuir* **1996,** *12* (24), 5768-5772.

163. Downer, A.; Eastoe, J.; Pitt, A. R.; Simister, E. A.; Penfold, J., Effects of hydrophobic chain structure on adsorption of fluorocarbon surfactants with either CF3- or H-CF2-terminal groups. *Langmuir* **1999,** *15* (22), 7591-7599.

164. Eastoe, J.; Paul, A.; Rankin, A.; Wat, R.; Penfold, J.; Webster, J. R. P., Fluorinated nonionic surfactants bearing either CF3- or H-CF2- terminal groups: Adsorption at the surface of aqueous solutions. *Langmuir* **2001,** *17* (25), 7873-7878.

165. Lebaupain, F.; Salvay, A. G.; Olivier, B.; Durand, G.; Fabiano, A. S.; Michel, N.; Popot, J. L.; Ebel, C.; Breyton, C.; Pucci, B., Lactobionamide surfactants with hydrogenated, perfluorinated or hemifluorinated tails: Physical-chemical and biochemical characterization. *Langmuir* **2006,** *22* (21), 8881-8890.

166. Mohamed, A.; Sagisaka, M.; Guittard, F.; Cummings, S.; Paul, A.; Rogers, S. E.; Heenan, R. K.; Dyer, R.; Eastoe, J., Low Fluorine Content CO2-philic Surfactants. *Langmuir* **2011,** *27* (17), 10562-10569.

167. Sarmoria, C.; Blankschtein, D., Conformational Characteristics of Short Poly(Ethylene Oxide) Chains Terminally Attached to a Wall and Free in Aqueous-Solution. *J. Phys. Chem.* **1992,** *96* (4), 1978-1983.